Springer Series in Optical Sciences 202

Juan Jimenez
Jens W. Tomm

Spectroscopic Analysis of Optoelectronic Semiconductors

Springer

Springer Series in Optical Sciences

Volume 202

Springer Series in Optical Sciences

The Springer Series in Optical Sciences, under the leadership of Editor-in-Chief William T. Rhodes, Georgia Institute of Technology, USA, provides an expanding selection of research monographs in all major areas of optics: lasers and quantum optics, ultrafast phenomena, optical spectroscopy techniques, optoelectronics, quantum information, information optics, applied laser technology, industrial applications, and other topics of contemporary interest.

With this broad coverage of topics, the series is of use to all research scientists and engineers who need up-to-date reference books.

The editors encourage prospective authors to correspond with them in advance of submitting a manuscript. Submission of manuscripts should be made to the Editor-in-Chief or one of the Editors. See also www.springer.com/series/624

More information about this series at http://www.springer.com/series/624

Juan Jimenez · Jens W. Tomm

Spectroscopic Analysis of Optoelectronic Semiconductors

Springer

Juan Jimenez
Condensed Matter Physics
University of Valladolid
Valladolid
Spain

Jens W. Tomm
Max-Born-Institut für Nichtlineare Optik
und Kurzzeitspektroskopie
Berlin
Germany

ISSN 0342-4111 ISSN 1556-1534 (electronic)
Springer Series in Optical Sciences
ISBN 978-3-319-42347-0 ISBN 978-3-319-42349-4 (eBook)
DOI 10.1007/978-3-319-42349-4

Library of Congress Control Number: 2016945144

Printed on acid-free paper

This Springer imprint is published by Springer Nature
The registered company is Springer International Publishing AG Switzerland

Preface

The book is written by two semiconductor physicists, who as experimentalists have used spectroscopic techniques throughout their entire careers. The main goal of their work has been the investigation of the properties of bulk semiconductor materials, epitaxial structures, nanostructures, as well as devices made from these materials. Thus, the text comprises their experience as experimentalists and was written to help experimentalists, e.g. Master or Ph.D. students in physics and engineering, to choose and understand the right analytical spectroscopic technique in order to extract specific information from their samples. It is also useful for people in academia and industry, who have to plan the application of spectroscopic techniques for characterization purposes and have to decide on the purchase the corresponding spectroscopic equipment. Moreover, it can serve as a general introduction to those who are interested in optical spectroscopy.

Thus, the book intends to be a guide to the field of optical spectroscopy. It addresses the potentials and limitations of four groups of spectroscopic techniques that are used for analytical purposes. These are *Raman*, *photoluminescence*, *cathodoluminescence*, and *photoelectrical spectroscopy*, which were selected because of their paramount relevance for the characterization of semiconductors. These techniques give the names to Chaps. 3–6 and make out the main body of this book. There are two additional chapters, Chaps. 1 and 2, which provide the knowledge base for these chapters. Chapter 1 gives an introduction to the subject of the spectroscopy of semiconductors. The basic mechanisms and equations which describe light–matter interaction are outlined and discussed in a textbook-like style. Chapter 2 gives an introduction into the basics of optical spectroscopy from an experimental point of view. Thus, Chap. 2 is like a link between the textbook

knowledge in Chap. 1, which addresses predominantly mechanisms, and the specialized information in Chaps. 3–6. Chapter 2, however, is organized in the same way as the "advanced" Chaps. 3–6. Their structure includes the following elements:

- At the beginning of the chapters *spectra* are presented and it is discussed how they are typically displayed.
- *Samples* and sample geometries are discussed. This leads to the "probed sample volume", to spatial resolution limits of the techniques, and to the question about "information depths".
- The topic of spectroscopic *equipment* is addressed. In some cases, like in Chap. 2, we mainly refer to commercial products. In other cases, as in Chaps. 4 and 6, guidelines are given on how to construct a setup.
- In all chapters, *methodology* is addressed. Parameters that can be varied are discussed. Different approaches, such as steady-state and transient methods are described, and the expected outcome is discussed.
- The *mechanisms* that form the spectra are addressed on the basis of the general knowledge which is provided in Chap. 1. This also includes the link to theory, which is not the topic of this book. This approach leads to the topic of the information that might be extracted from the spectra. This extraction is, of course, the goal of any analysis.
- Related or *derived techniques* are discussed. This includes, in particular, mapping and imaging approaches, i.e. multiple measurements at different locations on the samples. Many special spectroscopic techniques are introduced, as well, and their relationship to the standard techniques is indicated.
- Different *applications* are addressed. This includes cases studies and guidelines on how to analyze complex structures.

Most spectra, which are used in order to illustrate the text, are taken from original papers. This provides the link to current experimental results in the literature. They have been selected from the point of view of clarity and, at least in part, from the point of view of beauty.

Valladolid, Spain — Juan Jimenez
Berlin, Germany — Jens W. Tomm

Contents

Chapter 1
Introduction

Abstract This chapter gives an introduction to the *basics of light-matter interaction* in semiconductors, aiming to provide the readers with the background necessary to follow the other chapters of this book. In this chapter topics are addresses, such as the band structure, the density of states, quasi particles and elementary excitations, the optical constants (dielectric function), the role of the free carriers, the influence of temperature and stress on the optical response of semiconductors, the optical transitions, both absorption and emission; also, a description of the main defects in semiconductors. Their role in the optical properties is included, and the physics of low dimensional semiconductor structures in relation to the optical properties is also a matter of discussion.

1.1 Introduction

Since the 60s of last century optoelectronics started to have a relevant presence in diverse applications, especially telecommunications, photoelectric detectors, data displays, optical storage, and light sources, among other. This development was propitiated by the accomplishment of technological breakthroughs in the field of semiconductor materials. In particular, the advances in the semiconductor growth technologies were crucial for the development of the new optoelectronic devices. The development of semiconductor structures, and devices, demands a strong effort of comprehension of the semiconductor properties at different scales. In this sense, there is an increasing request of experimental techniques enabling the understanding of the main properties of semiconductor materials, both as grown, and after processing, e.g. annealing [1], ion implantation [2, 3], wet and dry etching [4–6], impurity diffusion [7], and other processes related to reduced size structures, e.g., QW intermixing [8]. The understanding of the basic optical phenomena in semiconductors is crucial not only for the design of optoelectronic devices, but also for achieving advances in the development of semiconductor structures allowing for new device concepts, e.g. semiconductor photonic crystals.

J. Jimenez and J.W. Tomm, *Spectroscopic Analysis of Optoelectronic Semiconductors*, Springer Series in Optical Sciences 202,
DOI 10.1007/978-3-319-42349-4_1

An optoelectronic device is an electronic device operating with light; therefore, it is subjected to the mechanisms of interaction between solids and light. Optoelectronic semiconductors have properties that can differ from those used in electronics, which is mainly dominated by Si, while its presence in optoelectronics is restricted to photoelectric devices. The semiconductors most widely used in optoelectronics are the III–V compounds and their alloys, and recently the wide bandgap semiconductors, mainly the III-nitrides; which many of them are direct band gap materials. Furthermore, their miscibility offers great possibilities for band gap engineering by alloying different compounds. In spite of the reduced route of some semiconductors in optoelectronics applications, the optical characterization methods are very powerful for the study of any type of semiconductors [9].

The rapid advances in semiconductor manufacturing and the associated technologies have increased the need of optical techniques for the semiconductor analysis, and in situ monitoring/control applications. Optical characterization techniques are unique for studying semiconductor properties: (i) they are non-invasive, (ii) they permit remote sensing; therefore, they are useful for in situ analysis; e.g. growth and other technological steps; (iii) they permit a high spatial resolution allowing to acquire maps of different properties of semiconductors in its diverse forms, from bulk materials to devices; (iv) the use of short laser pulses and fast detectors allows ultrafast phenomena to be investigated; (v) the availability of high sensitive multichannel detectors permits very fast spectral data acquisition suitable for in situ monitoring, but also the acquisition of very rich spectrum maps in reasonably time; (vi) they supply information on crystal quality, but also on lattice disturbances, or symmetry breakdown; (vii) they provide information on a large range of physical properties, e.g. stress, temperature, bandgap, thermal and electrical transport, alloy composition [10–15]; also information about defects and impurities is accessible to optical experiments [16–20]; finally, many optical techniques can be implemented at the production scale.

In this chapter, a resumed overview of the optical properties of semiconductors is presented as a sort of introduction to the rest of the volume. In the following chapters we will present how to analyze the optical properties of semiconductors by selected experimental techniques.

1.2 Optical Phenomena in Semiconductors

When a light beam impacts on a semiconductor surface a part of the incident light power is reflected; while the refracted part propagates across the material being progressively attenuated. The attenuation is the consequence of a series of processes of interaction between the photons of the light beam and the semiconductor atoms. The main light semiconductor interaction phenomena occurring inside the semiconductor are light absorption, and light scattering. Both, light absorption and light scattering, supply rich information about relevant physical parameters of semiconductors; e.g., the energy gaps, energy states of defects, elementary excitations as

excitons, phonons and plasmons, and other aspects relevant to the semiconductor properties; e.g. stress, light polarization. If the semiconductor is transparent to the light one can study the transmission spectrum; instead, if the semiconductor is opaque to the light the reflection spectrum is the one to record. The primary phenomena, reflection and light absorption, are the strongest ones, because of the lower order of interaction between the solid and the electromagnetic wave. The primary phenomena are macroscopically described by the optical constants of the solid; therefore, a macroscopic approach can be done in the frame of classic electrodynamics [21–23].

The propagating light is absorbed during its route across the semiconductor, it exchanges energy with the electrons and other particles, constituting an excitation source for secondary phenomena as luminescence, photocurrent among other. The object of this textbook is the way these phenomena can be studied.

A schematic picture of the main optical processes occurring in a semiconductor is shown in Fig. 1.1. All of the beams indicated in the Figure carry reach information about the semiconductor properties, which needs to be extracted by an adequate use of the experimental means, and data treatment.

The incident light beam impacts onto the semiconductor surface, resulting in a reflected and a refracted beam respectively, according to the laws deduced in classical electromagnetism for the interaction of an electromagnetic wave with a dielectric. The refracted beam undergoes absorption processes, in which it transfers energy to the lattice, generating e–h pairs, which when recombine reemit light with another wavelength characteristic of the material under study; this phenomenon is known as photoluminescence (PL) [24]. A full description of the mechanisms of light absorption and emission require of a quantum mechanical approach. Note also that the free charges generated by the light beam can be collected by electrodes giving the photoelectric phenomena, which are at the origin of very important optoelectronic devices as photodetectors, and photovoltaic devices; but also, they

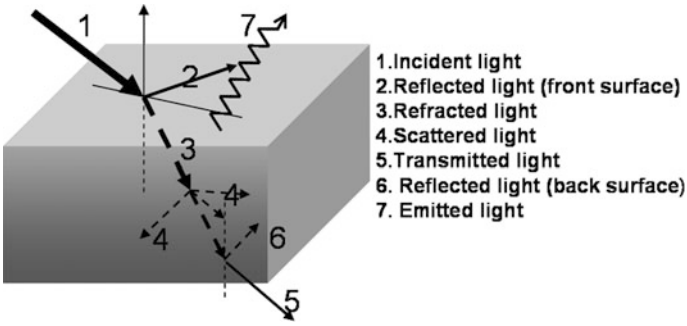

Fig. 1.1 Scheme of the different processes of interaction between light and a solid. *1* Incident light, *2* reflected light (front surface), *3* refracted light, *4* scattered light, *5* transmitted light, *6* reflected light (back surface), *7* emitted light

are at the origin of experimental techniques largely applied to the characterization of semiconductors and devices, e.g. the photocurrent techniques, described in Chap. 6 of this volume.

In addition to the absorption processes, the light inside the semiconductor can be scattered. Different scattering mechanisms can take place, which give rise to different experimental techniques. Among them, Brillouin scattering is the scattering by acoustic waves [25]; while the Raman spectroscopy corresponds to the scattering by optical phonons and other elementary excitations [26–30], Chap. 4. Rayleigh scattering is the elastic scattering phenomenon, which can be used to detect the presence of microscopic defects; e.g., dislocations, precipitates and other with size of the order of the light wavelength [31, 32].

The understanding of all these phenomena requires of the study of the fundamentals of the photon-semiconductor interaction. It permits to develop an appreciation of the intrinsic and extrinsic properties of semiconductors. Such analysis is essential to understand the basic principles of optoelectronic devices (light emitting diodes, lasers, photodetectors, and photovoltaics among other); also, they provide information about materials properties necessary for the development of optoelectronics devices.

The optical properties of semiconductors concern the phenomena occurring as a consequence of the presence of light in the semiconductor. On one side, one can consider the incidence of photons onto the semiconductor, and its response to such external light source. On the other side, one can consider the light generated by the semiconductor itself under an external excitation source. Both phenomena are extremely sensitive to the solid structure, and more specifically to the band gap structure. The fundamental bandgap is the threshold energy for different optical phenomena to be observed; in fact, the semiconductor is *transparent* to light with energy below the bandgap, while it becomes opaque to light with energy above the bandgap. Furthermore, it cannot emit light with energy above the bandgap.

There are different optical responses of semiconductors, which constitute the basis of the experimental tools used for the optical characterization; some of them are described along this volume. These techniques permit to measure different physical magnitudes, giving information about very relevant properties of the semiconductors related to the band structure, the presence of impurities and defects, the loss of periodicity, among other relevant physical magnitudes, e.g. stress and temperature, which can be characterized by optical spectroscopy techniques. These magnitudes are very relevant for the performance and reliability of devices [33–36].

An optoelectronic device can be either a detector or a source of light. However, what converts a semiconductor on a device is the possibility to generate and control the signals arising from the semiconductor, normally by means of an electric field. In this context we are interested on the response of the semiconductor to an external electromagnetic wave, but also on the mechanisms of light generation by the semiconductor.

The physical phenomena involved in these optical processes reveal both extrinsic and intrinsic properties. The semiconductors used in the industry are not

ideal periodic structures, but contain defects that disturb such a periodicity, changing in a significant way their optical and electronic properties; therefore, a huge interest is devoted to the study of the electro-optical signature of defects and impurities. On the other hand, extrinsic factors, as temperature and strain, have a strong influence on the intrinsic properties of semiconductors. Both of them are key factors accelerating the failure of optoelectronic devices [33–36]; therefore, is of prime interest the implementation of experimental techniques revealing changes in the optical properties by temperature and/or strain to be used as qualification tools for devices. Furthermore, the properties of the semiconductors can be tuned by strain, which is particularly relevant when using low dimensional structures, which admit elastic deformation allowing the tunability of the properties of the active parts of the devices.

The optical properties of semiconductors are related to their microscopic structure. Its understanding requires of the knowledge of several basic concepts, e.g.: band structure, fundamental bandgap, defect and impurity levels, quasiparticles, also known as collective excitations, e.g. phonons and plasmons, radiative and non radiative recombination, quantum confinement …

The list of optical characterization techniques is very extense; nevertheless, we will focus here on some of the most relevant of those techniques, e.g. spectroscopic reflectance techniques (Chap. 2), absorption, luminescence (Chaps. 3 and 5), photoelectric (Chap. 6), and among the light scattering techniques we will focus on Raman spectroscopy by phonons (Chap. 4). There are, by no means an exhaustive list of experimental techniques; however, the ones listed here are among the most widely used ones, being basic tools in many characterization laboratories.

As important as the lattice periodicity for practical applications is the breakdown of such periodicity, e.g. by defects, and impurities, but also the translational symmetry interruption by low dimensionality, which plays a paramount role in modern optoelectronic devices; in this context, one will also introduce the optical properties of structures with reduced dimension.

1.3 Band Structure and Fundamental Bandgap

An ordered solid is a structure in which the atoms occupy regular positions forming a lattice; when some of those atoms are ionized free electrons are available; however, these electrons are not purely free, but feel a periodic potential. The Bloch theorem establishes that the one electron wavefunction in a potential with the lattice periodicity is the product of a plane wave and a function with the same periodicity as the lattice [21]. The solution of the Schrodinger equation in such a potential results in continuous energy bands instead of the quantized discrete energy states observed in individual atoms [21, 22]. The band structure diagrams of GaAs [37] and Si [38] in the k space are shown in Fig. 1.2.

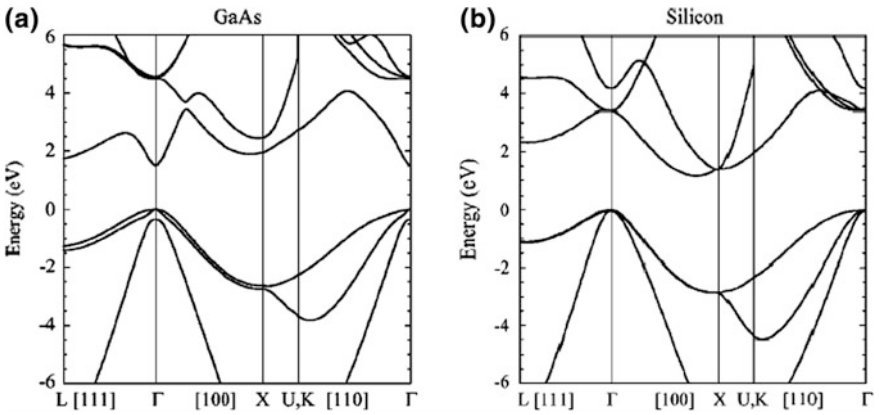

Fig. 1.2 Band diagrams of **a** GaAs [37] and **b** Si [38]

At zero temperature the valence band (VB) corresponds to the occupied electron states, while the conduction band (CB) corresponds to the empty electron states; both bands are separated by an energy gap, labelled as the forbidden bandgap, where the presence of electrons is forbidden. The energy interval between the minimum of the CB and the maximum of the VB is the fundamental bandgap, and is the minimum energy necessary to promote an electron from the filled electron states (VB) to the empty electron states (CB). One observes in Fig. 1.2 that in the case of GaAs the extrema of both bands occur at the Γ point of the Brillouin zone; one says that the bandgap is direct; which is not the case for Si, where the two extrema occur at different points of the Brillouin zone; in this case the bandgap is indirect. The direct or indirect nature of the bandgap has relevant consequences for the optical properties of the semiconductors. GaAs is a genuine optoelectronic semiconductor, while Si is the electronic material by excellence, but a poor optoelectronic semiconductor, even if this assertion must be put into context, depending on the type of optoelectronic device. These material specifications can be understood in terms of the band structure. The light emission energy is related to the bandgap; however, the intensity of the emission and the time response is governed by the band structure itself. Good light emitters are direct bandgap semiconductors, while indirect bandgap semiconductors are not.

The fundamental bandgap is an essential magnitude; it determines the threshold for intrinsic light absorption, but also the *maximum* energy at which a given bulk semiconductor can emit light. One of the great assets of semiconductors for their application in modern optoelectronic devices is the possibility of engineering the bandgap by alloying semiconductors. One can almost construct any band gap from the IR to the deep UV with the only constraint of the control of the lattice parameter and the layer thickness. The bandgap versus the lattice parameters for the most important semiconductors are represented in Fig. 1.3.

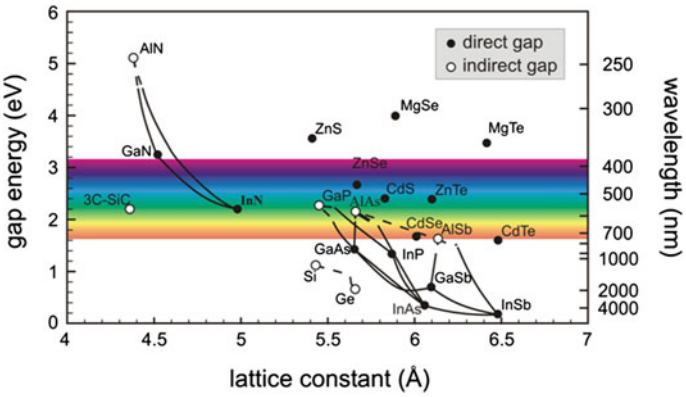

Fig. 1.3 Band gap versus lattice parameter for the main semiconductors (http://gorgia.no-ip.com/phd/html/thesis/phd_html/node4.html)

1.4 Quasi Particles in Solids

1.4.1 Electrons and Holes

In intrinsic semiconductors, electrons can only occupy either the valence band or the conduction band. At zero temperature, they are in the valence band, and they can start to populate the conduction band if energy higher than the bandgap is supplied. When an electron from the VB is promoted to the CB, it leaves an equivalent positive charge in the valence band, which is known as a hole.

Electrons and holes are free to move in the conduction and the valence bands respectively; however, as mentioned above, they have to move in a periodic potential, therefore, in the effective mass approximation they are considered as quasi particles, with either negative (electrons) or positive (holes) charge, but with a mass different from the free electron mass, because of the presence of the periodic potential; these are the effective masses, m_e^* and m_h^*, which are determined by the band structure. In fact, the masses of the electrons and holes are renormalized by the periodic potential to values smaller than the free electron mass [39].

Density of states

The jumps of electrons between the two allowed bands are crucial to the interaction between light and the semiconductor. The rates governing such jumps depend on the number of available states. The density of states, D(E), is the number of energy states available per unit energy, i.e. the number of states in the interval (E, E + dE), is $D_c(E)dE$.

$$D_c(E) = \frac{number\ of\ states}{V \times dE} \tag{1.1}$$

Assuming parabolic bands:

$$E(k) = \frac{\hbar^2 k^2}{2m^*}, \tag{1.2}$$

The density of states per unit volume of the conduction band is:

$$D_c(E) = \frac{1}{4\pi^2}\left(\frac{2m_e^*}{\hbar^2}\right)^{3/2}(E - E_c)^{1/2} \tag{1.3}$$

While the density of states of the valence band is:

$$D_v(E) = \frac{1}{4\pi^2}\left(\frac{2m_h^*}{\hbar^2}\right)^{3/2}(E_v - E)^{1/2} \tag{1.4}$$

It is useful to define the joint density of states; the optical transition rate between VB and CB is proportional to a joint density of states defined as:

$$D_j(E_{cv}) = \frac{1}{4\pi^3}\int \frac{dS_k}{|\nabla_k E_{cv}|} \tag{1.5}$$

where $E_{cv} = E_c - E_v$, and S_k is the energy surface over which $E_{cv}(k) = const$. The doubly band degeneracy due to the spin is considered by a prefactor 2. This integral will appear later on, when considering the interband optical transitions.

In an intrinsic semiconductor the occupation of the two bands depends on the temperature.

The electron density in the conduction band is:

$$n = \int_0^\infty D_c(E) f(E) dE \tag{1.6}$$

where f(E) is the Fermi-Dirac probability function. For electrons in the conduction band, $E > E_c$ ($E > E_v$), for non degenerate semiconductors in thermal equilibrium, $E_c - \zeta_c \gg KT$, ($\zeta_v - E_v \gg KT$) so the Fermi function reduces to the Boltzmann

distribution and the density of electrons in the CB and holes in the VB can be expressed as:

$$\begin{aligned} n &= N_c \exp\left(-\frac{E_c - \varsigma_c}{KT}\right) \\ p &= N_v \exp\left(-\frac{E_v - \varsigma_v}{KT}\right) \end{aligned} \tag{1.7}$$

where $N_c = 2(\frac{m_e^* KT}{2\pi\hbar^2})^{3/2}$ and $N_v = 2(\frac{m_h^* KT}{2\pi\hbar^2})^{3/2}$ are the effective density of states for the bottom (within about KT of the bottom) of the CB and the top (within about KT of the top) of the VB respectively. ζc and ζv are the Fermi levels for electrons and holes respectively.

In an intrinsic semiconductor:

$$np = N_c N_v \exp\left(-\frac{E_c - E_v}{KT}\right) = N_c N_v \exp\left(-\frac{E_g}{KT}\right) = n_i^2 \tag{1.8}$$

1.4.2 Excitons

A free exciton is a quasi-particle formed by an e-h pair bound each other by their Coulomb attraction [21–23]. The exciton is formed when an electron is excited from the VB to the CB, and the electron remains attached to the hole by the Coulomb force forming a hydrogen like quasi-particle; it can move through the crystal transporting energy but not charge. The exciton behaves like a hydrogen atom; therefore, the exciton has a number of discrete energy levels given by:

$$E_{n,exc} = \frac{\mu e^4}{2\hbar^2 \varepsilon^2} \frac{1}{n^2} = \frac{R_x}{n^2} \tag{1.9}$$

where ε is the dielectric constant, n an integer, R_x the Rydberg energy, and μ the reduced mass of the e-h pair:

$$\frac{1}{\mu} = \frac{1}{m_e^*} + \frac{1}{m_h^*} \tag{1.10}$$

The binding energy between electron and hole lowers the e-h transition energy with respect to the bandgap.

$$E(n) = E_g - E_{n,exc} = E_g - \frac{R_x}{n^2} \tag{1.11}$$

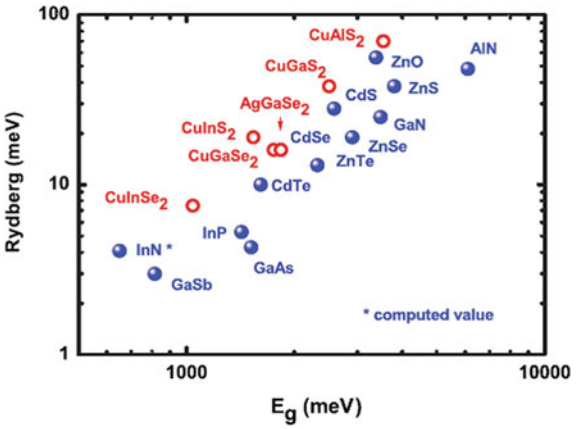

Fig. 1.4 Plot of the free exciton binding energy versus the band gap energy for different semiconductors [40]

In semiconductors, the large dielectric constant, results in a partial screening of the Coulomb interaction between the electron and hole pair; as a consequence, the exciton is weakly bound, and the distance between the electron and the hole is *large*; the exciton radius (Bohr radius) is larger than the Brillouin zone, which means that the exciton feels the periodic potential, behaving as a quasi-particle in a periodic potential. This kind of exciton is known as a Wannier-Mott exciton. Typical free exciton binding energies are given in Fig. 1.4 [40]. Note that large exciton binding energies are important for optoelectronic devices, since stable excitons at room temperature give strong light emission.

1.4.3 Phonons

The atoms forming the semiconductor lattice vibrate around its equilibrium position with characteristic vibration frequencies related to the atom masses and the force constants. The problem can be classically treated by solving the motion of a linear chain with two atoms per unit cell. The solution of this problem gives two vibration branches in the reciprocal space. When the two atoms of the unit cell vibrate parallel each other the vibration is acoustical, when they vibrate in opposition the vibration is optical. A three dimensional crystal presents three acoustic branches, one longitudinal and two transverse, and $3(N - 1)$ optical branches, where N is the number of atoms per unit cell. The phonon dispersion relations for Si [41] and GaAs [42] are shown in Fig. 1.5. The three optical modes in the zone center, $q = 0$, are degenerated in Si; while LO-TO splitting occurs in GaAs, and in general in polar semiconductors; the splitting is the consequence of the lack of inversion symmetry; in polar semiconductors the longitudinal vibrations induce an electric field, which constitutes and additional restoring force.

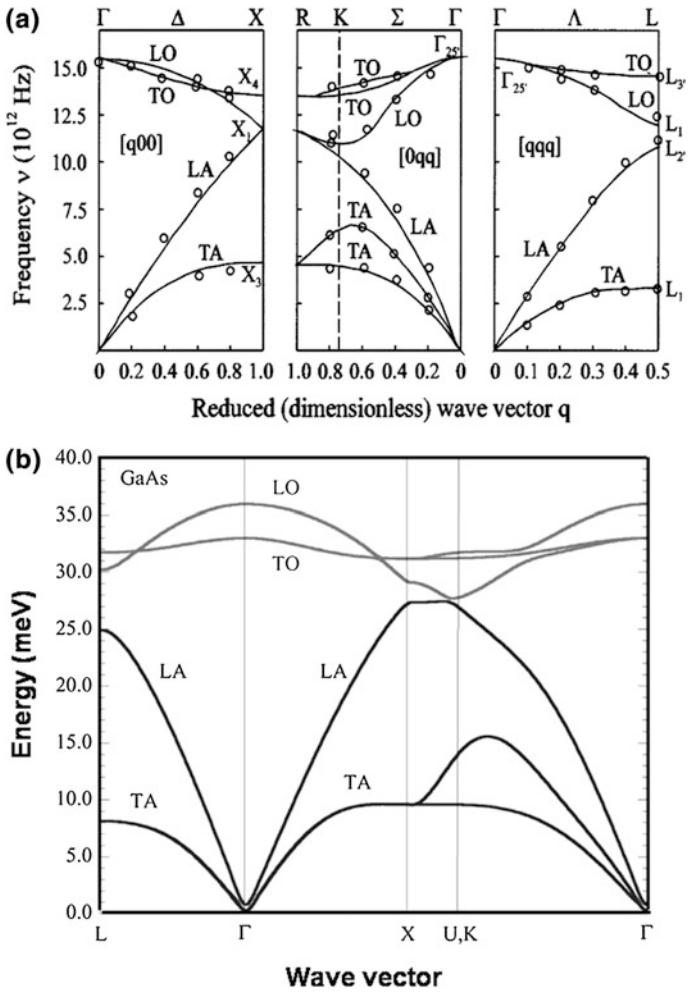

Fig. 1.5 Phonon dispersion relations **a** Si [41], **b** GaAs [42]

The collective vibrations when treated in the frame of the second quantization result in quasi-particles called phonons, with characteristic quantized energy, $\hbar\omega$. Light undergoes inelastic scattering by phonons, either acoustic, Brillouin scattering, or optic, Raman scattering (Chap. 3).

On the other hand, phonons are the intermediate actors for preserving the momentum selection rule in indirect electronic transitions. Also, they are the main thermal carriers in semiconductors.

1.4.4 Plasmons

When the conduction band is populated with free electrons, the Coulomb attraction between the free electrons and the positive ions constitutes a restoring force for the free electron motion, which can collectively oscillate with a characteristic frequency, ω_p, the plasma frequency. These plasma oscillations can be quantized in energy quantas, $\hbar\omega_p$, constituting elementary excitations, the plasmons. Its oscillation frequency depends on the free electron concentration, n [43], as:

$$\omega_p = 4\pi n^2/m^*\varepsilon_o \tag{1.12}$$

Plasmons are longitudinal oscillations. The macroscopic electric fields associated respectively with the plasmons and the LO phonons in polar semiconductors can interact in between giving additional longitudinal wave frequencies, (see Chap. 3).

1.5 Extrinsic Factors Affecting the Bandgap: Temperature and Stress

Stress and temperature are extrinsic agents, which play a crucial role in the operation, and reliability of devices. The band gap is sensitive to both of them; therefore, they can be monitored by means of the dependence of the band gap with either temperature or stress; which permits the use of optical measurements as sensitive tools for measuring both magnitudes.

1.5.1 Temperature

The band gap decreases with the increasing temperature because of the lattice expansion and the electron-phonon interaction, which soft the lattice bonds, resulting in a decrease of the bonding energy. The temperature dependence of the bandgap energy is usually described by the semi-empirical Varshni law [44]:

$$E_g(T) = \frac{E_o - \alpha T^2}{T + \beta} \tag{1.13}$$

where α and β are fitting parameters, and $E_g(T)$, and E_o are the band gaps at T and at 0 K respectively. The β parameter is supposed to be the Debye temperature; however it does not match with in many cases, even giving negative values; which is usually attributed to the weak theoretical bases of the Varshni law.

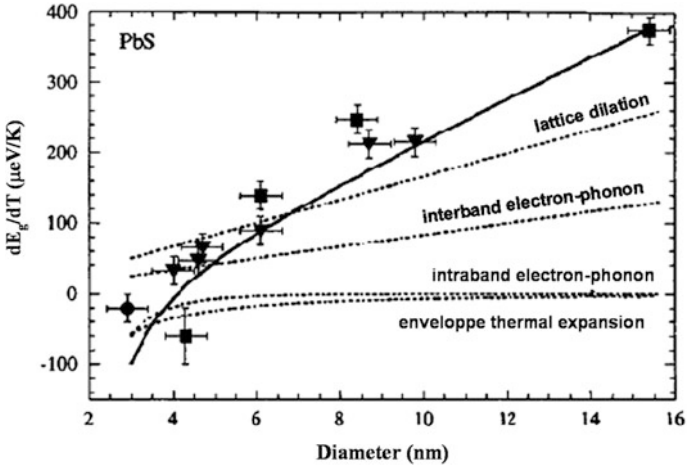

Fig. 1.6 dEg/dT in PbS QDs. The different contributions calculated are indicated in the figure by *dotted lines*. The *symbols* refer to QDs embedded in different matrices, *squares* glass matrix, *triangles* oxide glass matrix, *circles* polymer matrix. The *solid line* is the sum of the four contributions represented by the *dotted line* [49]

Alternative laws have been reported by Viña et al. [45] and O'Donnell et al. [46]. The variation of the bandgap with temperature in bulk semiconductors was the object of theoretical analysis in [47, 48]; the bandgap shrinkage with temperature is due to the thermal lattice expansion, and the electron-phonon coupling. In the case of reduced dimension structures the temperature dependence of the bandgap, dEg/dT is lowered by reducing the size of the structures, being even negative for the smaller quantum dot (QD) structures. This behaviour was reported in [49]; where, the temperature coefficient, dEg/dT, was studied as a function of the size of PbS quantum dots (QDs) showing a dramatic size dependence. In addition to the bulk contributions of the lattice thermal expansion, and the electron-phonon coupling, Olkhovets et al. [49] considered the mechanical strain, and the thermal expansion of the envelope wave-function. The temperature coefficient as a function of the QDs size, both experimental and theoretically calculated using the above mentioned four contributions is shown in Fig. 1.6.

1.5.2 Stress

The band edges are shifted by stress. Under hydrostatic stress the band gap is open for compression and is closed for tension. Under shear or biaxial stress the

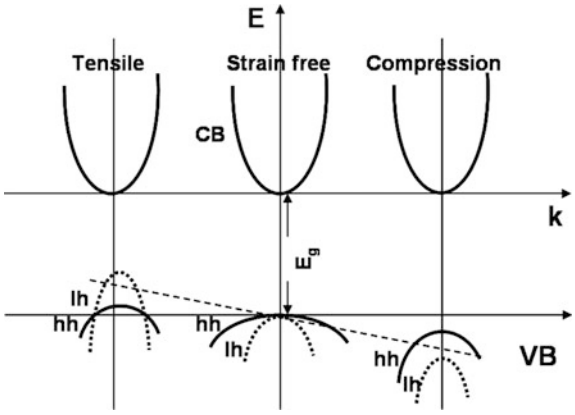

Fig. 1.7 Scheme of the band structure under stress, the band gap shift (*obliquus dashed line*) is due to the hydrostatic stress component, while the splitting of the valence band is induced by the biaxial stress. Note that the compressive stress reduced the effective mass of the hh band, and the tensile stress reverses the band positions with respect to the compressive case

degeneracy of the valence band at the Γ point of the Brillouin zone is lifted, and the valence band is split out in the heavy hole (hh) and the light hole (lh) valence bands (50, −52). The splitting of the bands is a function of the strain value. Figure 1.7 shows the band scheme under stress, both the hydrostatic and biaxial stress components are included.

The splitting in between the two transitions (lh-CB and hh-CB) under biaxial stress is proportional to the strain according to the following expression [51]:

$$E_{lh} - E_{hh} = 2b((C_{11} + C_{12})/C_{11})\varepsilon \tag{1.14}$$

where b is the shear deformation potential, and C_{11}, C_{12} are the stiffness coefficients. The strain is very precisely determined from the lh-ll splitting; often the strain is not high enough to separate the two transitions, which results in the broadening of the corresponding optical spectrum, e.g. luminescence or optical absorption.

1.6 Low Dimension Structures

1.6.1 Quantum Confinement

The interest on structures of reduced dimension is continuously increasing. The properties of the semiconductors are the consequence of its repetitive structure; however, when one dimension is reduced to a size for which the repetitive pattern is limited, the phenomenon of quantum confinement appears [53]. The electrons are

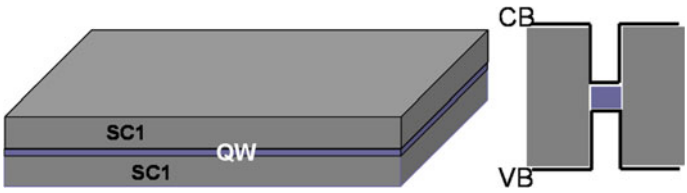

Fig. 1.8 Scheme of a QW, and its band structure

not more feeling the periodic potential along the direction with the reduced dimension.

The quantum confinement phenomenon results from electrons and holes being squeezed into a dimension that approaches a critical quantum dimension, called the exciton Bohr radius. The strongest confinement occurs when the confinement dimension is smaller than the Bohr radius. The result is an increase of the band gap with decreasing dimension; furthermore, the loss of the translational symmetry results in quantized states for the electrons and holes in the CB and the VB respectively, instead of the continuous bands of the ideal periodic solid. The confinement enhances the radiative recombination rate, even in indirect band gap materials [53]. On the other hand, one can also mention the confinement of phonons, which leads to changes in the phonon spectrum [54].

The simplest quantum confined structures are the quantum wells, which are the active parts of most of the commercial optoelectronic devices. A QW is a system formed by a thin (a few atomic layers) semiconductor layer sandwiched in between two semiconductor layers of higher bandgap energy, it corresponds to 1D confinement, Fig. 1.8.

The central layer of small bandgap energy is the QW, while the two surrounding layers of larger bandgap energy constitute the potential barriers. Its study began in the 70s of the last century [55]. Many textbooks and articles about one dimensional confinement structures are available [56–58]. Multiple quantum well (MQW) structures can be also constructed, they consists of a series of stacked QWs, separated by barrier layers with thickness avoiding electronic coupling between the wells. In the case of narrow spacers electronic coupling between the QWs can occur, and the electronic charge distribution can be delocalized along the direction normal to the QW plane, in this case the MQW structure is termed as a superlattice (SL), Fig. 1.9.

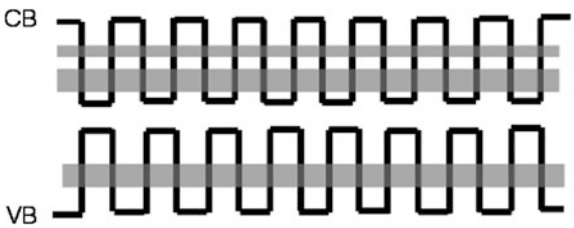

Fig. 1.9 Bandgap energy in a superlattice. The *shadowed areas* represent the minibands

These structures can be grown by molecular beam epitaxy (MBE) or metal-organic chemical vapour deposition (MOCVD) techniques, which permit to control the growth at the atomic layer scale.

If one considers an electron in the CB with an effective mass m_e^* in a potential well with infinite barriers, confinement appears in the direction perpendicular to the barriers. The quantized energy levels can be calculated by solving the Schrödinger equation for a particle in a potential well, using the effective mass envelope function approximation [59–61]. The electron energy states are discrete and depend on the QW thickness according to the following relationship (approximation to an infinity well)

$$E_n(k_x, k_y) = \frac{\hbar^2}{2m^*}\left[\left(\frac{n\pi}{L_z}\right)^2 + k_x^2 + k_y^2\right]$$
$$E_n = \frac{\hbar^2}{2m^*}\left(\frac{n\pi}{L_z}\right)^2 \tag{1.15}$$

The energy states in a QW are represented in Fig. 1.10. One should also note that the energy is inversely proportional to the effective mass, which means that the degeneracy of the VB is lifted, the heavy and light hole bands have different energy levels. One has also to take account of the biaxial stress splitting further the lh and hh bands; note that the QWs are frequently strained because of the lattice mismatch with

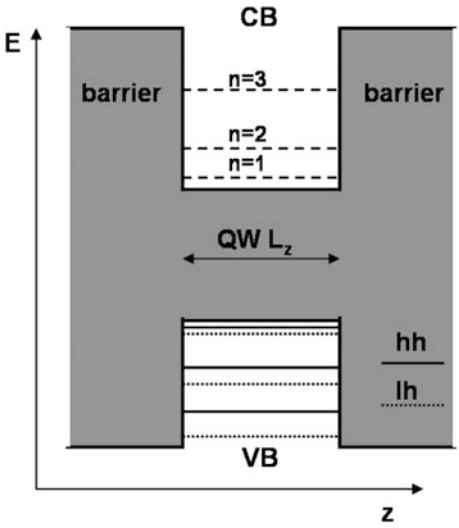

Fig. 1.10 Energy level scheme of a compressed QW

the barrier layers. There is a critical QW thickness below which the stress is elastically accommodated; beyond this critical thickness dislocations are formed [62].

Quantum confinement can be also achieved in two or three dimensions, i.e. quantum wires (QWRs), and quantum dots (QDs) respectively. Note that the quantum confinement gives an additional degree of freedom for band gap engineering.

1.6.2 The Density of States in Quantum Confined Structures

Contrarily to the continuous parabolic density of states reported for bulk semiconductors, a series of resonances appear in the density of states, corresponding to the discrete levels existing for the different dimensions of confinement, Fig. 1.10. Instead of the square-root dependence with the electron energy of bulk semiconductor (1.3, 1.4), the density of states for a QW presents a discrete distribution:

$$D_{QW}(E) = \frac{m^*}{\pi \hbar^2} n \tag{1.16}$$

where n is the quantum number of the energy level.

In quantum wires (2D confinement) the density of states is quantified but it depends on $(E - E_c)^{-1/2}$, while for quantum dots (3D confinement) it corresponds to δ functions (Fig. 1.11).

The localization of the states is very important for lowering the current injection levels in optoelectronic devices, e.g. the threshold current in laser diodes.

The dimension of these structures is smaller than the diameter of the Bohr exciton, which results in an increase of the exciton binding energy, which becomes stable at room temperature. In fact, the confinement of the electrons and holes keep

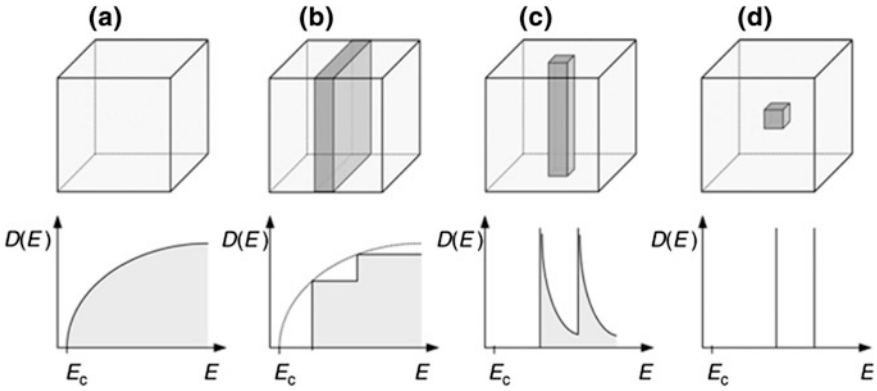

Fig. 1.11 Density of states for bulk (**a**), QWs (1D confinement) (**b**), QWRs (2D confinement) (**c**), and QDs (3D confinement) (**d**) [63]

them closer than in 3D periodic crystals. This makes that the absorption spectrum of low dimensional structures shows exciton related transitions at higher temperatures than bulk materials [55, 64].

1.7 Extrinsic Semiconductors. Energy Levels Inside the Forbidden Bandgap

Very important properties of semiconductors are altered by crystal imperfections. In this way, the controlled addition of impurity atoms permits to tailor the properties of the semiconductors for different applications. Defects in crystalline solids are normally classified according to their dimension as follows:

1. Point defects (zero dimensional defects)
2. Extended defects (dislocations, stacking faults, interfaces, surfaces, precipitates, grain boundaries …).

1.7.1 Point Defects

A point defect refers to an atom missing, or placed in an irregular site in the crystal lattice. Point defects include self interstitial atoms, interstitial impurity atoms, substitutional impurity atoms, vacancies, and antisites in compound semiconductors. One can also include the complexes formed by these defects, as Frenkel pairs, Fig. 1.12.

As mentioned above, electron states are forbidden inside the bandgap, the electrons can only occupy the VB at zero temperature; and they can start to populate the CB if energy higher than the bandgap energy is supplied. According to this picture high concentrations of free carriers at room temperature could only be achieved in narrow band gap semiconductors. However, when the lattice is disturbed by defects, electronic levels become allowed inside the forbidden bandgap. These levels are crucial to control the Fermi level position, and therefore to determine the carrier population of the bands, since they constitute reservoirs for free electrons and/or holes.

Concerning the role of defects in the optical response of semiconductors, one should remember that a semiconductor is characterized by the possibility of having free electrons in the CB and free holes in the VB, even at low temperature. This is achieved by the introduction of impurities, which have the property to transfer free charges to the allowed energy bands in a controlled way, by acting on the density of impurities and its ionization energy with respect to the corresponding band edge, either bottom of the CB or top of the VB.

The point defects can be intrinsic or extrinsic. The intrinsic (also native) defects are those that do not involve foreign chemical species, e.g., vacancies, interstitials, antisites in compound semiconductors, which are cations in the place of anions, or

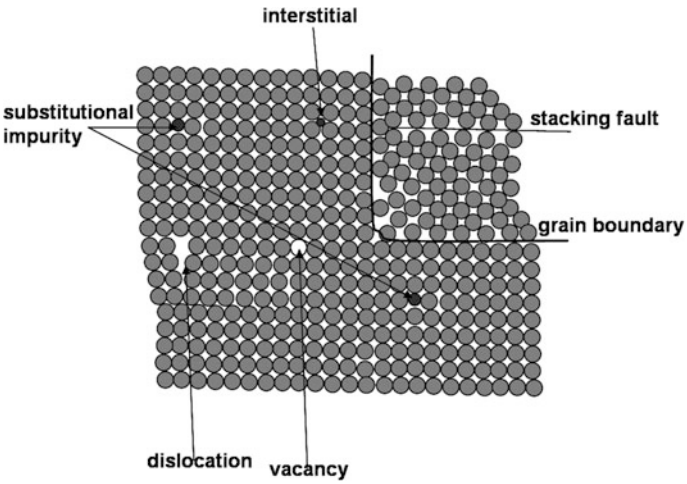

Fig. 1.12 Schematic representation of some of the most common lattice defects

viceversa; also Frenkel pairs, which are formed by a vacancy and an interstitial. These defects can have electro-optic activity; therefore, they contribute to determine the Fermi level position, also they are scattering centers contributing to the mobility of the free carriers, and to the optical properties of the semiconductors; its presence and density depends on the semiconductor growth conditions, and post growth treatments [65, 66].

Substitutional defects are foreign atoms replacing a host atom. They are intentionally introduced in order to give to the semiconductors their unique properties. It is the controlled incorporation of impurities which permits to exploiting the semiconductor materials for electronic and optoelectronic devices.

Impurities introduce energy levels inside the forbidden bandgap. The defects are classified as donors and acceptors. Donors have extra electrons; when the energy levels associated with donors are close to the CB edge they can be easily ionized populating the CB with conduction electrons. Acceptors have electron deficiency; therefore, when they are close to the VB edge can capture valence electrons, leaving extra holes in the VB.

Donors and acceptors to be effective need to be close to the band edges. According to their position with respect to the band edges one classifies defects regarding its energy level inside the forbidden bandgap as shallow and deep. The shallow levels are poorly localized, therefore, the wavefunction extends over several unit cells [67]. The deep levels have localized wave functions [68].

Both impurities and intrinsic defects can also be unintentionally introduced, which has unwanted consequences for the semiconductor properties, and thereafter for the device operation. This means that a strict control of the residual impurities and defects is necessary. Optical characterization techniques constitute relevant tools for such a purpose, because they supply very sensitive related signals;

therefore, optical techniques are currently used for characterizing the presence of defects and impurities in semiconductors.

1.7.2 Extended Defects

The extended defects are defects in which several atoms are involved. Among the extended defects one can list dislocations, stacking faults, precipitates, and grain boundaries [69]. The investigation of their electrooptic properties and the interaction with the point defects is crucial for the device operation. Generally, they are harmful for device performance and reliability; e.g., they play a paramount role in the device degradation during operation [70, 71].

Statistics of free carriers in doped semiconductors
The populations of neutral and ionized donors depend on the position of the energy level of the donor, E_D, with respect to the Fermi energy, according to the Fermi-Dirac statistics, neglecting p:

$$\begin{aligned} N_D^0 &= N_D \frac{1}{1+e^{\frac{E_D-F_e}{KT}}} \\ N_D^+ &= N_D\left(1-\frac{1}{1+e^{\frac{E_D-F_e}{KT}}}\right) \\ N_D &= N_D^0 + N_D^+ \end{aligned} \tag{1.17}$$

Equivalent expressions hold for holes.

Assuming that all shallow donors and acceptors are ionized, the neutrality condition is:

$$n + N_A^- = p + N_D^+ \tag{1.18}$$

which together with (1.8) gives:

$$\begin{aligned} n &= \frac{N_D^+ - N_A^-}{2} + \left[\left(\frac{N_D^+ - N_A^-}{2}\right)^2 + n_i^2\right]^{1/2} \\ p &= \frac{N_A^- - N_D^+}{2} + \left[\left(\frac{N_A^- - N_D^+}{2}\right)^2 + n_i^2\right]^{1/2} \end{aligned} \tag{1.19}$$

for n-type semiconductor $N_D^+ - N_A^- \gg n_i$ and $n = N_D^+ - N_A^-$

The electron concentration in the Boltzmann approximation ($E_D - F_e \gg KT$) is given by:

$$n \approx \left(\frac{N_D N_C}{2}\right)^{1/2} \exp\left(-\frac{E_c - E_D}{2KT}\right) \tag{1.20}$$

The presence of energy levels in the forbidden band allows transitions between defect related levels and the bands, being responsible for both extrinsic (sub-bandgap) light absorption and emission.

1.8 Doped Semiconductors: Effects on the Band Gap

When defects are present, their electronic occupancy depends on its energy levels with respect to the Fermi level. The energy levels in the bandgap can supply carriers to the bands, being the occupancy of the bands governed by the balance between the ionized donors and acceptors.

The electric compensation relation is:

$$\mathrm{n} + \mathrm{N_A^-} = \mathrm{p} + \mathrm{N_D^+} \tag{1.21}$$

for an n-type semiconductor, $N_D > N_A$, one can approximate $N_A = N_A^-$, and solving the electric compensation equation, for the low temperature range ($n < N_A$) one obtains for the free electron concentration:

$$n \cong \frac{N_c}{g}\frac{N_D - N_A}{N_A}\exp\left(-\frac{E_C - E_D}{KT}\right) \tag{1.22}$$

g is the degeneracy of the donor level. The CB occupancy depends on the concentration of donors and the donor energy, E_D, with respect to the CB. One can obtain a similar equation for holes.

$$p \cong \frac{N_v}{g}\frac{N_A - N_D}{N_D}\exp\left(-\frac{E_A - E_V}{KT}\right) \tag{1.23}$$

At high doping concentrations, many semiconductors characteristics change, due to either the high impurity concentration, or the associated high electron concentration. This is the case of the bandgap energy. In the presence of a significant concentration of impurities the effective bandgap (the energy necessary for transitions between the two bands) is shifted due to three main effects [72–78]:

i. The band filling, which is known as Burstein Moss effect [72–75]
ii. Band tailing due to electron—impurity interaction [75–77]
iii. Bandgap shrinkage due to e-e interaction, which is relevant above a certain critical electron concentration [78, 79].

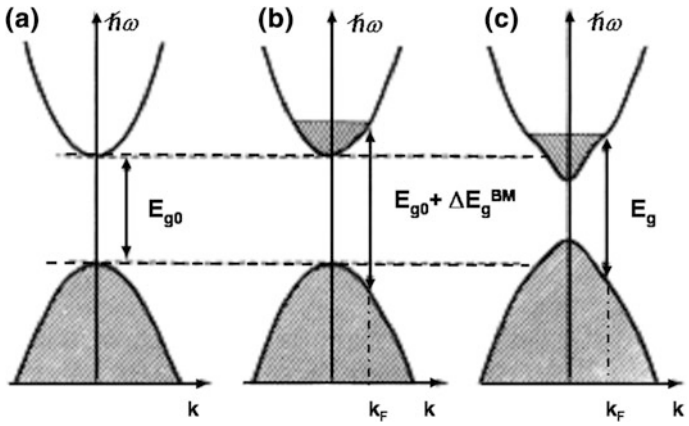

Fig. 1.13 Schematic parabolic band structure (**a**), band structure after heavy doping, showing the opening of the optical bandgap, $E_g^o + \Delta E_g^{BM}$, due to band filling (Burstein Moss effect) (**b**), bandgap shrinking due to many body interactions (**c**). The *shadowed zones* correspond to the occupied states [75]

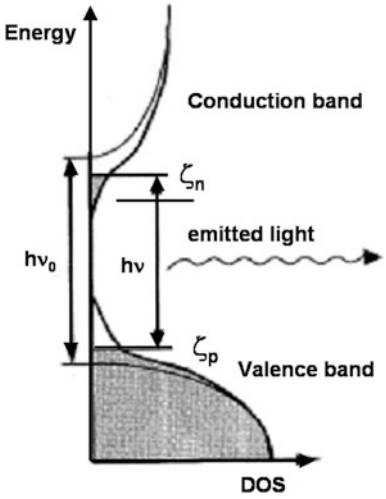

Fig. 1.14 Effects of heavy doping in the bandgap. $\zeta_{n,p}$ are the quasi Fermi levels for electrons and holes. The *narrow line* denotes de unperturbed DOS, while the *thick line* represents the DOS in the heavily doped semiconductor, showing band tailing effects resulting in effective band gap narrowing [77]

These effects are summarized in Figs. 1.13 and 1.14.

The Burstein Moss effect was initially described in relation to the absorption threshold shift in InSb with different levels of doping [73]. In fact, the transitions between the VB and the CB occur between states deep in the bands, depending on the density of free carriers, which shall fill the lower energy states of the CB, and the upper energy states of the VB, respectively. So that, the measured optical bandgap energy, E_{gap}, is related to the Fermi level position:

$$E_{gop} = E_g + E_F\left(1 + \frac{m_e^*}{m_h^*}\right) \tag{1.24}$$

Remember that for a degenerate electron gas the Fermi level with respect to the bottom of the conduction band is expressed as:

$$E_F = \frac{\hbar^2}{2m_e^*}\left(3\pi^2 n\right)^{2/3} \tag{1.25}$$

From which the $n^{2/3}$ dependence of the optical bandgap shift is deduced.

Lee et al. [80] reported the following empiric relation for the optical bandgap, E_{gap}, of Si-doped GaAs

$$E_{gop} = 1.426 + 2.4 \times 10^{-14} n^{2/3}(\text{eV}) \tag{1.26}$$

Note that the Burstein Moss shift is inversely proportional to the effective mass; therefore, the shift is more important in semiconductors with light effective masses, in particular, is significantly higher in n-type semiconductors than in p-type semiconductors.

Band tailing appears as a consequence of the random distribution of impurities, which results in potential fluctuations [76]. The consequence is the apparition of band tail states, both above or below the unperturbed band edge, with the consequence of the change in the density of states in the vicinity of the band edges [77], Fig. 1.13.

Finally, bandgap shrinkage occurs for increasing doping concentrations as a consequence of many body interactions, in particular electron-electron, and electron-ionized donor interactions. The band gap shrinkage follows $n^{1/3}$ dependence. Similar arguments are valid for the valence band in heavily doped p-type semiconductors.

In the case of GaAs the phenomenological bandgap shrinkage for n-type and p-type was given by Yao and Compaan [78]:

$$\begin{aligned} \Delta E_g(\text{meV}) &= -6.6 \times 10^{-5} n^{1/3} \\ \Delta E_g(\text{meV}) &= -2.4 \times 10^{-5} p^{1/3} \end{aligned} \tag{1.27}$$

The Burstein Moss effect is the dominant effect in n-type GaAs, therefore the optical bandgap is shifted to high energies for increasing electron concentration; however, in p-type GaAs the bandgap shrinkage is the dominant effect and the bandgap is shifted to the low energy for increasing hole concentration. The different behaviour between both types of semiconductor is due to the much lower effective mass of electrons with respect to the holes.

1.9 Interaction of the Semiconductor with Electromagnetic Waves

The optical processes in semiconductors deal with the interaction of light with the ions, electrons, impurities and defects constituting the semiconductor lattice. Many of the optical properties of semiconductors can be studied using classical electromagnetism; while other problems require of a quantum mechanics approach.

The particular property of semiconductors with respect to metals and insulators is the presence of both free and bound charges. Both of them interact with the electromagnetic waves and contribute to the physical phenomena reported here.

It is interesting to note the interest of the response of nanosized structures to the light. A case of interest is the interaction with semiconductor nanowires (NWs). See for example the electric field distribution inside a tapered SiNW under a laser beam, resonances and the distribution of the electric field inside the NW depend on the NW diameter, the laser wavelength, and the surrounding media [81–83], Fig. 1.15.

These small objects behave as optical antennas [84].

1.9.1 Macroscopic Approach. Optical Constants

In a solid the bound charges are displaced with respect to the ion cores under the action of the electric field associated with the electromagnetic wave, inducing a polarization proportional to the electric field:

$$P = \varepsilon_o \chi(\omega) E \tag{1.28}$$

where χ is the electric susceptibility, which is related to the dielectric function, $\varepsilon(\omega)$, according to the relation

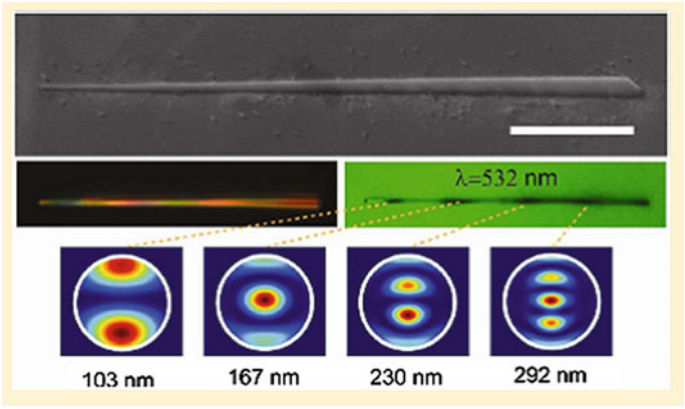

Fig. 1.15 Electric field inside a tapered Si NW, for different positions (different diameters) of the laser beam on the NW (532 nm) [83]

$$D = \varepsilon_o E + P = \varepsilon o(1+\chi)E = \varepsilon(\omega)E, \;\; \varepsilon(\omega) = \varepsilon o(1+\chi(\omega)) \tag{1.29}$$

The free charges also contribute to the dielectric function through the Ohm's law

$$J = \sigma(\omega)E \tag{1.30}$$

where $\sigma(\omega)$ is the electric conductivity.

Substituting both D and J in the Maxwell equations including both bound and free charges one obtains the dielectric function; which is a complex number.

$$\varepsilon(\omega) = \varepsilon_{lat}(\omega) + i\frac{\sigma(\omega)}{\varepsilon_0 \omega} \tag{1.31}$$

If one considers the transverse and longitudinal components of the electric field inside the semiconductor one obtains the dispersion relation for transverse waves:

$$q^2 = \omega^2/c^2\varepsilon(\omega) \tag{1.32}$$

Longitudinal waves only exist if $\varepsilon(\omega) = 0$; note that the existence of longitudinal waves is only possible in the complex dielectric medium.

The dielectric function is a complex number; therefore the wavevector of the electromagnetic wave in the solid is also complex, and the electric field inside the semiconductor can be written as a damped plane wave:

$$E = E_o e^{-q_i z} e^{i(q_r z - \omega t)} \tag{1.33}$$

where q_r and q_i are respectively the real and the imaginary parts of the wavevector.

The imaginary part of the wavevector is responsible for the wave damping inside the semiconductor. Now the question is: what damping mechanisms can occur inside the semiconductor?:

i. Photons interact with the lattice
ii. Photons interact with defects
iii. Photons interact with valence electrons
iv. Photons interact with free electrons.

The macroscopic properties of the dielectric medium can be described by a complex refractive index, which permits relating the dielectric function and the conductivity:

$$\tilde{n} = n + i\kappa = \sqrt{\varepsilon(\omega)} \tag{1.34}$$

So, the electric field inside the solid can be written as

$$E = E_o e^{-\kappa q_o z} e^{i(nq_o z - \omega t)} \tag{1.35}$$

where, q_o is the wavevector of the electromagnetic wave in the vacuum.

The complex part of the refractive index accounts for the wave damping when the electromagnetic wave propagates inside the semiconductor; the imaginary part of the refractive index is the extinction coefficient, while the real part, n, is the refractive index. Taking account of the intensity loss inside the semiconductor one can define the absorption coefficient. A fraction of the incident light is reflected, while the remaining intensity penetrates in the semiconductor, as it travels across, the wave exchanges energy with the solid according to the exchange mechanisms listed above; at a distance z from the surface the intensity of the wave is exponentially reduced, with respect to the ongoing wave intensity, the intensity loss is associated with a characteristic parameter labelled the absorption coefficient, α:

$$\begin{aligned} &I(z) = I_o' \exp(-\alpha z) \\ &(I_o' = I_o - I_R) \end{aligned} \tag{1.36}$$

where I_R is the reflected light intensity at the surface. α and I_R are functions of the wavelength. The intensity of the electric field decreases when travelling across the semiconductor, reaching 1/e of its value at the surface at a depth equal to 1/α (Beer-Lambert law).

Using (1.35) and (1.36) the absorption coefficient can be expressed as a function of the optical constants of the semiconductor:

$$\alpha = \frac{\omega \kappa}{cn} \tag{1.37}$$

In a conducting medium the absorption coefficient is related to the conductivity according to:

$$\alpha = \frac{\sigma}{nc\varepsilon_0} \tag{1.38}$$

1.10 The Oscillator Model for the Optical Constants

1.10.1 Dielectric Function

Lattice contribution

When considering the lattice absorption one can use a classic damped harmonic oscillator model for deducing the electrical susceptibility, which is related to the oscillator frequency, ω_0, the oscillator strength, f_0, and the damping parameter, Γ:

$$\chi = \frac{f_0 N e^2}{\varepsilon_0 m V} \frac{1}{\omega_0^2 - \omega^2 - i\Gamma\omega} \tag{1.39}$$

the real and imaginary parts are:

$$\chi' = \frac{f_0 N e^2}{\varepsilon_0 mV} \frac{(\omega_0^2 - \omega^2)}{(\omega_0^2 - \omega^2)^2 + \Gamma^2 \omega^2}$$
$$\chi'' = \frac{f_0 N e^2}{\varepsilon_0 mV} \frac{\Gamma\omega}{(\omega_0^2 - \omega^2)^2 + \Gamma^2 \omega^2} \tag{1.40}$$

The dielectric function adopts the form:

$$\varepsilon(\omega) = \varepsilon_0 + \frac{f_0 N e^2}{mV} \frac{1}{\omega_0^2 - \omega^2 - i\Gamma\omega} \tag{1.41}$$

Free electron contribution
In the Drude formalism the electronic contribution to ε(ω) corresponds to the dielectric function of an electron gas of density n:

$$\varepsilon(\omega) = \varepsilon_\infty \left(1 - \frac{\omega_p^2}{\omega(\omega - i\gamma)}\right) \tag{1.42}$$

where ω_p is the plasma frequency, and $\gamma = 1/\tau$, is a phenomenological damping parameter. Other approaches for the electron contribution to the dielectric function (Hydrodynamic, Mermin) will be revised in Chap. 3.

1.10.2 Kramers Kronig Relations

The relations between the real and imaginary parts of the dielectric function, in the electric field linear dependent range, are given by the Kramers Kronig relations:

$$\varepsilon_r(\omega) = 1 + \frac{2}{\pi} P \int_0^\infty \frac{\omega' \varepsilon_i(\omega')}{\omega'^2 - \omega^2} d\omega'$$
$$\varepsilon_i(\omega) = -\frac{2}{\pi} P \int_0^\infty \frac{\varepsilon_r(\omega')}{\omega'^2 - \omega^2} d\omega' \tag{1.43}$$

where, P indicates the principal value of the Cauchy integral.

Similar relations can be deduced for the electric susceptibility, and the refractive index. In general, the K-K relations permit to calculate the real part of the optical functions from the imaginary part and viceversa.

1.11 Optical Reflection

The reflectivity, r, defined as the ratio of the electric field of the reflected wave to that of the incident wave, in normal incidence obeys the relation:

$$r = \frac{\tilde{n} - 1}{\tilde{n} + 1} \tag{1.44}$$

while the reflectivity intensity, named as the reflectance, R, is given by:

$$R = |r|^2 = \frac{(n-1)^2 + \kappa^2}{(n+1)^2 + \kappa^2} \tag{1.45}$$

For finite incidence angles the optical constants can be experimentally determined by ellipsometry using the Fresnel formulas for the reflected light. For an angle of incidence θ_i, the reflectances of the parallel polarized/TM (p-polarized) and perpendicular polarized/TE (s-polarized) waves are related to the complex refractive index, ñ, according to the following formulas:

$$\begin{aligned} R_p &= \left(\frac{\tilde{n}^2 \cos\theta_i - \left((\tilde{n}^2 - \sin^2\theta_i) \right)^{1/2}}{\tilde{n}^2 \cos\theta_i + \left((\tilde{n}^2 - \sin^2\theta_i) \right)^{1/2}} \right)^2 \\ R_s &= \left(\frac{\cos\theta_i - \left((\tilde{n}^2 - \sin^2\theta_i) \right)^{1/2}}{\cos\theta_i + \left((\tilde{n}^2 - \sin^2\theta_i) \right)^{1/2}} \right)^2 \end{aligned} \tag{1.46}$$

As mentioned above, the real and complex parts of the dielectric function are related by the Kramers-Kronig relations, which permit to deduce one of them if one knows the other one.

It is interesting to note that semiconductors have large refractive index; therefore, the light generated inside the semiconductor can suffer total internal reflection; therefore, it cannot be extracted, and remains inside the medium. The critical angle of incidence for photons generated inside the semiconductor is rather small, e.g. 17° for GaAs. This will be relevant to the external quantum efficiency of light emitting devices, for which strategies for light extraction are necessary to improving the efficiency.

1.12 Optical Transitions. Light Absorption and Emission

The main optical loss mechanism is the absorption of light by the semiconductor.

Once the light penetrates inside the semiconductor it undergoes a series of absorption phenomena because of the exchange of energy between the refracted light beam and the different constituents of the solid.

1.12.1 Einstein Coefficients

The basic processes of interaction between light and matter are described by the Einstein coefficients. One can describe three interaction processes: (i) absorption, (ii) spontaneous emission, and (iii) stimulated emission.

Einstein described these processes as follows:

If one considers two energy levels of an atom, i and f, with populations N_i and N_f respectively, a light beam with energy ($E_f - E_i$) (angular frequency $\omega_{if} = \left(E_f - E_i\right)/\hbar$) can interact with the atom; by absorbing a photon an atom in the lower energy state, E_i, is excited to the upper energy level, E_f, absorption phenomenon, the rate of the atom population change is given by:

$$\frac{dN_i}{dt} = -B_{if}\, N_i\, e_\omega = -\frac{dN_f}{dt} \tag{1.47}$$

B_{if} is the absorption Einstein coefficient, and e_ω is the energy density of the incident photons, which is described by Planck's law.

The reverse transition can also occur and the excited electron can fall down to the initial state. This process can be achieved in two different ways, namely spontaneous or stimulated.

In the spontaneous emission one photon with energy $\hbar\omega_{if}$ is generated. The rate of spontaneous emission is

$$\frac{dN_i}{dt} = A_{fi}N_f = -\frac{dN_f}{dt} \tag{1.48}$$

A_{fi} is the Einstein coefficient for spontaneous emission, it has dimensions of time^{-1}, and the inverse of the Einstein coefficient is the characteristic time of the spontaneous emission transition, $A_{fi} = 1/\tau_{sp}$.

The transition from f to i can also be achieved with the participation of a photon with energy $\hbar\omega_{if}$. The electron in the f state can be induced by an incident photon to emit a photon when falling down to the i state, the two photons being in phase; this is the stimulated emission mechanism. The stimulated rate of decay of the excited states depends on the third Einstein coefficient, B_{fi}:

$$\frac{dN_f}{dt} = -B_{fi}\, N_f\, e_\omega = -\frac{dN_i}{dt} \tag{1.49}$$

One can also define the stimulated emission characteristic time, τ_{stim}, as:

$$\tau_{stim} = \frac{1}{B_{fi}e(\omega)} \tag{1.50}$$

In equilibrium the net rate of upward transitions equals to the net rate of downward transitions:

$$B_{if}\, N_i\, e_\omega = A_{fi}\, N_f + B_{fi}\, N_f\, e_\omega \tag{1.51}$$

By thermodynamic considerations Einstein established the relation between the three coefficients:

$$\begin{aligned} B_{if} &= B_{fi} \\ A_{fi} &= \frac{2\hbar\,\omega^3\, n^3}{\pi\, c^3} B_{fi} \end{aligned} \tag{1.52}$$

where n is the refractive index.

The three transitions are summarized in Fig. 1.16a. This holds for discrete levels. However, when dealing with semiconductors one has to consider the density of states and the occupancy of the bands, see Fig. 1.16b.

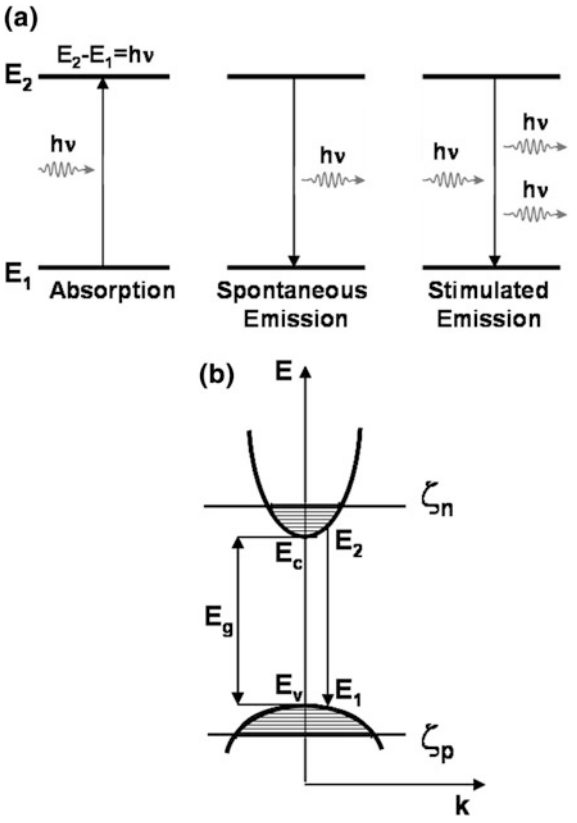

Fig. 1.16 **a** Two level scheme transitions. **b** Transition scheme in a semiconductor

1.12.2 Microscopic Description of the Optical Absorption in Semiconductors

The absorption process is described by quantum mechanics in terms of the electron photon interaction using time dependent perturbation theory. In the frame of a semiclassical approach the Hamiltonian describing the interaction between the electromagnetic wave and the electrons, uses a classical electric field for the electromagnetic wave, while the electrons are treated by Bloch functions in a quantum mechanics approach.

The Hamiltonian describing the motion of the electrons in the presence of the electromagnetic field is:

$$H = \frac{1}{2m}\left[p + e\frac{A}{c}\right]^2 + V(r) \tag{1.53}$$

where A is the vector potential, and V is the electric potential.

In the electric dipole approximation the electron-photon interaction Hamiltonian becomes:

$$\begin{aligned} H_{e-p} &= \frac{e}{mc}A \cdot p = -er \cdot E = H_+ e^{-i\omega t} + H_- e^{-i\omega t} \\ H_+ &= \frac{e}{2m}A_0 e^{iqr} \cdot p \\ H_- &= \frac{e}{2m}A_0 e^{-iqr} \cdot p \end{aligned} \tag{1.54}$$

In a semiconductor the fundamental transition refers to the transition of an electron from the VB to the CB. The two terms of the Hamiltonian correspond to the transition from the VB to the CB (absorption), while the reverse transition corresponds to the emission, either spontaneous or stimulated.

The electron in the valence band absorbs a photon ($\hbar\omega$) from the incoming light beam when the energy of the photons is enough to promote the electron through the forbidden band to the conduction band. The electron in state i has momentum k_i and energy $E_i(k_i)$, while the final state has momentum k_f and energy $E_f(k_f)$. The conservation rules establish both momentum and energy conservation:

$$\begin{aligned} \mathbf{k_f} &= \mathbf{k_i} + \mathbf{k} \\ E_f(k_f) &= E_i(k_i) + \hbar\omega \end{aligned} \tag{1.55}$$

These rules allow only transitions between different bands (interband transitions).

Using the Fermi's golden rule one can estimate the optical transition rates:

$$W_{\uparrow}(k_i) = \frac{2\pi}{\hbar}\sum_{k_f}\left|\left\langle \phi_{c\,k_f}|H_+|\,\phi_{v\,k_i}\right\rangle\right|^2 \delta_{k_i+q,k_f}\delta(E_c(k_f) - E_v(k_i) - \hbar\omega)$$
$$= \frac{2\pi}{\hbar}\left(\frac{eA_0}{2m}\right)^2 |p_{cv}|^2\,\delta_{k_i+q,k_f}\delta(E_c(k_i+q) - E_v(k_i) - \hbar\omega) = B_{if}\delta(E_c(k_f) - E_v(k_i) - \hbar\omega) \tag{1.56}$$

The δ Kronecker accounts for the momentum conservation, while the δ function entails the energy conservation. The summation is over all the final states in the conduction band respecting the conservation rules and the spin.

Contrarily to the isolated atoms, one has to integer to all the possible initial states weighted by the probability that the final state is empty to calculate the transition rate per second and unit volume:

$$R_{abs} = \frac{2}{V}\sum_{k_i} W\uparrow(k_i)f_v(k_i)(1 - f_c(k_f)) \tag{1.57}$$

The photon momentum is much smaller than the electron momentum, therefore the momentum conservation rule can be simplified to: $k_f = k_i = k$, which means that the optical transition is vertical in the k-space; Fig. 1.16b.

Assuming that the conduction band is empty, the absorption rate takes the form:

$$R_{abs}(\omega) = \frac{2\pi}{\hbar}\left(\frac{eA_0}{2m}\right)^2 |p_{cv}|^2\,2 * \int_{FBZ}\frac{d^3k}{(2\pi)^3}\delta(E_c(k) - E_v(k) - \hbar\omega) \tag{1.58}$$

The integral appearing in (1.58) is the joint density of states. Assuming parabolic bands:

$$E_c(k) = E_c + \frac{\hbar^2 K^2}{2m_e^*}$$
$$E_v(k) = E_v - \frac{\hbar^2 K^2}{2m_h^*} \tag{1.59}$$

The transition rate takes the form:

$$R_{abs}(\omega) = \frac{2}{\pi\hbar}\left(\frac{eA_0}{2m}\right)^2 |p_{cv}|^2\left(\frac{2\mu}{\hbar^2}\right)^{3/2}(\hbar\omega - E_g)^{1/2} \tag{1.60}$$

where, μ is the reduced mass of the e-h pair.

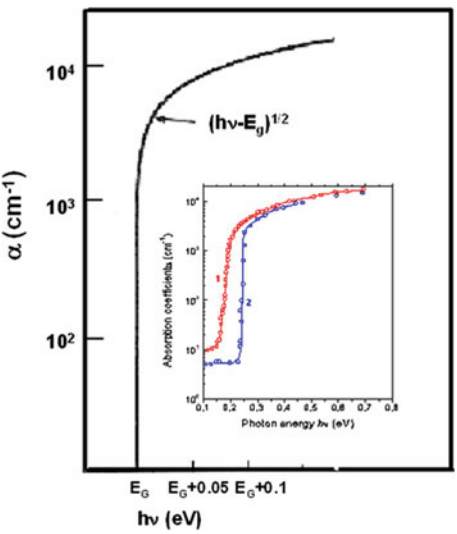

Fig. 1.17 Absorption coefficient versus photon energy. The inset is the experimental absorption edge of InSb at RT (1) and 5 K (2), showing tailing at RT due to CB filling [85]

The transition rate can be related to the absorption coefficient

$$\alpha(\omega) = \left(\frac{e}{m}\right)^2 \left(\frac{1}{2\pi\,\varepsilon_0\, n\omega c}\right) |p_{cv}|^2 \left(\frac{2\mu}{\hbar^2}\right)^{3/2} (\hbar\omega - E_g)^{1/2} \tag{1.61}$$

For a direct transition between the valence band and the conduction band the absorption coefficient varies as the square root of the difference between the photon energy and the fundamental bandgap. The bandgap measured from optical absorption is the optical bandgap. The absorption root square law is plotted in Fig. 1.17, together with the experimental values at 5K and RT of an InSb crystal [85].

This is valid for an intrinsic semiconductor with the VB filled and the CB empty, otherwise, one has to take care of the respective occupancy of the bands:

$$R_{abs}(\omega) = \frac{2\pi}{\hbar}\left(\frac{e\,A_0}{2m}\right)^2 |p_{cv}|^2\, 2 * \int\limits_{FBZ} \frac{d^3\,k}{(2\pi)^3} f_v(k)(1 - f_c(k)) \times \delta(E_c(k) - E_v(k) - \hbar\omega) = B_{vc} f_v(k)(1 - f_c(k)) \tag{1.62}$$

and the absorption coefficient is:

$$\alpha(\omega) = \left(\frac{e}{m}\right)^2 \left(\frac{1}{2\pi\,\varepsilon_0\, n\omega c}\right) |p_{cv}|^2\, 2 * \int\limits_{FBZ} \frac{d^3\,k}{(2\pi)^3} f_v(k) \times (1 - f_c(k))\delta(E_c(k) - E_v(k) - \hbar\omega) \tag{1.63}$$

1.12.3 Microscopic Description of the Stimulated Emission in Semiconductors

The emission corresponds to the reverse of absorption, the electron falls down from the upper level, f, to the lower level, i; in our case it refers to the transition of the electron in the CB to its equilibrium state in the VB. This transition can be stimulated by the electromagnetic wave; in fact, the electromagnetic wave induces the transition of the electron from the CB, down to the VB, loosing the energy emitted as a photon, which adds to the electromagnetic wave that stimulated the transition.

The transition probability for stimulated emission is:

$$W_{stim}(k_f) = \frac{2\pi}{\hbar}\sum_{k_f}\left|\left\langle \phi_{v\,k_i}|H_-|\,\phi_{c\,k_f}\right\rangle\right|\delta(E_c(k_f) - E_v(k_i) - \hbar\omega) \tag{1.64}$$

$$R_{stim}(\omega) = \frac{2\pi}{\hbar}\left(\frac{e\,A_0}{2m}\right)^2 |p_{cv}|^2\, 2 * \int_{FBZ}\frac{d^3\,k}{(2\pi)^3} f_c(k)(1 - f_v(k)) \times \delta(E_c(k) - E_v(k) - \hbar\omega) = B_{cv} f_c(k)(1 - f_v(k)) \tag{1.65}$$

The net stimulated emission rate is:

$$R_{stim} - R_{abs} = B_{cv}(f_v - f_c) \tag{1.66}$$

Note that under strong light excitation the non equilibrium free carrier concentration is very high, and a single Fermi level does not make sense, but one can consider that it splits out in a quasi Fermi level for electrons, F_e, and another for holes, F_h; the occupancy functions follow the Fermi Dirac statistics are:

$$f_v = \frac{1}{1 + e^{(E-\varsigma_h)/KT}} \qquad f_c = \frac{1}{1 + e^{(E-\varsigma_c)/KT}} \tag{1.67}$$

Under a large flux of photons, intense excitation, the quasi Fermi levels for electrons and holes are inside the conduction and valence bands respectively; then, one can define a reverse absorption coefficient:

$$\alpha_{stim}(\omega) = \left(\frac{e}{m}\right)^2\left(\frac{1}{2\pi\,\varepsilon_0\, n\omega c}\right)|p_{cv}|^2\, 2 * \int_{FBZ}\frac{d^3k}{(2\pi)^3} f_c(k) \times (1 - f_v(k))\delta(E_c(k) - E_v(k) - \hbar\omega) \tag{1.68}$$

The absorption rate has to consider the net balance between absorption and stimulated emission. Therefore, it can be obtained by dividing the difference of transition rates by the energy light flux, which is the product of the energy density and the group velocity:

$$\alpha(\omega) = \alpha_{\uparrow}(\omega) - \alpha_{\downarrow}(\omega) = \frac{B_{cv}(f_v - f_c)}{c/n} \tag{1.69}$$

Note that the net absorption coefficient determines the conditions for which gain and losses are dominant respectively. Light with energy $E_g < h\omega < F_c - F_h$ undergoes optical gain ($\alpha(\omega) < 0$) Bernard-Durrafourg condition [86]), while light with energy $h\omega > F_c - F_h$ undergoes optical losses ($\alpha(\omega) > 0$). The population inversion threshold occurs for $f_c = f_v$.

1.12.4 Microscopic Description of the Spontaneous Emission in Semiconductors

In the case of the spontaneous emission, the emission rate can be expressed as:

$$R_{sp}(\omega) = \left(\frac{e}{m}\right)^2 \left(\frac{\pi}{\varepsilon_0 n^2 \omega}\right) \frac{1}{V} |p_{cv}|^2 \, 2 * \int_{FBZ} \frac{d^3 k}{(2\pi)^3} f_c(k) \times (1 - f_v(k)) \delta(E_c(k) - E_v(k) - \hbar\omega) = A_{cv} f_c (1 - f_v) \tag{1.70}$$

A_{cv} is the Einstein coefficient for spontaneous emission.

$$R_{sp} = A_{cv} f_c (1 - f_v) \tag{1.71}$$

According to the relation between the Einstein coefficients, one can establish the relation between R_{stim} and R_{sp}

$$R_{stim} \approx R_{sp} \left(1 - \exp\left(\frac{E - \Delta F}{KT}\right)\right) \tag{1.72}$$

On the other hand, one can establish the relation between spontaneous emission and optical absorption by means of the van Roosbroeck-Shockley relation [87]:

$$R_{sp}(\hbar\omega) = \frac{8\pi n^2}{\hbar^3 c^2} \frac{(\hbar\omega)^2}{\exp(\frac{\hbar\omega - \Delta F}{KT}) - 1} \alpha(\hbar\omega) \tag{1.73}$$

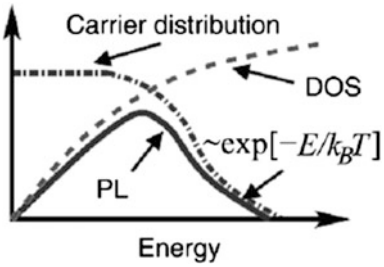

Fig. 1.18 The spontaneous emission signal (PL) is the product of the absorption spectrum, which is proportional to the join density of states and the quasi Fermi distributions of electrons and holes. The high energy tail is proportional to exp(−E/KT), therefore it provides the free electron temperature [88]

where n is the refractive index, α the absorption coefficient, and ΔF is the splitting between the quasi Fermi levels for electrons and holes respectively. This relation permits to convert the spontaneous emission spectrum into the absorption spectrum.

The spontaneous emission is the product of the absorption spectrum, which is proportional to the join density of states and the distribution of non equilibrium electron and holes, Fig. 1.18 [88].

1.12.5 Indirect Optical Transitions

The photon momentum in the optical transitions is negligible with respect to the crystal momentum, therefore the optical transitions were vertical in the k-space. However, in indirect bandgap semiconductors, Si, Ge, AlAs, GaP, SiC among other, the minimum of the CB and the maximum of the VB are separated away in the k-space. Therefore, the momentum conservation rule is not satisfied in band to band transitions, but one needs an extra contribution to conserve the momentum, Fig. 1.19. The extra momentum can be supplied by phonons. Other sources of extra momentum occur by the alloy disorder or scattering mediated by impurities, but in pure and lightly doped semiconductors the transitions between the bands are assisted by phonons.

The problem is treated in the frame of the second order perturbation theory, because the absorption process occurs in two steps, involving electron-phonon interaction, and electron-photon interaction respectively. The absorption coefficient in the vicinity of an indirect bandgap follows a quadratic dependence with the photon energy, instead of the square root dependence reported for direct band gap semiconductors (1.61) [89]:

$$\alpha(\omega) \approx (\hbar\omega - E_g - \hbar\omega_{ph})^2 \tag{1.74}$$

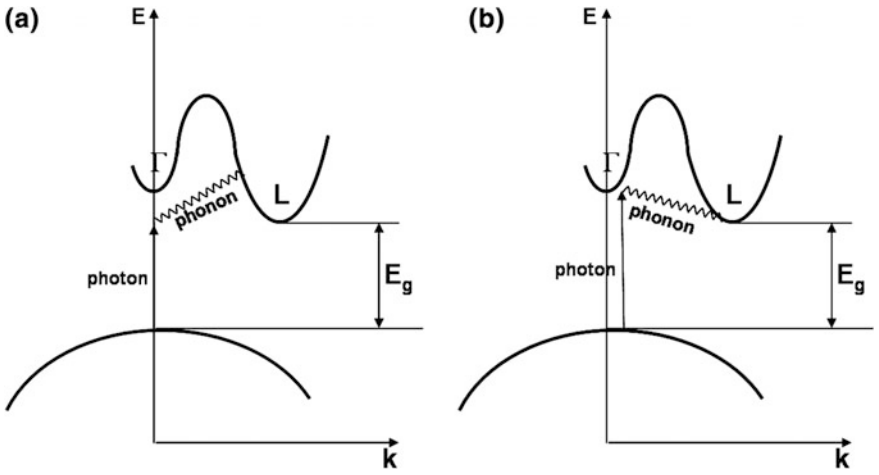

Fig. 1.19 Scheme of transitions in an indirect bandgap semiconductor. **a** Phonon absorption, **b** phonon emission

For an indirect band gap semiconductor the conservation of momentum requires that the absorption of a photon is assisted by a phonon, either absorbed or emitted [90].

1.12.6 The Influence of Disorder and Doping in the Absorption Coefficient. Urbach Tail

As mentioned above the band edge absorption follows a root square dependence with photon energy; however, an exponential tail is often observed bellow the bandgap energy [91–93]. This is the Urbach tail, which appears as a consequence of the transitions between tail states below the band edges, due to doping inhomogeneities, internal strains, or disorder, all giving rise to microscopic electric fields; also, fluctuations of the band edges due to lattice vibrations can contribute to the tail states. The absorption coefficient tail follows an exponential law [91]:

$$\alpha(\omega) = \alpha_0 \exp\left(\frac{\hbar\omega - E_0}{E_u}\right) \tag{1.75}$$

where α_0 and E_0 are materials parameters and E_u is the Urbach energy.

A scheme of the absorption plot including the Urbach tail is shown in Fig. 1.20 [94].

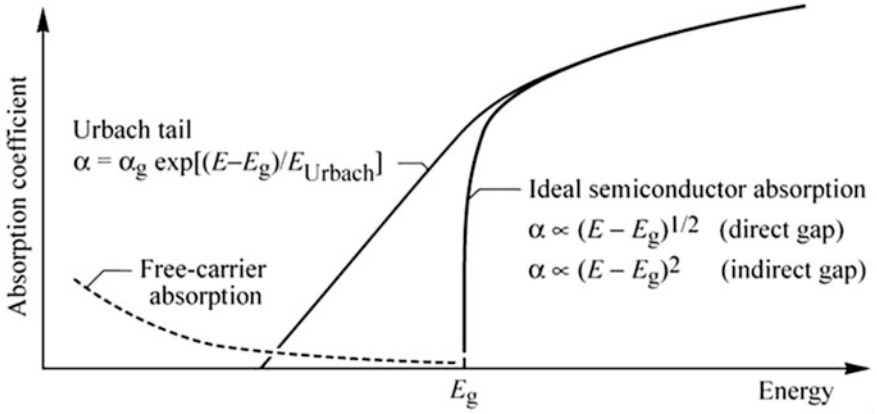

Fig. 1.20 Schematic plot of the optical absorption coefficient, showing the deviation of the expected behaviour for either direct or indirect bandgap as a consequence of the band tailing, and the contribution of the free carriers [94]

Other absorption processes

The main absorption process is the fundamental absorption when an electron transits from the VB to the CB. However, we have described the existence of energy levels inside the fundamental bandgap associated with impurities and/or intrinsic defects; therefore, one can consider the possible transitions from those levels to the free bands, but also the transitions in between them. This is also applicable to the case of quasi-particles as the excitons.

1.12.7 Defect and Impurity Absorption

The main extrinsic absorption processes are summarized in Fig. 1.20. In addition to the fundamental bandgap absorption one can distinguish donor to CB, VB to acceptor, VB to donor, acceptor to CB, and acceptor to donor transitions [65, 95–98]. Figure 1.21 shows the extrinsic absorption of the EL2 deep level in semi-insulating GaAs. The three curves correspond to the changes induced by light, which quenches the absorption by transferring EL2 into a metastable state [99] (Fig. 1.22).

1.12.8 Excitonic Absorption

The theory of excitons is beyond the scope of this text, it is based on many body formalisms. However, under appropriate experimental conditions one observes an

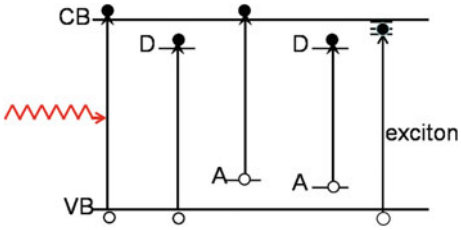

Fig. 1.21 Optical transitions in a semiconductor with defect levels in the forbidden gap

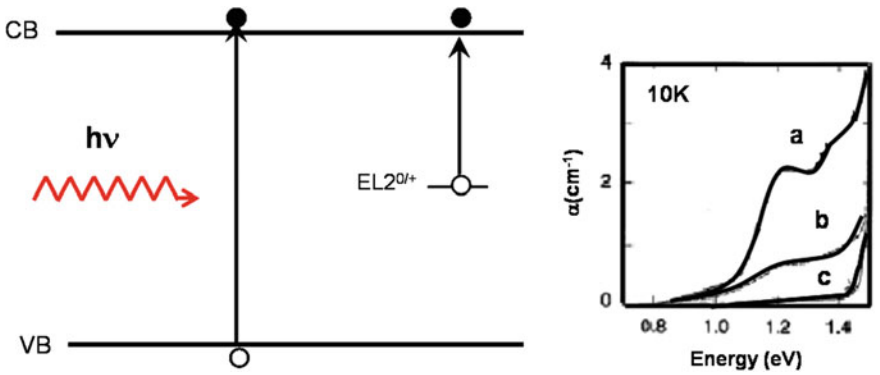

Fig. 1.22 Scheme of optical transitions of EL2 deep level in GaAs (*left*). Absorption coefficient of EL2 (**a**), showing the transformation to a metastable state optically inactive after persistent illumination for 1 min (**b**) and 10 min (**c**) with white light [99], (*right panel*)

absorption peak below the band gap energy, which is due the exciton formation. The absorption curve deviates from the $\alpha(\omega) \approx (\hbar\omega - E_g)^{1/2}$ law for band to band absorption. Excitons also contribute to the absorption above the bandgap energy, where a continuous absorption is observed, this continuum is described by the Sommerfeld factor, which depends on the energy difference between the CB continuum and the fundamental hydrogen level of the exciton [100].

The absorption spectrum of GaAs at different temperatures, showing the exciton absorption contribution, and the subsequent quenching of the exciton absorption once it is thermally dissociated at room temperature is shown in Fig. 1.23 [102].

The excitonic absorption in QWs is sensitive to temperature but not so dramatically as in the bulk, because the electron and hole confinement keep them close together increasing the binding energy, so excitonic transitions are observed up to room temperature in GaAs QWs, Fig. 1.24 [102].

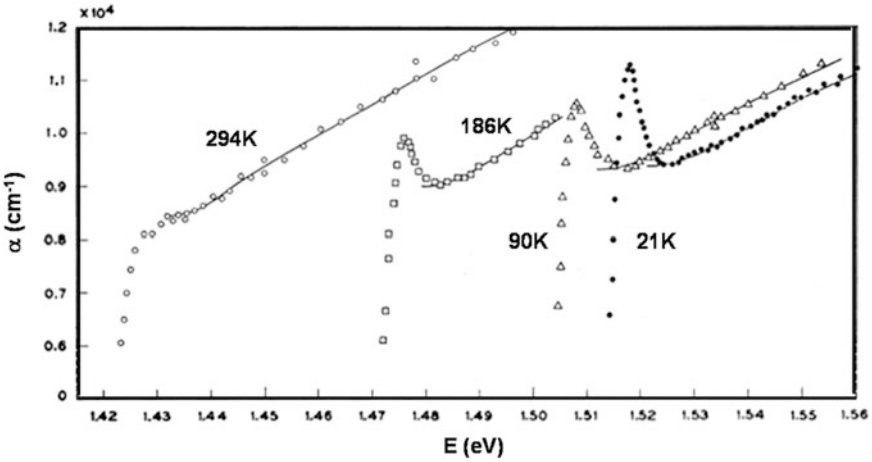

Fig. 1.23 Absorption coefficient of GaAs versus photon energy at different temperatures showing the free exciton absorption and its quenching at room temperature [101]

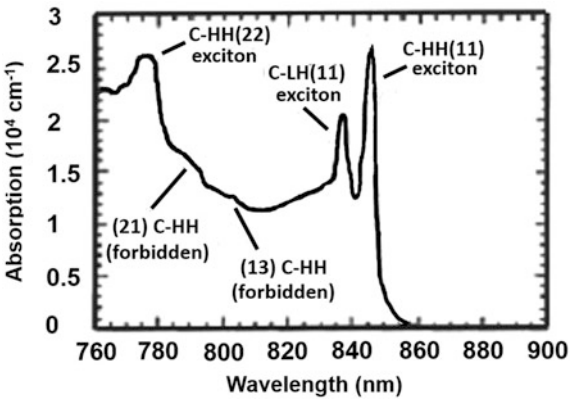

Fig. 1.24 Optical absorption of 10 nm thick GaAs/AlGaAs QW at room temperature, showing the excitonic transition [102]

1.13 Carrier Recombination. Luminescence

The absorption process generates carriers in excess of thermal equilibrium. They come back to equilibrium by the process of carrier recombination. In this process excess electrons of the conduction band fall down spontaneously to the valence band recombining with excess holes. The energy released in this process can be emitted as a photon. This emission is the luminescence phenomenon, which will be discussed in Chaps. 4 and 5 of this volume. It corresponds to the spontaneous emission described above.

Transitions other than band to band can occur when energy states in the forbidden band gap exist associated with defects and impurities. These states are revealed in the luminescence spectrum by characteristics emissions.

1.13.1 Non-radiative Recombination

The excess carriers can be also annihilated by recombination processes in which the energy released is not transformed into photons, but it is dissipated differently, namely generating phonons. Also, the energy can be transferred to another particle, either electron or hole, resulting in a hot carrier (Auger recombination) [103]; Auger recombination is more likely to occur in heavily doped semiconductorsor at very high excitation levels. Alternatively, the recombination energy can be transferred to a neighbor atom in the lattice, which can be removed from its lattice site, leaving behind a point defect; this process is known as recombination enhanced defect reaction (REDR) [104, 105]. This mechanism is relevant to the stability of devices under operation. All these mechanisms are known as non-radiative recombination (NRR) processes. The NRR processes establish competitive recombination paths with the radiative recombination processes; therefore, they play a relevant role in the internal quantum efficiency (IQE) of semiconductors. The internal quantum efficiency is defined as the ratio of the number of photons generated in the semiconductor to the number of generated e-h pairs, if one emits one photon for each generated e-h pair the quantum efficiency at that particular excitation wavelength is the unity. Note that the IQE is also used in solar cells as the ratio of the number of carriers collected by the solar cell to the number of photons of a given energy incident on the solar cell. Therefore, NRR processes reduce the IQE limiting the performance and reliability of devices.

1.13.2 Luminescence

Photoluminescence (PL) is the opposite to optical absorption; furthermore, it needs from optical absorption to occur; however, optical absorption is not the only way to produce free carriers in excess of thermal equilibrium necessary for the subsequent recombination, and luminescence emission; but other excitation sources can be used; in particular, the excitation can be achieved by means of energetic particles, e.g. electrons in cathodoluminescence (CL) emission (Chap. 5). Also, the excess charge carriers can be injected by an electric bias; this emission is known as electroluminescence, and is at the origin of the operation of the light emitting devices.

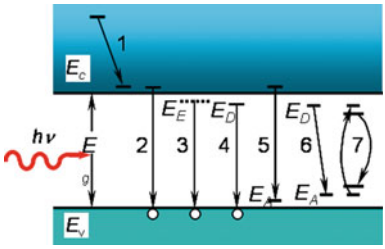

Fig. 1.25 Band gap diagram with the main recombination paths, *1* thermalization, *2* band to band, *3* exciton, *4* D-VB, *5* free to acceptor, *6* Donor acceptor pair (DAP) transition, *7* impurity internal transitions

The different recombination paths are schematically shown in the real space diagram of Fig. 1.25.

The recombination is characterized by a characteristic time, the recombination time.

If the equilibrium carrier populations are n_0 and p_0 respectively, under carrier generation using an external excitation source, the carrier populations are increased, becoming n and p, this excess carrier population decays to equilibrium by recombination.

$$\begin{aligned} n &= n_0 + \Delta n \\ p &= p_0 + \Delta p \\ \frac{dn}{dt} &= G - R_{sp} = -A(np - n_0 p_0) \end{aligned} \tag{1.76}$$

Therefore,

$$\begin{aligned} \frac{d\Delta n}{dt} &= -A(n_0 + p_0 + \Delta n)\Delta n \\ \Delta n &= (\Delta n)_0 \exp(-t/\tau_r) \end{aligned} \tag{1.77}$$

the recombination time is

$$\tau_r = [A(n_0 + p_0 + \Delta n)]^{-1} \tag{1.78}$$

For low generation $\Delta n \ll$ and the lifetime becomes

$$\tau_r = [A(n_0 + p_0)]^{-1} \tag{1.79}$$

In n-type semiconductor $n_0 \gg p_0$, therefore the minority carrier lifetime is

$$\tau_r = [An_0]^{-1} \tag{1.80}$$

While for high generation level $\Delta n \gg$, the lifetime is:

$$\tau_r = [A\Delta n]^{-1} \tag{1.81}$$

One can distinguish different lifetimes according to the classification provided by Bube [106]:

Free lifetime: lifetime of free carriers without considering trapping
Excited lifetime: lifetime of an excess carrier considering free and trapping times
Minority carrier lifetime: The free lifetime of the carrier type with lower density in extrinsic semiconductors.
Majority carrier lifetime: the same as before but for the carrier type with the higher density. Is the relevant parameter in electronic devices.
e-h pair lifetime: The free lifetime of an e-h pair, normally is determined by the lifetime of the first captured carrier, usually the minority carriers, specially under low excitation conditions. This is the relevant time for luminescence emission.

The spontaneous emission rate was deduced using the Fermi's Golden rule; it describes the rate at which electrons in filled states (CB) transit into empty states (VB). It is proportional to the probability of the upper level to be filled times the probability of the lower level to be empty. The sum is made over the initial and final states. Note that instead the absorption process where almost all the states in the bands are available, in the emission process only a narrow interval of energy states, around a few KT from the band edges, is available. The result is the very narrow luminescence linewidth as compared with the broad absorption transitions.

For parabolic bands, low doping and low excess carrier concentration (weak excitation), one can approach the Fermi occupation functions to Boltzmann distributions, and the spontaneous transition from CB to VB rate takes the form [107]:

$$R_{sp}(\omega) \approx \alpha(\hbar\omega - E_g)^{1/2} \exp(-\frac{\hbar\omega - E_g}{KT}) \tag{1.82}$$

The peak energy shifts and the full width at half maximum broaden with T as [107]:

$$\begin{aligned} E_{peak} &= E_g + \frac{1}{2}KT \\ FWHM &= 1.8KT \end{aligned} \tag{1.83}$$

In indirect transitions the participation of phonons is required in order to satisfy the momentum conservation rule, as it was discussed for the absorption in indirect bandgap semiconductors. The band edge luminescence obeys the following relation [107]:

$$R_{sp}(\omega) \approx \frac{(\hbar\omega + \hbar\omega_{ph} - E_g)^2}{1 - \exp(-\frac{\hbar\omega_{ph}}{KT})} \exp\left(-\frac{\hbar\omega + \hbar\omega_{ph} - E_g}{KT}\right) + \frac{(\hbar\omega - \hbar\omega_{ph} - E_g)^2}{\exp(\frac{\hbar\omega_{ph}}{KT}) - 1} \exp\left(-\frac{\hbar\omega - \hbar\omega_{ph} - E_g}{KT}\right) \quad (1.84)$$

The first term refers to phonon absorption, and the second to phonon emission. The peak energy and the FWHM also depend on T according to [107]:

$$\begin{aligned} E_{peak} &= E_g - \hbar\omega_{ph} + 2KT \\ FWHM &= 3.4KT \end{aligned} \quad (1.85)$$

Note that one has to take account of the dependence of E_g with T for the assessment of the peak shift with T.

1.13.3 Diffusion Length

In electroluminescence and CL, and in a minor extent in PL the high energy side of the intrinsic luminescence can be modified by the semiconductor self-absorption, because of the long path traveled by the photons when they are generated deeply in the semiconductor, e.g. in CL experiments one can reach penetration depths above one micrometer, for which non negligible absorption of the high energy luminescence photons occur, which is not the case for PL because the penetration depth of the excitation light is only a few tens of nm. However, the generated carriers run a certain distance before the recombination, this distance is the carrier diffusion length, L_D, which more precisely is the average distance between the carrier generation point and the recombination point. One can also relate the diffusion length to the recombination time, or the carrier lifetime.

$$L_D = (D\tau)^{1/2} \quad (1.86)$$

D is the diffusivity, and is expressed in m^2/s. The minority carrier lifetime and the diffusion length depend strongly on the recombination processes and the density of recombination centers, both radiative and non radiative.

This means that the recombination is not necessarily occurring inside the volume of light absorption, but the light generation volume is enlarged with respect to the carrier generation volume.

1.13.4 Surface Recombination

The surface of the semiconductors with its dangling bonds is a highly efficient recombination player. The excess carriers can reach the surface, when they are generated within the diffusion length distance, recombining there. Usually, the surface recombination is expressed as a surface current:

$$J_{surface} = -eS\Delta n \tag{1.87}$$

Δn is the excess carrier concentration at the surface with respect to the bulk equilibrium value. S is the surface recombination velocity (SRV), it is expressed in velocity units, ms^{-1} and depends on the nature of the semiconductor, the doping level, and the surface termination [108, 109].

Several strategies are defined to reduce S; e.g. surface passivation, dielectric coating.

1.13.5 Exciton Recombination

Often exciton recombination is dominant in the luminescence emission. Exciton luminescence depends on the exciton binding energy, for low binding energy it is only observed at low temperature. Wide bandgap semiconductors as GaN, and especially ZnO, have a large free exciton binding energy [110, 111], see Fig. 1.4, which should permit excitonic emission even at room temperature. The lineshape of the free exciton luminescence takes the following expression:

$$R_{sp}(\hbar\omega) \approx \frac{\hbar\Gamma}{2\pi} \frac{1}{\exp(\frac{\hbar\omega-\Delta F}{KT}) - 1} \frac{1}{(\hbar\omega - E_x)^2 + \left(\frac{\hbar\Gamma}{2}\right)^2} \tag{1.88}$$

where Γ is the full width at half maximum (FWHM) and E_X is the exciton binding energy.

For strong exciton phonon coupling it results in the following expression:

$$R_{sp}(\hbar\omega) \approx \frac{1}{(2\pi)^{1/2}\sigma} \exp\left(-\frac{(\hbar\omega - E_x)^2}{2\sigma^2}\right) \frac{1}{\exp(\frac{\hbar\omega-\Delta F}{KT}) - 1} \tag{1.89}$$

where $\sigma = 0.425\ \Gamma$.

References

1. J.M. Poate (ed.), *Laser Annealing of Semiconductors* (Elsevier, New York, 1982)
2. J.S. Williams, Mater. Sci. Eng. A **253**, 8 (1998)
3. S.O. Kucheyev, J.S. Williams, S.J. Pearton, Mater. Sci. Eng. R **33**, 51 (2001)
4. A.R. Clawson, Mater. Sci. Eng. R **31**, 1 (2001)
5. S. Murad, M. Rahman, N. Johnson, S. Thoms, S.P. Beaumont, C.D.W. Wilkinson, J. Vac. Sci. Technol. B **14**, 3658 (1996)
6. C. Constantine, D. Johnson, S.J. Pearton, U.K. Chakrabarty, A.B. Emerson, W.S. Hobson, A.P. Kinsella, J. Vac. Sci. Technol. B **8**, 596 (1990)
7. S.M. Hu, Phys. Rev. **180**, 773 (1969)
8. D.G. Deppe, N. Holonyak, J. Appl. Phys. **64**, R93 (1988)
9. J. Jimenez, I. De Wolf, J.P. Landesman, MicroRaman spectroscopy: fundamentals and applications. Optoelectronic Properties of Semiconductors and Superlattices, vol 17, ed. by J. Jiménez (Taylor and Francis, New York, 2002) (chapter 2)
10. I. De Wolf, Semicond. Sci. Technol. **11**, 139 (1996)
11. J. Christofferson, A. Shakonri, Rev. Sci. Instr. **76**, 024903 (2006)
12. D.A.B. Miller, D.S. Chemla, T.C. Damen, A.C. Gossard, W. Wiegmann, T.H. Wood, C.A. Bornus, Phys. Rev. B **32**, 1043 (1985)
13. X.F. Liu, R. Wang, Y.P. Yiang, Q.Z. Zhang, X.Y. Shan, X.H. Qiu, J. Appl. Phys. **108**, 054310 (2010)
14. L. Artús, R. Cuscó, J. Ibañez, N. Blanco, G. González, Díaz. Phys. Rev. B **60**, 5446 (1999)
15. R.E. Bailey, S. Nie, J. Am. Chem. Soc. **125**, 7100 (2003)
16. L. Pavesi, M. Guzzi, J. Appl. Phys. **75**, 4779 (1994)
17. M.A. Reshchikov, H. Morkoc, J. Appl. Phys. **97**, 061301 (2005)
18. F. Williams, J. Luminescence **7**, 35 (1973)
19. M.A. Reshchikov, H. Morkoc, S.S. Park, K.Y. Lee, Appl. Phys. Lett. **78**, 3041 (2001)
20. G. Callsen, M.R. Wagner, T. Kure, J.S. Reparaz, M. Bügler, J. Brunnmeier, C. Nenstiel, A. Hoffmann, M. Hoffmann, J. Tweedie, Z. Bryan, S. Aygun, R. Kirste, R. Collazo, Z. Sitar, Phys. Rev. B **86**, 075207 (2012)
21. P.Y. Yu, M. Cardona, *Fundamentals of Semiconductors* (Springer, Berlin, 1996)
22. P.K. Basu, Theory of Optical Processes in Semiconductors (Oxford University Press, Oxford, 1997)
23. M. Grundmann, The Physics of Semiconductors (Springer, Berlin, 2006)
24. G.D. Gililand, Mater. Sci. Eng. R **18**, 99 (1997)
25. W.A. Bassett, in *Dynamic Measurements of Elastic Moduli of Samples at High Pressure and Temperature*, ed. by M. Levy, H. Bass, R. Stern. Handbook of Elastic Properties of Solids, Liquids, and Gases, vol 1 (Elsevier, Amsterdam 2001), p. 469
26. M. Cardona, G. Guntherodt (eds.), *Light Scattering in Solids, Topics in Applied Physics*, vol. 8 (Springer, Heildelberg)
27. W. Richter, in *Resonant Raman Scattering in Semiconductors*, ed. by G. Hohler. Springer Tracts in Modern Physics, vol. 78 (Springer, Berlin 1976)
28. F.H. Pollak, in *Analytical Raman Spectroscopy*, ed. by J. Grasseli, B.J. Bulkin. Chem Anal. Ser., vol. 114 (Wiley, New York, 1991)
29. G. Abstreiter, M. Cardona, A. Pinczuk, in *Light Scattering in Solids IV*, ed. by M. Cardona, G. Guntherod. Topics in Appl. Phys., vol. 54 (Springer, Berlin 1984)
30. B. Prevot, J. Wagner, Prog. Crystal Growth Charact. **22**, 245 (1991)
31. K. Moriya, T. Ogawa, Jpn. J. Appl. Phys. **22**, L207 (1983)
32. T. Ogawa, Rev. Sci. Instruments **57**, 1135 (1986)
33. M. Fukuda, *Reliability and Degradation of Semiconductor Lasers and LEDs* (Artech House, Norwood, 1991)
34. O. Ueda, *Reliability and Degradation of III-V Optical Devices* (Artech House, Norwood, 1996)

35. M. Hempel, J.W. Tomm, F. Yue, M.A. Betiatti, T. Elsaesser, Laser Photonic Rev. **8**, L59 (2014)
36. J.W. Tomm, M. Hempel, MZiegler, T. Elsaesser, Laser Photonic Rev. **5**, 422 (2011)
37. J.P. Walter, M.L. Cohen, Phys. Rev. B **183**, 763 (1970)
38. M.L. Cohen, J. Chelicowsky, *Electronic structure and optical properties of semiconductors*. Springer Series in Solid State Physics, vol. 75 (Springer, Berlin, 1985)
39. W.A. Harrison (ed.), *Electronic Structure and the Properties of Solids*: The Physics of the Chemical Bond (Dover Publications, New York 1989)
40. B. Gil, D. Felbacq, S.F. Chichibu, Phys. Rev. B **85**, 075205 (2012)
41. W. Weber, Phys. Rev. B **15**, 4789 (1977)
42. L.J.T. Waugh, G. Dolling, Phys. Rev. **132**, 2410 (1963)
43. N.W. Ashcroft, D.N. Mermin, *Solid State Physics* (Holt saunders Internacional Editions, Philadelphia, 1976)
44. Y.P. Varshni, Physica **34**, 149 (1967)
45. L. Viña, S. Logotheidis, M. Cardona, Phys. Rev. B **30**, 1979 (1984)
46. K.P. O'Donnell, X. Chen, Appl. Phys. Lett. **58**, 2924 (1991)
47. P.B. Allen, M. Cardona, Phys. Rev. B **23**, 1495 (1981)
48. P.B. Allen, M. Cardona, Phys. Rev. B **27**, 4760 (1983)
49. A. Olkhovets, R.C. Hsu, A. Lipovskii, F.W. Wise, Phys. Rev. Lett. **81**, 3539 (1998)
50. S. Zemon, S.K. Shastry, P. Norris, C. Jagamath, G. Lambert, Sol. St. Commun. **58**, 457 (1986)
51. T.S. Moise, L.J. Guido, R.C. Barker, Phys. Rev. B **47**, 6758 (1993)
52. S.C. Jain, M. Willander, H. Maes, Semicond. Sci. Technol. **11**, 641 (1996)
53. T. Takagahara, K. Takeda, Phys. Rev. B **46**, 15578 (1998)
54. S. Tanaka, S. Onari, T. Arai, Phys. Rev. B **45**, 6587 (1992)
55. R. Dingle, W. Wiegmann, C.H. Henry, Phys. Rev. Lett. **33**, 827 (1974)
56. D. Bimberg (ed.). *Semiconductor Nanostructures* (Springer, Heidelberg, 2008)
57. J.H. Davies, *The Physics of Low Dimensional Semiconductors* (Cambridge University Press, Cambridge, 1998)
58. C. Weisbuch, Brazlian. J. Phys. **26**, 21 (1996)
59. G. Bastard, Phys. Rev. B **24**, 5693 (1981)
60. G. Bastard, J.A. Brum, IEEE Quantum Electron. **22**, 1625 (1986)
61. M. Altarelli, J. Lumin. **30**, 472 (1985)
62. J.W. Matthews, A.E. Blakeslee, J. Cryst. Growth **27**, 118 (1974)
63. R.A. Mogg, Z.Z. Zhang, in *Quantum Dot Technologies*, ed. by E.U. Rafailov. The Physics and Engineering of Compact Quantum Dot Based Lasers for Biophotonics (Wiley, New York, 2014)
64. R. Dingle, A.C. Gossard, W. Wiegmann, Phys. Rev. Lett. **34**, 1327 (1975)
65. M.D. McCluskey, E.E. Haller, *Dopants and Defects in Semiconductors* (CRC Press, Boca Raton, 2012)
66. M.D. Mac Cluskey, S.J. Jokala, J. Appl. Phys. **106**, 07101 (2009)
67. W.T. Masselink, Y.C. Chang, H. Morkoc, D.C. Reynolds, C.W. Litton, K.K. Bajaj, P.W. Yu, Sol. St. Electron. **29**, 205 (1986)
68. M. Scheffler, J. Bernholc, N.O. Lipari, S.T. Pantelides, Phys. Rev. B **29**, 3269 (1984)
69. D.B. Holt, B.G. Yacobi, *Extended Defects in Semiconductors* (Cambridge University Press, Cambridge, 2007)
70. B. Monemar, Phys. Scripta **24**, 367 (1981)
71. R.G. Walters, Prog. Quant. Electron. **15**, 153 (1991)
72. M. Bugajski, W. Lewandovski, J. Appl. Phys. **57**, 521 (1985)
73. I. Hamberg, C.G. Granqvist, K.F. Berggren, B.E. Sernelius, L. Engström, Phys. Rev. B **30**, 3240 (1984)
74. M. Feneberg, S. Osterburg, K. Lange, C. Lidig, B. Garke, R. Goldhahn, E. Richter, C. Netzel, M.D. Neumann, N. Esser, S. Fritze, H. Witte, J. Bläsing, A. Dadgar, A. Kros, Phys. Rev. B **90**, 075203 (2014)

75. E. Sernelius, K.F. Berggren, Z.C. Jin, I. Hamberg, Phys. Rev. B **37**, 10244 (1988)
76. B.I. Shklovskii, A.L. Efros, *Electronic Properties of Doped Semiconductors* (Springer, Berlin, 1984)
77. P. Van Mieghen, Rev. Modern Phys. **64**, 755 (1992)
78. H. Yao, A. Compaan, Appl. Phys. Lett. **57**, 147 (1990)
79. A.P. Roth, J.B. Webb, D.F. Williams, Phys. Rev. B **25**, 7836 (1982)
80. N.Y. Lee, H. Lim, J. Appl. Phys. **78**, 3367 (1995)
81. L. Cao, L. Laim, P.D. Valenzuela, B. Nabet, J.E. Spanier, J. Raman Spectrosc. **38**, 697 (2007)
82. L. Cao, J.S. White, J.S. Park, J.A. Schuller, B.M. Clemens, M.L. Brongersma, Nature Mater. **8**, 643 (2009)
83. F.J. Lopez, J.K. Hyun, U. Givan, I.S. Kim, A.L. Holsteen, L.J. Lauhon, Nano Lett. **12**, 2266 (2012)
84. B. Bharadwaj, B. Deutsch, L. Novotny, Adv. Opt. Photon. **1**, 438 (2009)
85. G.W. Gobeli, H.Y. Fan, Phys. Rev. **119**, 613 (1960) (http://www.ioffe.ru/SVA/NSM/Semicond/InSb/optic.html)
86. M.G.A. Bernard, G. Durafourg, Phys. Status Solidi **1**, 699 (1961)
87. W. Roosbroeck, W. Shockley, Phys. Rev. **94**, 1558 (1954)
88. R. Bhattacharya, B. Pal, B. Bansal, Appl. Phys. Lett. **100**, 222103 (2012)
89. L.H. Hall, J. Bardeen, F.J. Blatt, Phys. Rev. **95**, 559 (1954)
90. J. Noffsinger, E. Kioupakis, C. Van de Walle, S.G. Louie, M.L. Cohen, Phys. Rev. Lett. **108**, 167402 (2012)
91. F. Urbach, Phys. Rev. **92**, 1324 (1953)
92. C.W. Greef, M.R. Glyde, Phys. Rev. B **51**, 1778 (1995)
93. G.A. Slack, L.J. Schowalter, D. Morelli, J.A. Freitas, J. Cryst. Growth **246**, 287 (2002)
94. E.F. Schubert, *Light Emitting Diodes* (Cambridge University Press, Cambridge, 2006)
95. J. Pankove, *Optical Processes in Semiconductors* (Dover Publications, New York, 1975)
96. S.T. Pantelides, *Deep Centers in Semiconductors* (Gordon and Breach, New York, 1986)
97. M. Fukuda, in *Optical Semiconductor Devices*, ed. by K. Chang, in the Wiley Series in Microwave and Optical Engineering (Wiley, New York, 1999)
98. B. Pajot, B. Clerjaud, in *Optical absorption of impurities and defects in semiconducting crystals*, vol. 169, ed. by M. Cardona, P. Fulde, K. VonKlitzing, H.J. Queisser, R. Merlin, H. Stormer. Springer Series in Solid State Science (Springer, Berlin, 2013)
99. G.M. Martin, Appl. Phys. Lett. **39**, 747 (1991)
100. T. Ogawa, T. Takagahara, Phys. Rev. B **43**, 14325 (1991)
101. M.D. Sturge, Phys. Rev. **127**, 768 (1963)
102. J.D. Weeks, J.C. Tully, L.C. Kimerling, Phys. Rev. B **12**, 3286 (1975)
103. P.J. Dean, W.J. Choyke, Adv. Phys. **26**, 1 (1977)
104. D.V. Lang, L.C. Kimerling, Phys. Rev. Lett. **33**, 489 (1974)
105. L.C. Kimerling, Solid St. Electron. **21**, 1391 (1978)
106. R.H. Bube, *Electronic Properties of Crystalline Solids* (Academic Press, New York, 1974)
107. H.B. Bebb, E.W. Williams, in *Semiconductors and Semimetals*, vol. 8, ed. by R. K. Willardson, A.C. Beer (Academic Press, New York, 1972), p. 181
108. H.C. Casey, E. Buehler, Appl. Phys. Lett. **27**, 247 (1977)
109. E. Yablonovitch, D.L. Allara, C.C. Chang, T. Gmitter, T.B. Bright, Phys. Rev. Lett. **57**, 249 (1986)
110. D. Kovalev, B. Aberboukh, D. Volm, B.K. Meyer, H. Amano, I. Akasaki, Phys. Rev. B **54**, 2518 (1996)
111. U. Ozgur, Y.I. Alivov, C. Liu, A. Teke, M. Reschikov, S. Dogan, V.A. Avrutin, S.J. Cho, H. Morkoc, J. Appl. Phys. **98**, 041301 (2005)

Chapter 2
Basics of Optical Spectroscopy: Transmission and Reflection Measurements, Their Analysis, and Related Techniques

Abstract This gives an introduction to the spectroscopy of optoelectronic semiconductors from an experimental point of view. Thus the basic measurements, *transmission and reflection*, are introduced first. These techniques are then explicated, the microscopic processes that form the spectra are addressed, and the standard, mostly commercial, experimental apparatus is introduced. The topic of data analysis is discussed and the link to the optical constants (dielectric function) is addressed. Additionally, techniques are introduced which are derived from the basics such as photoreflection, ellipsometry, and several kinds of mapping techniques.

2.1 Introduction

This guide aims to help with the use of optical spectroscopy as a tool for diagnostics in optoelectronic materials. Although main the emphasis will be laid on the techniques that will be addressed in Chaps. 3–6, there are some basics, which must be stated before. This involves the determination of the *optical constants* by conventional linear spectroscopy, in particular such as transmission, absorption, and reflection measurements. Experiments that provide the optical constants of a material, e.g. $n(\hbar\omega)$ or $\alpha(\hbar\omega)$, allow us to link these results to theory, as well.

The results of transmission, absorption, and reflection measurements provide fundamental knowledge about the analyzed optoelectronic materials, e.g. information on bandstructure such as E_g or details of defect-related absorption features. The understanding of the basic methodology, in particular *knowledge about their limits*, is fundamental for continuing with the characterization by using more complex techniques. Furthermore, this chapter will familiarize the reader with selected spectroscopic techniques that are derived from the basic measurements, such as ellipsometry as a special type of reflection measurement and absorption mapping as a special type of transmission measurement.

Figure 2.1a shows transmission spectra from three Si-doped bulk GaAs wafers in a wide spectral range from the visible (VIS) to the mid-infrared (IR). Their

J. Jimenez and J.W. Tomm, *Spectroscopic Analysis of Optoelectronic Semiconductors*, Springer Series in Optical Sciences 202,
DOI 10.1007/978-3-319-42349-4_2

thickness (d) is $d = 1.1$ mm. Such heavily foreign-doped, and therefore highly conductive, wafers are used, e.g. in optoelectronics as a substrate for the growth of LEDs or diode laser structures. The high doping levels are needed for conducting the required high operation currents with small Ohmic losses.

The *abscissa* represents the wavelength (λ) given in µm. The wavelength represents a standard spectroscopic unit and is given typically in nm or µm for the VIS and IR, respectively. Alternatively, one could have also chosen to give the photon energy ($\hbar\omega$) in eV as abscissa unit by taking into account $\hbar\omega = hc/\lambda$. The use of the $\hbar\omega$-scale allows to point to energies or energy differences most easily. Therefore it is helpful for finding links to the electronic bandstructure of a material. Another common unit for the abscissa, in particular in IR spectroscopy, is the wavenumber (ν) in cm^{-1}. It represents an alternative energy scale, which is most suitable for the quantification of small energy differences. It is also the most common unit in Raman spectroscopy. Note that in *wavelength* 1000 nm = 1 µm = 0.0001 cm. The reciprocal value of the latter is 10,000 cm^{-1}, corresponding to 1.2395 eV with both units pointing to *energies*.

The *ordinate* represents the transmittance (T). The transmittance is given in fractions of unity or in percent. $T = 1$ is equivalent to $T = 100$ % and it points to an ideally transparent medium that, of course, does not exist.

The inset in Fig. 2.1a gives a simplified scheme of a transmission measurement and introduces two other important spectroscopic quantities namely the (internal) absorbtance (A) and the reflectance (R). If we start with $R = 0$, Lambert-Beer's law connects the quantities

$$T = \frac{I(\hbar\omega)}{I_0(\hbar\omega)} = e^{-\alpha(\hbar\omega)\cdot d}. \tag{2.1}$$

Here $\alpha(\hbar\omega)$ is the $\hbar\omega$-dependent *absorption coefficient* of the material and d the thickness of the sample. Converging one step closer to reality, we work with a finite, but spectrally constant $R(\hbar\omega) = R$ for the front surface, while still neglecting reflection at the rear as well as further reflections (or multiple reflections including both surfaces). This results in

$$T = (1 - R) \cdot e^{-\alpha(\hbar\omega)\cdot d}. \tag{2.2}$$

The quantity $\alpha(\hbar\omega) \times d$ is sometimes called *absorbance*, *absorbtivity*, or *optical density*.

R is typically estimated by using (1.45) with $\kappa = 0$. Analogously to T, both A and R are given either in fractions of unity or percent. Energy conservation requires

$$100\,\% \text{ or } 1 = R(\hbar\omega) + A(\hbar\omega) + T(\hbar\omega). \tag{2.3}$$

Figure 2.1b shows the same data sets as (a) on a stretched scale in a rather narrow spectral range around E_g. The measured T-values at E_g are zero. At first

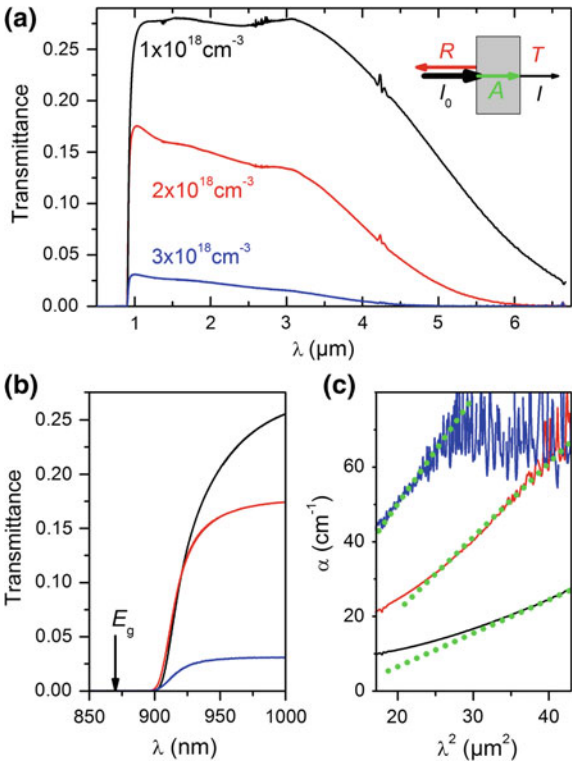

Fig. 2.1 **a** Transmission spectra of Si-doped bulk GaAs wafers. Their thickness is $d = 1.1$ mm. **b** The same spectra on an expanded abscissa scale in the spectral region around E_g. **c** Plot α versus λ^2 in the 4.0-6.5 μm spectral range. $\alpha(\lambda)$ has been determined from (2.2) assuming a constant value of $R = 0.29$

glance, one might be surprised and might assign this, to the unusual high doping level of these particular samples for instance; see (1.27). But this is not the full truth. The proper explanation in this case is the 'ample' sample thickness as it will be discussed in Sects. 2.2 and 2.3. Thus, it becomes clear that T is dependent on sample geometry, in particular on the sample thickness d. Therefore, one should be very cautious when making any assignments on the basis of pure transmittance spectra $T(\hbar\omega)$. Whenever possible, a plot $\alpha(\hbar\omega)$ should be preferred, which can be obtained, e.g. by using (2.2).

Figure 2.1c shows a plot α versus λ^2. The data sets shown in Fig. 2.1a are used again, but now they are restricted to the IR-range of $\lambda = 4.0$–6.5 μm. In order to compile this subfigure, $\alpha(\hbar\omega)$ has been determined from (2.2), assuming a $\hbar\omega$-independent value of $R = 0.29$. The latter value is estimated by using (1.45) and an $\hbar\omega$-independent $n = 3.3$ and $\kappa = 0$. This type of display allows the experimental verification of the validity of (1.42), which has been derived by using the oscillator model for the optical constants, consider $\lambda^2 \propto \omega^{-2}$. The linear slopes in Fig. 2.1c are a measure for the carrier concentrations and indeed the slopes (dotted lines) behave almost like 1:2:3, i.e. in the same way as the carrier concentrations of the three samples do. Thus, this rather simple experiment leads us to an important

application. A simple transmission measurement in the IR, i.e. in a spectral region where most semiconductors are transparent, can be used in order to determine the concentrations of free carriers, at least within certain concentration ranges.

A more complete analysis of the results of transmission measurements will be conducted on higher levels of data analysis in Sect. 2.3.

The borderline between classical linear optics, the topic of this chapter, and non-linear optics is rather floating. From the pure experimental point of view, we talk about *linear optical properties* as long as the result of the measurements does not depend on the intensity of the probe beam, which is used in a transmission measurement. Even though only a few photons may cause optical non-linearities (e.g. excitonic non-linearities even in bulk material or 'quantum interferences' in nanostructures), low test beam intensities, e.g. in transmission or reflection measurements, are recommended for all experiments. The term 'low' refers here to a trade-off between lowest possible excitation densities and acceptable signal-to-noise ratios of the measurements. Modifying the test beam intensity is always a good test to check in which regime one actually works.

2.2 Samples and Spectroscopic Equipment

2.2.1 Samples

The requirements for the samples are already partly visible in the scheme in Fig. 2.1. A suitable sample for transmission measurements should be homogeneous in terms of bulk properties, thickness, and surface properties. The latter is typically achieved by forming (polishing) a coplanar plate with a uniform d-value. The surface of these plates should be prepared in a way that its roughness is small compared to the wavelengths at which the measurement will be carried out.

As mentioned before, the thickness of the sample is an important parameter. Looking at Fig. 2.1b and (2.2), it becomes clear that if $T = 0$, e.g. at short wavelengths, or T = constant, e.g. at long wavelengths, no useful $\alpha(\hbar\omega)$-determination is possible. In the first case, there is only noise, whereas in the second case, the result of the measurement is exclusively determined by R. The lowest error for α is obtained if

$$\alpha(\hbar\omega) \times d \sim 1\,. \tag{2.4}$$

Therefore, d determines the α-range, in which the errors are minimized, and thereby determine the spectral range, in which a useful α-analysis is possible at all.

- Consequently, it may occur that, with a given sample, α can not be determined in a desired spectral range. If larger α-values are of interest, e.g. in an energy range above E_g, one can try to thin the sample. Thinning of bulk material works

well down to the $\sim$10 µm-range, at least if the sample is well attached to a transparent support pad. According to (2.4), a 10 µm thick sample allows the best α-determination at $\sim$1000 cm^{-1}. Using a standard instrument, the $\sim$10–5000 cm^{-1}-range becomes accessible.

- For measurements well above E_g, e.g. in direct semiconductors, even this might not be sufficient. Epitaxial layers on transparent substrates can cover the *d*-range range below 10 µm [1].
- Consequently, the determination of $\alpha(\hbar\omega)$ in a wider range might call for a *sample set* with samples of different thicknesses. Ideally, no further parameters should be modified, of course.

Bearing in mind (2.4), one can now understand why one can not determine E_g from the transmission measurement shown in Fig. 2.1b. Taking into account that $\alpha(E_g)$ of GaAs is not smaller than 3000 cm^{-1} with the given sample thickness of 1.1 mm, we can find an optical density of $\alpha(E_g) \times d > 330$. Therefore, $T(E_g)$ will be smaller than e^{-330}, which is not detectable, of course.

If, on the other hand, the expected absorption $\alpha(\hbar\omega)$ is too small compared to the thickest available sample, one should think about ways to artificially lengthen *d*, e.g. by using multiple internal reflections in a special multi-pass waveguide geometry. Although this might require additional sample preparation (polishing of angled surfaces for in- and out-coupling of the test beam), it may be the only way to arrive at experimental data.

We will now turn our attention towards the sample parts, which are actually probed by standard optical spectroscopy:

- In case of *transmission* measurements, the probed bulk is limited to the typically circular light spot which defines the lateral border of the measured area, also called *lateral spatial resolution*. The measurement averages across the entire sample thickness *d* ('information depth' = *d*). Thus, typically a cylindric sample part is analyzed.
- In a *reflection* measurement, the same holds true regarding the lateral light spot extension. The 'information depth', however, in semiconductors is rather small. It is below 1 µm in case of GaAs near E_g = 1.424 eV, and only $\sim$20 nm at 3 eV, corresponding to the E_1-transion energy [2]. As a rule of thumb, one can expect the 'information depth' at about 20 % of the probe wavelength, for photon energies substantially exceeding E_g.
- Obviously, reflection and transmission measurements do not regard the same part of the sample. This does not matter only as long as the samples are indeed homogeneous.
- For both types of measurements, transmission and reflection, we should mention that the measured cross-sectional spot is not exclusively determined by the probe light spot, but restricted to the fraction of this spot, which is actually imaged to the detector. This brings the apparatus into play that will be addressed in the next subsection.

2.2.2 *Spectrophotometer*

Transmission and reflection measurements are mostly carried out with commercially available *spectrophotometers* (SP). Figure 2.2a shows a typical spectrophotometer, including the main components, while (c) depicts the optical path in this particular device. SPs allow for transmission measurements, while reflection measurements typically require an extension; usually a small optical table, which is inserted into the sample chamber.

An SP represents a combination of several spectroscopic components, which are also independently commercially available. This includes

- Light sources with a preferably smooth spectrum. Suitable lamps are halogen lamps for the VIS and NIR, while SiC-globars (frequently misspelled glowbar) sources meet the requirements in the MIR.
- Monochromators containing gratings or (less common) prisms.
- Optical imaging equipment: Lenses, mirrors, fibers, diaphragms, etc.
- Detectors.

Using these components, one could easily assemble a homemade SP. Although this might be useful for a few very special experiments carried out by experienced spectroscopists, one should take into account that a commercial SP is an optimized system that incorporates a huge amount of know-how. This involves an architecture based on professional optics design and optimized by using matching components, but also methodology that went into the software. Therefore, we will not discuss how to set up a home-made SP. Some details on this issue, however, will be

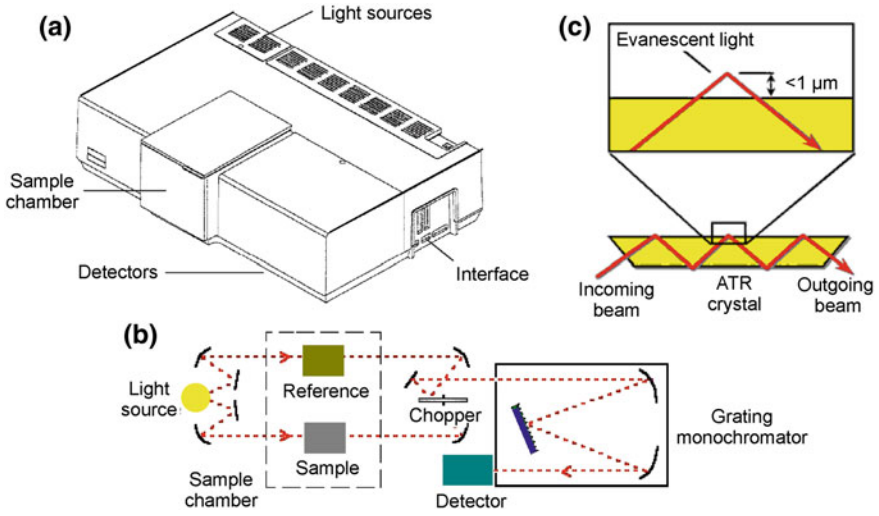

Fig. 2.2 **a** Spectrophotometer. **b** Schematic of the optical table of an ATR extension. **c** Typical optical path in a spectrophotometer

provided in Chap. 4 (Sect. 4.3), in which guidelines for the construction of PL setups are given. For many parameters, the requirements of both types of setups are similar. Although complete PL setups are also commercially available, most of the PL setups practically used in labs are homemade.

An important performance parameter of any SP is its *spectral resolution* $\lambda/\Delta\lambda$, where $\Delta\lambda$ is the smallest difference in wavelengths that can be separated for a given wavelength. $\lambda/\Delta\lambda$ amounts to several 1000 for typical grating-based SPs. It is determined by several parameters, in particular by the slit width, which determines the photon flux towards the detector, as well. Small slit widths increase the spectral resolution but make the signal at the detectors smaller and eventually the signal-to-noise ratios of the obtained spectra poorer. Thus, trade-offs must be found.

Photometric experiments typically require *two independent measurements*. One is done by introducing the sample into the optical path and the other one without the sample. The latter serves as a reference. These two measurements can be made either one after the other within the same optical path or at the same time by using two separate beam paths. These two approaches lead to two different device concepts, namely single beam (sequential approach) and double beam devices (parallel measurement). Naturally, single beam spectrometers are more compact, simpler, and cheaper. Double beam instruments are more complex, but easier in operation and more stable.

The SP shown in Fig. 2.2 is a double beam device. The scheme in (c) also reveals a frequently used technical feature: the chopper alternately images the two beams, namely the measuring beam and the reference, onto the same detector. Thus, the detector provides a signal that mirrors the disparity in intensity of the two beams. Sometimes, an appropriately designed chopper creates even three signals at each wavelength, namely a sample signal, a reference signal, and a dark signal. There are also double beam SPs, which do not involve this special type of beam combination technique. In this instance, the intensities of the two beams are measured by separate detectors. Both types of designs have pros and cons: in the case of using two detectors, their noise will sum up. The presence of a mechanical chopper, however, makes any system more susceptible to mechanical failures.

In Sect. 2.2.1, we explained why the sample thickness determines the spectral range, where α can be measured. Another parameter which is relevant in this context is the precision of the *T*-measurement. Although SPs are designed for high stability (reproducibility), this value is typically between 0.3 and one percent.

There are a number of additional relevant technical features of SPs:

- Some SP-designs include a pre-monochromator for the reduction of stray light.
- Complex SPs automatically change light sources, gratings, filters and detectors even within a sole scan. This ensures optimized conditions, even if extended wavelength ranges are covered by one single measurement.
- Filters, which are typically mounted into filter wheels, suppress contributions from higher orders of the gratings.

Due to the spread of the CCD detector technology, nowadays many monochromators do not scan spectrally by turning a dispersive element. They are designed as polychromators without any exit slit. A CCD camera is placed into the plane of the exit slit and monitors all wavelengths at the same time. This approach is also used for SPs.

The size of the light spot on the sample (lateral spatial resolution) is defined by the 'aperture' setting of the SP. This setting controls a wheel with apertures of different sizes, which are being placed in an image plane. If these setting are not sufficient for achieving, e.g. a desired spatial resolution, one can add additional (smaller) apertures directly into the (two) beam(s). This trick, however, will also increase the noise of the spectrum.

- Up to now, we implied that the transmission or reflection measurements are performed in a way in which the incident light falls perpendicular to the surface of the sample, which is investigated. There are cases where other angles are interesting. For instance, if one wants to check the properties of optical elements like mirrors, or if the reflection angle is used as a parameter for a special type of measurement, e.g. monolayer spectroscopy, thin film analysis, or for the investigation of photonic bandgap structures. For this purpose *variable-incident-angle-reflection-accessory* is offered. Such extensions are typically optical tables, which may be inserted into the sample compartment of the SP. Angles between 10° and 85° are typically accessible.
- At this point, it should be mentioned that most *reflection-extensions* for SPs do not exactly realize perpendicular incidence. Although the errors involved into this are mostly negligible, see (1.46), one should bear this simple fact in mind when thinking about results, in particular, if small deviations matter.
- *Attenuated Total Reflectance* (ATR) is another important option for measurements with SPs. This is a sort of absorption measurement with particular sensitivity to surfaces. The heart of an ATR accessory is the trapezoidal shaped ATR crystal; see Fig. 2.2b. It serves as a waveguide for the probe beam, which becomes totally internally reflected multiple times on its way through the ATR crystal. Typical ATR crystal materials are AMTIR (GeAsSe), Diamond, KRS-5, and (depending on the wavelength range of interest) also semiconductors like Ge, Si, and ZnSe. The sample is attached to the ATR crystal and the absorption measurement takes place via the *evanescent light penetrating into the surface of the sample* through the interface; see Fig. 2.2b. The resulting absorbance is proportional to the number of internal reflections of the probe beam (i.e. the number of interactions) and the penetration depth of the evanescence wave into the sample (i.e. something like an absorption length). *ATR extensions* for SPs are also often mounted on optical tables, which are inserted into the sample compartment.
- For the analysis of *diffuse transmission and reflection*, device vendors offer integrating spheres which are fitted to the particular SP.
- SPs can be equipped with *microscopes* in order to narrow down the sample area that is probed. Naturally, this reduces the total light throughput (as mentioned

before for home-made apertures) and requires more sensitive (less noisy) detectors.

If a spectrum is measured with a microscope, one can arrive at the transmittance at a particular location of a sample. In many cases, it is interesting to compare such a *local measurement* with one taken at another location. This allows for something like a homogeneity test of the sample and leads to what is called sample scanning or *mapping*. This important approach will be addressed separately in Sect. 2.5.

- Many device vendors offer a great variety of further accessory. This includes different types of sample holder, cuvettes, fluid cells, flow cells, cell holders, cell changers, auto-sampler units, turrets, etc.
- Some investigations must be conducted at special, mostly lower, temperatures. Thermostats allow to stabilize sample temperature around ambient temperature, whereas cryostats and closed-cycle coolers can reach cryogenic temperatures as low as 4.2 K and lower. Many vendors of SPs offer also such cryo-technical equipment as well or give recommendations at least.

2.2.3 *Fourier-Transform Spectrometer*

Although Fourier-Transform (FT) spectrometers are not SPs in the narrow sense, they will be given attention here. This is because of many similarities in architecture, operation, and particularly in the applications. Therefore, both types of device concepts are often competitors in the decision about the purchase of a spectrometer.

The main distinction between standard SPs and FT-spectrometers is the way how spectral information is obtained. In SPs, the light is dispersed by gratings, less common by prisms. Therefore, such devices are sometimes also called *dispersive spectrometers*. In FT-spectrometers, spectral discrimination is accomplished by sending the light through an interferometer, e.g., a Michelson interferometer. As a result an *interferogramm* (signal vs. optical paths difference) is obtained. Subsequently, this interferogramm is converted into a spectrum (signal vs. wavelength) by Fourier-transformation. The naming *Fourier-Transform-Spectrometer* points to this. At first glance, this approach appears rather indirect. It involves, however, a number of distinct practical advantages:

- First, there is the *throughput- or Jacquinot-advantage*. In conventional spectrometers, the spectral resolution is determined among others by the slit width of the monochromator. High spectral resolution requires a small slit width and therefore results in small signals at the detector; i.e. a poor signal-to-noise ratios. In contrast, the circular beams in FT-spectrometers ensure high detector signals at the central bursts of the interferogramms together with the rather moderate modulation by the interferometer. Furthermore, circular beams match detector geometries better than the rather longish image of the exit slit of a monochromator.

- Second, there is the *multiplex- or Fellgett-advantage*. All spectral contributions are measured simultaneously, resulting again in a better signal-to-noise ratio at the detector compared to conventional SPs.
- Third, there is a high absolute wavelength accuracy and stability, called the *Connes-advantage*. Typically, the position of the moving mirror in the interferometer is determined from the interference pattern of a stabilized HeNe-laser that is coupled into the interferometer, as well. The emission wavelength of this laser is well-known. As a result, the wavelength calibration of interferometers is much more accurate than the one of a monochromator because it is practically repeated in each measurement. All types of mechanical misalignments are continually compensated by the presence of this reference, resulting in unsurpassed long-term stability.
- In contrast to the dispersive devices, the spectral resolution is constant along the photon energy scale. It is governed by the optical path difference that can be achieved, while counting all the interference fringes. Therefore, high-resolution FT-spectrometers work with moving mirror path ways of up to 5 m. This calls for active stabilization during the measurement called *dynamic alignment*. Spectral resolutions $\lambda/\Delta\lambda$ are 10^4–10^5 with record values by up to two orders of magnitude beyond. Thus, $\lambda/\Delta\lambda$-values excel those of grating-based SPs by orders.
- The generation of stray light is less likely in FT-spectrometers, since the optical path involves fewer chances for light scattering compared to dispersive SPs.
- Except for the beamsplitter, FT-spectrometers do not require any optical elements through which the light has to pass. This makes them flexible in respect to measurements in different wavelength ranges.

Except for the Michelson interferometer that has already been mentioned, there are various other interferometer designs used by different manufacturers. This involves cube-corner retro-reflectors in Michelson-, but also in double-pendulum-interferometers. Nowadays, this also involves micro-mechanical interferometer designs, making FT-spectrometers more compact and affordable. All concepts have the listed, advantages and all benefit from the fact that they are mechanically less complex than any dispersive system.

FT-specific artifacts can be caused by sampling, computing, and necessary numerical procedures, such as apodization [3, 4]. Even the sample alignment can matter. In the past, the computers required for the FT represented a bottleneck leading even to special FT-processor architectures. Since nowadays all spectroscopic setups are connected to powerful personal computers anyway, this drawback vanished, and FT-spectrometers become more and more common. This includes even low-cost and mass applications, where most of the advantages listed above do not really matter but the micromechanical interferometers beat the gratings (in dispersive devices) in terms of costs.

Even most of the results that are presented in this chapter, see e.g. Figs. 2.1 and 2.3, were actually measured by FT-spectrometers and not by conventional SPs.

2.3 Extraction of the Optical Constants from Standard Measurements

In Sect. 2.1, we have already roughly implied how to extract optical constants from *T*-data. In the following, we will have a closer look. The results of transmission and reflection measurements are influenced by both the absorption and the dispersion of the sample. Consequently, there is no trivial way for accessing the optical constants.

Figure 2.3a, b show the result of IR transmission and reflection measurements (full circles) carried out at a narrow-gap PbTe/$Pb_{1-x}Eu_xTe$ multiple QW according to Yuan et al. [5]. The entire structure (including buffer) has a total thickness below 5 μm and has been grown on a transparent substrate. Considering the low-photon energy range, one can clearly see the complementary shape of the interference pattern in the transmittance and reflectance spectra. Taking into account that $A \sim 0$ in this spectral range, this nicely illustrates the validity of (2.3). At photon energies of ∼0.38 eV, the fundamental absorption of the buffer material becomes effective and the structure becomes opaque. At the same time, the interferences in the reflectance spectrum vanish as well. The authors modeled their transmittance data by calculating $n(\hbar\omega)$ and $\alpha(\hbar\omega)$ based on band-structure calculations for their multiple QW structure. The result is shown in Fig. 2.3a as a full line, while the $n(\hbar\omega)$- and $\alpha(\hbar\omega)$-spectra determined in this way are presented in (c). Note the extremely high refractive index, typical for this specific material group, the lead salts. Subsequently, for a final check, the reflectance spectrum has been fitted as well; see line in (b).

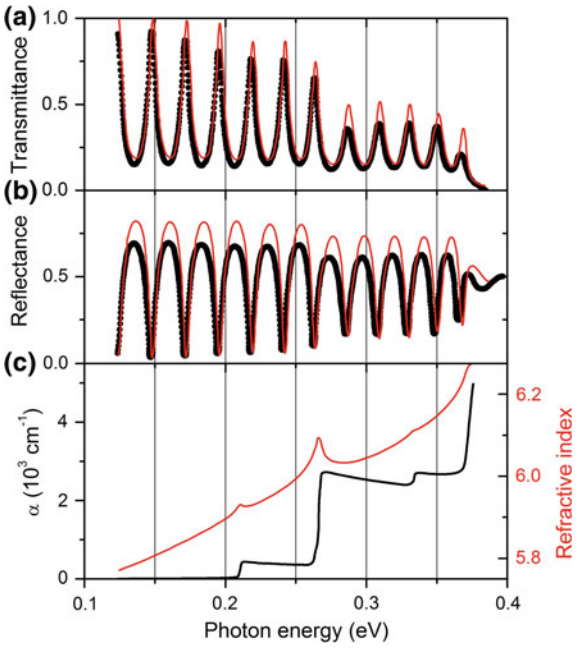

Fig. 2.3 Results of transmission (**a**) and reflection (**b**) measurements at a narrow-gap PbTe/$Pb_{1-x}Eu_xTe$ multiple QW according to Yuan et al. [5]. The full black circles represent the original data. **c** $n(\hbar\omega)$ and $\alpha(\hbar\omega)$ as calculated from the data. The *red lines* in (**a**, **b**) represent the expected transmission and reflection pattern as calculated from $n(\hbar\omega)$ and $\alpha(\hbar\omega)$ in (**c**)

The extraction of optical constants from transmission and reflection measurements via microscopic analysis of the electronic bandstructure of the materials involved is elegant, but also very complex. Therefore, it is not always feasible.

A phenomenological description, which waives the microscopic analysis of the electronic bandstructure, can be made by using Kramers-Kronig analysis; see (1.43) An example for this type of approach is the work by Moreels et al. [6], who in this way determined the optical constants $n(\hbar\omega)$ and $\alpha(\hbar\omega)$ of colloidal PbS quantum dots (QD) from transmission measurements.

Both of these approaches take into account the spectral dependencies of $n(\hbar\omega)$ and $\alpha(\hbar\omega)$ at the same time, as it should be.

But there are also spectral ranges, where one of the two quantities, $n(\hbar\omega)$ or $\alpha(\hbar\omega)$, is almost constant. This is partly visible even in Fig. 2.3. Below 0.2 eV, $\alpha(\hbar\omega)$ is almost zero, whereas at higher photon energies (>0.4 eV not shown), $n(\hbar\omega)$ becomes rater constant resulting in a constant reflectance. The two cases represent the situation when a sample is either transmitting or absorbing. In such border cases, analysis of the transmission spectra is substantially simplified and can be made as straightforward as demonstrated when discussing the results shown in Fig. 2.1.

Multiple reflections may appear in 'thin' low absorbing samples. They produce characteristic fringes as visible in Fig. 2.3a, in particular at lower photon energies. Describing the tide of events when light passes multiple times through a sample delivers

$$T = \frac{(1-R)^2 \cdot e^{-\alpha d}}{1 - R^2 \cdot e^{-2\alpha d}} \,. \tag{2.5}$$

In case of rough samples, it can be more appropriate to consider only one roundtrip of the light. If one sums up all contributions (initial pass and first full roundtrip), the result is

$$T = (1-R)^2 \cdot e^{-\alpha d} \cdot (1 + R^2 \cdot e^{-2\alpha d}) \,. \tag{2.6}$$

In fact, (2.6) represents the two first summands of the infinite series, which sum formula is represented by (2.5).

An experimental way to get rid of the problem related to knowledge of any $R(\hbar\omega)$-dependence, is to make two transmission measurements with two samples, which differ in one parameter only, namely d. For such an experiment

$$\frac{T_1}{T_2} = e^{-\alpha(d_1 - d_2)} \tag{2.7}$$

holds, where T_1 and T_2 are the experimentally measured transmissions and d_1 and d_2 are the thicknesses of the samples 1 and 2. This allows the direct determination of a $\alpha(\hbar\omega)$-spectrum. In practice, this elegant approach might fail if there are more parameters in which the samples differ or if spectrally very narrow features are analyzed.

Obviously, the spectral ranges for the useful application of transmission and reflection measurements are somewhat complementary. The value of E_g may be considered a rough delimiter in between. The sample thickness d, however, is another key parameter that ultimately determines the useful spectral range for transmission measurements. For reflection measurements, this parameter does not matter since only the surface is probed.

2.4 The Link Between the Optical Constants and Material Properties

In the preceding section, we discussed how to progress from $T(\hbar\omega)$- and $R(\hbar\omega)$-measurements to optical constants $n(\hbar\omega)$ and $\alpha(\hbar\omega)$, which are often used practically. If this is achieved, one can compare these curves to the results of theoretical bandstructure calculations. In the following, we will address a number of basic examples, which show how such a comparison could be implemented practically.

2.4.1 Absorption Spectra and Bandstructure

In the following subsection, we will discuss what transmission measurements can tell us about the intrinsic bandstructure of our samples. We will start with the spectral region $\hbar\omega > E_g$ and proceed towards longer wavelengths.

One can calculate $\alpha(\hbar\omega)$-spectra for the spectral range $\hbar\omega > E_g$ by assuming the validity of models for optical interband transitions, in which $\alpha(\hbar\omega) = 0$ holds for $\hbar\omega < E_g$. In Chap. 1, we have demonstrated this for in direct allowed transitions, see (1.61), and provided the result for indirect ones at least; see (1.74). Thus, theory is able to predict shapes of the *absorption edges* based on certain assumptions. In turn, experimental knowledge about shapes of absorption edges allows us to draw conclusions with respect to the nature of optical transitions, e.g. whether they are direct or indirect. Analysis of absorption edges is usually made by plotting $(\alpha\,\hbar\omega)^\kappa$ against the photon energy $\hbar\omega$. From (1.61), which holds for direct allowed transitions, e.g., it follows that a plot with $\kappa = 2$, i.e. $(\alpha\hbar\omega)^2$ versus $\hbar\omega$, is expected to result in a straight line. For other relevant (and strongly simplified) band-structure models, other plots result in straight lines:

$$\text{direct allowed transitions} \quad (\alpha\hbar\omega)^2 \text{versus } \hbar\omega \tag{2.8}$$

$$\text{direct forbidden transitions} \quad (\alpha\hbar\omega)^{2/3} \text{versus } \hbar\omega, \tag{2.9}$$

$$\text{indirect allowed transitions} \quad (\alpha\hbar\omega)^{1/2} \text{versus } \hbar\omega, \tag{2.10}$$

$$\text{indirect forbidden transitions} \quad (\alpha\hbar\omega)^{1/3} \text{versus } \hbar\omega\,. \tag{2.11}$$

The graphs based on (2.8–2.11) can be helpful for the identification of the band structure of a material as well as for the determination of its actual E_g-value. The latter is given by the intersection of the elongated straight line connecting the data with the abscissa. Such plots are sometimes called *Tauc-plots* because this approach has been successfully applied by Tauc [7] to amorphous semiconductor thin films such as *a*-Si and *a*-Ge. Another example is addressed in Fig. 2.4a, b, where a correspondent plot is shown for data obtained from (crystalline) silicon QDs [8]. The use of (2.10) was chosen for this plot as the indirect bandstructure of bulk silicon is known.

However, relying on this kind of plots, requires reliable experimental $\alpha(\hbar\omega)$-data in the spectral range just above E_g. This necessity demands very low sample

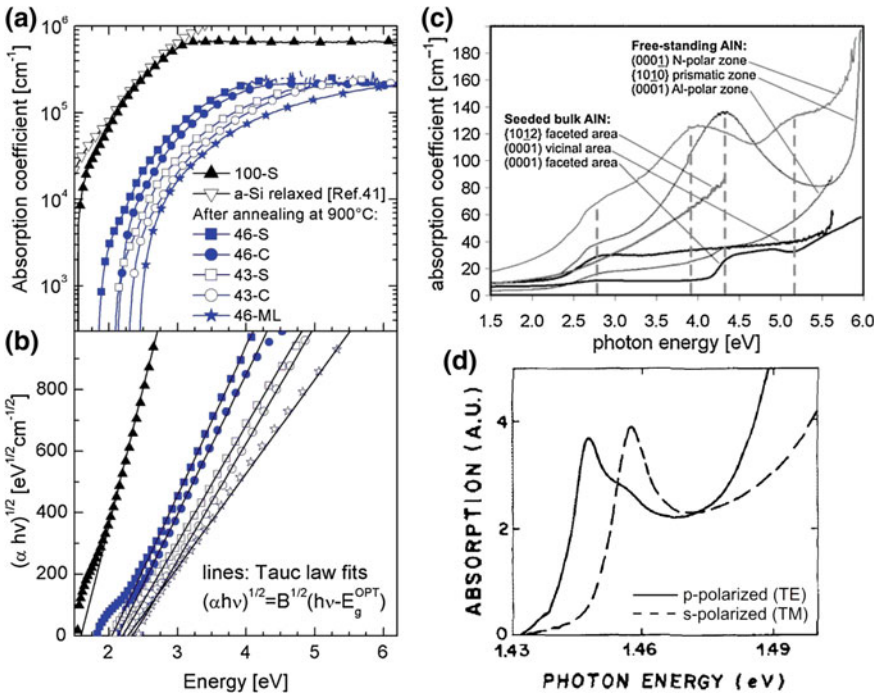

Fig. 2.4 **a** Absorption spectra of crystalline silicon QDs embedded in SiO_2 [8]. The labels represent sample numbers. **b** The same data displayed in a Tauc-plot. **c** Absorption spectra from different AlN samples. Their spectral shapes are related to oxygen-related impurity absorption [10]. **d** In-plane absorption of a GaAs single-QW embedded into a waveguide for parallel (*p,* TE) and perpendicular (*s,* TM) polarized light [11]

thicknesses; see Sect. 2.2.1. Therefore, the applicability of Tauc-plots is often restricted to layers that are either deposited [8] or epitaxially grown [9].

Moreover, there are well-pronounced *excitonic resonances* in many semiconductors in the particular spectral range around E_g. They lead to absorption peaks that are not considered in the models that predict the absorption edge shapes addressed above; see (2.8–2.11). One can circumvent this issue partly by skipping the spectral region close to E_g in the analysis. However, excitonic lines can also be broadened, see e.g. Fig. 1.23. Therefore, it might become very difficult to separate the excitonic contribution from the genuine shape of the absorption edge. Confining the analysis exclusively to appreciable higher photon energies than E_g is also not a perfect solution, since the practicality of the models, which provide the absorption edge shapes, gets worse, e.g. by non-parabolicity effects.

2.4.2 Absorption Spectra and Extrinsic Absorption

If one considers $\alpha(\hbar\omega)$ for $\hbar\omega < E_g$ in the spectral range slightly below E_g, a semilogarithmic plot often results in a straight line. This behavior is described by the Urbach rule; see (1.75) and Fig. 1.20. The slope that can be extracted from this kind of plot is called *Urbach energy* (or Urbach parameter or broadening parameter or broadening energy) E_u, while the presence of this effect is often called *broadening* or band *tailing*. A small value of E_u indicates a steep band edge. Thus, E_u is a measure for the broadening of the band edge. Temperature dependent E_u-analysis reveals two contributions:

- *T-independent* permanent broadening is caused by bandgap fluctuations induced by *structural disorder*. It represents a major broadening source in alloys and mixed crystal systems. Native lattice defects also contribute to this.
- *T-dependent* contributions are caused by phonons (*phonon disorder*). Additionally, defects may contribute via shallow levels, which can be degenerated with the band edge.

For photon energies substantially smaller than E_g, i.e. energetically below the Urbach-tail- region, transmission measurements may provide information about a variety of effects:

- *Free carrier absorption* causes absorption features in the infrared. Their origin is outlined in Chap. 1 and is illustrated by the experimental data that is shown in Fig. 2.1c.
- *Phonon-absorption* takes place in the infrared as well. This is sometimes called *Restrahlen* absorption, although this term has been originally introduced for the corresponding features in reflection spectra. The GaAs phonon energies of $\hbar\omega_{TO} = 33$ meV and $\hbar\omega_{LO} = 35$ meV, e.g., cause Restrahlen absorption at 8.0 and 8.5 THz or $\lambda = 37$ and $\lambda = 35$ µm, respectively.

- *Defect-related transitions* can produce absorption features at photon energies below E_g. According to the schemes in Figs. 1.22 and 1.25, a defect level, which is energetically located within the bandgap, serves as initial or final state, while one of the bands takes the respective part. The energetic position of the Fermi-level (above or below the defect level) determines its population and therefore also, which transitions become probable. Figure 2.4c shows broad oxygen-related absorption bands in AlN [10]. Since $E_g(\text{AlN}) \sim 6.2$ eV, all absorption bands which are in sight are of extrinsic nature. Sometimes such features are also called *impurity absorption*.
- The term *impurity absorption*is also used for another type of defect-related transitions that can be observed by transmission spectroscopy, in particular in the far infrared or THz-region. There are inner transitions in a hydrogen-like impurity, e.g. from 1s to 2p. For the foreign impurities of Sn, Si, and Cl in InSe, such transitions indeed have been observed in absorption measurements [12]. Taking into account the ionization energies (*impurity Rydberg*) of these shallow defects on the order of 17–19 meV, one expects—and the authors indeed found—1s-to-2p-transitions at $\lambda \sim 90$ μm or $\nu = 110$ cm^{-1}.
- The analysis of internal transition in atoms with incomplete inner shells, such as rare earths or transition metals, represent another example for a kind of impurity absorption. In particular in wide bandgap materials, the related absorption lines may appear energetically below E_g.

The mechanisms that were listed represent a number of examples, where regular transmission spectroscopy provides important insights. In any application case, the experimentalist should estimate the expected absorption coefficient first and then choose, at least if possible, the right sample thickness according to (2.4).

2.4.3 Absorption Spectra Obtained by Using Polarized Light

Another parameter that is important for the analysis of transmission spectra is *polarization*. Up to now, we always considered unpolarized light. From the point of view of an experimentalist, there are two main aspects.

First, one has to consider possible *unwanted polarization* if one works with SPs. Of course, their design is expected to exclude residual polarization effects. However, care should be taken anyway in particular if one expects polarization-dependent phenomena or introduces any homemade optical elements into the setup. Thus, unwanted polarization may represent a potential source of error.

Second, *intentional polarization* can provide additional information, in particular if the experiment generates a situation where optical properties of the investigated samples are not isotropic anymore. This can be the case if optically anisotropic materials are investigated, if external forces such as fields are applied to isotropic materials, or if anisotropic structures are made of originally isotropic materials.

The latter situation occurs if QW- and nanostructures are analyzed, where polarization-dependent selection rules apply:

- Figure 2.4d shows the in-plane absorption edges of a GaAs single-QW embedded into a waveguide for parallel (*p*) and perpendicular (*s*) polarized light [11]. The letters *p* and *s* refer to the direction of the ***E***-vector of the probe light with respect to the QW-plane. In this particular QW, there is a 10 meV split between heavy- (hh) and light-hole (lh) valence bands. This hh-lh-split can be seen directly as a shift between the two curves in Fig. 2.4d. According to the in-plane selection rules, *p*-polarized light excites hh- (3/4) and lh-related transitions (1/4), while for *s*-polarized light exclusively lh-related absorption is allowed (1). The numbers in the brackets give the oscillator strengths. Here, an in-plane transmission measurement clearly identifies the two lowest transitions in the QW. Moreover, the pronounced enhancement of the absorption edge in Fig. 2.4d clearly points to its *excitonic nature*. Notice that this data is measured at ambient temperature in a QW made of a material with a rather small exciton binding energy.[1]
- Polarization governs the inter-subband transitions in QWs, as well. Only the light, which is polarized in growth direction causes, allowed inter-subband transitions, as long as the effective mass approximation holds.

Polariscopy is a standard technique, which relies on a polarization-sensitive transmission measurement. With a *polariscope* one investigates how the transit through a sample affects the polarization state, e.g. the rotation of a linearly polarized test beam. This rotation can, e.g. provide information about stresses in semiconductors. If circular polarized light is used, the conversion into linearly polarized light is made with λ/4-plates under 45° incidence. Polariscopy is of particular interest if performed spatially resolved as a type of mapping. This will be addressed separately in Sect. 2.5.3. The reflection-based counterpart to polariscopy, namely ellipsometry, will be outlined in Sect. 2.5.2.

2.4.4 Reflection Spectra

The reflectivity at surfaces and interfaces is described by *Fresnel equations*; see (1.46). Reflection spectra taken for *perpendicular incidence* provide direct information about the refractive index of a material. For all other incidence angles, Fresnel equations indicate a per se polarization-sensitive result. This is employed in a number of analytical techniques, which are called *ellipsometry*; see Sect. 2.5.2.

Figure 2.5a, b show excitonic reflection features obtained from ZnO [13] and CdS [14] surfaces, respectively. There are dips near the spectral position of the free

[1]The hh-exciton binding energy (*Exciton Rydberg*) in bulk GaAs is $E_x \sim 4$–5 meV. In GaAs-based QWs, typical values are on the order of $E_x \sim 10$ meV.

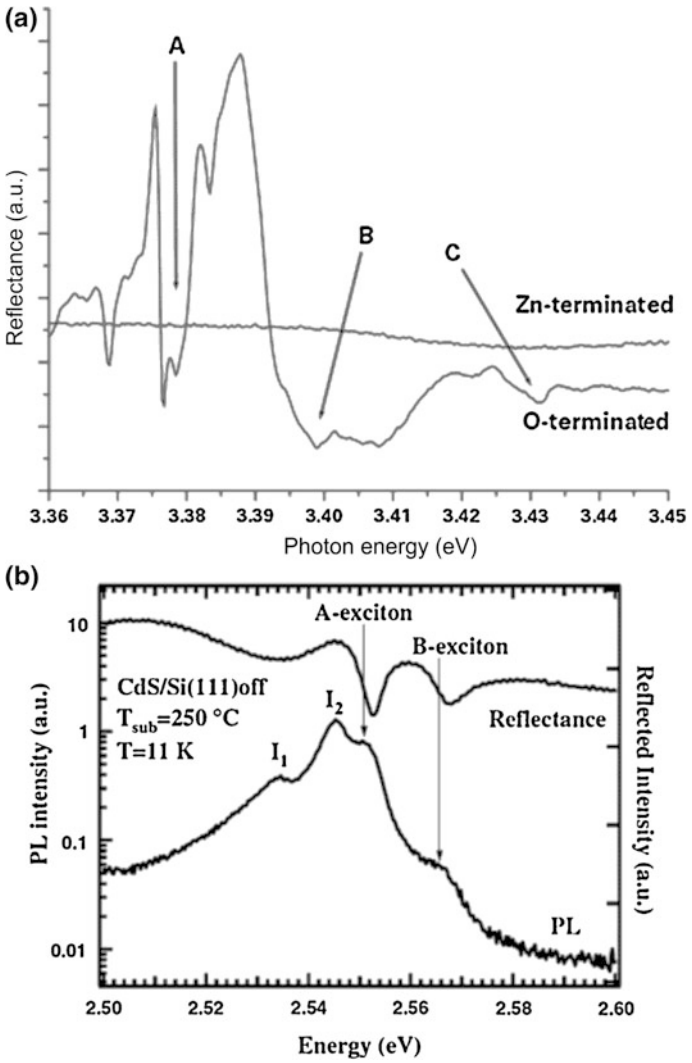

Fig. 2.5 Reflection spectra from ZnO [13] (*left*) and CdS [14] (*right*) surfaces

excitons, which are sometimes called *exciton gaps*. These dips are explained by the large oscillator strengths of free excitons. They lead to strong absorption, which reduces the intensity of the reflected light.

Besides the excitonic oscillators in the spectral region close to E_g, there are reflection features in the infrared (sometimes extended even to the THz-region). These features are called *Restrahlen* reflection band. Its microscopic causes are the lattice vibrations. Thus, it can be considered the manifestation of the phonons in reflectance spectra.

2.4.5 Modulation Spectroscopy and Photoreflection

Photoreflection is a spectroscopic technique that is based on reflectivity measurements. It is a special kind of modulation spectroscopy. Since the topic of *modulation spectroscopy* [15] itself is rather complex, we confine our discussion to photoreflection as one practical and rather frequently used example of modulation spectroscopy. In modulation spectroscopy, the derivative [16] of a spectrum is directly measured. This is accomplished by periodically modulating an external parameter. The quantity that is actually measured is the deviation of the spectrum with respect to this parameter. In the case of photoreflection, the external parameter is a laser spot, which generates non-equilibrium carriers at the position of a sample surface, where the reflectance is measured. Figure 2.6a depicts the scheme of a photoreflection setup. Except for the laser, chopper, and the rather unusual flat angle of incidence, the scheme resembles a regular SP as used in standard DC reflectance measurements (*test beam*). The chopped laser beam (*pump beam*), however, additionally generates a periodic change of the non-equilibrium carrier concentration at that location, where the reflectance is probed. Thus, the AC-signal that is measured by the lock-in amplifier represents the change in reflectivity ΔR with non-equilibrium carrier concentration. This change is normalized to the DC reflectance R, which is either measured in parallel by the lock-in amplifier or sequentially. Therefore the photoreflection signal is denoted as $\Delta R/R$. Figure 2.6b shows typical spectra from $In_{0.53}Ga_{0.47}Bi_xAs_{1-x}$layers with various Bi concentrations as measured at 15 K [17]. Their spectral shape at the observed resonances can be fitted, e.g. by Aspnes [16] formula

$$\Delta R/R(\hbar\omega) = \mathrm{Re}\left[Ce^{i\varphi}(\hbar\omega - E_j - i\Gamma_j)^{-m}\right]. \tag{2.12}$$

C and φ are the amplitude and phase of the basic line that is set to zero in Fig. 2.6b. E_j and Γ_j are the energy and the broadening parameter of the jth optical transition. The exponent m refers to the type of optical transition. For the example shown in Fig. 2.6b, a value of m = 2 is used for the description of the E_0 transition at low temperatures in quaternary $In_{0.53}Ga_{0.47}Bi_xAs_{1-x}$ layers.

With respect to the experimental effort, photoreflection is a comparably economic spectroscopic approach. However, there are some experimental peculiarities.

- Filters are urgently required, which make sure that no pump beam light reaches the detector. While unchopped light only shifts the operation point of the detector (which might move into saturation), chopped laser light up-shifts the basic line. This complicates the search for the signal as one is forced to work in less sensitive measuring ranges of the look-in amplifier.
- Pump and test beam should overlap in the sample surface plane. In an optimized setup, this overlapping area is imaged to the detector and matches its sensitive area exactly.
- A photoreflection signal only exists at certain resonances, i.e. in a small spectral range. For the particular example shown in Fig. 2.6b the *signal is a minimum*.

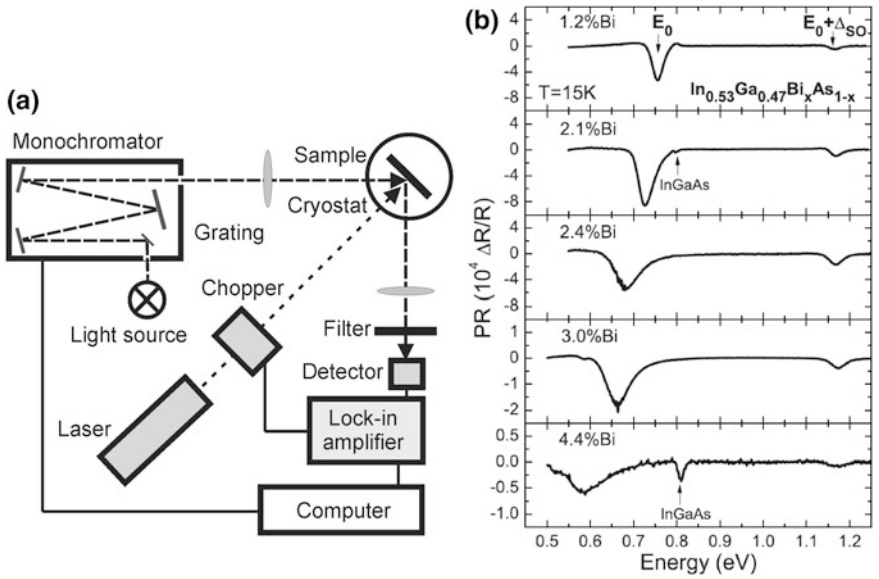

Fig. 2.6 **a** Schematic diagram of a photoreflectance setup. **b** Photoreflection spectra $In_{0.53}Ga_{0.47}Bi_xAs_{1-x}$ layers with various Bi concentrations taken at 15 K [17]

Therefore, any optical alignment, which relies on optimizing the signal (in this particular case, by minimizing it), must be made at the 'right' wavelength. In this situation, having reference samples with known photoreflectance behavior at hand is utmost helpful.

There are a number of very comparable reflection techniques based on modulation spectroscopy, e.g. *electroreflection*, *piezoreflection*, and *thermoreflection*. As already indicated by the naming, the photo-modulation is replaced by an electric field (sample bias), a mechanical load (piezoelectrical transducer), and temperature (periodic thermal cycling), respectively.

When we introduced the idea of modulation spectroscopy above, we did not go into detail about the microscopic mechanisms, why a modulation of the non-equilibrium carrier concentration results in a change in reflectivity. Non-equilibrium carriers have a multifaceted impact on the optical properties of a material. Among others, the spectral position of the absorption edge is modified by bandgap renormalization. Thus, the spectral position of the absorption edge (of the effective E_g-value) is periodically shifted across the fix spectral position of the test beam. This creates the photoreflection spectrum. The same holds for piezoreflection, where external strain impacts the bandstructure including the value of E_g. In case of thermoreflection, the absorption edge shifts according to the $E_g(T)$-dependence of the particular material. However, in case of electroreflection, additional modulation by an electric field lifts the translation symmetry of the crystal resulting in a "third derivative behavior" of electroreflection spectrum. This stands in contrast to the "first derivative behavior" of the other techniques mentioned above [16].

Up to now, we considered the modulation techniques as tools, e.g. for band structure analysis. The magnitude of the thermoreflection signal at the given test wavelength depends (among others) on the perturbation itself, e.g. its amplitude. This is used as a tool for temperature measurements, in particular for spatially-resolved temperature measurements. This approach is referred to as *thermoreflectance*; see Sect. 2.5.

The methods introduced above indirectly employ wavelength modulation by 'shifting the bandstructure' with respect to the fixed test beam wavelength. For the sake of completeness, we should mention at this point the option of direct *wavelength modulation* of the test beam, as well. This can be accomplished, e.g. by periodically moving the image of a moderately opened monochromator exit slit (and in this way a certain *wavelength interval*) across the particular sample position, which should be probed.

2.5 Related Techniques

In the preceding subsections, we progressed from standard transmission and reflection measurements, more or less automatically to techniques, which are based on these measurements but extend them. Examples are polariscopy and ellipsometry. In the following subsections, we will separately address a number of such techniques.

2.5.1 Photoacoustic Spectroscopy

Up to now, we stressed that transmission measurements can provide the optical constants, such as $\alpha(\hbar\omega)$ and $n(\hbar\omega)$. However, this approach must be considered an indirect one. What we are measuring with the detector in a T-measurement is the light that leaves the sample after having passed through it; cf. inset in Fig. 2.1. But what we are actually interested in is rather the light that remains in the sample, namely A, see (2.3). Therefore, it is obvious that there should be techniques, which quantify this important fraction of the test beam.

Photoacoustic spectroscopy is an established technique for a direct A-measurement. Here, the absorbed light is detected by monitoring the local heating that is caused by absorption. Local heating results in local thermal expansion (pressure), which results in a sound wave, which also gave this technique its name. Thus, photoacoustic spectroscopy resembles a transmission measurement, the sample itself being the detector. However, the detection of the sound wave generated in the sample requires additional auxiliary means. These are e.g. microphones, piezoelectric transducers, or optical techniques. All these approaches probe the small mechanical displacements caused by the sound wave. Neto et al. [18] report the

determination of transport properties and thermal diffusivity in GaAs and Si by photoacoustic spectroscopy.

The methodological approach of photoacoustic spectroscopy is used far beyond the field of semiconductor spectroscopy.

- It involves material science, where a number of derivatives of photoacoustic spectroscopy have been developed and used for the determination of thermal properties of materials such as thermal conductivity.
- Photoacoustic spectroscopy is widely used in the spectroscopy of gases and liquids.

Here, we should stress that the number of practical spectroscopic techniques that accomplish a direct *A*-measurement is rather small. In *photocurrent spectroscopy*, the sample serves as the detector as well. In contrast to thermal effects employed in photoacoustic spectroscopy, the mechanism of signal generation relies on electronic excitation of non-equilibrium carriers and their motion (transport). This technique will be addressed separately in Chap. 6.

2.5.2 *Ellipsometry*

Ellipsometry is a special kind of reflectance spectroscopy that uses Fresnel's equations; see (1.46). For a detailed introduction, see the book by Tomkins and Irene [19]. The basic idea underlying ellipsometry is to perform a reflection measurement with a test beam, of which the polarization state is intentionally prepared and known; see scheme in Fig. 2.7. The fixed angle of incidence is in the 50–75° range. After interacting with the surface, the reflected beam is analyzed and the changes are monitored. The beams lie in the plane of incidence, which also contains the normal to the sample surface. The term 'polarization state' is represented by the two parameters that describe an elliptically polarized wave, namely the *relative amplitude* $\tan(\psi) = X/Y$ (measured with the *analyzer*) and the *phase shift* Δ; see denotations in Fig. 2.7. The changes of these two angles during the reflection at a surface represent the *ellipsometric parameters (angles)* ψ and Δ, from which all further information is derived.

An ellipsometer consists of two arms, the one that prepares the polarization state (left) and the one that analyzes it (right). The compensator can be located in either one. Probably the simplest way to perform a measurement is *null ellipsometry*. Here, the compensator (retarder), which might be a $\lambda/4$-plate tilted by 45°, is rotated in a way that the elliptically polarized test beam is converted into a linear polarized one, which is then deleted by finding the right analyzer angle. *Photometric ellipsometry* involves measurements for different analyzer and compensator positions and extraction of information by modeling the curves that were obtained. In this context, rotating analyzers represent an option as well.

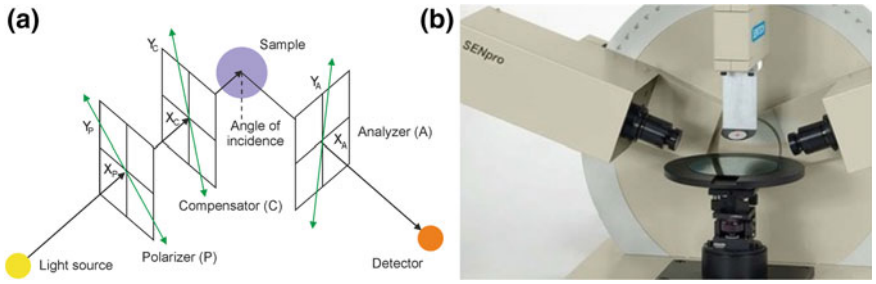

Fig. 2.7 **a** Schematic of an ellipsometric measurement. **b** Photo of an ellipsometer used for wafer inspection; see wafer on the table (Bernd Gruska)

When looking at Fig. 2.7, there are at least two parameters which obviously might be varied additionally, the angle of incidence and the wavelength of the test beam. While the second option leads to a technique that is called *spectroscopic ellipsometry*, the first is responsible for the fact that many ellipsometers include goniometric stages (*variable angle ellipsometry*). Such ellipsometers are able to analyze the optical constants of each single layer in multilayer systems, such as optical coatings as well as their thicknesses; see e.g [20]. Such setups involve complex software packages, which directly provide the desired values. Nevertheless, when using such software, one should be aware about the assumptions made for the derivation of the equations involved and the resulting limitations for application.

Ellipsometry also includes time-resolved measurements, even in the ultrafast region. Spatially resolved measurements are accomplished either by scanning or imaging ellipsometry.

2.5.3 Mapping

For all techniques that have been addressed up to now, the probed sample volume represents an important issue. It represents the region from where the information is averaged. If samples are not homogeneous, it is obvious that a comparison of multiple measurements taken at different locations could be a useful tool in order to quantify the inhomogeneity. This is the idea of scanning (one-dimensional, along a line) or mapping (two-dimensional inspection of an area). There are a number of important parameters related to mapping approaches:

- What quantity is measured? While in a scanning approach transmission or reflection *spectra* can still be displayed, a map requires a type of data reduction. As the examples at the end of this subsection will show, one can e.g. display the reflectance of transmittance at a special wavelength. In such cases, it seems

more economical to measure only once at this specific wavelength and to take the *scalar* instead of the full spectrum.

- The *spatial resolution* of a single measurement has been addressed in Sect. 2.2.1 already. In the mapping application, the resolution should be chosen in a way that the 'inhomogeneity effect', which should be imaged, is properly resolved. When using conventional microscopes, the diffraction limit sets the lower border.

  At this point, one should bear in mind that lateral resolution (that is addressed here) and depth resolution in the measurements (transmission, reflection) might differ by orders of magnitude.
- The *step width* for the mapping should be chosen together with the spatial resolution and the total area on the sample that should be mapped. Obviously, step width and spatial resolution should be almost similar in size in order to avoid overlaps or gaps in between the measurement positions. Together with the measuring time per position (single measurement), these requirements define the total measuring time.
- Finding the right tradeoffs between these parameters probably represents a key challenge in the mapping business.
- Up to now, we implicitly assumed that mapping takes place serially. In the advent of CCD cameras, parallel approaches are feasible and elegant; in particular, if not full spectra are taken, but e.g. only intensities at fix wavelengths.

These remarks will be illustrated by a number of examples.

Example: Transmission mapping

In Sect. 2.4.2, we discussed that transitions involving defect levels can produce absorption bands at photon energies $<E_g$. A technologically relevant defect level in GaAs, named EL2, has been *sequentially* mapped on a wafer scale with a scanning apparatus [21]. Later *parallel* EL2-mapping using an infrared camera has been demonstrated [22]. Figure 2.8a shows such an image of a GaAs wafer part, superimposed on the outline of a 100 mm wafer clearly showing the four-fold symmetry and cellular structure of the defect arrangement.

Wellmann et al. [23, 24], found that the below-E_g-absorption-coefficient in GaAs increases with actual carrier concentration and used this in order to map the doping level distributions in wafers; see Fig. 2.8b. The same approach has been applied to 4H-SiC- and 6H-SiC-wafers [25].

Moreover, transmission mapping approaches have been developed, which are based on similar principles as modulation spectroscopy as introduced in Sect. 2.4.4 for reflection. There is, e.g. the *modulated free-carrier absorption* technique. In this approach, the free carrier concentration is sinusoidally modulated by an additional laser and from the phase shift between excitation and absorption change, the non-equilibrium carrier lifetime (phase method) is determined. In this way, lifetime mapping has been demonstrated in multi-crystalline silicon solar cells [26]. An alternative approach, based on pump-probe measurements (transient method), rendered carrier lifetime mapping in SiC epitaxial layers possible [27].

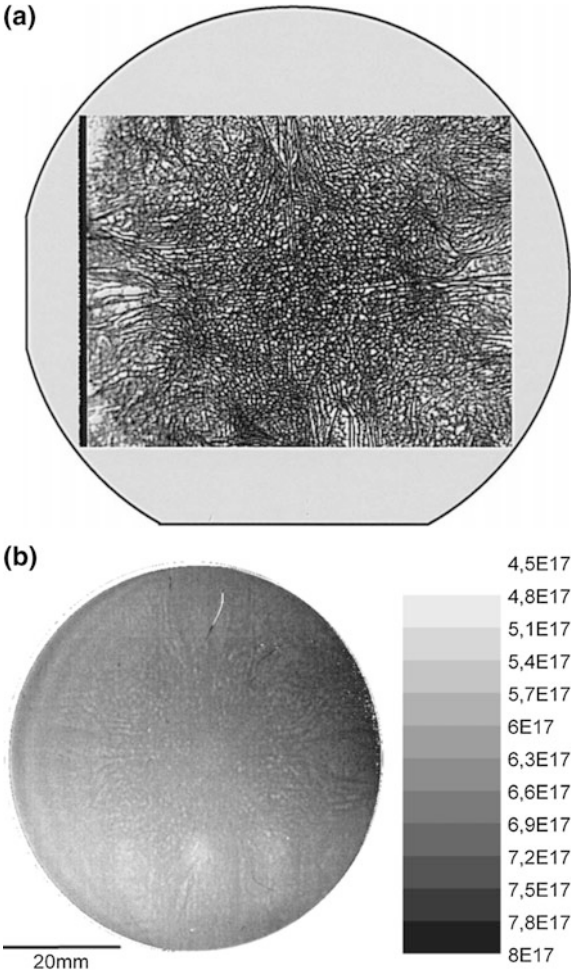

Fig. 2.8 Results of transmission mapping of GaAs-wafers. **a** Map of the EL2 defect distribution in an annealed GaAs-wafer [22]. **b** Mapping of the carrier concentration in a Te-doped GaAs-wafer [23]

Polariscopy has been introduced in Sect. 2.4.3. After being expanded from a single measurement to a mapping approach, this technique was used for imaging and quantification of stresses. Stresses can cause optical anisotropy of a material and cause double refraction of the transmitted light (birefringence). If appropriately calibrated, a polariscopic map can therefore be seen as stress map. As noted before for other techniques, the evolution turned from sequential to parallel measurements by CCD-based setups. An overview of the applications of polariscopy to rapid stress analysis in microelectronic materials and devices including Si-wafers is given by Horn et al. [28] Geiler et al. applied polariscopy to full wafer-shear stress imaging as well as to local stress analysis in GaAs wafers [29].

Example: Reflection mapping

When we use our eyes, we actually do something like reflection mapping using the sun light as the light source. From a more technical point of view, imaging and microscopy are in fact kinds of reflection mapping. An overview on this is, of course, beyond the scope of this book.

Monochromatic reflection mapping represents an interesting option, if the probe wavelength is sensitive to a parameter that varies across the mapped range. One example for such type of mapping is *thermoreflectance*. This approach again represents a type of modulation spectroscopy that became a relevant surface-temperature-mapping technique. For this type of measurement, the temperature of a sample is modulated and the reflectance change (in semiconductors it is caused by the temperature dependence of the refractive index) is used as a measure for the temperature modulation that is imaged in this way. Figure 2.9a shows facet temperature distributions at the front facets of quantum-cascade lasers for increasing operation currents (representing the perturbation) as determined by thermoreflectance [30]. Except for such GaAs semiconductor surfaces, many other materials change their reflectivity with temperature as well. Thus, the technique has been extended to various types of surfaces, among others even metal layers; see Fig. 2.9b [31]. Again the development went from sequential mapping to parallel measurements resulting in CCD-based thermoreflectance microscopy. Farzaneh et al. [31] reviewed principles and applications of this technique.

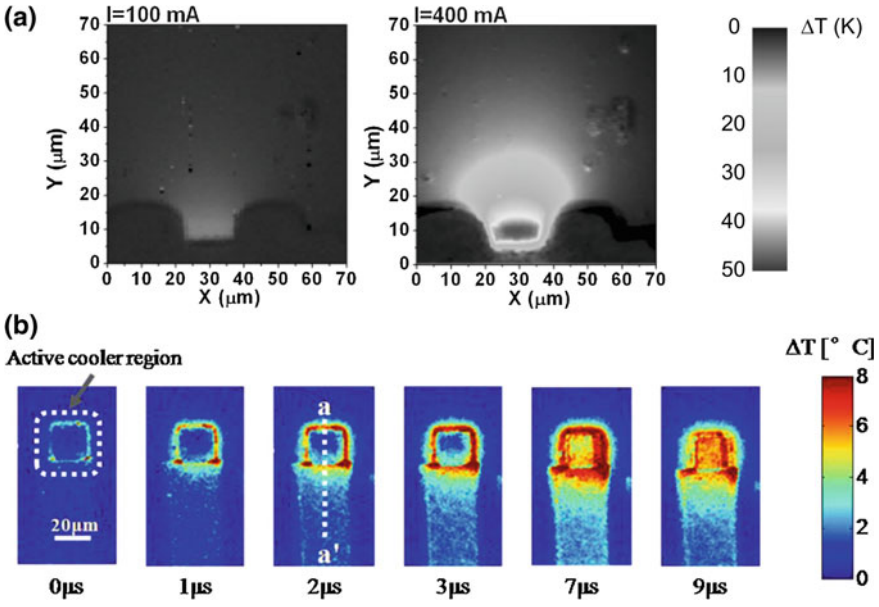

Fig. 2.9 **a** Facet temperature distributions at the front facets of quantum-cascade lasers measured by thermoreflectance [30]. **b** Thermal images of a 20 × 20 μm SiGe thermionic cooler. The image sequence shows temperatures during the first 9 μs after device excitation by a 700 mA pulse [31]

Near-field scanning optical microscopy

Near-Field Scanning Optical Microscopy (NSOM, sometimes also SNOM) represents a special type of mapping approach, which can be, among others, used for transmission and reflectance measurements as well. In fact, it is an 'optical type' of atomic force microscopy. The light source of a NSOM is a sub-micron sized aperture through which evanescent light, typically laser light, is coupled to the sample. Typical aperture diameters are on the order of 50–200 nm. The distance between aperture and sample surface is typically in the order of 5–10 nm only. Thus, the dimension of the aperture determines the spatial resolution, which clearly excels the diffraction limit. Most relevant applications of this scanning/mapping technique, however, do not employ genuine transmission and reflectance measurements. Therefore, we will address the NSOM technique by discussing examples coming from Raman, photoluminescence, and photoelectrical spectroscopy in Chaps. 3, 4, and 6, respectively.

References

1. H.C. Casey, D.D. Sell, K.W. Wecht, J. Appl. Phys. **46**, 250 (1975)
2. A. Badakhshan, R. Glosser, S. Lambert, J. Appl. Phys. **69**, 2525 (1991)
3. F.J. Harris, Proc. IEEE **66**, 51 (1978)
4. D.A. Naylor, M.K. Tahic, J. Opt. Soc. Am. A Opt. Image Sci. Vision **24**, 3644 (2007)
5. S. Yuan, G. Springholz, G. Bauer, M. Kriechbaum, Phys. Rev. B **49**, 5476 (1994)
6. I. Moreels, G. Allan, B. De Geyter, L. Wirtz, C. Delerue, Z. Hens, Phys. Rev. B **81**, 235319 (2010)
7. J. Tauc, R. Grigorov, A. Vancu. Phys. Status Solidi. **15,** 627 (1966)
8. S. Mirabella, R. Agosta, G. Franzo, I. Crupi, M. Miritello, R. Lo Savio, M.A. Di Stefano, S. Di Marco, F. Simone, A. Terrasi. J. Appl. Phys. **106,** 103505 1 (2009)
9. D.D. Sell, H.C. Casey, J. Appl. Phys. **45**, 800 (1974)
10. M. Bickermann, B.M. Epelbaum, O. Filip, P. Heimann, S. Nagata, A. Winnacker. Phys. Status Solidi B. **246,** 1181 (2009)
11. J.S. Weiner, D.S. Chemla, D.A.B. Miller, H.A. Haus, A.C. Gossard, W. Wiegmann, C.A. Burrus, Appl. Phys. Lett. **47**, 664 (1985)
12. J. Martinezpastor, A. Segura, C. Julien, A. Chevy, Phys. Rev. B **46**, 4607 (1992)
13. J. Fryar, E. McGlynn, M.O. Henry, A.A. Cafolla, C.J. Hanson, Phys. B Condens. Matter. **340**, 210 (2003)
14. S. Seto, Japanese Journal of Applied Physics Part 1-Regular Papers Brief Communications & Review Papers **44,** 5913 (2005)
15. M. Cardona, *Modulation spectroscopy*, Vol. Suppl. 11 (Academic Press New York, 1969)
16. D.E. Aspnes, Surf. Sci. **37**, 418 (1973)
17. R. Kudrawiec, J. Kopaczek, J. Misiewicz, W. Walukiewicz, J.P. Petropoulos, Y. Zhong, P.B. Dongmo, J.M.O. Zide, J. Appl. Phys. **112,** 113508 1 (2012)
18. A.P. Neto, H. Vargas, N.F. Leite, L.C.M. Miranda, Phys. Rev. B **41**, 9971 (1990)
19. *Handbook of Ellipsometry*, Vol., ed. by H.G. Tompkins, E.A. Irene (William Andrew, Inc. and Springer-Verlag GmbH & Co. KG, 2005)
20. J. Wagner, H. Obloh, M. Kunzer, M. Maier, K. Köhler, B. Johs, J. Appl. Phys. **89**, 2779 (2001)
21. S.K. Brierley, D.S. Lehr, Appl. Phys. Lett. **55**, 2426 (1989)

22. D.J. Leahy, J.M. Mooney, M.N. Alexander, M.M. Chi, S. Mil'shtein, Infrared Phys. Technol. **39**, 83 (1998)
23. P.J. Wellmann, A. Albrecht, U. Kunecke, B. Birkmann, G. Mueller, M. Jurisch, Eur. Phys. J. Appl. Phys. **27**, 357 (2004)
24. U. Kunecke, P.J. Wellmann, Eur. Phys. J. Appl. Phys. **34**, 209 (2006)
25. R. Weingartner, M. Bickermann, S. Bushevoy, D. Hofmann, M. Rasp, T.L. Straubinger, P.J. Wellmann, A. Winnacker, Mater. Sci. Eng. B Solid State Mater. Adv. Technol. **80**, 357 (2001)
26. S.W. Glunz, W. Warta, J. Appl. Phys. **77**, 3243 (1995)
27. A. Galeckas, V. Grivickas, J. Linnros, H. Bleichner, C. Hallin, J. Appl. Phys. **81**, 3522 (1997)
28. G. Horn, J. Lesniak, T. Mackin, and B. Boyce, Review of Scientific Instruments **76,** 045108 1 (2005)
29. H.D. Geiler, H. Karge, M. Wagner, S. Eichler, M. Jurisch, U. Kretzer, M. Scheffer-Czygan, Mater. Sci. Semicond. Process. **9**, 345 (2006)
30. D. Wawer, T.J. Ochalski, T. Piwonski, A. Wojcik-Jedlinska, M. Bugajski, H. Page. Phys. Status Solidi A. **202,** 1227 (2005)
31. M. Farzaneh, K. Maize, D. Luerssen, J.A. Summers, P.M. Mayer, P.E. Raad, K.P. Pipe, A. Shakouri, R.J. Ram, and J.A. Hudgings, J. Phys. D Appl. Phys. **42** (2009)

Chapter 3
Raman Spectroscopy

Abstract Deals with lattice vibrations studied by *Raman spectroscopy*. First, a description of the fundamentals of this technique is provided. Special emphasis is paid to a detailed description of the main experimental issues, e.g. spectrometers, detectors, optics, and how to use them. A detailed analysis of the "information depth" and lateral resolution is given. A discussion of the alternatives to improve the resolution is presented, in particular, the confocality, and tip enhanced methods are introduced. Several case applications highlighting the capabilities of the technique are presented; in particular, the measurement of stresses in silicon based devices, the coupled phonon-plasmon modes that allow to study in a contact-less way the transport parameters at a submicron scale; the use of the micro-Raman spectroscopy as local temperature probe, or the influence of the low dimensionality in the Raman spectrum are presented.

3.1 Introduction

Raman spectroscopy is widely used as an optical characterization tool for investigating semiconductors in bulk, thin film, nanostructured, and device forms [1–10].

When light interacts with a solid, several phenomena take place, e.g. reflection, absorption, and light scattering. The light scattering can be either elastic (Rayleigh), or inelastic (Chap. 1). The Raman effect is an inelastic scattering phenomenon in which elementary excitation energy quanta of the solid are exchanged with the excitation electromagnetic wave. In Raman spectroscopy, those elementary excitations are optical phonons. Because lattice vibrations are very sensitive to the local structure and lattice environment, the Raman spectrum supplies information about the physical factors that disturb the local order or modify the interatomic distances. A great number of fundamental properties of semiconductors can be studied by Raman spectroscopy, i.e., crystal orientation, lattice temperature, symmetry breakdown, strain, chemical composition, among others; moreover, electronic and thermal properties can also be probed. This information is crucial to build up a diagnosis about the properties of the semiconductors as basic materials, as well as the changes

J. Jimenez and J.W. Tomm, *Spectroscopic Analysis of Optoelectronic Semiconductors*, Springer Series in Optical Sciences 202,
DOI 10.1007/978-3-319-42349-4_3

induced after the different processing steps undergone by the semiconductor during the device fabrication. In fact, all the physical factors mentioned above affect fundamental properties of the semiconductors, with the concomitant consequences on the device performance and reliability. Strain and temperature are important reliability issues in electronic devices. In fact, many problems concerning failed devices can be linked to the defects generated by stresses during the device processing [11], or the thermal stresses generated during the device operation [12, 13]. On the other hand, the increasing importance of "small" structures in microelectronics and optoelectronics, demands to probe small volumes of materials; in this way the strong advances in sensitive multichannel detectors (CCD detectors) have spurred the Raman capabilities as a microscopy technique [14–17]. By combining a high precision translation stage, sensitive multichannel detectors, large magnification optical microscope objectives and bright spectrometers high spatial resolution Raman imaging becomes possible. One understands by imaging the representation of Raman spectral parameters over a certain area of which each pixel has an associated spectrum; from those one can extract the Raman parameters using fitting routines; the images are defined by three coordinates (x, y, z), where x and y are the surface spatial coordinates, and z represents the corresponding Raman parameter which the distribution is imaged. The parameters of a Raman peak are the frequency (wavenumber), intensity, polarization, and linewidth. When more than one Raman band is present, the ratios between the different Raman bands can be also obtained. A significant development of the Raman imaging methods applied to different problems has been achieved in the very last years [18–29]. The chronological observation of the data reported in these articles permits to build up a synopsis of the evolution followed by the Raman imaging technique.

A crucial problem of probing small volumes is the low efficiency of the Raman scattering as compared to other optical signals, approximately one out of 10^{12} photons is inelastically scattered; note that the Raman scattering is a second order optical phenomenon, compared to first order optical phenomena like luminescence and absorption, which give much more intense signals. Figure 3.1 shows Raman and luminescence spectra at room temperature of a GaAs bare substrate, obtained with the same spectrometer and under the same excitation and detection conditions. The large difference between the two signals evidences the difficulties of the Raman imaging, and highlights the progresses carried out in the field of the micro-Raman (μ-R) spectroscopy in the last years. Raman imaging emerges as a valuable tool for device development and diagnosis, which is today used as a routine tool for the microelectronics industry, in particular, for the assessment of local stresses in microelectronics [30–32], but also, for the local lattice temperature assessment in devices under operation [33–35]. The variety of information provided by Raman spectroscopy combined with the slightly sub-micrometric spatial resolution of the optical microscope, the relative experimental simplicity, and its non invasive character, make of Raman spectroscopy an essential tool for the characterization of semiconductors and devices.

The phonon energies are normally very small, one uses wavenumber unities, typically the spectral window of the one phonon spectra of the most common

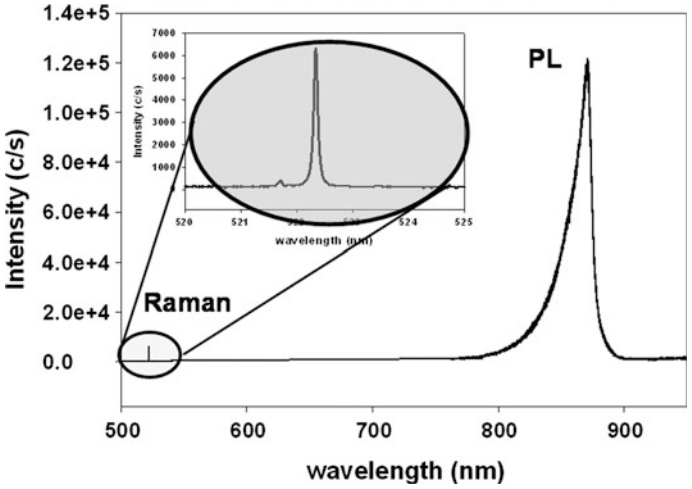

Fig. 3.1 Raman and photoluminescence spectra of a GaAs substrate obtained under the same excitation and detection conditions

semiconductors ranges from 200 to 1000 cm^{-1} wavenumbers (0.0248–0.124 eV), which means that the one phonon peaks in the Raman spectrum are very close to the Rayleigh radiation, which the intensity is orders of magnitude more intense than the Raman signal. Therefore, a Raman spectrometer does necessarily have a very efficient laser beam cut-off system. For this, one uses double or triple monochromators, and spatial and spectral filters. Actually, either notch, or edge filters are used, which allow to simplify the spectrometers, improving their luminosity, which is crucial for Raman imaging applications because of the necessity to acquire a large number of spectra in a reasonable lapse of time. By improving the instrumentation, especially notch filters, and the sensitivity of the multichannel detectors, the cost in terms of time of the Raman experiments has been dramatically reduced, with the corresponding extension in the number of applications of Raman spectroscopy as an effective tool for the characterization of semiconductors. The main target of this chapter is to provide the reader with a practical approach to the use of Raman spectroscopy, and then to illustrate a number of case applications, where the practical know-how is highlighted in order to supply criteria for the application of the experimental bases developed along the chapter. An exhaustive discussion of the fundamentals of Raman spectroscopy is out of our scope; there are numerous and excellent book texts and review articles supplying profound discussions about the Raman scattering fundamentals [1–6, 16, 17, 36–38]. We will only supply here the basic ideas necessary for further discussions, and introducing the readers not familiarized with the Raman spectroscopy with the fundamentals of this technique. We will emphasize the main problems concerning semiconductor characterization that can be afforded with Raman spectroscopy and how to approach them, based on our own practical experience.

3.2 The Light Scattering by Phonons

Light ongoing onto a solid undergoes several interaction processes with the solid, as described in previous chapters, among them light scattering, either elastic or inelastic. The Raman effect consists of the coupling of the electromagnetic field of the incident light with the optical phonons through the induced electric dipole moment. The incident photons, characterized by their energy, wavevector, and polarization, are inelastically scattered by the crystal. The inelastic component (Raman) of the outgoing light is characterized by its corresponding intensity, energy, wavevector, and polarization, which are determined by the structure and nature of the solid. The relation between the incident and the scattered light is governed by the corresponding Raman scattering selection rules, which are determined by the lattice symmetry and the nature of the crystal [38]. The energy exchange between the incident light and the solid can only take the values of the phonon energies. When the lattice absorbs the energy necessary to excite a phonon the Stokes (S) component of the spectrum is observed, whereas the release of a phonon to the electromagnetic wave results in the anti-Stokes (AS) component of the Raman spectrum. Usually, Raman experiments deal with the S component, because its intensity is several times that of the AS component. The AS-component takes a relevant role when dealing with temperature measurements. We will discuss about temperature later on, because contact-less temperature measurements are very important for the device reliability analysis; on the other hand, the thermal aspects are crucial in nanostructures, where the thermal conductivity, and heat dissipation are dramatically affected by the low dimensionality [39]; e.g. Si nanowires (NWs) immersed in low heat dissipation media present evident signs of overheating in the presence of a laser beam for the acquisition of the Raman spectrum [40–42].

3.2.1 Wavevector and Energy Selection Rules

The energy and momentum conservation rules for first-order Raman scattering (only one phonon process) are

$$\hbar\omega_i \pm \hbar\omega_{ph} = \hbar\omega_s \tag{3.1}$$

$$\mathbf{K}_i \pm \mathbf{q} = \mathbf{K}_s \tag{3.2}$$

where ω refers to the wavenumber, and $\mathbf{K}$ to the wavevector of incident (subscript i) and scattered (subscript s) photons, respectively, and ω_{ph} and $\mathbf{q}$ are the wavenumber and wavevector of the phonon involved in the scattering process. The sign + applies to the AS component and the sign − refers to the S scattering.

In the visible range, in which the Raman excitation is usually done, $\omega_i \gg \omega_{ph}$, which should mean that, $\mathbf{K}_i \cong \mathbf{K}_s \cong \mathbf{K}$ is of the order of 10^4–10^5 cm^{-1}. The

maximal value of q (q_{max}) of the Brillouin zone is about 10^8 cm^{-1}, which is about 10^3–10^4 times the wavevector of the visible light. For a typical backscattering Raman experiment excited with photons of λ wavelength in the visible range, for a material with an absorption coefficient for those photons of $\alpha \sim 10^4$–10^6 cm^{-1} and refractive index n, the maximum value of q is given by:

$$q_{max} = 4\pi n/\lambda \tag{3.3}$$

which results in values around 10^6 cm^{-1} for materials with high refractive index ($n \sim 4$). This should mean that only phonons of the zone center can be seen in the first-order Raman spectrum. Only phonons around the zone center, Γ, see the phonon dispersion in Fig. 1.5, are allowed by the momentum selection rule. We will see later on that the breakdown of the lattice symmetry relaxes the momentum selection rule allowing scattering with the participation of phonons of the full Brillouin zone; which will represent a crucial issue for the study of semiconductor nanostructures, which constitutes, nowadays, one of the most relevant application cases of the Raman spectroscopy [43, 44].

3.2.2 Symmetry Selection Rules

Raman scattering is a second-order optical process, which should contain a great deal of symmetry information as compared to first-order optical processes. The symmetry selection rules are easily explained in the frame of a semiclassical description of the Raman effect; for the quantum mechanics approach see [38]. The electric field, $\mathbf{E}(\omega_i)$, of the incident electromagnetic wave induces a dipole moment in the solid:

$$\mathbf{P}(\omega_s) = \varepsilon_o \chi \, \mathbf{E}(\omega_i) \tag{3.4}$$

where $\boldsymbol{\chi}$ is the generalized dielectric susceptibility tensor, which can be expanded as a function of the normal coordinates of the atoms in the lattice, u_{jo}. $\mathbf{P}$ adopts the following expression [3, 15]:

$$\mathbf{P} = \varepsilon_o \chi^{(o)} \mathbf{E_o} e^{i\omega_i t} + \varepsilon_o \chi^{(1)} u_{jo} \mathbf{E_o} e^{i(\omega_i + \omega_p)t} + \varepsilon_o \chi^{(2)} u_{jo}^2 \mathbf{E_o^2} e^{i(\omega_i + 2\omega_p)t} \tag{3.5}$$

The first-order Raman scattering effect is described by the second term of this expansion; it depends on the first derivative of the susceptivility, $\chi^{(1)}$, and involves only one phonon. The differential Raman scattering cross section for Stokes scattering by phonons can be written as:

$$\frac{d\sigma}{d\Omega} = V^2 \left(\frac{\omega_s}{c}\right)^4 \left| e_i \cdot \chi^{(1)}_{mn} \cdot e_s \right|^2 (n_p + 1) \quad (n_p \text{ for AS scattering}) \tag{3.6}$$

where $\mathbf{e_i}$, and $\mathbf{e_s}$ are the polarization vectors of the incident, and scattered beams, $\chi^{(1)}_{mn}$ is the mn component of the first derivative of susceptibility tensor, and n_p is the phonon occupancy Bose factor.

The non vanishing conditions for the factor $|e_i \cdot \chi^{(1)}_{mn} \cdot e_s|$ are determined by the crystal point group symmetry, and the polarization of the incident, and scattered light beams.

One should restrict to cubic, diamond (Si, Ge) and zinc blende (III-Vs), and hexagonal, wurtzite (nitrides, ZnO, SiC), symmetries, which the point groups are O_h, and T_d, and C_{6v} respectively, because the semiconductors with the highest technological relevance belong to these symmetries. Because of the high refractive index of these semiconductors the usual experimental geometry is backscattering. We will comment later on about the scattering geometry when exciting through a large numerical aperture (NA) microscope objective. According to the point symmetries of those semiconductors the polarization selection rules for backscattering configuration can be summarized as:

Cubic Symmetry

For cubic symmetry the zone center longitudinal (LO) and transverse (TO) optical modes are splitted, $\omega_{LO} \neq \omega_{TO,}$ for polar semiconductors (T_d symmetry), and degenerate ($\omega_{LO} = \omega_{TO)}$ for nonpolar semiconductors (O_h symmetry). The observation of the transverse and longitudinal modes depends on the scattering geometry, which is determined by the scattering crystal plane and the polarization of the incident and scattered light beams. In the laboratory system the scattering geometry is specified by the Porto's notation; this notation consists of a four letters code, (a (bc)d), where a is the incident ligth propagation direction, b is the incident light polarization direction ($\boldsymbol{e_i}$), c is the scattered light polarization direction ($\boldsymbol{e_s}$), and d is the scattered light outgoing direction [45]. The Raman scattering selection rules in (100) and (110) surfaces for cubic symmetry using the Porto notation, are shown in Tables 3.1 and 3.2. These surfaces are the most technologically relevant ones; for other scattering surfaces the reader can consult [3, 38].

The Raman selection rules for backscattering on surface (100) are given in Table 3.1.

On surface (110) the rules are given in Table 3.2.

Table 3.1 Raman scattering selection rules for cubic semiconductors, plane (100)

$\boldsymbol{e_i}$	$\boldsymbol{e_s}$	Porto	LO	TO
[110]	[110]	z (y′y′) $\bar{z}$	√	⊗
[110]	[110]	z (x′y′) $\bar{z}$	⊗	⊗
[010]	[010]	z (y y) $\bar{z}$	⊗	⊗
[010]	[100]	z (y x) $\bar{z}$	√	⊗

Table 3.2 Raman scattering selection rules for cubic semiconductors, plane (110)

e_i	e_s	Porto	LO	TO
[100]	[100]	z (x x) $\bar{z}$	⊗	⊗
[101]	[10$\bar{1}$]	z (x′z′) $\bar{z}$	⊗	⊗
[101]	[101]	z (x′x′) $\bar{z}$	⊗	√
[100]	[001]	z (xz) $\bar{z}$	⊗	√

Table 3.3 Raman scattering selection rules for wurtzite semiconductors, basal and prismatic planes

Porto	E_2	A_1(LO)	A_1(TO)	E_1(LO)	E_1(TO)
z (x x)$\bar{z}$	√	√	⊗	⊗	⊗
z (x y)$\bar{z}$	√	⊗	⊗	⊗	⊗
x (y y)$\bar{x}$	√	⊗	√	⊗	⊗
x (z y)$\bar{x}$	⊗	⊗	⊗	⊗	√
x (z y)$\bar{y}$	⊗	⊗	⊗	√	√

Hexagonal Symmetry

Wurtzite semiconductors are acquiring a high technological interest because of its large bandgap, among them GaN, ZnO and SiC are technologically very relevant. They belong to the C_{6v}^4 space group with two formula units in the primitive cell. According to the irreducible representation of this point group the vibration modes are: $\Gamma_{opt} = A_1 + E_1 + 2E_2 + 2B_1$ the zone center phonons have E, and A symmetry. The B_1 modes are silent, the A_1 and E_1 modes are polar, and have longitudinal and transverse branches, while the E_2 modes are non polar. The Raman configurations of allowed modes in backscattering on the basal and prismatic planes are [46, 47], Table 3.3.

Mixed Modes

In the case of wurtzite semiconductors the LO-TO splitting is larger than the A_1−E_1 splitting, which results in mixed modes under scattering off the crystal axis; when the phonon propagation is not parallel to the crystal axis the Raman modes present intermediate frequencies between those of A_1 and E_1 modes [46, 48–52]; the resulting modes are called quasi modes and their frequencies are:

$$\begin{aligned}\omega_{QTO}^2 &= \omega_{E1TO}^2 \cos^2\Phi + \omega_{A1TO}^2 \mathrm{sen}^2\Phi \\ \omega_{QLO}^2 &= \omega_{A1LO}^2 \cos^2\Phi + \omega_{E1LO}^2 \mathrm{sen}^2\Phi\end{aligned} \tag{3.7}$$

Φ is the angle formed by the (0001) crystal axis and the phonon propagation direction. The quasimodes are very important in nanostructures where the random orientation of the surface can give mixed modes, leading to confusion in the interpretation of the spectra. The frequencies of the mixed A1(LO) and E1(LO), and A1(TO) and E1(TO) modes in ZnO are shown in Fig. 3.2.

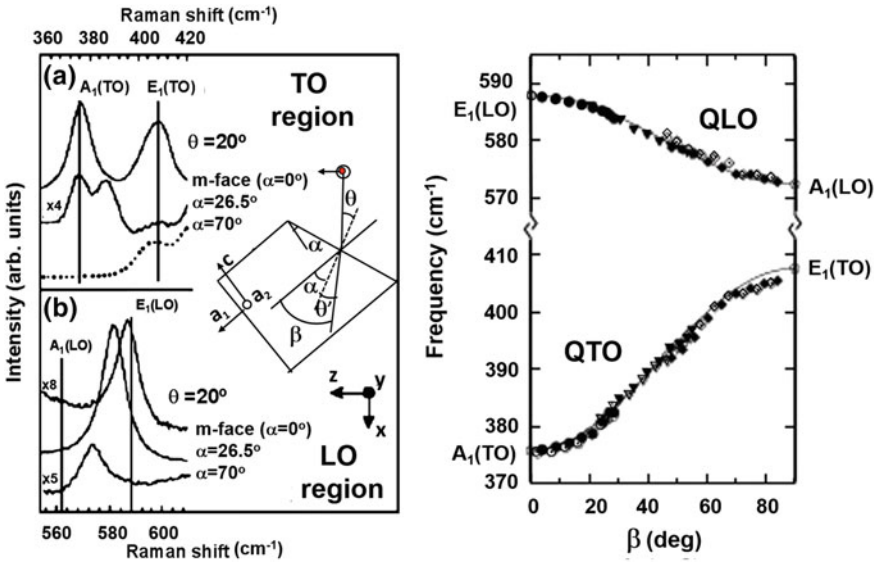

Fig. 3.2 Raman spectra on tilted surfaces in ZnO crystals, showing the presence of mixed modes (*left panel*). Peak wavenumber of the mixed modes as function of the tilt angle (*right panel*) [52]

3.3 What Semiconductor Properties Can Be Investigated with Raman Spectroscopy?

We briefly summarize here some of the properties that can be studied with Raman spectroscopy; and what Raman experimental aspects can be used to afford such problems. A list, by no means exhaustive, of the potential problems that can be, and have been studied, by Raman spectroscopy is given below, some application cases will be described once we had introduced the experimentation details.

1. ***Symmetry breakdown***. This problem deals with the symmetry failures leading to the relaxation of the Raman scattering selection rules, either polarization or momentum selection rules. The apparition of forbidden modes in the Raman spectrum allows one to study different problems, such as structural disorder [53], crystal inclusions and twining [54, 55], nanosized structures [43, 44, 56].
2. ***Chemical composition***. This study concerns the identification of the Raman bands, which are associated with different chemical bonds present in the semiconductor. Raman spectroscopy allows one to study technologically relevant problems as the composition of alloyed semiconductors [46, 57–67], atomic segregation [68–70], oxidation [71–73], and intermixing phenomena [74–79].
3. ***Doping***. There are two approaches to study doping by means of the Raman spectrum; one of them concerns the study of local vibration modes [80–86], that

allows one to detect the vibrations of elements with lower mass than the host atom. The other approach is based on the interaction between phonons and free carriers [87–96].

4. **Strain**. The bond lengths in strained materials are different from those of the unstrained ones; therefore, strain shifts the Raman peaks; the sign of that shift depends of the type of strain (compressive or tensile), $\Delta\omega$ being proportional to the strain [97]. One needs to establish the strain tensor to give accurate strain estimations, which in the case of μ-R experiments is limited by the scattering geometry. This is a successful application of μ-R spectroscopy applied to semiconductor devices, for which an exhaustive literature is available [30–32, 58, 98–103]. Strain can influence the electronic properties of the semiconductor structures; for example, the strain can reverse the order of heavy and hole subbands [104], or may produce changes in the band offsets [105] of the heterostructures.
5. **Temperature**. The Raman spectrum is sensitive to the lattice temperature. The intensity ratio between the S and AS bands, the wavenumber, and linewidth change with temperature, which allows one to use Raman spectroscopy as an absolute lattice temperature probe [1, 14, 106–110]. The potential use of the μ-R as a non invasive lattice temperature probe in devices under operation was already discerned by Todoraki in 1986 [33], who studied the temperature increase at the facet and inside the cavity of AlGaAs based lasers using the S/AS intensity ratio. Since that, significant progresses have been achieved, and the use of Raman spectroscopy as a local temperature probe, with slightly submicrometric spatial resolution, has been applied over the recent years to different devices under operation, constituting a valuable diagnosis tool, because of the relevant role played by temperature in the failure of devices [34, 111–117].

Thereafter, we will try to show how to identify the problems, and how to use the experimental means to carry out the analysis of the experimental data. Prior to this, we should make a description of the experimental setup for Raman spectroscopy.

3.4 Experimental Description

3.4.1 Raman Spectrometer

Actually, there is a large variety of Raman spectrometers. Most of the problems concerning the characterization of semiconductors present requirements that cannot be fulfilled by all the commercially available standard spectrometers. Therefore, more sophisticated spectrometers are required if one wants to do reliable characterization of semiconductors. In fact, the problem of identifying a chemical inclusion in a material composite does not demand the same apparatus as required for precise stress mapping in a trench isolation of an integrated circuit, or the temperature assessment close to a transistor gate under operation. Therefore, Raman

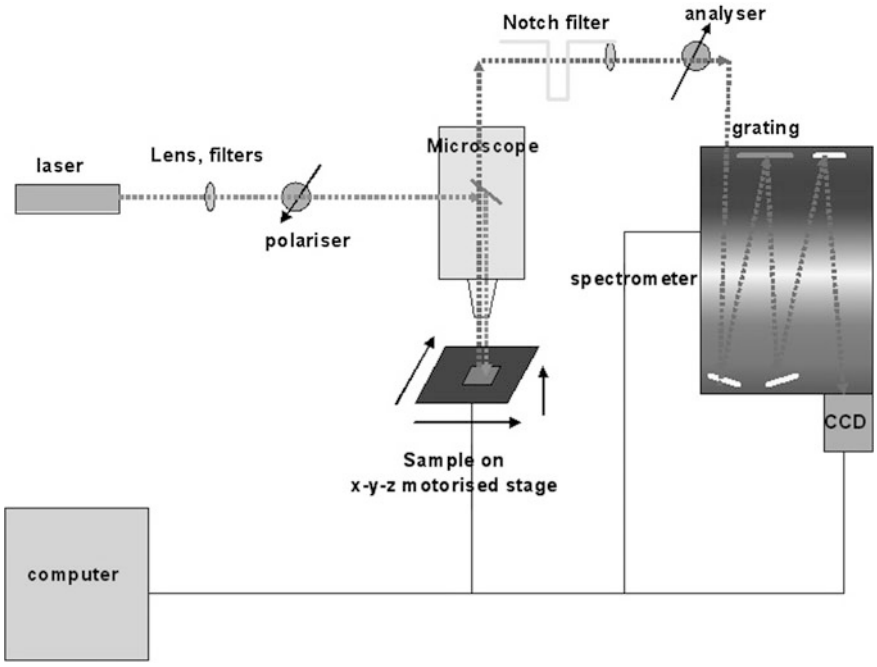

Fig. 3.3 Scheme of a μ-R apparatus

research in semiconductors demands high resolution spectrometers and highly sensitive multichannel detectors. We will focus herein on μ-R spectrometer apparatus, which are the ones more extensively used nowadays.

The main parts of a μ-R instrument are the laser light sources, the optical microscope, a stepping motor driven x-y-z stage, the collecting optics, a spectrometer, a multichannel detector, and a computer with the suitable software for data acquisition and hardware control. Figure 3.3 shows a simple scheme of a μ-Raman spectrometer apparatus, with its different parts.

Different optic components, e.g. filters, lenses, pin holes, polarisers, and mirrors, are inserted along the beam path. Among other, a wheel of neutral density filters to control the intensity of the incoming laser beam. The intensity control can also be achieved with two polarizers, which the polarization axes rotate one with respect to the other in order to graduate the excitation intensity in a continuous way from 0 to 100 % of the laser power; simultaneously the second polarizer controls the polarization of the incident beam. The control of the laser power is very important for temperature and/or stress measurements; in particular, it is critical when dealing with systems with poor thermal dissipation, e.g. NWs, for which very low laser powers have to be used if one wants to minimize the sample overheating. A pin hole for confocality, beam expanders, lenses, and narrow band-pass filters to remove the laser plasma lines are also intercalated. The intensity of the laser plasma

lines lies around the order of the Raman signals. They are very useful for wavenumber calibration; the simultaneous acquisition of the Raman signal and a plasma line permits to dispose of a wavenumber reference in order to correct the possible derives induced by the spectral instabilities occurring during the experiments. In some cases, the plasma lines can disturb the Raman spectrum; however, their intensity can be substantially reduced lengthening the beam path between the laser, and the sample, because they are non coherent radiation. Eventually, one can also use the lines of a Ne lamp, or similar, for wavenumber calibration, necessary for precise Raman spectroscopic measurements.

In a μ-R spectroscopy instrument the light is focused through an optical microscope, with objectives of different magnification, from 10× to 100×, and numerical apertures (NAs), resulting in spot sizes in the focal plane ranging from ≈10 μm down to <1 μm. Most Raman instruments have both the micro, and the macro option; nevertheless, the micro configuration is the most widely used one at present. When mapping a surface special attention must be paid to preserve the focus; for this purpose, the μ-R apparatus are equipped with autofocus systems, which allow mapping relatively large areas of the semiconductor without losing the focus.

The scattered light is collected through the objective lens itself, and is guided through the outgoing optics into the spectrometer. An analyser can be placed in the beam path of the scattered light in order to combine it with the exciting light polarization for the study of the Raman symmetry selection rules. The response of the spectrometer gratings depends on the polarization of the light arriving to them, therefore, a scrambler, which randomizes the light polarization, is often inserted just before the entrance slit of the monochromator. Besides, different lenses can be used to focus the beam onto the entrance slit of the spectrometer.

The classical Raman apparatus consists of a single or double pre-monochromator and a spectrometer. The pre-monochromator, with holographic gratings, can be used to reject the elastically scattered light (Rayleigh radiation). This light has a much higher intensity, several orders of magnitude, than the Raman signals, and rejecting it is required for the observation of the Raman bands, which are spectrally close to the Rayleigh radiation. The double monochromator can be disposed in subtractive mode, in which it acts as a very narrow bandpass filter rejecting the Rayleigh light, or additive mode, then the spectrometer behaves as a triple monochromator, with the corresponding improvement of the spectral resolution. The gratings are moved with a cosecant bar drive that gives a linear response in wavenumber units. Nowadays, the Raman instruments make use of narrow band holographic notch filters [118] to cut out the Rayleigh light. The notch filter rejects a narrow spectral band around the exciting laser wavelength, allowing the rest of wavelengths to pass; on the other hand, these filters to be effective the power density must be below a threshold value; nevertheless, this is not a major limitation, because the laser excitation power in modern μ-R systems is substantially lowered with respect to former apparatus. Usually, notch filters have coefficients of suppression of laser irradiation $>10^4$; while the typical damage thresholds are above 10 W/cm^2 power density. Actually, razor filters are also being used, because they

permit to remove the laser beam, and having longer life than the notch filters. However, because these filters are edge filters that cut below a certain wavelength, transmitting the wavelengths above it, they do not allow measuring the anti-Stokes part of the spectrum, contrarily to the notch filters. As a result, the instruments with notch filters are substantially simplified with respect to the former triple grating spectrometers. They have a larger throughput than the conventional Raman instruments, for this reason these spectrometers are those mainly used today for Raman mapping, where high signal to noise ratios are required to achieve Raman maps with a reasonable time cost. When one needs to approach the Rayleigh light one uses supernotch filters, with narrower spectral cut-off ranges than standard notch filters.

3.4.2 The Detectors

Actually, Raman instruments use two-dimensional charge coupled device (CCD) detectors, with high quantum efficiency and very low noise. These detectors are the main support of mapping applications, since they allow reducing the acquisition times by a substantial amount. Another important issue is the cooling system, normally liquid nitrogen refrigeration is better, because of the lower noise, but also, because of the absence of fan induced vibrations, which can have negative influence on the measurements under large magnification microscope objectives, or when using the system for tip enhanced Raman spectroscopy (TERS). As already mentioned the Raman spectroscopy is a low light level experiment; therefore, a key step towards the extension of the Raman spectroscopy applications lies in the substantial reduction of the acquisition time by improving the sensitivity of the detectors.

There are several types of CCD detectors; the main categories are the front illuminated, and the back illuminated CCDs. The front illuminated detectors have typical quantum efficiencies (QE) of only 50%; while in the back illuminated CCDs the QE scales up to nearly 90%. However, the back illuminated CCDs present etaloning in the red and near infrared (NIR) spectral ranges, Fig. 3.4.

Etaloning is a phenomenon causing interferences, which severely disturb the spectrum. New CCDs for low light level detection are based on the back

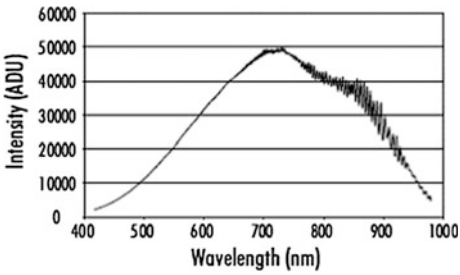

Fig. 3.4 Typical spectrum of a tungsten bulb lamp obtained with a back illuminated CCD detector. One observes etaloning for wavelengths longer than 700 nm, being very marked in the 800–900 nm spectral window

illuminated depth depletion technology, the so-called electron multiplying CCDs (EMCCD) allowing to reduce significantly the etaloning, while providing high QE from ultraviolet (UV) to near infrared. The spectral range of Si CCDs extends from 400 to 1050 nm, or from 200 to 1050 nm when provided with UV enhanced coating. These spectral ranges cover the usual energies used in Raman spectroscopy and permit to use the instrument also as a photoluminescence (PL) spectrometer for most of the semiconductors of interest.

The instabilities of the system, which can occur as a consequence of the variation of the room temperature, or accumulated heating at the spectrometer gratings, can result in spectral shifts, which need to be corrected; the plasma lines of the laser, or the light lines from external calibration lamps, e.g. Ne lamp, are excellent spectral references. On the other hand, if the temperature of the detector is not stable, it will also affect the measured peak frequency. Note that many practical problems deal with Raman relative shifts below 1 cm^{-1}, which makes the system extremely sensitive to the above mentioned instabilities; stable references are required, namely laser plasma lines or calibrated lamps.

3.4.3 Laser Sources

The use of different laser sources has very relevant consequences on the Raman spectrum, since the laser wavelength concerns the Raman intensity, the penetration depth, the lateral resolution, and the spectral resolution. The Raman intensity is proportional to $(1/\lambda^4)$. The penetration depth depends on the absorption coefficient, which changes with λ, the lateral resolution in a μ-R apparatus is diffraction limited, therefore, the beam diameter at the focus plane is proportional to the wavelength. Because of the dependence of the depth penetration and beam diameter with λ, the scattering volume decreases with decreasing excitation wavelength. The grating dispersion increases from the UV to the red, this means that the number of cm^{-1}/CCD-pixel is higher for UV excitation than for red excitation using gratings with the same groove density; therefore, if one wants to achieve comparable spectral resolutions in an instrument in different spectral windows, one has to increase the groove density of the gratings from the red to the UV. Visible laser sources are mostly used for the excitation of the Raman spectrum. Semiconductors with band gap below the excitation energy are not transparent to the laser beam, which results in very shallow penetration depth. Wide band gap semiconductors are transparent to visible photons; therefore, the laser beam crosses throughout the full thickness of the sample; in this case one uses confocal microscopy to select the depth of the sample under study. When probing very thin layers, one needs very heavily absorbed light excitation, then UV sources are very useful, since the probe depths for UV light are very shallow, this was the case for a single layer of SiGe nanocrystals (4–5 nm diameter) embedded in a SiO_2 matrix on a Si substrate, which the Raman spectrum could only be observed with UV excitation [119], Fig. 3.5 shows the spectra obtained with either visible or UV excitation; the spectrum

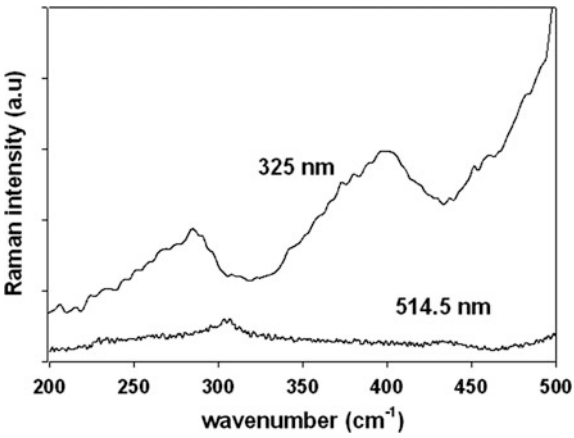

Fig. 3.5 Raman spectra of SiGe nanocrystals embedded in a silicon dioxide matrix. The spectra are recorded under different excitation photons. The spectrum obtained with UV excitation (325 nm) shows the typical Raman bands of SiGe, while the spectrum recorded with 514.5 nm excitation only shows the presence of the Si substrate (second order Raman spectrum) [119]

acquired with UV excitation shows the Ge-Ge and the Si-Ge bands of the SiGe nanocrystals, while the spectrum acquired with the 514.5 nm laser line only shows the spectrum of the underlying Si substrate.

Resonant Raman Excitation

Another way to increase the Raman sensitivity is the use of resonant excitation. Resonant conditions by polar phonon modes are obtained for excitation energies near the critical points of the band structure. According to third order perturbation theory the Raman tensor can be written as:

$$\chi_{mn}(\omega_i, \omega_s) \propto \sum_{ee'} \frac{\langle g|p_m|e'\rangle\langle e'|H|e\rangle\langle e|p_n|g\rangle}{(E_{e'} - \hbar\omega_s)(E_e - \hbar\omega_i)} \tag{3.8}$$

where, p_m, and p_n are the dipole components of the scattered, and incident light, H is the electron-phonon interaction Hamiltonian, ω_i and ω_s are the frequencies of the incident and scattered photons respectively. In a resonant event the electron is excited from the ground state, g, to an excited state e with energy E_e, which is transferred to another excited state, e′ with energy $E_{e'}$, with the emission of a phonon (Stokes). When the energy of the excitation light is close to an electronic transition the denominator of (3.8) becomes very small, with the consequent huge enhancement of the Raman efficiency, which can reach orders of magnitude over the non resonant excitation conditions. Resonant excitation is necessary to study very thin layers, as QWs; because the Raman signal is proportional to the scattering volume, the Raman signal arising from the QW is very weak under non resonant conditions because of the very small QW volume probed by the laser beam. However, under resonant excitation, the Raman signal of the QW can be scaled up to become observable. To set-up a resonant Raman scattering apparatus is necessary to use tunable excitation sources; generally, Ti-sapphire, and organic dye systems are used. Only polar phonon modes are resonantly enhanced. The Raman spectra of an $Al_{0.15}Ga_{0.85}N$/GaN/ $Al_{0.15}Ga_{0.85}N$ single QW, obtained under resonant and non

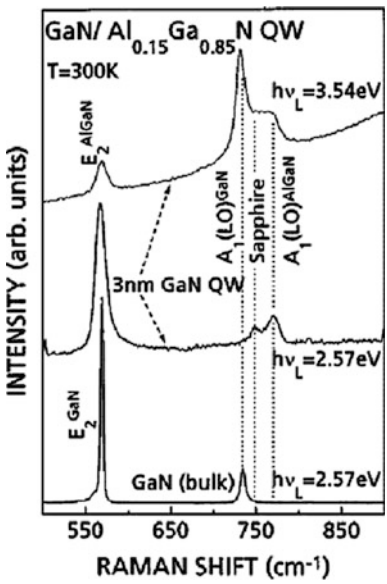

Fig. 3.6 Raman spectra of a 3 nm wide GaN/AlGaN QW and a bulk GaN reference sample under non resonant (2.57 eV) and resonant (3.54 eV) excitation. Note the enhancement of the polar A1 (LO) Raman mode of the GaN QW under 3.54 excitation. Compare the intensity of the A1(LO) band from the GaN QW with the intensity of the non polar E2 (AlGaN) band, showing a strong enhancement for 3.54 eV excitation, while for the non resonant excitation the non polar mode, E2, is the more intense [79]

resonant conditions are shown in Fig. 3.6, one observes the importance of the resonant conditions for enhancing the bands related to polar phonon modes [79].

3.4.4 Raman Imaging

First, one should make some settlements about the meaning of the term "imaging". It is equivalent to the meaning that will be given in Chap. 5. It has been largely associated with the excitation of a large area at once, and then the detection within a narrow spectral window, normally corresponding to a specific Raman peak; this was initially used for detecting inclusions in mineral samples, by selecting the adequate spectral window. However, with the high sensitivity CCD detectors and the spectroscopic capabilities of the Raman spectrometers, one can introduce the term spectral imaging, currently used in CL. In this case the full Raman spectrum is acquired for each selected point of a region of interest defined on the sample under study.

Raman imaging can be achieved using different technical solutions, which basically differ each other on the excitation method. The Raman spectral imaging aims to construct images representing the spatial distribution of the Raman parameters over a certain sample surface, in order to give a picture of the spatial distribution of certain physical or chemical properties that could be associated with different spectral parameters of the spectrum.

Actually, based on the sensitivity improvements introduced with the CCD multichannel detectors the usual way to do Raman imaging is by point by point

illumination with the exciting laser beam focused onto the sample surface by the microscope lenses. One defines a region of interest (ROI) to be mapped, and one defines the number of pixels to be measured; the step size shall also contribute to determine the spatial resolution together with the beam size. The laser beam excites a sample point and the Raman spectrum is acquired, then a neighbour point is excited, and the spectrum is acquired, and so on. At the end of the acquisition one has a set of Raman spectra each one associated with a pair of spatial coordinates. The spectra are fitted and parameters such as the peak intensity, peak wavenumber and linewidth are determined. These parameters can now be displayed in two dimensional plots, which permit to image the spatial distribution of certain properties, e.g. stress. The scan of the laser beam over the sample can be done in two different ways: the sample is moved from one pixel to other by a high precision motorized X-Y stage, or the laser beam is scanned over the sample by means of a vibrating mirror. The first method is the one used nowadays, because of the difficult setting-up of the vibrating mirror, and also because of the limited surfaces that can be scanned with the mirror, because of the off optical axis excitation for large scanning distances. An alternative concept uses a bundle of optical fibers each one carrying the spectrum of a small area of the sample [120].

The point by point method provides a good spatial resolution and uniform illumination over the scanned area as far as the laser beam is focused onto the sample surface, which can be done using autofocus devices. Autofocus is usually based on monitoring the intensity of the back-reflected laser light measured by a photodiode, which feedbacks a piezo-electric driver mounted on the microscope objective. This procedure is not suitable in composite samples where the reflectivity presents variations due to the differences in the local composition of the sample. An alternative way to keep the focus might be the definition of the plane of the ROI and then correct the focus according to the tilt of that plane; obviously this procedure can only be used with flat surfaces, while for surfaces with local topographic variations the reflected light method should be more precise. Furthermore, this method is compatible with confocal microscopes; which is not the case for global illumination methods. Due to the low light level of the Raman signal the acquisition of the Raman images is usually time consuming; therefore, it is not always a reasonable approach. In such cases, one has the choice of selecting small ROIs or making line scans, which reduce substantially the acquisition time. Nevertheless, in spite of the weak Raman signal, numerous examples of Raman imaging applied to different problems can be found today in the literature [25, 121]; Fig. 3.7 shows the Raman images of the peak wavenumbers of the three bands (Si-Si, SiGe and Ge-Ge) in a SiGe NW, which permits to asses the composition along the NW [122]. The continuous improvements achieved in the detectors sensitivity encourages the future of Raman imaging.

The temperature increase induced by defects in an AlGaN/GaN field effect transistor under operation, is mapped in Fig. 3.8 [123]; while the stress distribution in a Si chip bonded to a copper substrate [124], is shown in Fig. 3.9.

The approach based on the global illumination of a certain surface of the sample, requires of optical tunable filters, for achieving spectrum imaging. In fact, in this

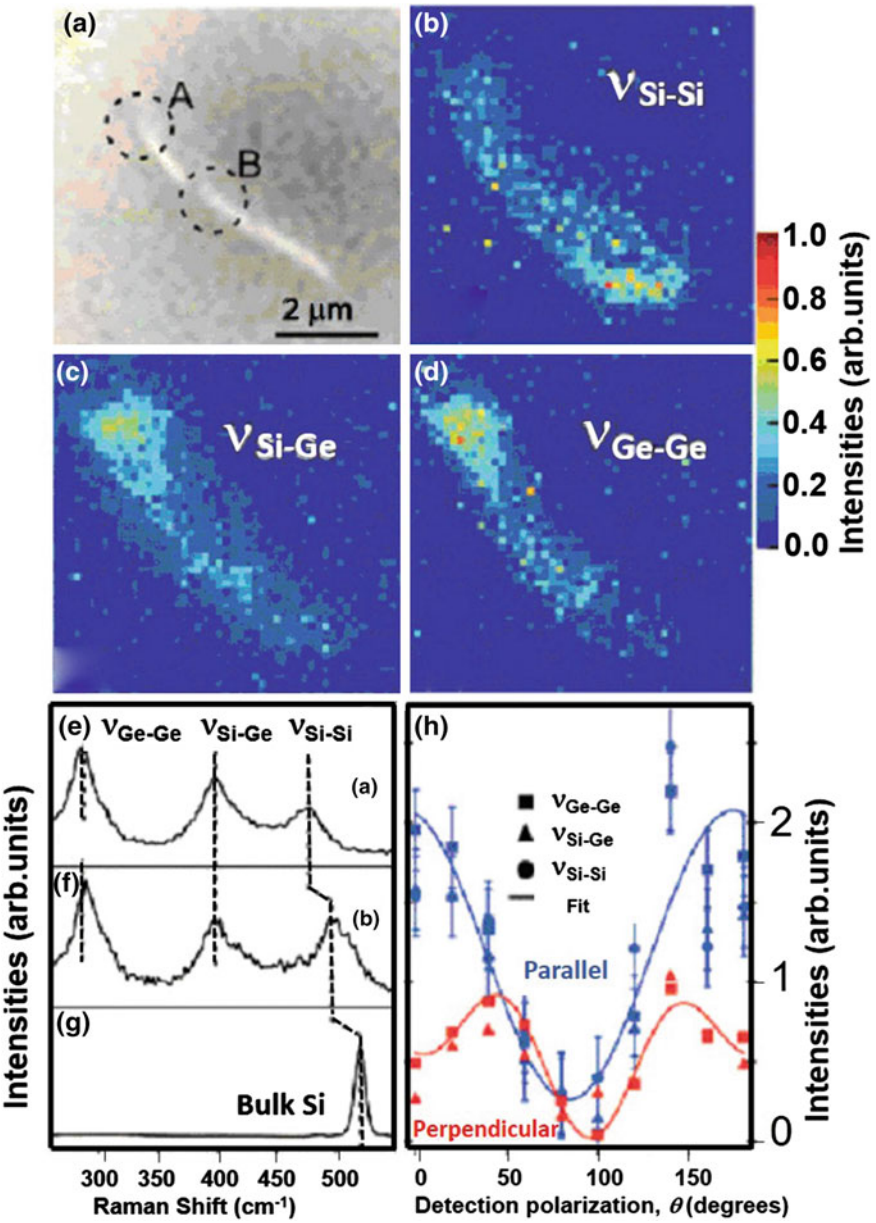

Fig. 3.7 Confocal Raman imaging of a SiGe NW. **a** optical micrograph image. **b** vsi-si, mode, **c** vSi-Ge mode, **d** vge-Ge mode. **e** Raman spectrum in point *A* of (**a**), **f** Raman spectrum in point *B* of (**a**), **g** raman spectrum of reference bulk Si. **h** Intensity of the three Raman modes as a function of the detection polarization angle, for both parallel and perpendicular excitation [122]

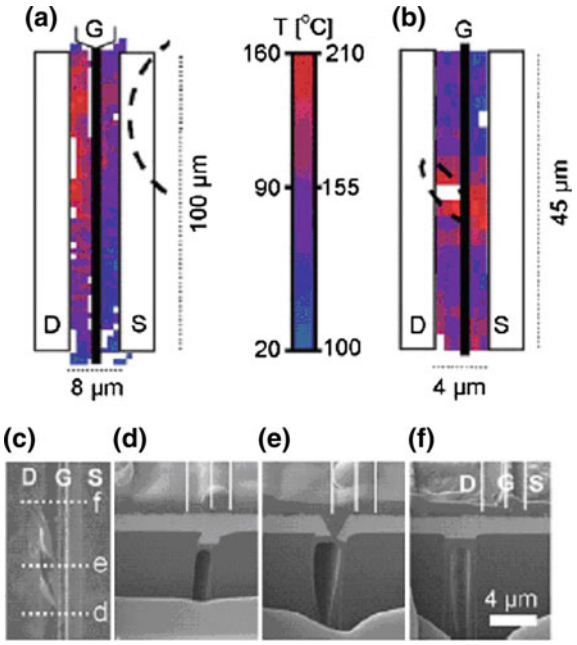

Fig. 3.8 Thermal maps of the source drain gap in an AlGaN/GaN transistor. **a** Temperature map in a single finger transistor operated at 18 W/mm, **b** temperature recorded in a part of a multifinger device operated at 9 W/mm. The defect regions are indicated by dashed lines, **c** top view of the focus ion beam (FIB) image of the defect zone in the multifinger device, **d–f** are different regions indicated by the dashed lines in **c** [123]

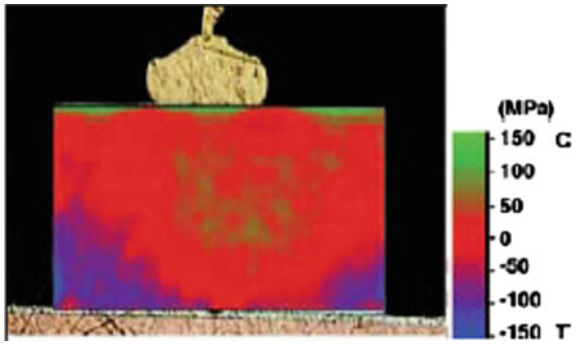

Fig. 3.9 Stress distribution in a Si chip bonded to a copper substrate [124]

case one acquires with a CCD detector successive large area monochromatic images varying the optical bandpass. The local spectra for each camera pixel are reconstructed from the successive images acquired in different spectral windows by varying the bandpass window. This method has been used for photoluminescence (PL) mapping [125]; however, although these filters can provide a reasonable spectral resolution for luminescence, their spectral resolution does not match the spectral resolution demanded by the very narrow Raman bands compared to the broad PL bands. The state of the art of these filters makes them suitable for mapping the Raman intensity of different bands and establishing their relative intensities, but not for achieving fine lineshape analyses. On the other hand, all the methods using

global illumination are not compatible with confocal microscopy, which is only allowed for the point by point measurement.

3.4.5 The Lateral Resolution

Raman spectroscopy is increasingly becoming an optical microscopy technique. In a conventional μ-R spectrometer the laser beam is focused onto the sample by the microscope optics. The theoretically predicted spot size at the focal plane, defined as the diameter outside which the intensity of the diffraction limited spot has dropped to $1/e^2$ of its value in the center of the spot, is given by the Abbe formula:

$$d = \frac{1.22\,\lambda}{NA} \tag{3.9}$$

where NA is the numerical aperture of the objective, and λ is the wavelength of the exciting laser beam. In this equation, it is assumed that the laser beam completely fills the objective. Equation 3.9 shows that the spot diameter can be reduced by either decreasing the laser wavelength, or increasing the numerical aperture of the objective. Beam diameters as small as 0.6 μm can be obtained with a 100× objective, NA = 0.95 with the 488 nm line an Ar laser as the exciting source. Using UV excitation will further reduce the diameter; however, the NA of the commercial UV objectives is smaller, which partially compensates the effect of the shorter wavelength. In practice, the beam diameter is always larger than the one calculated with (3.9). A simple way to determine the lateral resolution of the Raman microprobe is to monitor the change in the intensity of the Raman signal by scanning the laser beam across the edge between two regions (the so-called knife-edge method), one of them Raman active, and the other Raman inactive, e.g. a Si substrate with a thin metal stripe deposited by evaporation. In this experiment carried out by De Wolf [14], the sample was moved by small steps, using a high resolution X-Y stage; the steps must be smaller than the diameter of the focused laser beam, in order to overlap the laser spots of adjacent measurement points; this is important if one wants to achieve Raman images of structures smaller than the laser beam diameter. The scan was performed across the edge of the metal stripe, in 0.1 μm steps, crossing from the Si surface (the beam only excites the Si substrate) to the metal stripe (the beam only impacts the metal stripe). The Raman signal was measured at each step and the intensity was determined. When the laser beam crosses the edge of the metal stripe it shares both the metal stripe and the Si substrate, then the Raman signal of Si starts to be observed with an intensity that depends on the beam fraction coming into contact with the Si side; remember that the Raman signal is proportional to the scattering volume, the maximum intensity is reached once the laser beam is only probing the Si side. The 514.5 nm line of the Argon laser was used in these experiments.

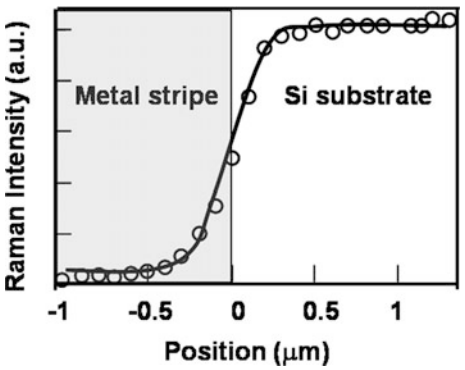

Fig. 3.10 Raman intensity across metal knife edge, the *solid line* is the fitting using a Gauss laser intensity profile [14]

Figure 3.10 shows the change in the intensity of the Si Raman peak with the position across the stripe edge. The beam diameter, Φ, was determined by fitting the Raman intensity profile across the border between the metal stripe and the Si substrate with a Gauss function, according to the laser beam intensity profile. The spatial resolution was estimated at 0.88 μm, instead of the nominal 0.66 μm calculated with Abbe formula, (3.9). Several reasons can account for such a discrepancy; e.g. the non optimal beam focusing. It is interesting to note the differences concerning the lateral resolution of μ-R and micro-photoluminescence (μ-PL) techniques. The laser beam is similar for both techniques, this means that the excitation volume is the same in both techniques; however, the volume from which the signal is generated is different for both phenomena. Raman is a light scattering technique; therefore, the signal is generated inside the excitation volume. PL is based on the generation of e-h pairs, which can out-diffuse and recombine out of the volume where they were generated, which means that the lateral resolution of the μ-PL technique is determined by both the generation volume and the diffusion length of the minority carriers, or excitons, depending on the luminescence mechanism studied.

We have shown that the lateral resolution is determined by the excitation wavelength, λ, and the microscope objective, therefore, we are limited to slightly submicrometric resolutions in the best favourable case. Better resolution can be achieved by Scanning microscopy: Raman-Near-field scanning optical microscopy (RNSOM) [126–130], tip enhanced Raman spectroscopy (TERS) [131, 132]. Also, one can detect small objects, with dimensions below the μ-R resolution, by using high precision motorized X-Y stages, where the spectra are acquired with scanning steps separated each other by distances much shorter tan the laser beam diameter, and if possible shorter than the size of the small object, e.g., a nanowire (NW). This procedure requires that the Raman signal would be high enough in order to detect the Raman spectrum of a so small volume. For example, in Fig. 3.11 the Raman image of an isolated Si NW, obtained with steps of 0.1 μm, is shown. The map of the temperature induced by the laser beam heating is also shown. For each step the share between the small object and the focused laser beam varies depending on the

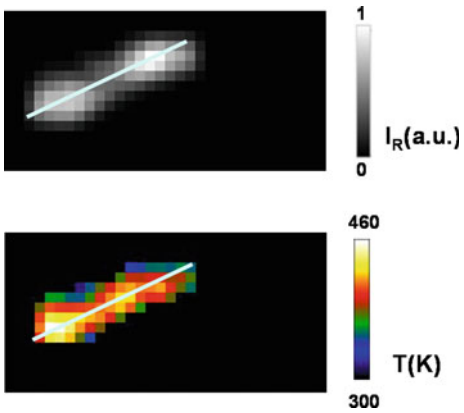

Fig. 3.11 Raman intensity map of a Si NW (*upper panel*), Temperature map, the temperature is induced by the laser beam, the NW was free standing therefore it has a very low heat dissipation, which results in a temperature increase that depends on the position of the NW inside the laser beam

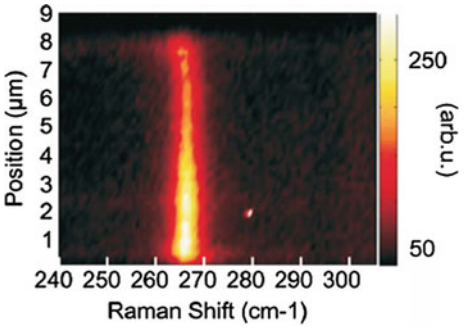

Fig. 3.12 Waterfall plot of the Raman spectra obtained along a zincblende GaAs NW with light polarization parallel to the NW axis. The TO phonon mode is observed [134]

position of the laser beam. This procedure allowed imaging individual NWs by means of their Raman spectrum acquired along the NW [133]; a similar procedure was followed in [122], Fig. 3.7, and by Zardo et al. [134] in GaAs NWs, Fig. 3.12.

The fact that the laser beam size is larger than the object has non negligible consequences on the excitation conditions; in fact, the effective excitation power depends on the position of the object inside the laser beam spot [135, 136]; therefore, when one studies two or more NWs simultaneously crude misinterpretations can occur because of the very different excitation conditions of the two NWs, Fig. 3.13.

Beyond the Diffraction Limit. NanoRaman

Because of the importance of reduced dimension structures, below the wavelength dimension, one needs to improve the lateral resolution of the Raman apparatus. An option is the use of a near field scanning microscope (NSOM) combined with a μ-R apparatus. In this arrangement the excitation is done through a tapered optical fiber in the close proximity of the sample surface, around 10 nm to fulfill the near field condition. This permits to overcome the Abbe's theoretical limit for optical microscopy resolution, which under near field conditions is determined by the fiber aperture. The Raman signal will be collected in far field by the optical microscope

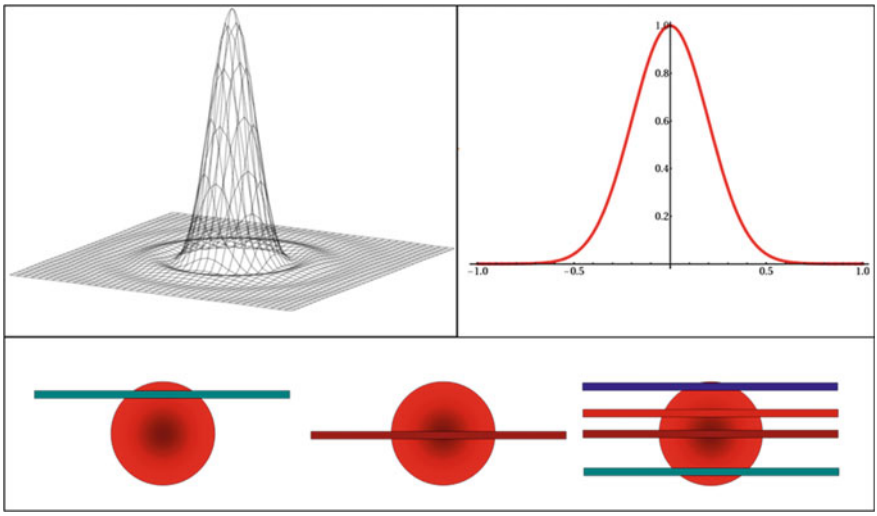

Fig. 3.13 Scheme of the influence of the NW position inside the laser beam. *Upper panels* represent the Gaussian laser intensity distribution, and the *lower panels* illustrate the different excitation conditions for the NWs depending in their position with respect to the beam axis

attached to the spectrometer. However, this is not so simple, because the acquisition of the Raman spectrum in this experimental configuration is rather difficult. As we have mentioned the Raman signal is intrinsically weak, about one photon out of 10^{12} is scattered. If one adds the very low laser power output of the fiber, especially for small aperture fibers, and the very small volume excited, one ends in a difficult acquisition signal situation, with a rather poor signal to noise ratio detection, demanding long detection times. Webster et al. [127] developed a scanning near field optical Raman microscope (SNORM), with which they acquired Raman images of scratched Si in total image acquisition time of circa 9 h. One has to improve the Raman signal in order to reduce the average acquisition time aiming to achieve images in a shorter time. Yoshikawa et al. [137] developed a high resolution SNORM apparatus using ultraviolet (UV) resonant Raman excitation. They characterized Si nanostructures reducing the acquisition time by one order of magnitude with respect to the pioneer work by Webster et al. [127]. SNORM experiments are limited by the very low signal, furthermore, the aperture of the optic fibers does not provide a dramatic increase of the spatial resolution, typically 200 nm, if one looks for a noticeable signal to noise ratio.

It is possible to increase the lateral resolution by resonantly enhancing the Raman signal. Using instead of the optical fiber a metallic tip to enhance the electric field of the excitation light beam one can enhance the Raman signal by a factor $(E/Eo)^4$, where E is the resonantly enhanced electric field, and Eo is the excitation electric field in far field configuration. The electric field is enhanced at the tip end, so if the sample is very close to the tip the Raman signal is resonantly enhanced in

the region in close proximity with the tip. An enhancement factor of 12,000 was achieved in Si [138]. Scanning the tip will permit to take a Raman image with a spatial resolution given by the tip size, typically one can get lateral resolutions around 30 nm. This technique is called tip enhanced Raman spectroscopy (TERS), it is carried out with an atomic force microscope (AFM), provided of a metallic tip, attached to a μ-R spectrometer [139].

3.4.6 Probe Depth

The probe depth is also a big concern of the Raman spectroscopy. It is very important for many experiments, especially if one considers that many semiconductor devices are based on multilayer structures, which can demand in depth analysis.

The Raman signal arises from the excitation volume, defined by the diameter of the focused laser beam, as discussed before, and the in-depth penetration of the excitation light, which depends on the absorption coefficient. Therefore, the Raman probe depth depends on the degree of transparency of the sample to the excitation light. De Wolf [14, 30] gave a definition of the probe depth as the depth at which the scattered light intensity drops to 10% of its value at the surface, note that the Raman light is very close in energy to the excitation light, therefore one has to consider the way inside the sample of the Raman scattered photons, which are absorbed with the concomitant weakening of the outgoing Raman signal. The probe depth estimated was:

$$d_p = \frac{-\ln 0.1}{2\alpha} = \frac{2.3}{2\alpha} \tag{3.10}$$

Instead of the usually assumed probe depth of:

$$d_p = \frac{1}{2\alpha} \tag{3.11}$$

The Raman probe depths, calculated according to the criterion of (3.10) for several semiconductors and laser wavelengths are given in Table 3.4, using the absorption coefficients listed in [140].

Note the remarkable differences between the penetrations of the different wavelengths; in this context, the use of UV lasers allows the study of very thin layers as already mentioned. This is also important in samples where one needs to neglect the influence of the substrate; e.g., in Ge nanocrystals embedded in an SiO_2 layer on a Si substrate, the second order spectrum of the Si substrate has been often misinterpreted as the spectrum associated with the Ge nanocrystals as it was evidenced in [141, 142], see in Fig. 3.14 the second order spectrum arising from a bare Si substrate together with the spectrum arising from Ge nanocrystals. Using UV

Table 3.4 Penetration depth for different laser sources, calculated with (3.10), and absorption coefficient data from [140]

	He–Ne 632 nm	YAG 532 nm	Ar + 514.5 nm	Ar + 488 nm	He–Cd 325 nm
Si (nm)	2910	934	762	569	94
Ge (nm)	70	20.5	19.2	19	10
GaAs (nm)	294	145	126	94	15.6
InP (nm)	188	113	102	83	16.8

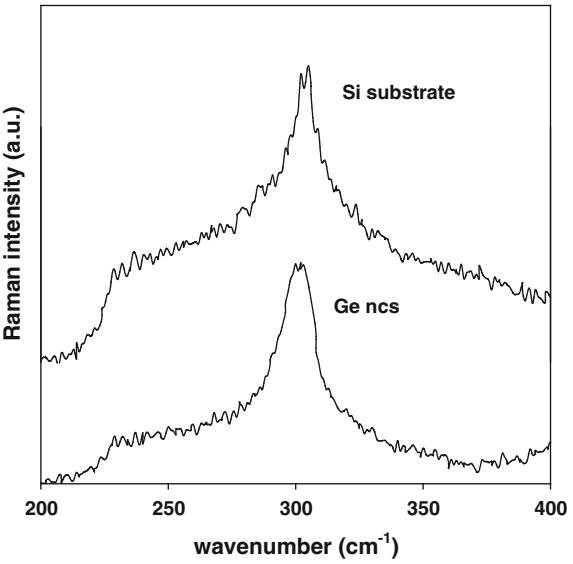

Fig. 3.14 Raman spectrum of a bare Si substrate, and Raman spectrum arising from Ge nanocrystals embedded in SiO_2, on a Si substrate. Some articles in the literature have misinterpreted these spectra, assigning the second order spectrum of the Si substrate to Ge nanocrystals [142]

excitation allows reducing the contribution of the substrate because of the lower penetration. In fact, in the cases with very small amount of matter, as the case of very narrow layers, thin isolated NWs, or low density of nanocrystals, one can estimate a threshold volume for the Raman spectrum observation, below which the Raman spectrometer is unable to detect its presence [70, 119, 142]. Obviously this depends on the characteristics of the Raman setup, including the detection, and the excitation conditions, under resonance conditions the detection requirements are different.

The excitation light with energy above the band gap is strongly absorbed, most of the III-Vs and group IV semiconductors are opaque to visible excitation; therefore, the penetration depth is less than a few hundred nms. If one wants to make in depth analyses, one can consider diverse experimental approaches:

1. Using different laser wavelengths, one needs for this several lasers, which need to be aligned consecutively, or tunable lasers.

2. Cleaving the sample and rastering the laser beam on the cleaved side
3. Using low angle bevelled surfaces
4. Using a confocal microscope when the sample is transparent to the laser radiation

The use of a tunable laser, e.g. Ti-sapphire, or an organic dye, can be useful for in depth distribution analysis; however, because one needs to reject the laser light at the entrance of the spectrometer, the use of the tunable laser is only practical with a triple monochromator, with which one can reject any laser wavelength. In spectrometers equipped with rejecting filters one should be limited to a reduced number of excitation lines; however, exchanging the filters and the laser lines is a tedious operation, which requires optical adjustments for each of them, and the subsequent realignments.

The acquisition of the Raman spectra on a tranverse cleaved surfaces is not a good solution for improving the depth resolution, because the depth resolution in this arrangement is the same as the lateral resolution, which means that one cannot resolve structures with very thin layers. Note that in a typical multilayer structure with quantum wells (QWs), e.g. a laser diode, the thickness of the active parts, QWs, is only a few nms, therefore, it is orders of magnitude smaller than the beam diameter, making the measurement non sense, unless that resonant excitation conditions are used. This approach can be affordable for TERS profiling, for which the small tip enhanced area diameter permits to improve the resolution.

Bevelled Surfaces

More useful for the in depth analysis is the use of low angle bevelled surfaces [96, 121, 143, 144] Fig. 3.15a; in samples lapped with a bevel angle of a few degrees and under heavily absorbed laser light one can achieve in-depth analysis of multilayer structures. The main problem concerns the bevel itself; if it is done by lapping, the surface can be damaged with the corresponding consequences for the Raman spectrum which is very sensitive to symmetry breakdown, e.g., activation of forbidden modes, induced stresses, and laser induced overheating which deforms the Raman bands [145]. A solution could be the preparation of bevels using wet etching, which demands a very good control of the etching process, or the use of dry etching techniques to shape a clean low angle bevel. A detailed description of the low angle bevel preparation in polycrystalline Si solar cells is reported in [96], where in depth p-doping in crystallized Si thin film solar cells was established studying the lineshape of the Raman spectrum, across the bevel Fig. 3.15b.

Using the low angle bevels, one can artificially increase the depth length scales taking account of the stretching factor S(α) [96], Fig. 3.15a.

$$d^* = d/\text{sen}\alpha = S(\alpha)d \tag{3.12}$$

where d* is the distance along the bevel, and d is the thickness. Also one can proceed by oblique scanning which will further increase the depth resolution.

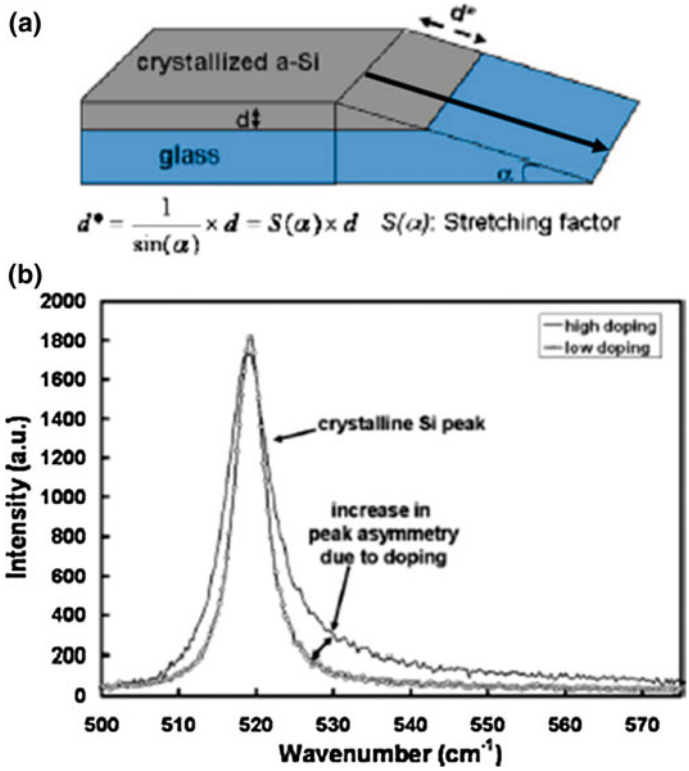

Fig. 3.15 **a** Scheme of a low angle bevelled surface for in depth Raman analysis, the *arrow* indicates the sense of scanning. **b** Raman spectra in the crystallized Si layer revealing different levels of doping [96]

Using this procedure grain boundaries in multicrystalline Si solar cells were studied with enhanced spatial resolution [121].

Confocal Microscopy

When using non opaque conditions, confocal Raman systems can be used to perform depth profiling. The non opaque conditions using conventional Raman arrangements mostly refer to wide band-gap semiconductors (GaN, ZnO, SiC), which are transparent to the standard visible laser sources used in the commercial Raman spectrometers. The principle of confocality is described in Fig. 3.16 [146].

The laser is focused through a pinhole, and the objective lens onto the sample. The scattered light is focused onto the confocal pinhole, which has adjustable aperture. As far as the diameter of the confocal pinhole is reduced, more of the light originating from regions above and below the focal plane will be rejected. The confocal pin hole is basically a spatial filter; only the Raman signal arising from the focal plane is allowed to enter into the spectrometer when the pin hole is closed to a small diameter. However, the resolution is limited by the compromise between the

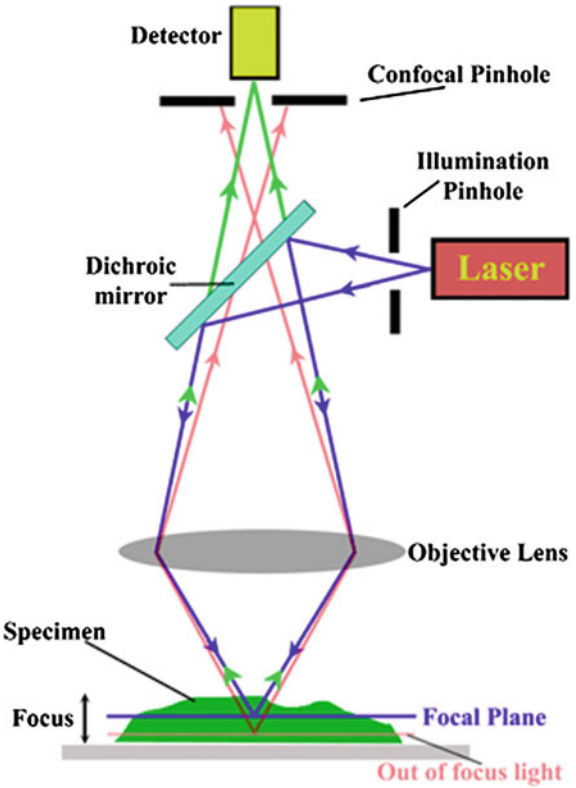

Fig. 3.16 Scheme of the confocal microscopy principle [146]

pinhole diameter and the Raman signal. By focusing the laser beam at different plane depths, a depth profile can be obtained [147]. Depth resolutions about 0.2 μm have been reported [148, 149]. Figure 3.17 shows the depth appearance of different phonon bands in diamond as obtained by confocal microscopy [149].

3.4.7 The Microscope Objectives

We have already addressed some comments about the microscope objectives, which are essential parts of the μ-R system. The objectives are characterized by different figures, in particular, the magnification, the NA, the working distance and the spectral range of transparency.

The numerical aperture is defined as NA = n senθ, where n is the refractive index of the immersion media, and θ is the angle of the cone formed by the optical axis and the external rays emerging from the objective, Fig. 3.18.

Because the refractive index of air is close to one, the NA is very close to senθ. Objectives with large NA are very luminous because of the large angle of

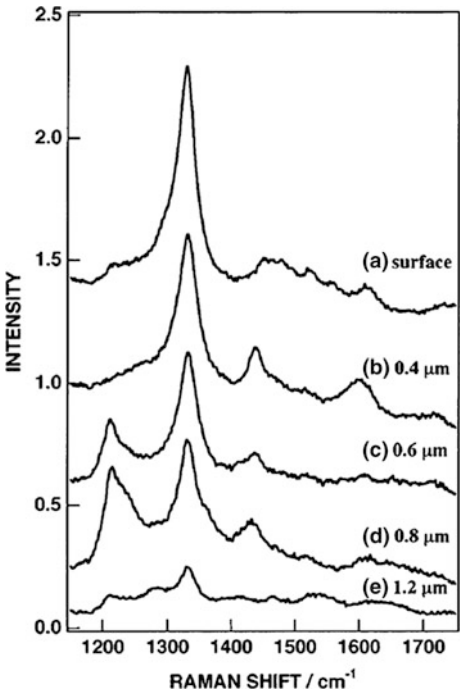

Fig. 3.17 Raman spectra of diamond obtained at different depths using confocal microscopy [149]

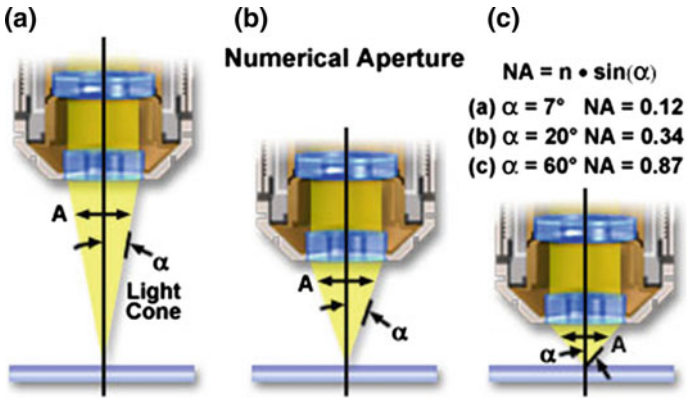

Fig. 3.18 Optical microscope objectives with different NAs (http://www.microscopyu.com/articles/formulas/formulasna.html)

collection; but with respect to the excitation, one cannot ascertain that the associated electric field of the excitation light is in the sample plane, which means that the Raman microprobe is not a priori in a true backscattering configuration. Bonera et al. [24] made use of the large numerical aperture to allow observations other than the backscattering to study the strain field induced by scratches in a Si wafer, reducing the number of assumptions necessary to set up a strain model compatible with the measurements; we will discuss later on about this. However, the large refractive index of common semiconductors, reduces the effective incidence angle. According to Snell's law, for an objective with NA = 0.95, the maximum angle of dispersion inside the scattering medium (refractive index $\approx$ 4) is 14°. Only for very large NA, one has a significant tilt with respect to the sample normal axis, which could have incidence on the backscattering geometry. This has been recently reported by Tada et al. [32], who observed forbidden TO modes in (100) Si, only using very large NA (1.3) oil immersion objectives. Inside the scattering medium the light transmission angle scales from 14° to 20° for NA increasing from 0.95 to 1.3.

The experiments of Bonera et al. [24] were done in Si for which the zone center optical phonons are degenerated. Therefore, it is difficult to discriminate between the LO and TO modes. However, in polar semiconductors, one can test the Raman selection rules under microscope excitation. The Raman spectra of GaAs was measured on both the bare (001) substrate face, and the freshly cleaved (110) face with different objectives. The spectra are shown in Fig. 3.19 revealing a minor presence of forbidden modes; one observes that in good quality surfaces [freshly cleaved (110)] only the TO mode is observed, even with the 0.95 NA objective. Therefore, the selection rule leakage observed in some spectra recorded with a 0.95 NA objective is likely due to the very surface of the sample and/ or tilting with respect to the crystal axis.

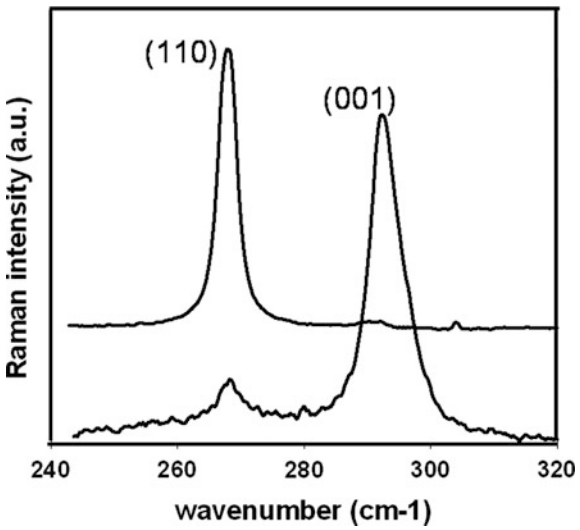

Fig. 3.19 Raman spectra recorded with a $\times$100, 0.95 NA objective on GaAs (110) freshly cleaved surface and on bare (001) GaAs wafer surface. Evidence the low contribution of the large NA objective to the symmetry selection rule leakage

The working distance of the objective is the distance between the objective lens and the sample. Conventional large magnification objectives have very short working distances, which makes them not suitable for certain experimental scenarios. When one uses cryostats, or furnaces, one needs a minimum distance between the objective lens and the sample, therefore, one uses ultralong work distance (ULWD) objectives, which have smaller NAs than their conventional counterparts, therefore they give larger beam diameters, but permit to place the sample at a distance of several mm away from the objective.

3.5 Case Applications

3.5.1 Stress in Si Microelectronic Devices

As mentioned above, Raman spectroscopy is a sensitive tool to measure stress in semiconductors. The effect of stress on the Raman spectrum of the main semiconductors and heterostructures is well documented in the literature [101, 103]. In the case of microelectronic devices a simplistic analysis of the stress can be done from the peak shift, which is positive under compressive stress, and negative under tensile stress. However, the correlation between the Raman shift and the stress requires of a careful analysis of the stress tensor; especially in structures as those constituted in microelectronic integrated circuits. Integrated circuits are complex mosaics where dissimilar materials are deposited at different temperatures, and assembled together forming different geometries. Inherent to this technology is the generation of stresses in both the films and the substrates. The origin of the stresses can be thermal, associated with the different thermal expansion of the different materials involved, or the temperature gradients. It can also be intrinsic because of the different lattice parameters of the materials forming the complex structures, or can be associated with the geometry of the structure: for example, stresses induced in the substrate at film edges, as is the case of oxide isolation trenches. The existence of these stresses constitutes a serious problem for device operation, since they can trigger the formation of defects, such as dislocations [150], or voids, leading to the generation of cracks that will reduce the device lifetime [98, 151].

In a simple analysis of the Raman data a downshift in the optical phonon frequency of Si of 1 cm^{-1} can be translated into −180 MPa, for hydrostatic stress, −430 MPa for in-plane uniaxial stress, and −900 MPa for in-plane biaxial stress [99]. These figures give an idea of the ambiguity of the stress measurements when a realistic description of the stress tensor is lacking. Note that, all the non-zero components of the stress tensor contribute to the Raman shift. This is particularly critical when using μ-R, which as discussed above works in nearly backscattering geometry; for which in the case of cubic semiconductors with (001) surface orientation, the usual surface for the majority of microelectronic devices, only the LO

phonon is allowed; therefore, in a conventional μ-R experiment, the stress induced Raman shift is monitored by the LO phonon band only; which means that the amount of stress estimated is only a weighted average of the stress components; because all the other stress tensor components contributing to the peak shift are not affordable. In fact, depending on the relative magnitude of the different stress components, upshift or downshift of the Raman peak can occur. A priori, the scattering geometry of the μ-R apparatus avoids the acquisition of data about the two transverse phonons, TO on (001) surfaces. Note that this is not a problem of Raman spectroscopy itself, but it is inherent to the experimental set-up necessary to map stresses in micrometric structures.

A method for the full assessment of the stress tensor in Si using conventional micro Raman spectroscopy in [112] Si was developed in [152]. Because in this scattering configuration the two phonon modes are allowed, using polarized excitation beams and analyzed scattered beams they could determine the frequency shift of the three phonon modes (one LO and two TO); however, in most of the microelectronic problems this is not the case, and one only has access to the (100) surfaces.

The peak wavenumbers of the optical phonon modes in the presence of strain, can be obtained by solving the secular equation [98, 153, 154]. The strain tensor, $\boldsymbol{\varepsilon}$, is related to the stress tensor, $\boldsymbol{\sigma}$, by Hooke's law, $\boldsymbol{\varepsilon} = \mathbf{S}\boldsymbol{\sigma}$, where $\mathbf{S}$ is the compliance tensor. In the case of simple stress models, e.g., uniaxial or biaxial stress, this relation is simple. For example, for uniaxial stress, σ, along the $\langle 100 \rangle$ crystal direction, one has $\varepsilon_{11} = S_{11}\,\sigma$, $\varepsilon_{22} = S_{12}\,\sigma$, and $\varepsilon_{33} = S_{12}\,\sigma$, where the S_{ij} are the elastic compliance tensor elements. The relation between the frequency shifts and the stress for the zone center modes is given by the following equations:

$$\begin{aligned}
\Delta\omega_1 &= \frac{1}{2\,\omega_o}(pS_{11} + 2qS_{12})\sigma \\
\Delta\omega_2 &= \frac{1}{2\,\omega_o}[pS_{12} + q(S_{11} + S_{12})]\sigma \\
\Delta\omega_3 &= \frac{1}{2\,\omega_o}[pS_{12} + q(S_{11} + S_{12})]\sigma
\end{aligned} \tag{3.13}$$

p, q, and r are the deformation potentials. The eigenvectors are not changed, which means that the Raman tensor and the corresponding polarization vectors are the same as if they were stress free.

In the case of silicon for backscattering on (001) surfaces, only the LO Raman mode is allowed, and the relation between the wavenumber of this mode, and the stress is given by the third relation in (2.15). Using the available values for p, q, r, ($p = -1.85\omega_0^2$, $q = -2.31\omega_0^2$, $p = -0.71\omega_0^2$) and S_{ij} ($S_{11} = 7.67 \times 10^{-12}$ Pa^{-1}, $S_{12} = -2.134 \times 10^{-12}$ Pa^{-1}, $S_{44} = 12.5 \times 10^{-12}$ Pa^{-1}) [153, 154], one obtains for uniaxial stress along the $\langle 100 \rangle$ axis the following linear relation, between the LO phonon frequency shift and the stress [30]:

$$\sigma(\text{MPa}) = -430\,\Delta\omega_3\left(\text{cm}^{-1}\right) \tag{3.14}$$

For biaxial stress, which is the usual situation of heteroepitaxial films deposited on (001) subtrates, with stress components along ⟨100⟩ and ⟨010⟩ (σ_{xx} and σ_{yy}), the LO phonon frequency shift is given by [30]:

$$\Delta\omega_3\left(\text{cm}^{-1}\right) = \frac{1}{2\,\omega_o}\left[pS_{12} + q(S_{11} + S_{12})\right](\sigma_{xx} + \sigma_{yy}) \tag{3.15}$$

$$\sigma(\text{MPa}) \approx -860\,\Delta\omega_3\left(\text{cm}^{-1}\right) \tag{3.16}$$

From these figures, one observes that 100 MPa induce a shift of 0.23 cm^{-1} for in-plane uniaxial stress; using high resolution spectrometers one can reach spectral resolutions close to 0.02 cm^{-1}, which means that Raman spectroscopy can give stress accuracy around 10 MPa.

The relation between Raman shift and uniaxial stress along a certain crystal direction has been experimentally derived for most of semiconductors [103, 155]. Usually, this relation is linear, or low-order polynomial, see Table 3.5 where stress coefficients for different semiconductors are listed. In simple scenarios, where the stress is well defined, e.g. uniaxial, biaxial, or, hydrostatic, the stress can be straightforwardly determined from the Raman shift. As above mentioned, in microelectronics the stress scenario is complex; in fact, for each pair of spatial coordinates one has a relation between the peak wavenumber and the six different non vanishing components of the stress tensor, which are the unknown variables.

Table 3.5 Calculated stress coefficients for Raman shift for bulk materials (column 2) and for several heterostructures (column 4) [103]

Bulk	$\partial\omega_{LO}/dP$ (cm^{-1}/GPa)	Heterostructure (layer/substrate)	$\partial\omega_{LO}/dP$ (cm^{-1}/GPa)
GaAs	4.77	GaAs/AlAs	4.72
InP	5.87	GaAs/Si	4.24
InAs	4.16	GaAs/GaP	4.43
ZnSe	3.78	InP/GaAs	5.75
Ge	4.48	InAs/GaAs	3.83
GaP	4.46	ZnSe/GaAs	3.30
AlSb	5.73	Ge/Si	3.96
		InAs/Si	3.51
		GaP/Si	4.22
		GaP/InP	5.03
		InAs/InP	3.89
		AlSb/GaSb	5.84
		InAs/GaSb	4.28
		InAs/AlSb	4.22
		ZnSe/ZnS	3.37

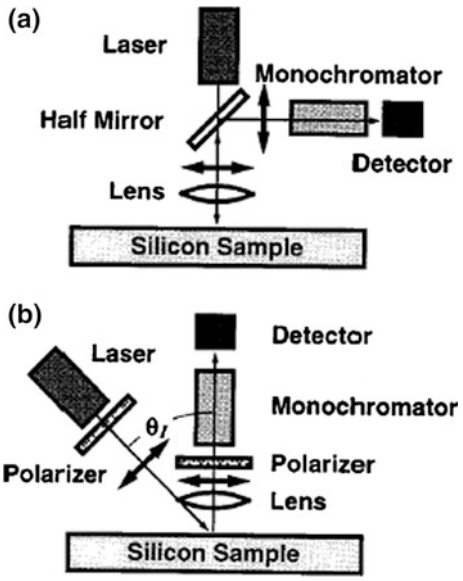

Fig. 3.20 Experimental arrangement for off-axis Raman spectroscopy. See the tilted incidence of the laser beam [152]

Because of the above discussion, obtaining quantitative information about the stress, demands to assume a strain model, necessary to reduce the number of stress tensor elements.

Another way to afford this problem in a μR apparatus consists of the polarized off axis configuration. In this experimental approach one looks for measuring the complete stress tensor, by detecting the three Raman active phonon modes as above pointed out [99, 100, 152, 156]. In this experimental configuration the incident laser beam is tilted away from the normal axis, the incident beam is polarized and the scattered beam is analyzed, Fig. 3.20; the deviation from the normal incidence makes the three phonons allowed, and by using the polarizers, one can weight their respective contribution, according to the Raman polarization selection rules, and the azimuth angle between polarizer and analyzer.

The Raman intensity in terms of the polarization selection rule is given by the expression:

$$I(\omega)\alpha \sum_j \left|\mathbf{e}_s^T \mathbf{R}_j \mathbf{e}_i\right|^2 \tag{3.17}$$

where $\mathbf{R_j}$ is the Raman tensor of the j phonon mode, e_s^T is the polarization vector of the scattered light (T denotes the vector transpose) and $\mathbf{e}_i$ is the polarization of the incident beam. By combining the incident angle, and the incident and final polarizations one can shape the spectrum, which is not only a function of the stress, but also of the experimental configuration. This procedure was used in a macro configuration, and tested with Si wafers undergoing different mechanical loads; for more details see [99, 100, 152]. Bonera [99], and Ossikovski [100], used different

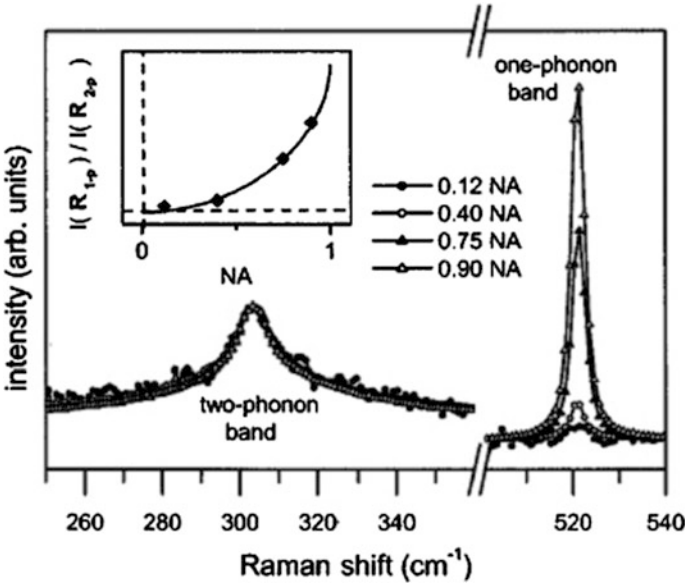

Fig. 3.21 Raman spectra measured with objectives of different NA. The one phonon band was normalized to the 2 phonon band (300 cm^{-1}), and the relative intensity was plotted as a function of the NA (see the *inset*) [99]

approaches based on the off-axis polarized Raman spectroscopy, to determine the stress tensor with a μR apparatus. Bonera et al. [99] made use of the large NA objectives, in order to tilt the observation directions with respect to the z axis, Fig. 3.21.

Ossikovski [100] used a modified μR apparatus, where the microscope was settled up in oblique backscattering geometry, see Fig. 3.22; which is similar to the experiments by Loechelt [156], but improved because of the high spatial resolution provided by the microscope optics.

A big concern of the off axis polarized Raman spectroscopy is the effective incidence angle, which due to the large refractive index of the semiconductor samples is relatively small; the effective tilt angles are limited by Snell's law. In particular, in the case of Si for a large numerical aperture objective (NA = 0.95), the effective angle formed by the external excitation rays with the z axis inside the semiconductor is only 14°, for decreasing numerical apertures, e.g. an standard commercial ×10 objective with NA = 0.25, it is practically non relevant, and one can say that it works in pure backscattering configuration; see the discussion of Sect. 3.4.7 regarding the influence of the NA of the objectives in the Raman spectrum of GaAs.

In the case of multicrystalline Si, the different orientations of the grains should allow the detection of the three Raman modes, which can be probed in backscattering using different polarization configurations. Becker et al. [23] carried out a

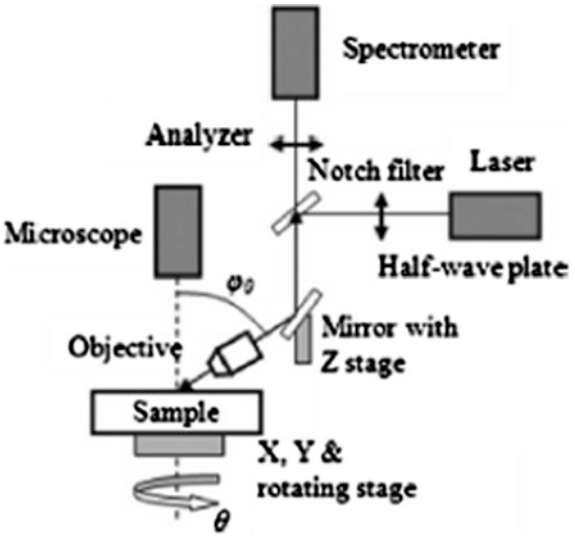

Fig. 3.22 Experimental arrangement for off-axis μ-R apparatus. Compare this to the scheme shown in Fig. 3.21 [100]

detailed study of the grain orientation and the internal stress at the grain boundaries. The stress map across a grain boundary was revealed, see Fig. 3.23.

Tada et al. [32] have demonstrated that quantitative stress analysis can be achieved by means of the polarization dependence of the Raman spectrum measured in low symmetry surfaces; they combined weakly absorbed 364 nm excitation light with large NA (1.3) oil immersion objective, allowing thus the measure of the stress components in shallow trench isolation s (STI) structures, revealing the stress relaxation due to cleavage, Fig. 3.24, [32].

All these procedures demand a tedious experimentation; therefore, the experimentation time cost is substantially reduced when one can build up a reliable stress model. As an example, the local mechanical stresses in Si near the local oxidation of silicon (LOCOS), polysilicon buffered LOCOS (LOPOS), and polysilicon encapsulated LOCOS (PELOCOS) structures were obtained using stress models describing the stress tensor in such structures [30]. A detailed description of the stress model in Si_3N_4/poly Si isolation trenches of different widths on a Si wafer can be found in [31]. These films are known to introduce stresses in the silicon substrate with shear stress gradients at the film edges. The Raman spectra were acquired along a scanning line crossing the trenches with step intervals of 0.1 μm, starting from a position far away the edge, corresponding to the stress free Si substrate, which is taken as the zero stress reference. The relative shift of the peak with respect to the stress free peak is plotted as a function of the spatial position. As the border is approached one observes a negative shift indicating tensile stress; at the border it suddenly changes from negative to positive (compressive), and depending on the width of the stripe it partially relaxes inside the stripe. In order to give the magnitude of the stress, uniaxial stress along the width of the stripe was assumed, which was a reasonable hypothesis in the center of the stripe; but it fails around the

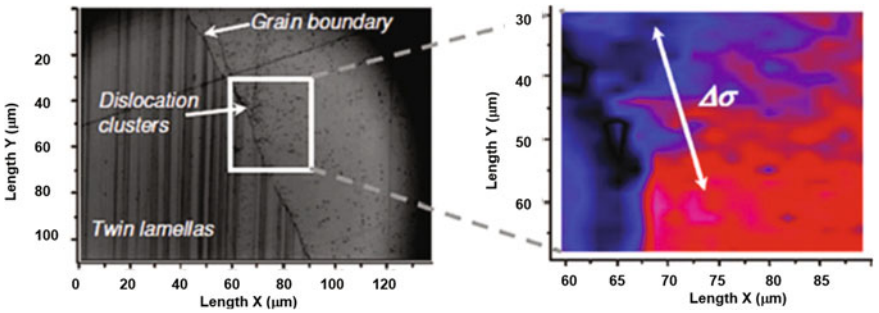

Fig. 3.23 Stress distribution in multicrystalline Si. Optical microscopy image of a multicrystalline Si wafer, with a grain boundary separating a region of twin lamellas and an arbitrarily oriented grain (*left panel*). The *right panel* is the peak frequency image revealing a stress field close to the grain boundary. The *white arrow* represents the difference stress tensor estimated by taking account of the crystal orientation. The *red color* means compressive stress

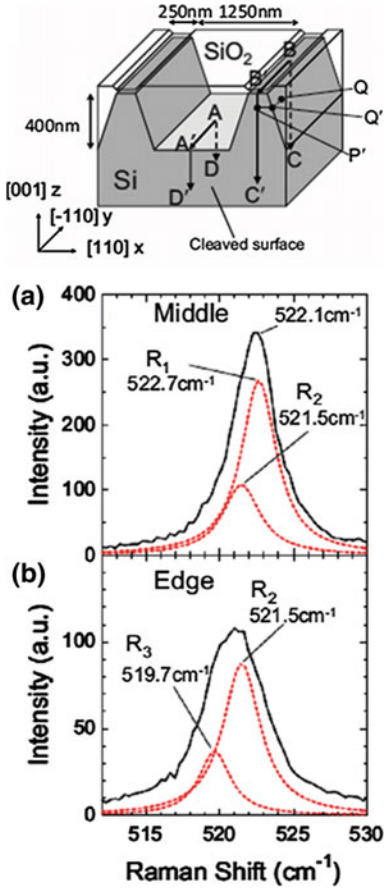

Fig. 3.24 Raman spectra measured in a shallow trench isolation on Si, with an 1.3 NA oil immersion objective. At this high NA, there is an effective deviation from the true backscattering geometry, and the LO and TO modes split out by the stress are observed [32]

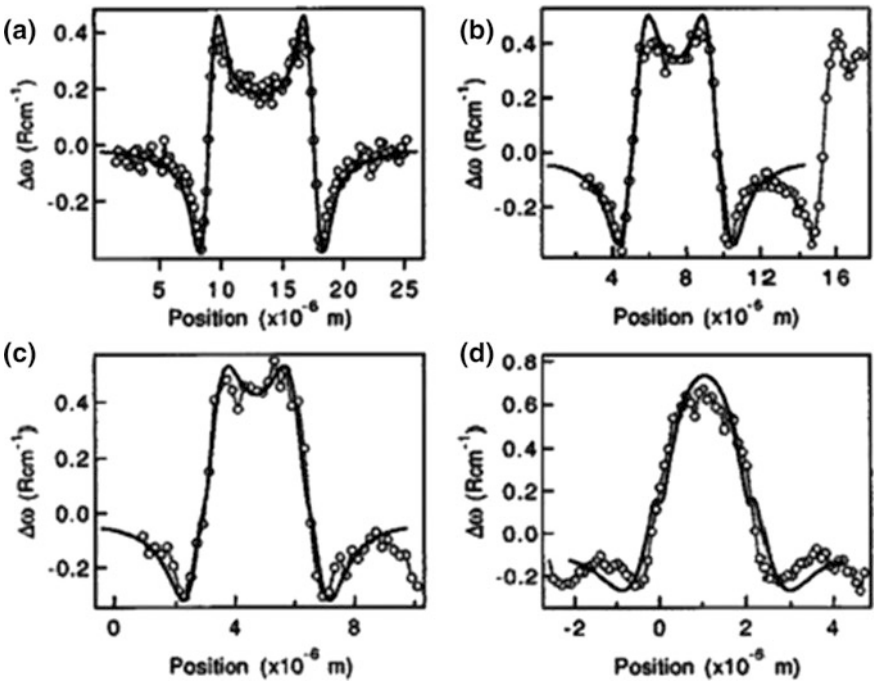

Fig. 3.25 Stress distribution across Si_3N_4/poly-Si isolation trenches of different widths: **a** 9.4 μm, **b** 5 μm, **c** 4 μm, **d** 2.5 μm. *Symbols* are the experimental data and *lines* are the calculated values according to a defined stress model [31]

stripe borders, because of the presence of shear stress components. The authors used the edge force model proposed in [157]. The results of the theoretical model were fitted to the Raman data obtaining an excellent agreement, confirming thus the satisfactory choice of the stress model, Fig. 3.25.

Lifting the degeneracy may lead to the splitting of the Si peaks (LO-TO), which are resolved into a singlet (s), and a doublet (d). The two peaks are distinguishable from each other if the splitting is larger than the FWHM of the peaks, around 3 cm^{-1}, which corresponds to stresses above the GPa. Such a high stress is not usual in microelectronics; therefore, the common aspect of the observed first order Raman band is that of a peak shifted and slightly broadened according to the magnitude of the splitting, see in Fig. 3.25 the splitting between the two phonon modes. Nevertheless, the scenario is complex, because the slight band broadening can also occur under inhomogeneous stress distribution inside the scattering volume, which is quite possible around the typical stress distributions present in microelectronic structures. One cannot neglect the laser induced local heating; indeed, when exciting an opaque media with a laser beam focused to a 1 μm diameter spot, one can induce local heating of the sample, with the corresponding increase in temperature, by no means small, which will result in a downshift of the

Raman frequency; furthermore, the local heating should also introduce temperature gradients that might induce non negligible local compressive stresses, which have to be contemplated [12, 13].

How can we distinguish the different scenarios? A complex Raman signal with the contribution of different vibration modes is sensitive to the polarization of both the incident and the scattered light. Rotating the polarization should allow ascertaining whether a broadened phonon mode is due to splitting or not. In the case that the broadening is due to an inhomogeneous stress distribution, one could narrow the peak by reducing the probing volume, either increasing the NA of the objective, or reducing the beam diameter by reducing the laser wavelength, which also decreases the probe depth. The temperature effect can be discriminated by measures at different laser power densities. Nevertheless, the interpretation of the broadening data remains complex, and needs additional information about the local homogeneity in terms of stress.

In general, monitoring the plasma lines (or a line from a calibration lamp) is necessary for calibration purposes during stress measurements with Raman spectroscopy. The frequencies of these peaks are independent of stress or heat in the sample and are stable over the whole run of the experiment, which allows to dispose of a reliable control reference for experiments prolonging on time, therefore subjected to experimental instabilities.

3.5.2 Doping

One of the main issues for the applications of semiconductors is the control of doping, since it determines the carrier concentration and mobility, which are major transport parameters regarding the operation performance of devices. The measurement of those parameters is essential for the prediction of the device operation properties.

In this context, one needs to know about the incorporation of the dopants to the lattice, and also to measure the transport parameters. As mentioned above, there are two ways of studying the presence of impurities by Raman spectroscopy; one is the study of the local vibration modes (LVMs), and the other is the assessment of the transport properties, free carrier concentration and mobility, by means of the interaction between phonons and plasmons. Initially, they were discussed by Varga [158] and observed by Mooradian and Wright [87, 88] in n-type GaAs, with different free electron concentrations. Usually, transport measurements are carried out by electrical methods, namely, Hall effect, resistivity measurements, surface photovoltage (SPV)…. Some of those methods require of electrical contacts and give average values for those parameters over relatively large areas/volumes. Regarding the incorporation of dopants, they can be identified by secondary ion mass spectroscopy (SIMS). However, SIMS provides only the presence of the chemical species, without information about their lattice positions. Raman spectroscopy appears as a very useful technique to study doping, and more specifically doping activation, with potential advantages over the other methods; because, the Raman probe is

contactless and non destructive, it provides local measurements, and can be used "in situ" during growth, or processing. On the other side of the balance, the sensitivity to free carrier concentrations below a few 10^{17} cm^{-3} is low. The carrier density and mobility have been determined by Raman spectroscopy for different semiconductors with different doping levels; e.g., 3C-SiC [159], hexagonal SiC (4H and 6H polytypes) [160–164], GaP [165, 166], GaN [46, 167–172], InN [173], ZnSe [174], GaAs [93, 175–181], GaSb [182, 183], InP [184], III-V alloys [185, 186]. Furthermore, local analyses of the distribution of the free carriers have been also carried out, e.g. distribution of impurities in GaP [186], carrier distribution in modulated doped 6H- SiC [187]; doping modulation in conformal GaAs layers [188], carrier concentration around crystal defects; carrier distribution around the dislocation atmospheres in Si-doped GaAs [189]; oval defects in GaAs layers [190]; micropipes in SiC [25, 191], carrier distribution around foreign polytype inclusions in SiC [55]; doping growth striations in n-GaAs [192], Si delta-doped GaAs [193], among other.

Phonon-Plasmon Coupled Modes

The free carriers in semiconductors form a plasma wave, see Sect. 1.4.4. The macroscopic electric field associated with this plasma wave interacts with the polarization field associated with the LO phonons in polar semiconductors. This coupling, in semiconductors with high carrier mobility and low carrier effective masses, splits the LO phonon in two longitudinal optic-plasmon coupled (LOPC) modes, L_+ and L_-. The L_- branch, shifts from 0 cm^{-1} to the TO frequency, whereas the L_+ branch shifts from the LO frequency to the plasma frequency, ω_p, for increasing free carrier concentration [3–5, 36, 87, 88]. For low free carrier concentration the L_+ branch is phonon-like, and the L_- branch is plasmon-like, whereas for high free carrier concentration L_+ is plasmon-like, and the L_- branch becomes phonon-like. As a consequence of the coupling, the Raman spectrum is the result of the spectrum arising from the surface charge depleted layer, and the neutral region beneath it. Figure 3.26a shows a typical spectrum of n-type GaAs, and Fig. 3.26b shows the wavenumbers of the two LOPC branches as a function of the free electron concentration.

The analysis of the LOPC modes supplies information concerning the free carrier concentration and the mobility. The Raman intensity is proportional to the imaginary part of the inverse of the dielectric function, including the lattice vibrations, and the free carrier contributions:

$$I(\omega) \sim \mathrm{Im}\left(-\frac{1}{\varepsilon(\omega)}\right) \tag{3.18}$$

Different models, based on different choices of the dielectric function including the electron and phonon contributions, are used for fitting the experimental results. According to this three main models are currently used, see Sect. 1.10.1, Drude [160, 165, 194], Hydrodynamic (HD) [195–197] and Linhard-Mermin (LM) [177, 178, 198] formalisms. The accuracy of these models depends on their ability to describe the main phonon-plasmon interaction processes, namely:

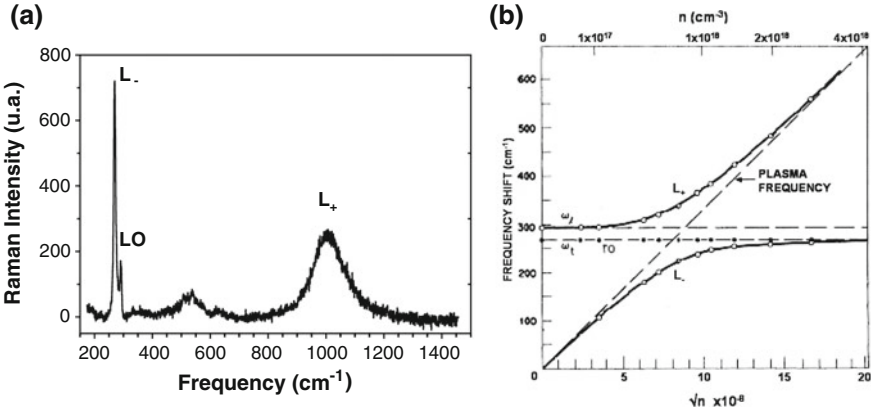

Fig. 3.26 **a** Raman spectrum of n-doped GaAs showing the two LOPC branches. **b** Frequency shift of the two LOPC branches as a function of the free electron concentration in n-GaAs, the *horizontal dashed lines* represent the LO and TO phonon peak frequencies [87, 88]

- The Landau damping of the collective Plasmon modes [1, 199]
- The spatial dispersion of the Plasmon modes [174]
- The finite temperature effects
- The non parabolicity of the energy bands [200]

These models have been implemented with different compound semiconductors and their accuracy was validated by electric measurements, e.g. Hall effect. Most of the analyses reported are based on simple models, e.g. Drude and HD, which allows a simple estimation of the free carrier concentration from the Raman parameters.

In the Drude formalism the dielectric function, $\varepsilon(\omega)$, for an electron gas of density N_e is:

$$\varepsilon(\omega) = \varepsilon_o \left(1 + \frac{\omega_{LO}^2 - \omega_{TO}^2}{\omega_{TO}^2 - \omega^2 - i\omega\Gamma} - \frac{\omega_p^2}{\omega(\omega - i\gamma)} \right) \tag{3.19}$$

where $\omega_{LO\ and}$ ω_{TO} are the phonon peak frequencies (expressed in wavenumbers), γ is a phenomenological damping parameter, and ω_p is the plasma frequency, (1.12), [87, 88]:

The frequencies of the two zone center (q = 0) LOPC branches are the solutions of $\varepsilon(\omega) = 0$. Therefore in this formalism the plasma frequency is easily deduced from the LOPC peak frequencies according to the expression:

$$L_{\pm}^2 = 1/2\left(\omega_{LO}^2 + \omega_p^2(0)\right) + 1/2\left[\left(\omega_{LO}^2 + \omega_p^2(0)\right)^2 - 4\omega_p^2(0)\omega_{TO}^2\right]^{1/2} \tag{3.20}$$

In this formalism, one does not consider the spatial dispersion of the phonons, nor the thermal distribution of the electron velocities, nor the non parabolicity of the

conduction band. These limitations allow this formalism to supply a very rough estimation of the free carrier concentration. Indeed, the comparison with Hall data normally gives circa 30% deviation in the estimation of the free carrier concentration using (3.20).

In the HD model one introduces the dispersion of plasmons, and the distribution of thermal velocities:

$$\varepsilon(\omega) = \varepsilon_o \left(1 + \frac{\omega_{LO}^2 - \omega_{TO}^2}{\omega_{TO}^2 - \omega^2 - i\omega\Gamma} - \frac{\omega_p^2}{(\omega^2 - \langle v^2 \rangle q^2 - i\omega\gamma)} \right) \tag{3.21}$$

$$\langle v^2 \rangle = \frac{3KT}{m^*} \frac{F_{3/2}(\eta)}{F_{1/2}(\eta)} \tag{3.22}$$

The plasmon dispersion reads as

$$\omega_p^2(q) = \frac{N_e\, e^2}{m^*\, \varepsilon_0} + \frac{3}{5}(q\, v_F)^2 \tag{3.23}$$

where **q** is the phonon wavevector, and v_F is the Fermi velocity.

In n-type GaAs with free electron densities up to 3×10^{18} cm^{-3}, the HD model is useful to calculate the phonon-plasmon spectra [201]. This approach is only valid for parabolic energy dispersion for electrons, this is the reason why the HD model works within reasonable accuracy for low electron concentration. For higher electron concentration the conduction band filling results in a significant contribution of non parabolic states.

The four plasmon–phonon interaction processes can be accounted for by the Linhard-Mermin model; for which the dielectric function takes the form:

$$\varepsilon(\omega) = \varepsilon_o \left(1 + \frac{\omega_{LO}^2 - \omega_{TO}^2}{\omega_{TO}^2 - \omega^2 - i\omega\Gamma} - \frac{\left(1 + i\frac{\Gamma}{\omega}\right)[\chi^0(q, \omega + i\Gamma)]}{1 + i\frac{\Gamma}{\omega}\left[\frac{\chi^0(q,\omega+i\Gamma)}{\chi^0(q,0)}\right]} \right) \tag{3.24}$$

with

$$\chi^0(q,\omega) = \frac{2\, e^2}{2\, \pi^3\, q^2\, \varepsilon_0} \int f(E_F, T, k) \times \left(\frac{E(q+k) - E(k)}{[E(q+k) - E(K)]^2 - [\hbar\omega]^2} \right) d^3\, k \tag{3.25}$$

$f(E_F,T,k)$ is the Fermi distribution function.

The LM model allows a precise description of the electronic part of the dielectric function giving satisfactory fit to the Raman spectrum of coupled plasmon-phonon modes. However, the LM model is computationally complex, and the fitting to the spectra is time consuming.

Cuscó et al. [202] used a modified HD model, which allowed extending the concentration limit of applicability of the HD model. In this modified model they

took account of the band non-parabolicity and the thermal dispersion by introducing an optical effective mass:

$$\frac{1}{m^*_{opt}} = \frac{1}{m^*_0}\left[1 + 5\alpha\frac{KT}{E_0}\frac{F_{3/2}(\eta)}{F_{1/2}(\eta)}\right] \tag{3.26}$$

$F_{3/2}$ and $F_{1/2}$, are the Fermi integrals, α is here a coefficient accounting for the non parabolicity of the conduction band, and η = EF/KT.

According to this approach the dielectric function reads as:

$$\varepsilon(\omega) = \varepsilon_o\left(1 + \frac{\omega^2_{LO} - \omega^2_{TO}}{\omega^2_{TO} - \omega^2 - i\omega\Gamma} - \frac{e^2 N_0}{m^*_0}F_{1/2}(\eta)\frac{1 + \frac{5}{12}\frac{\alpha}{E_0}\langle v^2\rangle}{(\omega^2 - \langle v^2\rangle q^2 - i\omega\gamma)}\right) \tag{3.27}$$

$$\mathrm{N_0} = 2(\mathrm{KTm^*_0}/2\pi\hbar^2)^{3/2} \tag{3.28}$$

They demonstrated that this approach gave values very close to those of LM model over a wide range of electron concentrations in n-type InP, Fig. 3.27.

The electron mobility is related to the plasmon damping constant, γ, according to the following equation:

$$\mu = \frac{e}{m^*\gamma} \tag{3.29}$$

While the agreement between the spectroscopic and electrical measurements for the carrier concentration was quite fair; the Raman mobility is underestimated with respect to the electrically measured mobility (μ_H/μ_R = 2), see [177] for more details.

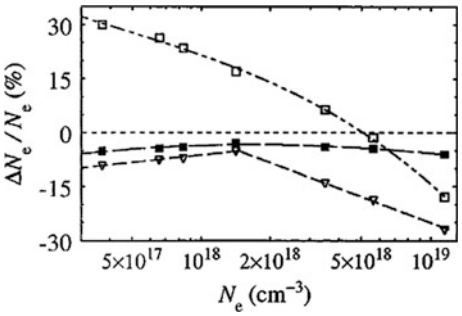

Fig. 3.27 Deviation of the electron densities calculated by Drude model (*open squares*), HD model (*inverted triangles*) and modified HD (*filled squares*) with respect to the LM value, *dashed horizontal line*. The values represented by the *symbol* were calculated from experimental data in n-doped InP. Note the close agreement between the modified HD values and the LM reference for a large range of electron concentrations [202]

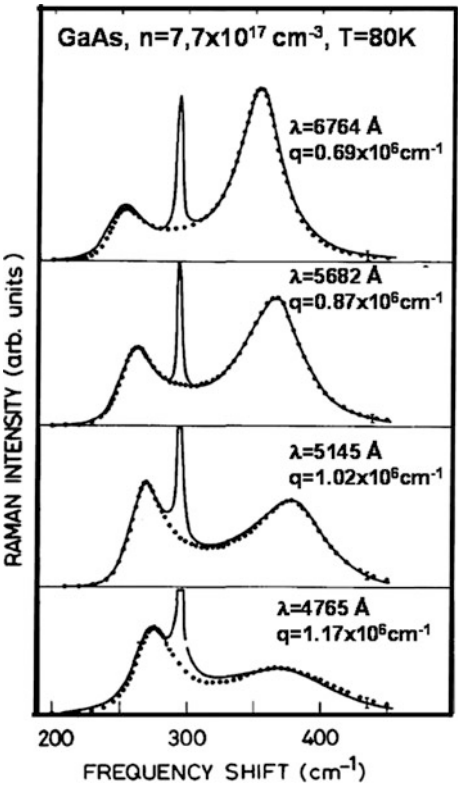

Fig. 3.28 Raman spectra of n-type GaAs ($n \cong 7.7 \times 10^{17}$ cm^{-3}) using different excitation wavelengths. The *dotted lines* are the calculated LOPC modes using LM dielectric function [177]

In summary, when one wants to use LOPC modes for the assessment of the transport parameters one can apply the HD model below a certain free electron concentration with a good accuracy. However, for higher concentrations, LM model is required; but, if one looks for a higher simplicity the modified HD model gives a reasonable accuracy over the full concentration range.

Space Charge Region (SCR)

Typical Raman spectra on undoped and Si-doped n-type GaAs are shown in Fig. 3.28; The spectrum of the doped sample consists of an LO phonon, and the coupled L_+, and L_- modes. The phonon mode arises from the space charge region (SCR) depleted of free carriers, whereas the LOPC modes arise from the neutral volume beneath the SCR.

Therefore, the ratio of the LO phonon intensity to the intensity of the LOPC modes is related to the relative volumes of SRC and neutral regions probed by the laser beam. This means that the relative intensity of the bands is not only governed by the free carrier concentration, that determines the SCR width, but is also determined by the excitation wavelength; therefore the aspect of the spectrum depends on the laser wavelength, see Fig. 3.29, where the Raman spectra of n-type

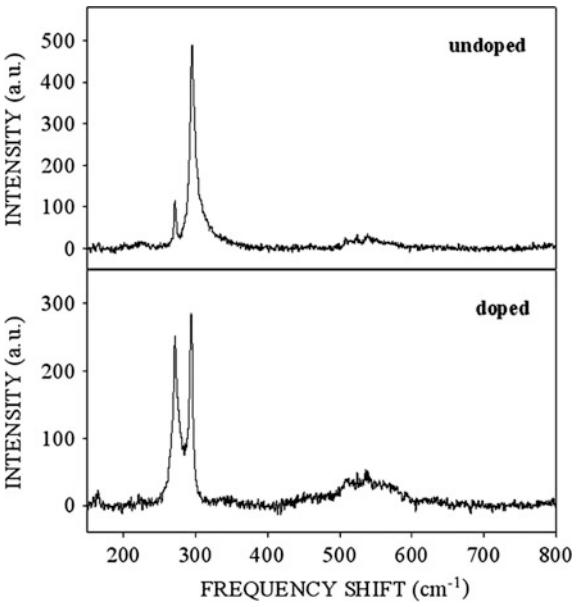

Fig. 3.29 Raman spectra of undoped GaAs (*upper panel*), and Si-doped GaAs (*lower panel*), The L_+ LOPC branch is not well resolved because overdamping, compare this spectrum with the spectra of Fig. 3.29

GaAs ($n = 7.7 \times 10^{17}$ cm^{-3}) acquired with different exciting laser wavelengths are shown [177]. One observes how decreasing the wavelength, lower penetration depth, the LOPC bands decrease its intensity, because the scattering volume is mostly occupied by the SRC, which for this free electron concentration is ≈30 nm depth, compared to the probe depth of 126 nm for 514 nm excitation in GaAs [177]. One has better sensitivity to the LOPC modes with long excitation wavelengths, because of the higher penetration.

It should be noted that sometimes the L_+ branch is damped and cannot be clearly resolved, which occurs mainly when the semiconductor is heavily doped, heavily compensated, or defect-rich for example in dry etched material [203]; in such cases is useful to use the L_- branch, which is less affected by damping, to estimate the free electron concentration. One has to be careful with the contribution of the TO phonons to the experimental L_- branch, because even in forbidden configuration it can be activated by the presence of defects, Fig. 3.29 (upper panel). In the spectrum of n-type GaAs, Fig. 3.30 (lower panel), one observes the L_- branch arising from the neutral region and the LO phonon mode arising from the charge depleted region. The L_+ branch is not well resolved due to damping; furthermore, it is superposed to the second order spectrum of the depleted region (2LO, 2TO, and LO + TO two phonon bands). Therefore, it cannot supply reliable information about the free carrier concentration.

The SRC width can be determined from the ratio between the intensities of the LO phonon mode arising from the SRC region and the L_- branch of the LOPC arising from the neutral region

$$(I(LO)/I(L_-)) = \beta(e^{2\alpha d} - 1) \tag{3.30}$$

where, β is a scattering constant (β = (I_o(LO) – I(LO)), I_o(LO) is the intensity of the LO Raman band in a semiinsulating sample (e.g. n < 1 × 10^{14} cm^{-3} in GaAs), α is the absorption coefficient, and d the space charge region width, which is related to the free electron concentration by the following expression:

$$d = \left(\frac{2\,\varepsilon_0\,\varepsilon_r\,\Phi_B}{e^2\,n}\right)^{1/2} \tag{3.31}$$

ε_r is the static dielectric constant, Φ_B is the surface built-in potential.

Taking for GaAs β = 2.72, m* = 0.0632 m_o, ε_r = 10.6, α = 91 × 10^3 cm^{-1}, Φ_B = 0.48 eV [93], the electron concentration can be expressed as:

$$n(\mathrm{cm}^{-3}) = \frac{1.9 \times 10^{17}}{\left[\ln\left(1 + 0.37\,\frac{I_{LO}}{I_{L_-}}\right)\right]^2} \tag{3.32}$$

Damped Plasmon Modes

For materials with overdamped plasmons (ω_p/γ < 1) i.e., large effective masses and low mobility semiconductors as SiC, GaN, and GaP, only the L_+ branch with a broad asymmetric shape is observed. In the case of p-type semiconductors one has also to consider the contribution of free holes from different sub-bands. The coupled modes have to account for the LO phonons, the light holes, and the heavy holes, and all their crossed interactions. The plasma frequency, ω_p, and the plasma damping constant, γ, have to be calculated by fitting the line-shape of the coupled LO modes; this line shape is given by [92, 165]

$$\mathrm{I}(\omega) \sim \mathrm{A}(\omega)\mathrm{Im}\left(-\frac{1}{\varepsilon(\omega)}\right) \tag{3.33}$$

where ε (ω,0) is the dielectric function (phonon + electronic contribution) for the Brillouin zone center (q = 0), and A(ω) is given by the following expression [61–63, 92]:

$$A(\omega) = 1 + 2C\omega_{TO}^2\,\frac{\omega_p^2\gamma(\omega_{TO}^2 - \omega^2) - \omega^2\Gamma(\omega^2 + \gamma^2 - \omega_p^2)}{\Delta} + \left(\frac{C^2\omega_{TO}^4}{\Delta}\right)\frac{\omega_p^2[\gamma(\omega_{LO}^2 - \omega_{TO}^2) + \Gamma(\omega_p^2 - 2\omega^2)] + \omega^2\Gamma(\omega^2 + \gamma^2)}{\omega_{LO}^2 - \omega_{TO}^2} \tag{3.34}$$

$$\Delta = \omega_p^2\gamma[(\omega_{T0}^2 - \omega^2) + \omega^2\Gamma^2] + \omega^2\Gamma(\omega_{L0}^2 - \omega_{T0}^2)(\omega^2 + \gamma^2) \tag{3.35}$$

C is the so-called Faust-Henry coefficient [203], which is related to the Raman intensity ratio of the LO and TO phonon bands:

$$\frac{I_{LO}}{I_{TO}} = \left(\frac{\omega_e - \omega_{LO}}{\omega_e - \omega_{TO}}\right)^4 \frac{\omega_{TO}}{\omega_{LO}} \left(1 + \frac{\omega_{TO}^2 - \omega_{LO}^2}{C\omega_{TO}^2}\right)^2 \tag{3.36}$$

where ω_e is the exciting photon energy in wavenumber units.

The LOPC lineshape in p-type GaAs is shown in Fig. 3.30a, after the data calculated by Pages et al. [175]; note that only one coupled mode is observed with frequency varying between the TO, and LO frequencies, depending on the hole concentration, Fig. 3.30b [176].

In high-mobility polar semiconductors the frequency of the L_+ band is used for determining the free electron concentration in Drude and HD models. In low-mobility semiconductors ω_p, and γ are fitting parameters, from which both free carrier concentration, and mobility can be obtained. The Raman data were found to

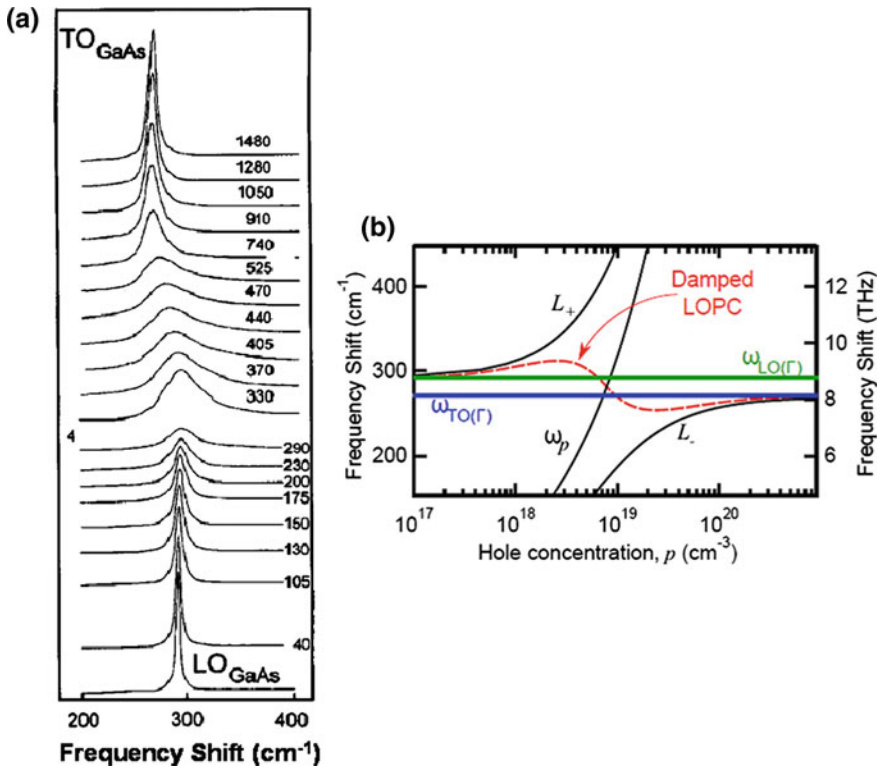

Fig. 3.30. **a** Calculated LOPC modes in p-type GaAs for different free hole concentrations (expressed by the plasma frequency, see the labels in the spectra), showing only one LOPC mode with peak frequency varying between in between LO and TO peak frequencies [175]. **b** Peak frequency of the damped LOPC plotted as a function of the free hole concentration [176]

agree reasonably well with transport data obtained by other experimental techniques, e.g. Hall effect [162, 163]. This allows one to classify the μ-R technique as a contact-less local probe for the assessment of different electronic parameters as free carrier concentration, mobility, net doping concentrations ($n \sim N_D - N_A$, or $p \sim N_A - N_D$), and SCR width. The possibility of determining these parameters, and their fluctuations at the micrometric scale, is very attractive for semiconductor and devices characterization.

Photogenerated Carriers

Attention has to be paid to photogenerated carriers. In fact, the laser power densities available with a μ-R apparatus might be high enough to photoinject a non negligible excess photocarrier concentration. The presence of these excess carriers can influence the Raman spectrum. This is particularly critical for materials with very low surface recombination velocity (SRV), because of the slow removal of the excess photogenerated carriers; e.g. InP [204, 205]. Micro-Raman spectra obtained on [101] semi-insulating InP, with increasing laser intensity are shown in Fig. 3.31. One observes a progressive broadening of the LO phonon as the result of the excess carriers photoinjected by the laser beam. Other polar semiconductors, e.g. GaAs, require higher laser intensity to observe a similar effect, because of the higher SRV.

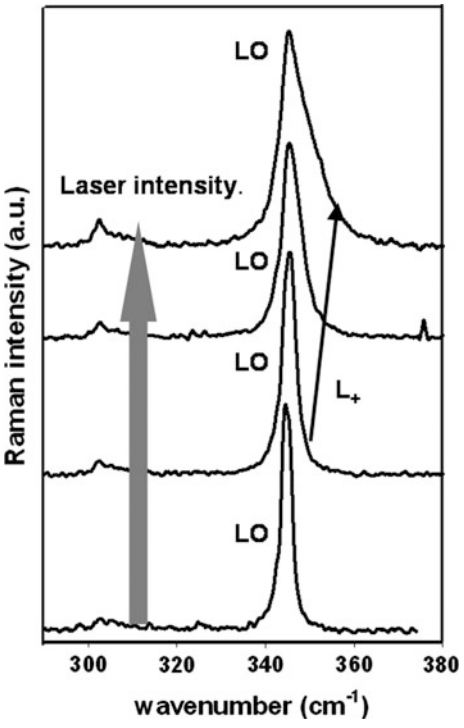

Fig. 3.31 Raman spectra of semi-insulating [101] InP at different laser intensities, showing the progressive apparition of the L_+-LOPC mode in the high wavenumber flank of the LO band for increasing laser intensity, as a consequence of the photogeneration of free carriers

Local Vibration Modes (LVM)

Doping is a crucial process in semiconductors. The incorporation of impurities does not necessarily mean that an equivalent concentration of free carriers is generated. Clear examples of this are the strong difficulties of p-doping in wide band gap semiconductors as GaN and ZnO [206]. The incomplete doping activation can arise from:

i. The non incorporation of the dopant atom in the correct lattice site, e.g. the atom occupies an interstitial position in the lattice, or forming clusters.
ii. The passivation of dopants by the formation of complexes with other atoms and/or native defects; for example, Mg-doped GaN is strongly compensated when grown under H-rich atmosphere in organo metallic chemical vapour deposition (OMCVD) growth [207].
iii. Amphoteric impurities occupying different lattice sites, which can contribute to the electrical compensation, e.g. Si in GaAs is preferably a donor, Si_{Ga}, but for increasing Si incorporation, it starts also to replace As, forming Si_{As}, which is an acceptor that compensates the Si_{Ga} donors.

Therefore, the knowledge about these features is a major challenge to improve the doping mechanisms. The use of the LOPC modes, does only provide information about the Fermi level position, but does not supply information about the nature of the donor or acceptor levels, and their structure. Local vibration modes (LVMs) can provide such information. Doping impurities lighter than the host atoms give local vibration modes with frequency vibrations higher than those of the host atoms. Furthermore, the frequency and fine structure of the LVMs supply information about the lattice position and the presence of complexes, with other impurities. There is an extensive bibliography, about the study of local LVMs in Si [86, 208], GaAs [83], and more recently GaN [82, 85]; and ZnO [81], where the analysis of the LVMs can help to understanding the structure and electrical activation of the shallow acceptors in these semiconductors. Usually, the LVMs are detected by infrared spectroscopy (Chap. 2); however, the improvement on the sensitivity of the Raman detection has increased the application of Raman spectroscopy to the detection of LVMs.

Boron doped Si was studied in the early 80s [208]. Boron is lighter than Si and produces a local mode at 620 cm^{-1} for ^{11}B, and 644 for ^{10}B. These modes are only observable for high B concentrations ($>10^{19}$ cm^{-3}). Because B is an acceptor, at such high concentration, the Fermi level is located inside the valence band, and Raman active inter valence band transitions can take place; the result is a broad scattering continuum, which is superposed to the Raman bands, resulting in Fano interferences that deforms the lineshape of both phonon modes and LVMs. In the late 80 s, attention was paid to Si in GaAs by means of resonant Raman studies [83]. Recent studies of LVMs for studying the incorporation of dopants (Si and Be) in GaAs NWs are also available [209].

Nowadays, a big effort is devoted to study the LVMs associated with p-type dopants in GaN and ZnO, because of the challenging problem of p-doping in these

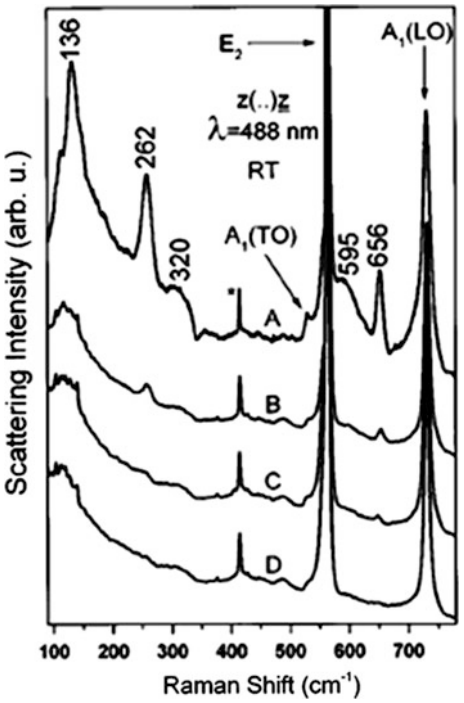

Fig. 3.32 Raman spectra Mg-doped GaN (normalized to E2 intensity) for different Mg concentrations. The peak marked with an *asterisk* arises from the sapphire substrates [82]

semiconductors. In the case of Mg-doped GaN, several spectral ranges of LVMs have been studied. In particular, five local modes in the high frequency range at 2129, 2148, 2166, 2185 and 2219 cm^{-1}, which have been assigned to Mg-H complexes with different configurations [82]. Also, low frequency LVMs, in the region of the optical and acoustic phonons, structures at 136, 262, 320, 595, and 656 cm^{-1}, have been measured in Mg-doped GaN; see Fig. 3.32. Polarization selection rule experiments reveal A_1 symmetry for these modes. Under high doping concentration, lattice disorder is introduced, in fact, the bands centred around 320 and 595 cm^{-1}, were associated with lattice disorder, because they correspond to maxima in the phonon density of states. While the three other modes were associated with LVMs of Mg, which the concentration, $\cong 10^{19}$ cm^{-3}, was estimated to be sufficient to give observable LVM contribution.

3.5.3 Temperature Measurements Using μ-R *Spectroscopy*

The elastic and vibronic behavior of semiconductors plays a very relevant role in processes as electron-phonon coupling, phonon-phonon interactions, and phonon transport. They are substantially changed with temperature; on the other hand, the stability of the semiconductor devices can be severely affected by the temperature increase during device operation [12, 13, 16, 17].

The temperature is enhanced during device operation, and is known to play a paramount role on the failure of electronic and optoelectronic devices, especially those supplying high power [210, 211]. When designing a device, it is very important to take account of the operation temperature, being the thermal management a crucial issue of the device packaging. The lattice temperature is enhanced by self-heating during device operation; furthermore, local temperature enhancement can occur in the presence of defects, which can induce huge thermal stress gradients; for example, in a high electron mobility transistor (HEMT) heat is generated in a sub-micrometer region nearby the gate [212]. In this context, the measurement of the local lattice temperature in a device under operation is crucial to the understanding of the device failure. Because of the localized heat sources, the need for temperature probes with submicrometric spatial resolution appears obvious; in this context the μ-R spectroscopy has been demonstrated as a very useful non-invasive temperature probe, suitable for the measurements of local heating in devices. This potential has been exploited from the early experiments by Todoroki [33] who measured the temperature at the facet mirror and inside the cavity of AlGaAs based laser diodes. Thereafter, Brugger et al. [34] studied the facet mirror temperature in QW AlGaAs ridge lasers. Todoroki established a relation between the temperature increase and the formation of dark line defects (DLDs). Todoroki reported a facet temperature enhancement, with DLDs propagating from the hot facet inside the cavity, establishing a clear relation between the local self heating and the formation of DLDs. Since that, an extensive investigation has been developed about the use of the μ-R spectroscopy as a local temperature probe. It appears as a very suitable temperature probe when high spatial resolution is required, or when alternative methods used for thermal mapping (e.g., IR microscopy [213–217] or liquid crystal thermography [218] fail, normally because of the lateral resolution requirements.

The main parameters characterizing a Raman band are the intensity, the peak frequency, and the linewidth. These parameters are sensitive to temperature changes; which can be used for the temperature measurements. One of the advantages of Raman spectroscopy as a thermometer is that it measures the lattice temperature, instead of the free carrier temperature measured by methods that use interband transitions, namely, luminescence and optical absorption. Note that both temperatures, electron and lattice, can differ, contributing in different ways to the device operation and degradation.

Peak Wavenumber and Linewidth as Parameters for the Temperature Measurement

The peak wavenumber and linewidth of the one phonon Raman bands vary with the lattice temperature. The temperature dependence of the phonon frequency and FWHM is the consequence of the anharmonic terms in the vibrational Hamiltonian of the crystal lattice. Anharmonicity includes the thermal expansion of the lattice, and phonon-phonon interactions. The peak frequency is modified according to the following relation:

$$\Delta\omega = \omega(\mathrm{T}) - \omega_0 = \Delta\omega_{\mathrm{th-e}}(\mathrm{T}) + \Delta\omega_{\mathrm{p-p}}(\mathrm{T}) \tag{3.37}$$

where ω_0 is the harmonic frequency of the phonon band, $\Delta\omega_{\mathrm{th-e}}(\mathrm{T})$ corresponds to the thermal expansion shift, and $\Delta\omega_{\mathrm{p-p}}(\mathrm{T})$ is the frequency shift due to phonon decay into phonons of lower energy.

The thermal expansion term for an isotropic crystal is:

$$\Delta\omega_{th-e} = -\omega_0\gamma \int_0^T 3\alpha(T)dT \tag{3.38}$$

where γ is the Gruneisen parameter and α is the linear thermal expansion coefficient.

The phonon decay term can be written as:

$$\Delta\omega_{\mathrm{p-p}}(\mathrm{T}) = \mathrm{A}[1 + 2\mathrm{n}(\omega_0/2, \mathrm{T})] + \mathrm{B}[1 + 3\mathrm{n}\ (\omega_0/3, \mathrm{T}) + 3\mathrm{n}^2(\omega_0/3, \mathrm{T})] \tag{3.39}$$

where one only considers the decay of the zone center phonons into two phonons with $\omega_0/2$ wavenumber (third order processes), and 3 phonons with $\omega_0/3$ wavenumber (fourth order processes), other phonon combinations can hold, n is the Bose-Einstein factor, and A and B are constants.

The estimation of the local temperature from the wavenumber shift of a phonon line requires essentially of a good calibration, a satisfactory spectral resolution, and the isolation of the problem, in order to establish an unambiguous relation between the Raman shift and the lattice temperature, as the Raman spectrum is also sensitive to other intrinsic and/or extrinsic factors; for example in the case of thin layers, one should also consider the strain induced by the thermal mismatch [219, 220]. In such a case one should add a term accounting for the thermal stress, which in the case of layers grown along the [001] axis takes the form:

$$\Delta\omega_{stress}(T) = \omega_o\left(\tilde{K}_{12} - \frac{C_{12}}{C_{11}}\tilde{K}_{11}\right)\varepsilon_{||} \tag{3.40}$$

where $\tilde{K}_{11}$ and $\tilde{K}_{12}$ are the phonon-deformation potentials, C_{11} and C_{12} are the elastic constants, and $\varepsilon_{||}$ is the in-plane strain. The in-plane strain is induced by the different thermal expansion of the two adjacent layers, or between the layer and the substrate.

The temperature dependence of the in-plane strain produced by the different thermal expansion coefficients between the layer and the substrate during post-growth cooling is [220]:

$$\varepsilon_{||}(T) = \frac{L_S(T) - L_L(T)}{L_L(T)} = (1 - \varepsilon_g)\frac{1 + \int_{Tg}^{T}\alpha_S(T)dT}{1 + \int_{Tg}^{T}\alpha_L(T)dT} - 1 \tag{3.41}$$

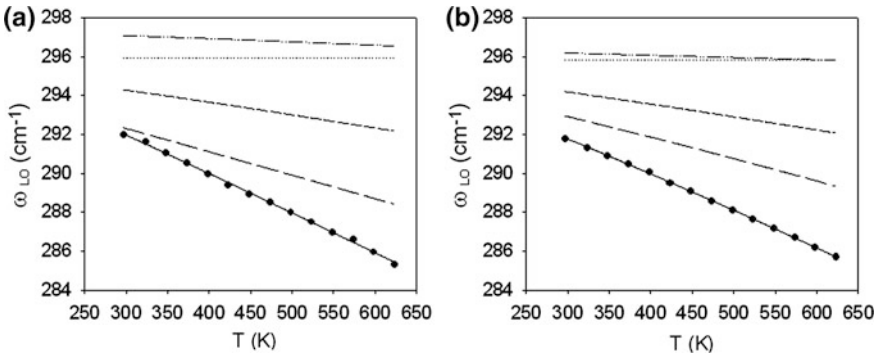

Fig. 3.33 Decomposed contributions of the linear thermal expansion (*short dashed line*), anharmonic terms (*long dashed line*), and strain (*dot-dot-dashed line*), in a GaAs/Si conformal layer. **a** Conformal layer, **b** seed layer. The *symbols* are the experimental data, and the *solid line* is the fitting to the experimental data considering all the contributions. The *dotted horizontal line* is the LO peak wavenumber at 0 K [219]

where α_S and α_L are the linear expansion coefficients of the substrate and the layer respectively, L_S and L_L the temperature dependent lengths of the substrate and layer, and ε_g is the residual strain in the layer at the growth temperature, T_g; Fig. 3.33 shows the different contributions to the peak shift as a function of T in conformal GaAs layer grown on an Si substrate [219].

Care about the stability of the system, as it was argued for stress measurements, is necessary in order to ensure that only the intrinsic contribution to the change in phonon frequency is being measured. Therefore, the same comments done about the procedure used for measuring the Raman shift associated with stress are still valid here.

The FWHM is determined by the anharmonic terms according to the following expression [109, 221]:

$$\Delta\Gamma(\mathrm{T}) = \mathrm{C}[1 + 2\ \mathrm{n}(\omega_0/2, \mathrm{T})] + \mathrm{D}[1 + 3\ \mathrm{n}\ (\omega_0/3, \mathrm{T}) + 3\ \mathrm{n}^2(\omega_0/3, \mathrm{T})] \quad (3.42)$$

However, the linewidth presents some specific features that make more difficult its use for temperature measurements. It is well known, that as a consequence of the anharmonicity, the Raman bands are broadened for increasing temperature. However, one needs a very fine correction of the instrument slit function. In fact, the experimental Raman phonon lineshape is the convolution of the phonon peak itself (Lorentz function), and the instrument slit function (Gaussian like), giving the so-called Voigt profile [222, 223]; therefore, an accurate analysis of the linewidth, needs a previous treatment in order to extract the alone Lorentz profile. Note that the difference between the experimentally measured FWHM, Γ_V, and the true Lorentzian FWHM, Γ_L, decreases with increasing the spectrum width, which means that the potential error associated with the instrument is reduced for broad bands, while it cannot be neglected for narrow bands. This is a general issue to be

considered when extracting information from the linewidth of the Raman peaks. The deconvolution of the Raman band permits to extract the true lineshape:

$$I(\omega) \propto \int \frac{\exp\left(-\frac{(\omega-\omega')^2}{(\Gamma_g/2)^2}\right)}{(\omega'-\omega_o)^2+(\Gamma_L/2)^2} d\omega' \tag{3.43}$$

where ω_o and Γ_L are the wavenumber and FWHM of the Raman band (Lorentzian), and Γ_g is the linewidth of the Gaussian Raman instrument function, which can be measured from the attenuated Rayleigh radiation line, or from plasma lines.

The Raman Intensity as a Temperature Probe. Stokes/AntiStokes Intensity Ratio

The lattice temperature can be also determined from the phonon band intensities. The integrated intensity of the Stokes Raman band depends on the lattice temperature through the phonon Bose factor ($I_S \sim (n_p + 1)$), while the integrated intensity of the AS band is proportional to n_p, [1, 14].

The use of the two bands permits to remove the Raman cross sections, which are complex to determine, allowing to giving a relation between the two Raman intensities, which are measurable quantities, and the absolute temperature,

$$\frac{I_{Stokes}}{I_{anti-Stokes}} \alpha \frac{n_p+1}{n_p} = \exp\left(\frac{\hbar\omega}{KT}\right) \tag{3.44}$$

The only prerequisite for the temperature measurement is the determination of the proportionality constant in (3.44), which involves both power terms in ω_S, and ω_{AS}, and the different apparatus (monochromator + detector) response in the spectral windows of the S and AS signals. This proportionality factor can be estimated by calibrating the Stokes-to-anti-Stokes intensity ratio for a series of known temperatures, for example in a bare Si substrate. This method of measuring the temperature was used in the early Raman temperature measurements [33]. It has the advantage, that it provides an absolute measurement of the lattice temperature, free of other contributions, e.g. stress. Usually, one needs two measurements, one for the S component and the other for the AS component; this component at moderate temperatures is weak, but it increases its intensity for elevated temperatures. Actually, the Raman spectrometers use edge filters for removing the Rayleigh radiation, these filters do not allow to measure the AS component, for which one should use notch filters. Recent works devoted to temperature mapping of devices under operation are using the peak wavenumber as the thermometric property [115, 224].

Temperature measurements with a μ-R instrument raise some questions about the influence of the excitation. Raman microprobes work under relatively high laser power density excitation conditions. Therefore, under "strong" optical absorption, local heating might be induced by the laser beam [135, 143]. Note that one needs a reasonable signal to noise ratio; therefore, sometimes the laser power density

necessary to achieve the measurements, especially for the AS component, can be high enough to induce heating. Therefore, one needs to set-up the experimental conditions in order to avoid laser induced heating. It is important to say that such a heating is strongly dependent on the laser wavelength and the sample nature, in particular, its thermal conductivity is crucial. This problem is substantially reduced when the sample is transparent to the excitation laser light. This is one of the reasons why successful temperature measurements in operating devices have been mainly carried out in wide bandgap semiconductor based devices, excited with visible light using confocal microscopy [225]. In high power devices operating at high temperature the laser beam might burn out the device.

The intensities of the Stokes and anti-Stokes components are not more valid when the laser photon energy approaches an electronic resonance of the material (E_0, $E_0 + \Delta_0$, E_1, $E_1 + \Delta_1$ transitions) [37]. The proximity of such a resonance can render the Stokes-to-anti-Stokes ratio erroneous in terms of the temperature estimation. This is particularly critical for devices formed of ternary and/or quaternary semiconductor alloys, which under the band structure evolution with the temperature increase can suddenly enter in resonance with the excitation, making meaningless the S/AS ratio. In the case of wurtzite semiconductors, this problem is overcame with the study of non-polar modes, free of resonance, e.g. the E_2 mode in GaN [226].

A major application of the μ-R temperature probe is the measurement of the local temperature in operating devices, where some of the critical dimensions can be in the sub-micron range (like many of the transistor structures used today in the microelectronics industry); on the other hand, the self heating sources associated with defects can be very local. All that means that the temperature might not be uniform over the volume probed by the laser beam (see Sect. 3.4.5). Raman measurements average the temperature over the scattering volume. In such cases, one can assume that the temperature can be locally higher than the measured one. One could also make assumptions about the temperature gradients that could allow fitting the Raman bands leading to precise temperature estimation. However, sometimes, several alternative physical hypotheses about the temperature gradients may lead to similar line profiles.

Ostermeier et al. [111] measured the evolution of the phonon frequency to estimate the temperature increase in the active region of Si n-MOSFET's with different gate lengths. The accuracy of the measurement was around 2 K, for a spectral resolution of 0.04 cm^{-1}. The temperature profile across the polysilicon gate material in the source-to-drain interval is shown in Fig. 3.34.

The use of the μ-R probe on the channel region of a GaAs MESFETs with usable signal-to-noise ratio, often results in a high density of photocarriers, which couple to the LO phonon band, disturbing it, and making no sense to the temperature measurement. This problem is directly related to the polar nature of the III-V semiconductors and the low surface recombination velocity (SRV). In the case of laser diodes, the Raman spectra taken on the facets [(110) surfaces] are free of this problem because the LOPC modes follow the same symmetry selection rules as the LO modes. Note also, that the photocarrier generation when the device is biased can

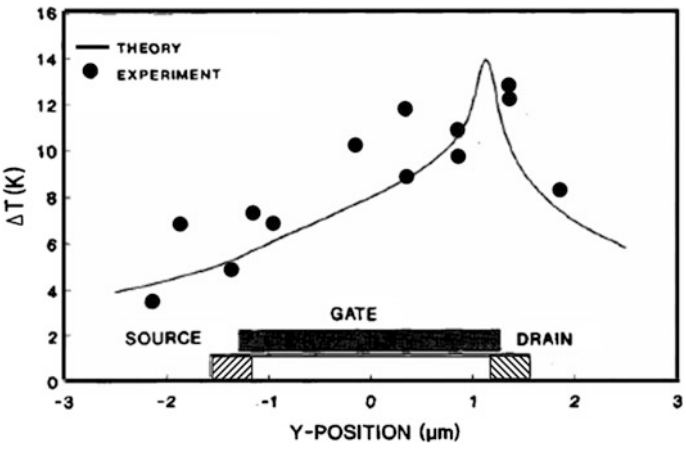

Fig. 3.34 Measured and calculated source to drain temperature of a MOSFET with 2.5 μm gate length, operated at a drain current of 2.05 mA [111]

induce the burnout of the device; therefore, the laser beam intensity must be very low to avoid heating and relevant e-h generation [117]. High resolution temperature measurements were carried out in GaAs p-HEMT multifinger devices, obtaining higher temperature inside the source drain gap, than the temperature measured by infrared thermography, consequence of the higher spatial resolution of the μ-R probe [117].

In wurtzite semiconductors the problem of the photocarriers and the LOPC modes can be circumvented by the use of the non-polar E_2 phonon as the thermometric property. The polar modes, e.g. A_1(LO), can be greatly influenced by the coupling with plasmons, due to changes in the free carrier concentration with temperature, and the plasmon damping. The fact that these semiconductors are transparent to the excitation, is detrimental to the spatial resolution, and therefore one needs to use confocal optics, to go down to the sub-micrometric resolution.

The motivation for the use of the micro-Raman technique to map the local temperatures can be specified as:

- It has been recognized very early that one part of the thermal management problem of devices is strongly localized at specific positions, e.g. the emitting facet of the laser diodes, and the gate of transistors. The heating of the facets eventually leads to the so-called "catastrophic optical damage" (COD) of laser diodes, while local heating can induce thermal stresses, which can be the ultimate cause of the formation of extended defects, leading to the irreversible degradation of the devices [12, 13].
- Infrared thermocameras have improved dramatically in the late years, however they do not provide the same spatial resolution as the Raman microprobe [117], instead they present the advantage of easier and faster experimental procedure.

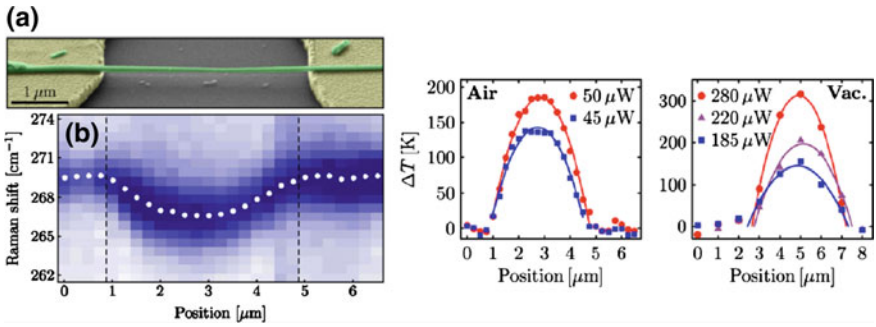

Fig. 3.35 Raman image, obtained by measuring the Raman spectra along a GaAs NW bridged between two metallic pads. The *dashed lines* are the limits of the metallic pads, the TO peak frequency is highlighted by the *white dots*. The laser is the heat source, the temperature is measured from the TO peak frequency shift under the laser exposure. The temperature of the NW depends on the position of the laser beam. The temperature distribution is shown in the *right panels* for different laser powers and different surrounding media, air and vacuum. Thermal conductivity of the NW can be deduced from these data [227]

– It can be used for measuring the thermal conductivity of NWs. Soini et al. [227] measured the thermal conductivity of a GaAs NW by monitoring the Raman map over the NW using the laser beam as the local heat source, Fig. 3.35.

3.5.4 Size Effects. Phonon Confinement

The one phonon Raman bands of crystalline solids present a well defined narrow lorentzian lineshape. When the translational symmetry is disturbed, which is the case of materials with high concentration of structural defects, or nanostructures with dimension enough small to result in a finite correlation length of the optical phonons, the one phonon Raman spectrum is deformed. We will focus here on the application of Raman spectroscopy to the characterization of nanosized semiconductors, which is today a relevant field of research, because of the increasing interest on these semiconductor structures, and the usefulness of Raman spectroscopy for analyzing different physical problems related to the size of the structures.

Due to the Heisenberg's uncertainty principle the momentum selection rule, that specifies that only $q \approx 0$ phonons are allowed for first order Raman scattering, is relaxed in finite size structures, for which the participation in the Raman scattering of phonons out of the zone center becomes allowed. According to this, the phonon uncertainty roughly corresponds to $\Delta q \sim 1/L$, where L is the finite dimension, e.g. the diameter of a spherical nanoparticle, the diameter of a cylindrical nanowire, and the thickness of thin film structures, in the 3D, 2D and 1D confinement configurations respectively. If one looks to the phonon dispersion relation plots, the result

of the participation of phonons out of the zone center in the Raman scattering is the down frequency shift and the asymmetric broadening of the phonon bands according to the phonon dispersion relations, Fig. 3.2. Precisely, the phonon band lineshape can be used to extract relevant information about the nanostructures.

The way to extract such information consists of the adoption of a phenomenological model for the phonon confinement. Early analyses by Richter et al. (RWL) [43] consisted of a model based on the phonon confinement inside the crystallite; for a nanocrystal with a diameter L, the phonon wavefunction is the superposition of single crystal eigenfunctions with q vectors around q_0, being represented as:

$$\Psi(q_0, r) = W(r, L)\varphi(q_0, r) \tag{3.45}$$

$$\varphi(q_0, r) = u(q_0, r)e^{iq_0 \cdot r} \tag{3.46}$$

where

$u(q_0,r)$ has the periodicity of the lattice
W(r,L) is the phonon localization function.

One can then represent the nanocrystal wavefunction as:

$$\Psi(q_0, r) = W(r, L)\varphi(q_0, r) = \Psi'(q_0, r)u(q_0, r) \tag{3.47}$$

Expanding Ψ' in a Fourier series one obtains:

$$\Psi'(q_0, r) = \int C(q)e^{iqr}dq^3 \tag{3.48}$$

The first order Raman spectrum intensity is expressed as:

$$I(\omega) \approx \int \frac{|C(q)|^2}{|\omega - \omega(q)|^2 + \left(\frac{\Gamma_0}{2}\right)^2} d^3q \tag{3.49}$$

$\omega(q)$ is the phonon dispersion function and Γ_0 is the natural width of the crystalline phonon band.

In the Gaussian distribution proposed by RWL [43] the coefficients of the Fourier series are:

$$|C(q)|^2 \propto \exp\left(\frac{-q^2L^2}{4}\right) \tag{3.50}$$

This distribution function works for spherical nanocrystals, it corresponds to the case of 3D phonon confinement. One should also consider the importance of thin films, e.g. quantum wells, which are confined only in one dimension, and nanowires confined in two dimensions. Campbell and Fauchet [44] tried different confinement

functions, also changing the boundary conditions with respect to those assumed by RWL. The functions for slabs, 1D confinement, and NWs, 2D confinements, adopt the following expressions [44]:

$$|C(q)|^2 \propto \exp\left(\frac{-q^2L^2}{16\pi^2}\right)\left|1 - erf\left(\frac{iqL}{\sqrt{32}\pi}\right)\right|^2 \tag{3.51}$$

$$|C(q_1,q_2)|^2 \propto \exp\left(\frac{-q_1^2L_1^2}{16\pi^2}\right)\exp\left(\frac{-q_2^2L_2^2}{16\pi^2}\right)\left|1 - erf\left(\frac{iqL}{\sqrt{32}\pi}\right)\right|^2 \tag{3.52}$$

Because the laser probing volume is much larger than the object size, normally one probes from a few nanostructures to hundreds of them. Electron microscopy observations, both SEM and TEM, often reveal non homogeneous size of the nanostructures population; which, is also reflected in the Raman spectrum, where distributions of sizes are often necessary in order to giving the full description of the Raman spectrum [228–232]. Figure 3.36 shows the calculated Raman parameters for Si nanocrystals and Si NWs as a function of the confinement dimension [233].

One has to take account of other possible contributions to the shape of the phonon spectrum of nanostructred semiconductors in order to give a reliable interpretation of the spectrum. The phonon confinement results in downshift, and broadening of the one-phonon Raman band, see the Raman spectra calculated for Si NWs with different diameters, Fig. 3.37.

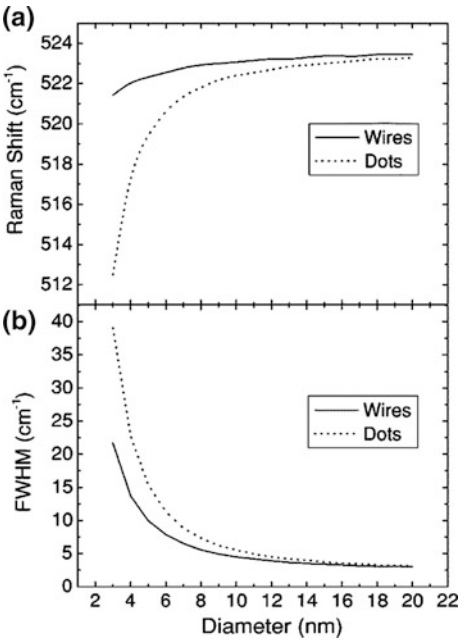

Fig. 3.36 Calculated Raman parameters for Si nanodots and NWs as a function of the diameter [233]

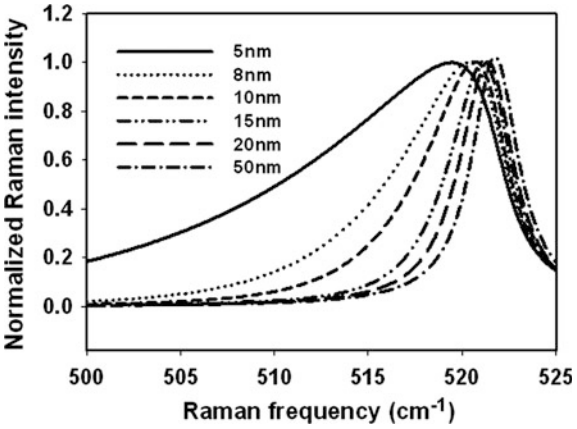

Fig. 3.37 Calculated Raman spectra of Si NWs with different diameters

However, similar effects can be observed in nanostructures with causes different to the phonon confinement. An example of this are the NWs; which the Raman spectrum is frequently different from the one expected from the diameter measured in the electron microscope. There are different causes that can contribute to this observation. The Raman spectrum is frequently acquired on bundles of NWs; therefore, the Raman spectrum is the average over NWs of different diameters [230–232]. Also, thermal effects are very important; in fact, NWs have thermal conductivities well below their bulk counterparts [234, 235]; on the other hand, they are usually in air which slows down the thermal dissipation; therefore, the NWs can undergo a substantial heating under the laser beam excitation [40, 42, 135, 136]. A careful analysis of the laser/NWs interaction reveals that the temperature distribution inside the NW depends on the laser power, the laser wavelength, the dimensions of the NW, both diameter and length, and the off-axis between the laser beam and the NW [135, 136]. All these factors contribute to reach very different temperatures between the NWs probed by the laser beam during the Raman measurement on a bundle of NWs [40, 135, 136]. The only way to analyze the Raman spectrum free of this influence is working with individual NWs [228, 236–248] under excitation conditions preventing the NW overheating [136, 235].

Semiconductor NWs are optical antennas, which permits Raman signals enhancement with respect to the bulk material. Under the laser beam a series of resonances appear depending on the laser wavelength and the NW diameter. These resonances permit to measure the Raman spectrum of single NWs with a high signal to noise ratio. In this sense, μ-R is a powerful tool to study the interaction between NWs and electromagnetic waves; which is a crucial problem in nanooptics.

The μ-R spectroscopy of single NWs allows to achieve the study of different NW based structures; e.g. doped GaN NWs trhough the LOPC modes [236], core/shell CdSe NW heterostructures [237], GaAs/GaP core shell heterostructures [238, 239], local modes in ZnO nanocolumns, and its relation to the luminescence efficiency [240], the electric dipole behaviour of the NWs and diameter dependent

electromagnetic resonance [241–244], strain measurements in bent InP NWs [245], doping in InN NWs [246], stress in Si NWs [247], UV Raman enhancement in single Si NWs [248].

All these examples highlight the great potential of μ-R spectroscopy for the study of NWs. In spite of the very small scattering volume, the choice of optimal experimental conditions permits sufficient signal to noise ratio in order to achieve fine analyses of the experimental data.

References

1. M. Cardona, G. Guntherodt (eds.), *Light Scattering in Solids, Topics in applied Physics*, vols. 8, 50, 51, 54, 66, 68 (Springer, Heildelberg)
2. W. Richter, Resonant raman scattering in semiconductors, in *Springer Tracts in Modern Physics 78*, ed. by G. Hohler (Springer, Berlin, 1976)
3. F.H. Pollak, Analytical Raman spectroscopy. Chem. Anal. Ser. 114, ed. by J. Grasseli, B.J. Bulkin (Wiley, New York, 1991)
4. G. Abstreiter, E. Bauser, A. Fischer, K. Ploog, Appl. Phys. A **16**, 345 (1978)
5. B. Prevot, J. Wagner, Prog. Crystal Growth, Charact. **22**, 245 (1991)
6. P. Bruesch, *Phonons: Theory, and Experiments I.* Springer Series in Solid State Sciences, vol. 34, ed. by M. Cardona, P. Fulde, H.J. Queisser (Springer, Berlin, 1982)
7. I. Zardo, G. Abstreiter, A. Fontcuberta, Raman spectroscopy on semiconductor nanowires, nanowires, ed. by P. Prete. ISBN: 978-953-7619-79-4, (InTech, Rijeka 2010). doi:10.5772/39514
8. R.L. McCreery, Raman spectroscopy for chemical analysis, in *Monographs of Analytical Chemistry and its applications,* vol. 57 , ed. by J.D. Winefordner (Wiley, New York, 2000)
9. R. Ian Lewis, G.M. Edwards (eds.), *Handbook of Raman Spectroscopy: From the Research Laboratory to the Process Line* (Marcel dekker, New York, 2001)
10. C.S.S.R. Kumar (ed.), *Raman Spectroscopy for Nanomaterials Characterization* (Springer, Berlin, 2012)
11. J. Tomm, J. Jimenez, Screening and Packaging Techniques for Highly Reliable Quantum Well High Power Lasers (MacGraw Hill, New York, 2006)
12. A. Martín-Martín, M. Avella, M.P. Iñiguez, J. Jiménez, M. Oudart, J. Nagle, Appl. Phys. Lett. **93**, 171106 (2008)
13. A. Martín-Martín, M. Avella, M.P. Iñiguez, J. Jiménez, M. Oudart, J. Nagle, J. Appl. Phys. **106**, 173105 (2009)
14. J. Jimenez, I. De Wolf, J.P. Landesman, Micro Raman spectroscopy: fundamentals and applications, Chap. 2, in *Optoelectronic properties of Semiconductors and Superlattices*, vol. 17, ed. by J. Jiménez (Taylor and Francis, New York, 2002)
15. G.Turrell, J. Corset (eds.), *Raman Microscopy: Developments, and Applications* (Academic Press, New York, 1996) (references therein)
16. S. Nakashima, H. Hangyo, IEEE J. Quantum Electron. **25**, 965 (1989)
17. XXX
18. Y. Gogotsi, C. Baek, F.K. Kirscht, Semicond. Sci. Technol. **14**, 936 (1999)
19. P.J. Pauzauskie, D. Talaga, K. Seo, P. Yang, F. Lagugné, J. Am. Chem. Soc. **127**, 17146 (2005)
20. P. Martin, A. Torres, J. Jiménez, A. Rodriguez, J. Sangrador, T. Rodríguez, J. Appl. Phys. **96**, 155 (2004)
21. V. Poborchii, T. Tada, T. Kanayama, Appl. Phys. Lett. **94**, 131907 (2009)

22. Y. Xiang, I. Zardo, L.Y. Cao, T. Garma, M. Heib, J.R. Morante, J. Arbiol, M.L. Brongersma, A. Fontcuberta, Nanotechnology **21**, 105703 (2010)
23. M. Becker, H. Scheel, S. Christiansen, H.P. Strunk, J. Appl. Phys. **101**, 063531 (2007)
24. E. Bonera, M. Fanciulli, D.N. Batchelder, J. Appl. Phys. **94**, 2729 (2003)
25. S. Nakashima, J. Phys. C **16**, S25 (2004)
26. C.E. Murray, K.L. Saenger, O. Kalenci, S.M. Polvino, I.C. Noyan, B. Lai, Z. Cai, J. Appl. Phys. **104**, 013530 (2008)
27. H. Chen, Y.K. Li, C.S. Peng, H.F. Liu, Q. Huang, J.M. Zhou, Q.K. Xue, Phys. Rev. B **65**, 233303 (2002)
28. M. Bowden, D.J. Gardiner, Appl. Spectrosc. **51**, 1405 (1997)
29. E. Bonera, Application note from Spectroscopy Products Division, Renishaw SPD/AN/093 Issue 1.0, Nov 2003
30. I. DeWolf, J. Raman Spectrosc. **30**, 87 (1999)
31. I. Wolf, H.E. Maes, S.K. Jones, J. Appl. Phys. **79**, 7148 (1996)
32. T. Tada, V. Poborchii, T. Kanayama, J. Appl. Phys. **107**, 113539 (2010)
33. S. Todoraki, J. Appl. Phys. **60**, 61 (1986)
34. H. Brugger, P.W. Epperlein, S. Beeck, G. Abstreiter, Inst. Phys. Conf. Ser. **106**, 771 (1990)
35. A. Sarua, A. Bullen, M. Haynes, M. Kuball, IEEE Trans. Electron Devices **54**, 1838 (2007)
36. T. Katoda, *Extended Abstracts of the 16th International Conference on Solid State Devices and, Materials*, Kobe, Japan 1984, ed. by D.J. Lockwood, SPIE Proceedings, vol 1336, 13, p. 185, (1990)
37. J. Geurts, Prog. Cryst. Growt Charact. **32**, 185 (1996)
38. W. Hayes, R. Loudon, *Light Scattering in Solids* (Wiley, New York, 1978)
39. D.G. Cahill, W.K. Ford, K.E. Goodson, G.D. Mahan, A. Majumdar, H.J. Maris, R. Merlin, S.R. Phillpot, J. Appl. Phys. **93**, 793 (2003)
40. A. Torres, A. Martín-Martín, O. Martínez, A.C. Prieto, V. Hortelano, J. Jiménez, A. Rodríguez, J. Sangrador, T. Rodríguez, Appl. Phys. Lett. **96**, 011904 (2010)
41. R. Jallilian, G.U. Sumanasekera, H. Chandrasekharan, M.K. Sunkara, Phys. Rev. B **74**, 155421 (2006)
42. H. Scheel, S. Reich, A.C. Ferrari, M. Cantoro, A. Colli, C. Thomsen, Appl. Phys. Lett. **88**, 233114 (2006)
43. W. Richter, Z.P. Wang, L. Ley, Solid State Commun. **39**, 625 (1981)
44. H. Campbell, P.M. Fauchet, Solid State Commun. **58**, 739 (1986)
45. K. Nakamoto, *Infrared and Raman spectra of inorganic and coordination compounds: Part A: theory and applications in inorganic chemistry* (Wiley-Interscience, New York, 1997)
46. H. Harima, J. Phys. Cond. Matter **14**, R967 (2002)
47. R. Cuscó, E. Alarcón, L. Artús, J. Jiménez, M. Callahan, B. Wang, Phys. Rev. B **75**, 165202 (2007)
48. R. Loudon, Adv. Phys. **13**, 423 (1964)
49. V.Y. Davidov, N.S. Averkiev, I.N. Goncharuk, D.K. Nelson, I.P. Nikitina, A.S. Polkovnikov, A.N. Smirnov, M.A. Jaccobson, O.K. Semchinova, J. Appl. Phys. **82**, 5097 (1997)
50. T. Azuhata, M. Ono, K. Torii, T. Sota, S. Chichibu, S. Nakamura, J. Appl. Phys. **88**, 5202 (2000)
51. H. Siegle, G. Kaczmarczyk, L. Filippidis, A.P. Livinkchuk, A. Hoffmann, C. Thomsen, Phys. Rev. B **55**, 700 (1997)
52. E. Alarcón, R. Cuscó, L. Artús, J. Jiménez, B. Wang, M. Callahan, J. Phys. C **20**, 445211 (2008)
53. G. Braunstein, D. Tuschel, S. Chen, S. Tong Lee, J. Appl. Phys. **66**, 3515 (1989)
54. J. Jimenez, E. Martin, C. Prieto, Matter. Lett. **12**, 132 (1991)
55. E. Martin, J. Jimenez, M. Chafai, Solid State Electron. **42**, 2309 (1998)
56. J. Gonzalez-Hernandez, G.H. Azarbayejani, R. Tsu, F.H. Pollak, Appl. Phys. Lett. **47**, 1350 (1985)
57. R. Tsu, SPIE Int. Soc. Opt. Eng. **276**, 78 (1981)

58. J.C. Tsang, P.M. Mooney, F. Dacol, J.O. Chu, J. Appl. Phys. **75**, 8098 (1994)
59. J. Olivares, P. Martin, A. Rodriguez, J. Sangrador, J. Jimenez, T. Rodriguez, Thin Sol. Films **351**, 56 (2000)
60. S. Adachi, J. Appl. Phys. **58**, R1 (1985)
61. J. Groenen, R. Carles, G. Landa, C. Guerret-Piecourt, C. Fontaine, M. Gendry, Phys. Rev. B **58**, 10452 (1998)
62. J. Groenen, S. Christiansen, M. Albrecht, W. Dorsch, H.P. Strunk, H. Wawra, G. Wagner, Appl. Phys. Lett. **71**, 3856 (1997)
63. R. Hattori, K. Yamashita, Y. Ohta, S. Takamiya, S. Mitsui, Spring Meeting of the Japan Society of Applied Physics (1986)
64. J.S.C. Chang, K.W. Carey, J.E. Turner, L.A. Hodge, J. Electron. Mater. **19**, 345 (1990)
65. A. Gomyo, K. Kobayashi, S. Kawata, I. Hino, T. Suzuki, J. Cryst. Growth **77**, 367 (1986)
66. J. Finders, J. Geurts, A. Kohl, M. Weyers, B. Opitz, O. Kayser, P. Balk, J. Cryst. Growth **107**, 151 (1991)
67. M. Maassen, O. Kayser, R. Westphalen, F.E.G. Guimaraes, J. Geurts, J. Finders, P. Balk, J. Electron. Mater. **21**, 257 (1992)
68. P.M. Amirthraj, F.H. Pollak, Appl. Phys. Lett. **45**, 789 (1984)
69. M. Weizmann, N.H. Nickel, I. Sieber, B. Yau, J. Non. Crystal. Sol. **352**, 1259 (2006)
70. M. Avella, A.C. Prieto, J. Jiménez, A. Rodríguez, J. Sangrador, T. Rodríguez, Sol. St. Commun. **136**, 224 (2005)
71. G.P. Schwartz, Proc. SPIE Int. Soc. Opt. Eng. **276**, 72 (1981)
72. L.Z. Liu, X.L. Wu, Z.Y. Zhang, T.H. Li, P.K. Chu, Appl. Phys. Lett. **95**, 093109 (2009)
73. K. Pinardi, S.C. Jain, M. Willander, H.E. Maes, R. Van Overstraeten, J. Appl. Phys. **84**, 2507 (1998)
74. N. Hara, T. Katoda, J. Appl. Phys. **69**, 2112 (1991)
75. R. Schorer, E. Friess, K. Eberl, G. Abstreiter, Phys. Rev. B **44**, 1772 (1991)
76. S. OBrien, D.P. Bour, J.R. Shealy, Appl. Phys. Lett. **53**, 1859 (1988)
77. A. Saher-Helmy, A.C. Bryce, C.N. Ironside, J.S. Aitchison, J.H. Marsh, Appl. Phys. Lett. **74**, 3978 (1999)
78. C.K. Chia, S.J. Chua, S. Tripathy, J.R. Dong, Appl. Phys. Lett. **86**, 051905 (2005)
79. D. Behr, R. Niebuhr, K. Bachem, U. Kaufmann, Appl. Phys. Lett. **70**, 363 (1997)
80. A.S. Barker, A.J. Sievers, Rev. Modern Phys. **47**, 51 (1975)
81. F. Friedrich, M.A. Gluba, N.H. Nickel, Appl. Phys. Lett. **95**, 141903 (2009)
82. A. Kaschner, H. Siegle, G. Kaczmarczyk, M. Strasburg, A. Hoffmann, C. Thomsen, U. Birkle, S. Einfeldt, D. Hommel, Appl. Phys. Lett. **74**, 3281 (1999)
83. M. Ramsteiner, J. Wagner, H. Ennen, M. Maier, Phys. Rev. B **38**, 10669 (1988)
84. M. Cardona, S.C. Shen, S.P. Varma, Phys. Rev. B **23**, 5329 (1981)
85. H. Harima, T. Inoue, S. Nakashima, M. Ishida, M. Taneya, Appl. Phys. Lett. **75**, 1383 (1999)
86. M. Hiller, E.V. Lavrov, J. Weber, Phys. B **401–402**, 197 (2007)
87. A. Mooradian, G.B. Wright, Phys. Rev. Lett. **22**, 999 (1969)
88. A. Mooradian, A.L. McWhorter, Phys. Rev. Lett. **19**, 999 (1967)
89. J. Wagner, K.H. Ko, J. Lagowski, Phys. Rev. B **43**, 5163 (1991)
90. R. Cuscó, J. Ibañez, L. Artús, Phys. Rev. B **57**, 12197 (1998)
91. D. Olego, M. Cardona, Phys. Rev. B **24**, 7217 (1981)
92. S. Nakashima, H. Yugami, A. Fujii, M. Hangyo, H. Yamanaka, J. Appl. Phys. **64**, 3067 (1988)
93. P.D. Wang, M.A. Foad, C.M. Sotomayor-Torres, S. Thoms, M. Watt, R. Cheung, C.D.W. Wilkinson, S.P. Beaumont, J. Appl. Phys. **71**, 3754 (1992)
94. U. Fano, Phys. Rev. **124**, 1866 (1961)
95. N.H.N. Nickel, P. Lengsfeld, I. Sieber, Phys. Rev. B **61**, 15558 (2000)
96. R.M.B. Agaiby, M. Becker, S.B. Thapa, U. Urmoneit, A. Berger, A. Gawlik, G. Sarau, S.H. Christiansen, J. Appl. Phys. **107**, 054312 (2010)
97. A.K. Sood, E. Anastassakis, M. Cardona, Phys. Stat. Sol. b **129**, 505 (1985)
98. I. De Wolf, Semicond. Sci Technol. **11**, 139 (1996)

99. E. Bonera, M. Fanciulli, D.N. Batchelder, Appl. Phys. Lett. **81**, 3377 (2002)
100. R. Ossikovski, Q. Nguyen, G. Picardi, J. Schreiber, J. Appl. Phys. **103**, 093525 (2008)
101. F. Cerdeira, C.J. Buchenauer, F.H. Pollak, M. Cardona, Phys. Rev. B **5**, 580 (1972)
102. D.J. Lockwood, J.M. Baribeau, Phys. Rev. B **45**, 8565 (1992)
103. L.J. Cui, U.D. Venkateswaran, B.A. Weinstein, F.A. Chambers, Semicond. Sci. Technol. **6**, 469 (1991)
104. B. Rockwell, H.R. Chandrasekhar, F.H. Pollak, L.L. Chang, L. Esaki, L. Gualtieri, G.P. Schwartz, in *The Physics of Semiconductors*, ed. by E.M. Anastassakis, J.D. Joannopoulos (World Scientific; Singapore, 1991), p. 929
105. C.G. Walle, R.M. Martin, Phys. Rev. B **35**, 8154 (1987)
106. J. Raptis, E. Liorakapis, E. Anastassakis, Appl. Phys. Lett. **44**, 125 (1984)
107. J. Jiménez, E. Martín, A. Torres, J.P. Landesman, Phys. Rev. B **58**, 10463 (1998)
108. H.W. Lo, A. Compaan, J. Appl. Phys. **51**, 1565 (1980)
109. M. Balkanski, R.F. Wallis, E. Haro, Phys. Rev. B **28**, 1928 (1983)
110. G. Irmer, M. Wenzel, J. Monecke, Phys. Stat. Sol. B **195**, 85 (1996)
111. R. Ostermeier, K. Brunner, G. Abstreiter, W. Weber, IEEE Trans. on Electron. Dev. **39**, 858 (1992)
112. J.P. Landesman, B. Depret, A. Fily, J. Nagle, P. Braun, Appl. Phys. Lett. **72**, 1338 (1998)
113. E. Martin, J.P. Landesman, P. Braun, A. Fily, Microelectron. Reliab. **38**, 1245 (1998)
114. W.C. Tang, H.J. Rosen, P. Buchmann, P. Vettiger, D. Webb, J. Appl. Phys. **68**, 5930 (1990)
115. R.J.T. Simms, J.W. Pomeroy, M.J. Uren, T. Martin, M. Kuball, Appl. Phys. Lett. **93**, 203510 (2008)
116. M. Kuball, J.W. Pomeroy, S. Rajasingam, A. Sarua, M.J. Uren, T. Martin, A. Lell, V. Harle, Phys. Stat. Sol. a **202**, 824 (2005)
117. A. Sarua, A. Bullen, M. Haynes, M. Kuball, IEEE Trans. Electron Dev. **54**, 1838 (2007)
118. M. Delhaye, E. Da Silva. Publication of ISA (Dilor-Jobin Yvon-Spex)
119. A. Rodríguez, T. Rodríguez, A.C. Prieto, J. Jiménez, A. Kling, C. Ballesteros, J. Sangrador, J. Electron. Mater. **39**, 1194 (2010)
120. E. Cchmalzlin, B. Moralejo, M. Rutowska, A. Monreal-Ibero, C. Sandin, N. Tarcea, J. Popp, M.M. Roth, Sensors **14**, 21968 (2014)
121. M. Becker, U. Gosele, A. Hofmann, S. Christiansen, J. Appl. Phys. **106**, 074515 (2009)
122. J.E. Yang, W.H. Park, C.J. Kim, Z.H. Kim, M.H. Jo, Appl. Phs. Lett. **92**, 263111 (2008)
123. J.W. Pomeroy, M. Kuball, D.J. Wallis, A.M. Keir, K.P. Hilton, R.S. Balmer, M.J. Uren, T. Martin, P.J. Heard, Appl. Phys. Lett. **87**, 103508 (2005)
124. C. Jian, I. De Wolf, *Proceedings of 3th Electronics Packaging Technology Conf*erence (EPTC 2000), Singapore (2000)
125. S. Bull, A.V. Andrianov, I. Harrison, M. Dorin, R.B. Kerr, J. Noto, E.C. Larkins, I.E.E.E. Trans, Instr. Meas. **54**, 1079 (2005)
126. S. Webster, D.N. Batchelder, D.A. Smith, Appl. Phys. Lett. **72**, 1478 (1998)
127. J. Grausem, B. Humbert, A. Burneau, J. Oswalt, Appl. Phys. Lett. **70**, 1671 (1997)
128. D. Zeisel, B. Dutoit, V. Deckert, T. Roth, R. Zenobi, Anal. Chem. **69**, 749 (1997)
129. S. Webster, D.A. Smith, D.N. Batchelder, Spectrosc. Eur. **10**, 22 (1998)
130. A. Tarun, N. Hayazawa, M. Motohasi, S. Kawata, Rev. Sci. Instr. **79**, 013706 (2008)
131. A. Tarun, N. Hayazawa, S. Kawata, Anal. Bioanal. Chem. **394**, 1775 (2009)
132. S. Berweger, C.C. Neacsu, Y. Mao, H. Zhou, S.S. Wong, M.B. Raschke, Nature Nanotechnol. **4**, 496 (2009)
133. J. Anaya, J. Jimenez, A. Rodriguez, T. Rodríguez, MRS Symp. Proc. **1627**, L09–L38 (2014)
134. I. Zardo, S. Conesa-Boj, F. Peiró, J.R. Morante, J. Arbiol, E. Uccelli, G. Abstreiter, A. Fontcuberta, Phys. Rev. B **80**, 245324 (2009)
135. J. Anaya, A. Torres, A. Martín-Martín, J. Souto, J. Jiménez, A. Rodríguez, T. Rodríguez, Appl. Phys. A **113**, 167 (2013)
136. J. Anaya, A. Torres, A.C. Prieto, V. Hortelano, J. Jiménez, A. Rodríguez, T. Rodríguez, Appl. Phys. A **114**, 1321 (2014)
137. M. Yoshikawa, M. Murakami, Appl. Spectrosc. **60**, 479 (2006)

138. N. Kazemi-Zanjani, E. Kergrene, L. Liu, T.K. Sham, F. Lavigné-Labarthet, Sensors **13**, 12744 (2013)
139. A. Hartschush, M.R. Beversluis, A. Bouhelier, L. Novotny, Phil. Trans. R. Soc. Lond. A **362**, 807 (2004)
140. D.E. Apsnes, A.A. Studna, Phys. Rev. B **27**, 985 (1983)
141. A.V. Kolobov, J. Appl. Phys. **87**, 2926 (2000)
142. A.C. Prieto, A. Torres, J. Jiménez, A. Rodríguez, J. Sangrador, T. Rodríguez, J. Mater. Sci.: Mater. Electron. **19**, 155 (2007)
143. J. Jimenez, E. Martin, J. Garcia, J. Piqueras Appl. Phys. A **55**, 566 (1992)
144. J. Jimenez, E. Martin, J. Garcia, J. Piqueras, Mater. Sci. Eng. B **20**, 144 (1993)
145. J.W. Tomm, V. Strelchuk, A. Gerhardt, U. Zeimer, H. Kissel, J. Jiménez, J. Appl. Phys. **95**, 1122 (2004)
146. J. Kasai, Y. Katayama, Rev. Sci. Instrum. **66**, 3738 (1995)
147. N. Domènech-Amador, R. Cuscó, J. Jiménez, L. Artús, Appl. Phys. Express **7**, 021001 (2014)
148. Y. Kaenel, J. Stiegler, J. Michler, E. Blank, J. Appl. Phys. **81**, 1726 (1997)
149. M. Nishitani-Gano, T. Ando, K. Yamamoto, K. Watanabe, P.A. Dennig, Y. Sato, M. Sekita, Appl. Phys. Lett. **70**, 1530 (1997)
150. Z. Li, R.C. Picu, J. Appl. Phys. **108**, 033522 (2010)
151. X. Pan, C. Wee Tan, J. Miao, J. Kasim, Z. Shen, E. Xie, Thin Sol. Films **517**, 4905 (2009)
152. G.H. Loechelt, N.G. Cave, J. Menéndez, J. Appl. Phys. **86**, 6164 (1999)
153. E. Anastassakis, A. Pinczuk, A. Burstein, F.H. Pollak, M. Cardona, Solid St. Commun. **8**, 133 (1970)
154. E. Anastassakis, A. Cantarero, M. Cardona, Phys. Rev. B **41**, 7529 (1990)
155. S.C. Jain, M. Willander, H.E. Maes, Semicond. Sci. Technol. **11**, 641 (1996)
156. S. Narayanan, S.R. Kalidindi, L.S. Schadler, J. Appl. Phys. **82**, 2595 (1997)
157. S. Hu, J. Appl. Phys. **70**, R53 (1991)
158. B.B. Varga, Phys. Rev. **137**, 1896 (1965)
159. H. Yugami, S. Nakashima, A. Mitsuisshi, J. Appl. Phys. **61**, 354 (1987)
160. M.V. Klein, B.N. Ganguly, P.J. Colwell, Phys. Rev. B **6**, 2380 (1972)
161. H. Harima, S. Nakashima, T. Uemura, J. Appl. Phys. **78**, 1996 (1995)
162. S. Nakashima, H. Harima, J. Appl. Phys. **95**, 3541 (2004)
163. M. Chafai, A. Jaouhari, A. Torres, R. Antón, E. Martín, J. Jiménez, W.C. Mitchel, J. Appl. Phys. **90**, 5211 (2001)
164. J.C. Burton, L. Sun, M. Pophristic, S.J. Lukacs, F.J. Long, Z.C. Feng, L.T. Ferguson, J. Appl. Phys. **84**, 6268 (1998)
165. G. Irmer, V.V. Toporov, B.H. Bairamov, J. Monecke, Phys. Status Silidi b **119**, 595 (1983)
166. G. Irmer, W. Siegel, G. Kühnel, J. Monecke, F.M. Yauoka, B.H. Bairamov, V. Toporov, Semicond. Sci. Technol. **6**, 1072 (1991)
167. M. Kuball, J.W. Pomeroy, S. Rajasingam, A. Sarua, M.J. Uren, T. Martin, A. Lell, V. Harle, Surf. Interface Anal. **31**, 787 (2001)
168. T. Kozawa, T. Cachi, H. Kano, Y. Taga, H. Hashimoto, J. Appl. Phys. **75**, 1098 (1994)
169. H. Harima, H. Sakashita, S. Nakashima, Mater. Sci. Forum **264–8**, 1363 (1998)
170. H. Harima, H. Sakashita, T. Inoue, S. Nakashima, J. Cryst. Growth **189/190**, 672 (1998)
171. F. Demangeot, J. Frandon, M.A. Renucci, M.A. Ggrandjean, B.B. Beaumont, J. Massies, P. Gibart, Solid St. Commun. **106**, 491 (1995)
172. P. Perlin, J. Camassel, W. Knap, T. Taliercio, J. Chervin, T. Suski, I. Grzegory, S. Porowski, Appl. Phys. Lett. **67**, 2524 (1995)
173. R. Cuscó, J. Ibañez, E. Alarcón, L. Artús, Phys. Rev. B **79**, 155210 (2009)
174. J. Kraus, D. Hommel, Semicond. Sci. Technol. **10**, 785 (1995)
175. O. Pages, M.A. Renucci, O. Briot, R. Aulombard, J. Appl. Phys. **80**, 1128 (1996)
176. A. Steele, R.A. Lewis, M. Henini, O.M. Lemine, D. Fan, Y.I. Mazur, V.G. Dorogan, P.C. Grant, S.Q. Yu, G.J. Salamo, Opt. Express **22**, 11680 (2014)
177. K. Wan, J.F. Young, Phys. Rev. B **41**, 10772 (1991)

178. G. Abstreiter, R. Trommer, M. Cardona, A. Pinczuk, Solid State Commun. **30**, 703 (1979)
179. M. Ramsteiner, J. Wagner, P. Hieisinger, K. Köhler, U. Rössler, J. Appl. Phys. **73**, 5023 (1993)
180. H. Shen, F.H. Pollak, R.N. Sacks, Appl. Phys. Lett. **47**, 891 (1985)
181. K. Kuriyama, K. Sakai, M. Okada, Phys. Rev. B **53**, 987 (1996)
182. J.E. Maslar, W.S. Hurst, C.A. Wang, Appl. Spectrosc. **61**, 1093 (2007)
183. J.E. Maslar, W.S. Hurst, C.A. Wang, J. Appl. Phys. **104**, 103521 (2008)
184. J. Ibañez, R. Cuscó, L. Artús, Phys. Stat. Sol. b **223**, 715 (2001)
185. K. Sihna, A. Mascarenhas, S.R. Kurtz, J.M. Olson, J. Appl. Phys. **78**, 2515 (1995)
186. R. Cuscó, L. Artús, S. Hernández, J. Ibañez, M. Hopkinson, Phys. Rev. B **65**, 035210 (2001)
187. S. Nakashima, H. Harima, N. Ohtami, M. Katsuno, J. Appl. Phys. **95**, 3547 (2004)
188. A.M. Ardila, O. Martínez, M. Avella, J. Jiménez, B. Gérard, J. Napierala, E. Gil-Lafon, Appl. Phys. Lett. **79**, 1270 (2001)
189. P. Martin, J. Jimenez, C. Frigeri, L.F. Sanz, J. Weyher, J. Mater. Res. **14**, 1732 (1999)
190. P.S. Doval, H.D. Bist, S.K. Mehta, R.K. Jain, J. Appl. Phys. **77**, 3934 (1995)
191. H. Harima, T. Hosoda, S. Nakashima, Mater. Sci. Forum **338–342**, 603 (2000)
192. M. Herms, G. Irmer, J. Monecke, O. Oettel, J. Appl. Phys. **71**, 432 (1992)
193. A. Mlayah, R. Carles, E. Bedel, A. Muñoz-Yagüe, J. Appl. Phys. **74**, 1072 (1993)
194. R. Fukasawa, S. Perkowitz, Phys. Rev. B **50**, 14119 (1994)
195. V. Vorlicek, I. Gregora, W. Kausche, J. Menendez, M. Cardona, Phys. Rev. B **42**, 5802 (1990)
196. H. Lee, M.V. Klein, J. Appl. Phys. **81**, 1899 (1984)
197. R. Cuscó, E. Alarcón-Lladó, L. Artús, W.S. Hurst, J.E. Maslar, Phys. Rev. B **81**, 195212 (2010)
198. N.D. Mermin, Phys. Rev. B **1**, 2362 (1970)
199. R. Tsu, Phys. Rev. **164**, 380 (1967)
200. W. Richter, U. Nowak, H. Jurgensen, U. Rössler, Solid St. Commun. **67**, 199 (1988)
201. U. Nowak, W. Richter, G. Sachs, Phys. Stat. Sol. b **108**, 131 (1981)
202. L. Artús, R. Cuscó, J. Ibañez, N. Blanco, G. González-Díaz, Phys. Rev. B **60**, 5456 (1999)
203. M. Herms, G. Irmer, J. Monecke, O. Oettel, J. Appl. Phys. **71**, 432 (1992)
204. C.H. Casey, E. Buelhler, Appl. Phys. Lett. **30**, 247 (1977)
205. T. Nakamura, T. Katoda, J. Appl. Phys. **55**, 3064 (1984)
206. B. Zhang, S.H. Wei, A. Zunger, Phys. Rev. B **63**, 075205 (2001)
207. W. Goetz, N.M. Johnson, D.P. Bour, H. Amano, I. Akasaki, Appl. Phys. Lett. **67**, 2666 (1995)
208. M. Chandrasekhar, H.R. Chandrasekhar, M. Grimsditch, M. Cardona, Phys. Rev. B **22**, 4825 (1980)
209. M. Hilse, M. Ramsteiner, S. Breuer, L. Geelhaar, H. Riechert, Appl. Phys. Lett. **96**, 193104 (2010)
210. M. Fukuda, *Reliability and Degradation of Semiconductor Lasers and LEDs* (Artech House, Boston, 1991)
211. O. Ueda, *Relaibility and Degradation of III-V Optical Devices* (Artech House, Boston, 1996)
212. S. Rajasingen, J.W. Pomeroy, M. Kuball, M.J. Uren, T. Martin, D.J. Herbert, K.P. Hilton, R. S. Balmer, IEEE Electron. Dev. **25**, 456 (2004)
213. D.D. Griffin, Appl. Optics **7**, 1749 (1968)
214. C. Canali, F. Chiussi, G. Donzelli, F. Magistrali, E. Zanoni, Microelectron. Reliab. **29**, 117 (1989)
215. K. Decker, S. Ko, D. Rosato, J. High Density Interconnect. **3**, 26 (2000)
216. J.D. MacDonald, G.C. Albright, Electron. Cooling **3**, 26 (1997)
217. J.W. Tomm, M. Ziegler, M. Hempel, T. Elsaesser, Laser Photonics Rev. **5**, 422 (2011)
218. C.E. Stephens, F.N. Sinnadurai, J. Phys. E: Scientific. Instrum. **7**, 641 (1974)
219. A.M. Ardila, O. Martínez, M. Avella, J. Jiménez, B. Gérard, J. Napierala, E. Gil-Lafon, J. Appl. Phys. **91**, 5045 (2002)

220. A. Link, K. Bitzer, W. Limmer, R. Sauer, C. Kirchner, V. Schwegler, M. Kamp, D.G. Ebling, K.W. Benz, J. Appl. Phys. **86**, 6256 (1999)
221. P. Verma, S.C. Abbi, K.P. Jain, Phys. Rev. B **51**, 16660 (1995)
222. T. Sundius, J. Raman Spectr. **1**, 471 (1973)
223. B.P. Asthana, W. Kiefer, Appl. Spectr. **37**, 334 (1983)
224. M. Kuball, J.W. Pomeroy, S. Rajasingam, A. Sarua, M.J. Uren, T. Martin, A. Lell, V. Harle, Phys. Stat. Solidi a **202**, 824 (2005)
225. R.J. Simms, J.W. Pomeroy, M.J. Uren, T. Martin, M. Kuball, IEEE Trans. Electron Dev. **55**, 478 (2008)
226. M. Kuball, J.M. Hayes, M.J. Uren, T. Martin, J.C.H. Birbeck, R.S. Balmer, B.T. Hughes, I.E. E.E. Electron, Dev. Lett. **23**, 7 (2002)
227. M. Soini, I. Zardo, E. Uccelli, S. Funk, G. Koblmüller, A. Fontcuberta, G. Abstreiter, Appl. Phys. Lett. **97**, 263107 (2010)
228. B. Li, D. Yu, S.L. Zhang, Phys. Rev. B **59**, 1645 (1999)
229. S. Battacharyya, S. Sauni, Appl. Phys. Lett. **84**, 1564 (2004)
230. K.W. Adu, H.R. Gutiérrez, U.J. Kim, P.C. Eklund, Phys. Rev. B **73**, 155333 (2006)
231. K.W. Adu, Q. Xiong, H.R. Gutiérrez, G. Chen, P.C. Eklund, Appl. Phys. A **59**, 1645 (2006)
232. Q. Lu, K.W. Adu, H.R. Gutiérrez, G. Chen, K.K. Lew, P. Nimmatoori, X. Zhang, E.C. Dickey, J.M. Redwing, P.C. Eklund, J. Chem. Phys. C **112**, 3209 (2008)
233. S. Piscanec, M. Cantoro, A.C. Ferrari, J.A. Zapien, Y. Lifshitz, S.T. Lee, S. Hoffmann, J. Roberston, Phys. Rev. B **68**, 241312R (2003)
234. D. Li, Y. Wu, P. Kim, L. Shi, P. Yang, A. Majumdar, Appl. Phys. Lett. **83**, 2934 (2003)
235. J. Anaya, T. Rodríguez, J. Jiménez, Sci. Adv. Mater. **6**, 1 (2014)
236. K. Jeganathan, R.K. Debnath, R. Meijers, T. Stoica, R. Calarco, D. Grutzmacher, H. Luth, J. Appl. Phys. **105**, 123707 (2009)
237. J.H. Kim, H. Kim, H. Rho, Y.J. Choi, J.G. Park, J. Phys. D Appl. Phys. **47**, 135104 (2014)
238. M. Montazeri, M. Fickenscher, L.M. Smith, H.E. Jackson, J. Yarrison-Rice, J.H. Kang, Q. Gao, H.H. Tan, C. Jagadish, Y. Guo, J. Zou, M.E. Pistol, G.E. Pryor, Nano Lett. **10**, 880 (2010)
239. Q. Gao, H.H. Tan, H.E. Jackson, L.M. Smith, J. Yarrison-Rice, J. Zou, C. Jagadish, Semicon. Sci. Technol. **26**, 014035 (2011)
240. D.N. Montenegro, V. Hortelano, O. Martínez, M.C. Martínez-Tomas, V. Sallet, V. Muñoz-Sanjosé, J. Jiménez, J. Phys. D Appl. Phys. **46**, 235302 (2013)
241. L. Cao, L. Laim, P.D. Valenzuela, B. Nabet, J.E. Spanier, J. Raman Spectrosc. **38**, 697 (2007)
242. F.J. Lopez, J.K. Hyun, U. Givan, I.S. Kim, A.L. Holsteen, L.J. Lauhon, Nano Lett. **12**, 2266 (2012)
243. L. Cao, B. Nabet, J.E. Spencer, Phys. Rev. Lett. **96**, 157402 (2006)
244. J. Frechette, C. Carraro, Phys. Rev. B **74**, 161404R (2006)
245. J. Chen, G. Conache, M.E. Pistol, S.M. Gray, M.T. Borgstrom, H. Xu, L. Samuelson, U. Hakanson, Nano Lett. **10**, 1280 (2010)
246. E.O. Chafer-Nolte, M.E. Pistol, T. Gotschke, F.A. Ambacher, E. Sutter, P. Sutter, D. Grutzmacher, R. Calarco, Nanotechnology **21**, 315702 (2010)
247. M.J. Süess, R.A. Minamisawa, R. Geiger, K.K. Bourdelle, H. Sigg, R. Spolenak, Nano Lett. **14**, 1249 (2014)
248. V. Poborschii, T. Tada, Y. Morita, T. Kanayama, P.I. Geshev, Phys. Rev. B **83**, 153412 (2011)
249. W. Duncan, J. Vac. Sci. Tech. A **14**, 1914 (1995)
250. D.T. Hon, W.L. Faust, Appl. Phys. **1**, 241 (1973)

Chapter 4
Photoluminescence (PL) Techniques

Abstract Introduces the *photoluminescence* (PL) technique. This includes the layout of homebuilt PL setups and their methodology, including relevant parameters or the "information depth." Most importantly, the diversity of the observed PL lines and bands is described systematically and their microscopic nature is addressed. Steady-state and transient PL as well as related techniques, such as PL-excitation spectroscopy, are explained, and the results that are to be expected are discussed. This also includes PL mapping and PL imaging approaches. Case studies and guidelines on how to analyze complex structures complete the chapter.

4.1 Introduction

At first glance, the PL spectrum from a given semiconductor material or structure can be expected to represent the spectrum of spontaneous interband emission. This spectrum is created by the recombination of non-equilibrium carriers, which are generated by the absorption of photons, which are typically provided by an excitation laser source. The optical excitation led to the naming 'PL'.

According to Chap. 1, see (1.73), virtually a one-to-one correspondence to the absorption spectrum is expected. In a real-world semiconductor, however, this straight link is disturbed by many-particle effects and extrinsic effects such as the presence of surfaces, defects, disorder, carrier localization, etc. In practice, a PL spectrum includes mostly information that complements what one can obtain from absorption measurements. Therefore, PL and absorption spectroscopy can be considered as completely independent analytical tools. The spectral range, in which both types of measurements provide important and complementary information, is often the same, namely the range around the fundamental energy gap (E_g). Therefore, typical PL spectra cover the spectral range around E_g, this type of PL is often called *edge emission*. This term points to the interband absorption edge, a major resonance of any semiconductor's interaction with electromagnetic radiation. Sometimes, PL can be detected at higher or lower photon energies than E_g as well. These types of PL will be addressed later in this chapter.

J. Jimenez and J.W. Tomm, *Spectroscopic Analysis of Optoelectronic Semiconductors*, Springer Series in Optical Sciences 202,
DOI 10.1007/978-3-319-42349-4_4

While sensitive experimental setups allow for monitoring PL spectra from almost all semiconductor materials, in direct semiconductors PL spectroscopy is expected to provide richest information. Thus, we will focus our following considerations to direct materials. These are mainly the III-V compounds such as GaAs, InP, GaN, and II-VI materials such as ZnS, CdTe, ZnO. But there are many other materials, among them ternary and quarternary mixed crystal systems consisting of the binaries mentioned above, such as $Ga_{1-x}Al_xAs$ or $In_xGa_yAl_{1-x-y}P$. Since Si is the most important semiconductor overall, we will address the PL-spectroscopy of this indirect material as well.

These materials might be available as bulk crystals, but nowadays typical objects of PL investigations are rather structures made of epitaxial films involving layers consisting of different materials (heterostructures), or nanostructures such as quantum wells (QW), quantum wires, and quantum dots (QD).

According to the E_g-values of these materials, the edge PL range covers the whole spectral region from the MIR (e.g. InSb) to the UV (e.g. GaN, ZnO); see Fig. 1.3.

A PL spectrum from a sample with three QWs of different thicknesses is shown in Fig. 4.1 [1]. These QWs, which are separated by 36 nm wide barriers, are successively grown. The QW thicknesses can be seen in Fig. 4.1, already assigned to the corresponding PL line. We will start our survey with formal issues, namely by addressing the denotations of abscissa and ordinate scales.

The abscissa represents the photon energy in eV. This type of display allows pointing to energies or energetic distances most easily and thus finding links to the energetic bandstructure of the material. Alternatively, the authors could have also chosen to give the wavelength in nm as an abscissa unit. This represents the standard spectroscopic unit when dealing with the visible spectral range. A less common unit for the abscissa is wavenumbers (cm^{-1}), which represents an alternative energy scale, that is most suitable for giving small energetic distances (1.2395 eV corresponds to 10,000 cm^{-1} or 1000 nm), in particular in the infrared. The reader might recall from Chap. 3 that cm^{-1} is the standard unit for specifying Raman shifts that represent small energetic distances as well.

The ordinate in Fig. 4.1 is given in 'arbitrary units' (a.u.). In most cases, experimentalists choose to state the detector signal as it was obtained in the

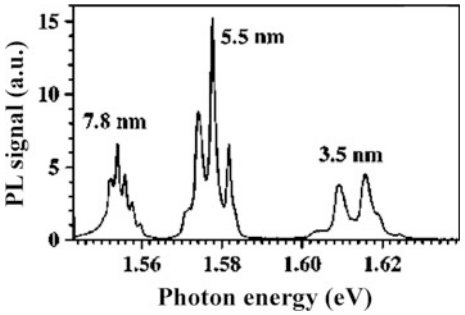

Fig. 4.1 PL spectrum from a structure containing 3 QWs with thicknesses of 3.5, 5.5, and 7.8 nm. The QWs are separated by 36-nm $Al_{0.17}Ga_{0.83}As$ barriers leading to only a weak coupling between them. The measurement was performed at T = 5 K, the excitation photon energy was 1.74 eV [1]

measurement here. Such a 'practical' approach might be valid as long as small spectral ranges are considered, within which the setup (including lenses, mirrors, windows, gratings, detectors, …) shows rather smooth spectral characteristics.

The spatial resolution in the PL experiment shown in Fig. 4.1 is determined by the particular setup and the chosen experimental conditions, but, to a great extent by the particular sample itself. Since the presented spectrum stems from three QWs arranged on top of each other, it is more or less obvious, from what locations the emission lines originate: each QW contributes to one PL line that is split further into 4–6 peaks [2][1]. In this particular case, the spectral positions of the 3 lines allow an unambiguous assignment of the 'vertical' local origin to the resulting PL line. In most cases, however, such assignments are more complicated and often the application of further techniques is required to support the assignments. The lateral spatial resolution is, of course, determined by the excitation spot diameter that is described by its full width at half maximum (FWHM). But there are additional parameters. Their impact to the lateral spatial resolution will be addressed in Sect. 4.2.

4.2 Probed Sample Region

4.2.1 Vertical Spatial Resolution—The 'Information Depth'

Finding an answer to the question in which part of the sample the PL emission is generated becomes substantially more difficult if bulk material is considered as in case of Fig. 4.1. This leads us to the often raised question about the *information depth* of a particular PL experiment. When trying to give an answer by using a rule of thumb, one could estimate the PL information depth (d_{PL}) by

$$d_{PL} \leq \frac{1}{\alpha_{exc}} + L_D, \tag{4.1}$$

In which α_{exc} is the absorption coefficient of the excitation light and L_D the vertical[2] ambipolar diffusion length of the photo-excited non-equilibrium carrier pairs.

A more precise approach requires the solution of rate equations in order to figure out where the non-equilibrium carriers that generate the PL signal, become created.

[1]The authors explain the split of each of the 3 PL lines into 4–6 peaks to be caused by monolayer fluctuations of the QW thicknesses. Consequently, the energetic distance between two neighboring peaks represents the shift caused by a thickness variation in one single monolayer of atoms. Therefore, the figure illustrates that a given thickness fluctuation (here by one monolayer) causes a larger split for a thinner, and a smaller one for a thicker QWs PL spectrum.

[2]The term 'vertical' ambipolar diffusion length (i.e. along the z-axis) is used here in order to distinguish between diffusion along the growth axis and lateral in-plane diffusion. For bulk material this distinction is not required.

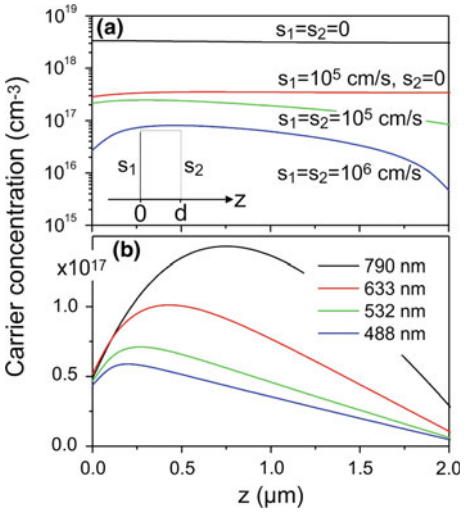

Fig. 4.2 Carrier concentration profiles across a 2 μm thick GaAs layer as calculated by the described rate-equation approach. The parameters used in (**a**) are: excitation wavelength 633 nm; $\alpha_{exc} = 40{,}000\ cm^{-1}$; $L_D = 4\ \mu m$; $\tau = 20$ ns; $D = 8\ cm^2/s$; $I_0 = 1\ W/cm^2$. The parameters used in (**b**) are: $s_1 = s_2 = 5\times10^5$ cm/s; $L_D = 4\ \mu m$; $\tau = 20$ ns; $D = 8\ cm^2/s$; $I_0 = 1\ W/cm^2$. The *inset* on *top* shows the geometry of the layer which is considered

As a simple one-dimensional case, we consider a homogeneous layer with the thickness d; see inset in Fig. 4.2a. Notice that the treatment of this case will include the case of pure bulk material, as well. In the steady-state case, the non-equilibrium carrier concentration at a position along the growth axis $\delta n(z)$ is determined by

$$0 = g(z) \quad - \frac{\delta n(z)}{\tau} \quad + D\frac{\partial^2 \delta n(z)}{\partial z^2} + \mu E \frac{\partial \delta n(z)}{\partial z}, \tag{4.2}$$

where the generation rate $g(z)$ is determined by the absorption of the excitation light according to

$$g(z) \ = \frac{I_0}{\hbar\omega_{exc}} \eta_{exc} \cdot \alpha_{exc} \cdot (1 - R)\ e^{-\alpha_{exc} \cdot z}. \tag{4.3}$$

The terms following the generation term $g(z)$ in (4.2) describe recombination, diffusion, and drift of non- equilibrium carriers (from t left to right). The parameters describing these processes are the non-equilibrium recombination lifetime τ, the ambipolar diffusion constant D, and the mobility μ. E stands for electric fields, which will not be considered in the following; i.e. $E = 0$.

The parameters in (4.3), I_0, $\hbar\omega_{exc}$, R, and η_{exc} are the excitation density (typically given in W/cm^2), the excitation photon energy, the reflectance of the excited semiconductor surface, and the efficiency of carrier pair generation by photons, respectively. The latter is typically set to unity. Diffusion and carrier lifetime are linked by $L_D^2 = D\tau$.

The fact that surfaces are locations of enhanced recombination is taken into account by appropriate boundary conditions at front and rear surfaces, located at $z = 0$ and $z = d$, respectively; see inset in Fig. 4.2a:

$$-D\frac{\partial \delta n}{\partial z}|_{z=0} = -s_1 \delta n(0) \tag{4.4}$$

$$-D\frac{\partial \delta n}{\partial z}|_{z=d} = s_2 \delta n(d) \tag{4.5}$$

The proportionality factors s_1 and s_2 are phenomenological measures for the contribution of the surface to the recombination. They have the dimension of velocities. Therefore, they are referred to as *surface recombination velocities*. The analytical solution of this boundary value problem has been derived and discussed by Duggan and Scott [3]. Figure 4.2 shows carrier distributions in a 2 µm thick GaAs layer as obtained with the solution of (4.2–4.5). The parameters are given in the caption and have been chosen accordingly. When it is assumed that the PL signal magnitude (I_{PL}) depends linearly on δn, the area under the curves is a measure for the expected I_{PL}-values, whereas the shape of the curves reports on the origins of the PL contributions to the total I_{PL}. Figure 4.2a illustrates the massive impact of the surface recombination to the carrier distribution within the sample and thus, to the PL. Notice that typical samples, such as epitaxial layers, have only one 'free' surface, whereas the other one is represented by an interface to another layer or a substrate. In this case the term 'surface recombination' should be replaced by *interface recombination*. However, the need to consider the recombination at this boundary still remains and the equations that were given describe this case, as well.

Figure 4.2b illustrates the effect of the excitation wavelength. For this purpose, we selected a number of typical laser wavelengths. As expected, a shorter excitation wavelength reduces the 'information depth,' but I_{PL} likewise. Since we used a constant power I_0 for the calculation, this is in part due to the lower number of exciting photons (factor of $\sim$1.6 when changing from 790 to 488 nm), but to a greater extent (factor $\sim$2) the I_{PL}-reduction is caused by the fact that for 488-nm excitation, the carrier cloud is generated closer to the front surface. Again we see the determinant effect of the surface recombination.

To anyone dealing with PL spectroscopy, we expressively recommend inserting the parameters of their actual experiment into these equations. This helps to get a feel for the method and the potential outcome of the experiments.

When we bear in mind this knowledge about the carrier profiles across the sample, we are able to give a more profound answer to the question about d_{PL}, at least more exact than the estimate given in (4.1) at the beginning of this section. Assuming linearity for $I_{PL}(z) \propto \delta n(z)$, the carrier distribution will provide us directly the local contribution of carrier pairs along the z-axis to the PL signal.

Nevertheless, these results just do not yet provide a complete description of the situation. Several effects are still neglected:

- Equation (4.2) is written for non-equilibrium electrons δn, assuming a 'symmetric' generation behavior of the non-equilibrium holes δp. Therefore, we used an ambipolar diffusion constant D and an ambipolar diffusion length L_D in (4.1) and (4.2). Although above-bandgap absorption is indeed expected to result in

bipolar generation ($\delta n = \delta p$), extrinsic recombination and 'trapping'[3] might drastically alter this on a ps timescale, [4, 5] i.e. might be substantially faster than any of the processes ('bipolar' recombination, diffusion) included in the rate equations above.

- As mentioned before, when pointing to (4.2), electric fields are not included into our considerations. Such fields might even cause electrons and holes to become spatially separated, making the assumption of ambipolar diffusion less legitimate. The same holds for near-to-surface modifications of the band characteristics such as band bending. Bended bands might result either in carrier accumulation or depletion. Even an inversion of the conductivity type could take place. Obviously, these effects have an impact on the generated carrier cloud and thus modify d_{PL}, as well.
- *Reabsorption* of photons represents an important issue that might modify PL signals in shape and magnitude. Obviously, PL signal damping is determined by two parameters, namely the absorption coefficient at the photon energy of the PL line considered, and d_{PL} of the actual PL line.
  As mentioned above, the major PL contributions from semiconductors are expected to be in the spectral region around E_g. In this range, the absorption coefficient $\alpha(\hbar\omega)$ undergoes its strongest changes, as well. Therefore, differently shaped PL lines are affected by reabsorption to a different extend. In other words: reabsorption reshapes PL spectra, and since $\alpha(\hbar\omega)$ grows with increasing $\hbar\omega$, reabsorption tends to be most effective for the PL lines at the highest photon energies. We will come back to this, when we address the different mechanisms contributing to the PL and CL in chapters 4.4 and 5, respectively.

The reason why we do not involve these effects quantitatively into the preceding calculations, is not the lack of knowledge how to describe them, but rather the lack of knowledge about the actual parameters required for a proper description of these extrinsic effects. Therefore, in many studies they are simply ignored or their consequences are sometimes even assigned to other mechanisms. For instance, since it is difficult separate the effects of band bending from those caused by surface recombination, experimentally determined *s*-values are sometimes interfered with band-bending effects. Nevertheless, one should always be aware of these factors that potentially, may not necessarily, have substantial impact on shape and magnitude of PL spectra. The same holds for CL and will be addressed in Sect. 5.4.

The conclusion from the preceding paragraphs should be the following: *In general, PL is a qualitative method.* If only one parameter is varied only, even quantitative estimates may become possible.

[3]The term 'trapping' is used to describe a special type of defect-related carrier kinetics. It involves the fast capture of free charge carrier into defect centers, where they remain a comparably long time. If subsequent recombination takes place, this trap is also called 'recombination center'. Alternatively, the carrier could also be re-emitted into its original band, e.g. by thermal activation.

Information depth in structures
So far the discussion in Sect. 4.2 was devoted to homogeneous material. Most samples, however, are multiple-layered epitaxial structures consisting of various materials including, e.g., graded[4] layers, QWs, and QDs. When determining the spatial distribution of the sources of a PL-signal, one should find answers to the questions listed below by following the succession of effects involved in the PL signal generation; starting with the absorption of the excitation laser light and ending with the emergence of the photons from the semiconductor surface:

- Where do the exciting photons get absorbed and where carrier pairs are generated?
- Are the created carrier pairs free to move (i.e. diffuse) or are they localized?
- If they are free; are they likely to diffuse together (ambipolar diffusion) or do they rather tend to become spatially separated, as known, e.g., from *pn*-junctions?
- Are they (or one type of them) likely to be trapped into potential valleys formed by defects, QWs, or QDs?
- Where will they finally recombine, i.e. become converted to photons that create the PL signal, and which layers and interfaces do the photons have to pass before escaping the semiconductor material? Will there be re-absorption, which again might re-shape the PL spectrum?

Such considerations have to be made anew for each structure. This brings out, why a straight answer to the question about d_{PL}, as given tentatively by (4.1), will be always incomplete.

4.2.2 Lateral Spatial Resolution

As long as the FWHM of the excitation laser spot is large enough compared to L_D, the lateral spatial resolution is determined by the excitation spot. This holds in most PL setups. An improved spatial resolution is also reached, if not the entire excitation spot is imaged to the detector. The related details will be addressed in the next section, when we discuss the *imaging optics* of the PL spectrometer. Furthermore, spatial electron-hole separation and ultra-long drifts may lead to effective enhancements of the spot size, including the generation of distinct spatial PL pattern [6]. Consequences of this will be addressed in Sect. 4.7.3.

Notice that the relation between laser spot size and L_D changes, if the PL experiment is conducted using a microscope. This approach is called *micro-PL*. If a near-field scanning optical microscope (NSOM, sometimes also SNOM) is used for

[4]The term 'graded' layer stands for a 'graded-gap' structure in this context, i.e. a structure where E_g increases or decreases, e.g., along the z-axis. Such structures are typically made of mixed crystal systems such as $Ga_{1-x}Al_xAs$ with a changing mole fraction x(z). In practice, such structures can serve as carrier collectors in device structures.

conducting PL experiments, the laser spot size will definitely be smaller than L_D. Lateral diffusion within the x-y-plane will cause an additional reduction of the steady-state $\delta n = \delta p$ value compared to what is predicted by the one-dimensional model, which involves diffusion into z-direction only; see Sect. 4.2.1. This will substantially affect the PL signal; for details see Sect. 4.7.4.

4.2.3 The Impact of Actual Spatial Carrier Distributions to the PL-Line Shape

According to (1.70) in Chap. 1, the spontaneous emission spectrum from a semiconductor is a homogeneously broadened line. Therefore, its lineshape is expected not to be dependent on the excitation power that is implicitly represented by δn (described by the energetic position of the quasi-Fermi-levels). For actual PL lines from semiconductor samples, however, this statement is not always true. There are very often non-linear dependencies $I_{PL}(\delta n)$ for particular PL lines, at least in certain excitation density ranges. Therefore, one can expect both smearing effects as well as line broadening of individual lines, which are caused by the convolution of PL contributions from locations within the excitation spot, where δn differs. This statement holds for both lateral and vertical δn-gradients; see Sects. 4.2.1 and 4.2.2, respectively. Notice that this broadening mechanism is intrinsically related to PL measurements

4.3 PL Setups and Methodology

4.3.1 Standard cw PL Setup

A standard PL setup is depicted in Fig. 4.3. As a matter of fact, a PL setup has to meet the same requirements as a Raman setup, see Chap. 3, and in fact one can measure PL with Raman spectrometers, as well. In both techniques a laser excites a sample and a relatively small amount of photons emerge from the sample which

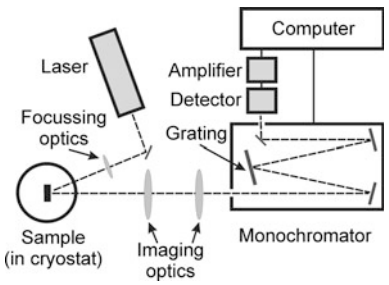

Fig. 4.3 Schematic diagram of a standard PL setup

have to be picked up and analyzed. In Raman spectroscopy, PL sometimes contributes to backgrounds and is considered a residual effect (often called fluorescence or phosphorescence). Except for the different microscopic origins of the analyzed light, namely recombination and scattering, the most striking 'technical' distinction between PL and Raman experiments is the energetic distance between the photon energy of the laser excitation and the spectral features to be analyzed. For Raman spectroscopy, this distance often only amounts to a few meV (and even less). In contrast, for standard PL measurements several hundred meV of energetic separation are not unusual. Very low energetic separations as in Raman spectroscopy are rather the exception. Therefore the suppression of scattered and strayed excitation laser light is important in PL spectroscopy, but not as crucial as for nearly all kinds of Raman measurements.

We will now address the optical elements as depicted in Fig. 4.3, following the sequence in which they contribute to the PL-signal creation.

Excitation source: In almost all PL setups, a laser provides the optical excitation. Typically its wavelength is shorter than the wavelength that corresponds to the E_g-value of the investigated material. This allows for the generation of free electron-hole pairs. 'Classical' continuous wave (cw) excitation lasers are gas lasers such as Argon-ion (mostly 488 and 514 nm), HeNe (633 nm) and HeCd (325 and 442 nm). They are complemented, and at least partly, replaced by solid-state lasers such as Nd:YAG and frequency doubled Nd:YAG emitting at 1064 and 532 nm, respectively. Tunable lasers, such as Ti:Sapphire (750–1000 nm) are more costly. Semiconductor lasers, which are nowadays available from the UV to the MIR are becoming more and more important as light sources for PL experiments. This involves also stabilized semiconductor laser-based modules with emission wavelengths across the entire visible spectrum. Another recent type of potential PL excitation sources are *white light sources*. The term *white light source* denotes continuum sources based on mode-locked lasers, whose radiation is coupled into photonic fibers. Such sources provide some 10 W of total power in the wavelength range 400–2400 nm. In particular the high brightness of these sources, i.e. the 'laser-like' beam shape, makes them very promising tools for spectroscopists. Relevant parts of this broad spectrum can be picked out, for instance by filters.

Filters: Neutral density filters are typically placed between laser and focusing optics. They are not shown in Fig. 4.3, they serve for the proper adjustment of the laser power. Their drawback is that their physical exchange might lead to a displacement of the laser beam on the sample. Filter wheels with graded coatings allow to circumvent this potential source of errors. Another option is the use of crossed polarizers. Since many excitation lasers provide polarized radiation already, often one polarizer is sufficient for the desired outcome. Of course, this approach fails, if the polarization of the excitation light is a relevant parameter for the planned experiment. In standard measurements, however, this is mostly not the case. Damping of the excitation laser light is definitely a challenge, in particular, if the excitation density variation includes changes by several orders of magnitude. In such a situation, the combination of absorbing and reflecting filters with wheels or

other types of graded filters represents a good choice and helps avoiding damage to the filters or the samples.

If gas lasers serve as the excitation source, additional filters might be required in order to sort out residual lines from the laser plasma. Therefore one frequently refers to these filters as *plasma filters*.

Focusing optics: The focusing optics defines the diameter of the excitation spot (FWHM) on the sample surface. Often the focusing optics has to direct the excitation beam to samples which are mounted into a cryostat in order to enable measurements at low temperatures. Therefore, the effective aperture ratio of the cryostat might be another boundary condition for the focusing optics.

Sample: In many PL setups, the excitation laser beam hits the sample not perpendicular but of an angle. Advantageously, this angle is chosen in such a way that the reflected fraction of the excitation laser beam does not encounter the imaging optics. Perpendicular incidence is mostly implemented in such a way that the same lens system (e.g. an objective) is used for both focusing the excitation laser and picking up the luminescence. This approach is often used in (confocal) micro-PL setups; see Sect. 4.7. For a standard PL setup, however, it might be favorably to separate the alignments of the excitation laser beam and the imaging optics from each other. If mirrors optics are used, the excitation laser beam is often fed through a hole in the mirror that collects the PL radiation. This might allow for perpendicular incidence, as well. One advantage of perpendicular excitation is the circular excitation spot, whereas the need to eliminate the reflected excitation laser light, which frequently exceeds the magnitude of the PL signal by many orders, appears as a drawback.

Imaging optics: The proper design of the imaging optics of a PL setup should maximize the number of photons eventually arriving at the detector. If we take the isotropic character of the spontaneous PL emission into account, this is not a trivial goal. The key parameters are the aperture ratios of cryostat, collecting lens or mirror (1st one after the sample), monochromator, and detector. In addition, the excitation spot size, the detector area, and slit widths at the monochromator should be adapted to the magnification provided by the imaging optics. These parameters cannot be chosen independently and at least the excitation spot diameter and the slit widths at the monochromator are parameters that are often a subject of modification within a single measurement campaign. In many cases, the already existing equipment in a lab, e.g. the monochromator with a given aperture further limits the degrees of freedom for the experimentalist. Typical imaging optics are lenses or lens systems. Fibers might be more convenient but often promise less total light collection compared to free optics. Mirror optics is required if the setup will be used in multiple spectral ranges, if extremely broad spectra are expected, or if one aims for measurements in the MIR spectral range.

Ideally, maximizing the number of photons which arrive at the detector will be achieved if the excitation spot is imaged exactly to the detector area without any losses at other ‘bottlenecks’, such as the slits of the monochromator.

For a given detector, this determines either the possible size of the excitation spot or the magnification of the imaging optics. The magnification, however, is also

determined by the apertures of the collecting part (signal pickup at the cryostat) and the transformation part to the detector. Thus, the diameters of the cryostat window and the detector size can already limit all other degrees of freedom.

As a simple rule-of-thumb, one should treat the PL emission from a sample as a light bundle with a beam-parameter-product ($w_0\Phi$) *that is* (*hopefully almost*) *conserved on its way towards the detector. The* $w_0\Phi$*-value is determined by the radius of the excitation spot on the sample* (w_0) *and the opening half-angle* (Φ) *of the initial aperture* (*e.g., the cryostat window or the first collection lens*). *Each change of one of these two parameters, e.g., by an optical element, is followed by a complementary change of the other one.*

When we consider these issues, it should always be possible to make even a raw estimate of the fraction of spontaneous emission that reaches the detector. Nevertheless, a standard PL setup does not allow for the determination of absolute external quantum efficiencies. While the shapes of PL spectra are typically highly reproducible for subsequent measurements, the absolute PL signal often fluctuates by values of some 10–30 %, in particular if the sample is removed and newly aligned in the following experiment. This situation is very similar in all other types of photometric measurements.

If high reproducibility of absolute signals is required, fixed alignments and mechanical stoppers (that force the samples to defined locations) can be very helpful. Parallelly mounted reference samples with well-known and long-term stable emission can be useful tools, as well.

Monochromator: The right choice of the monochromator and its grating(s) is, like the design of the whole setup, a tradeoff again. The compromise that can be found is somewhere between the contradicting demands for high intensity of light (low focal length) and high spectral resolution (long focal length). A larger grating promises high light throughput. It has to be ensured that it is also blazed for the desired wavelength and that the imaging optics illuminates its entire area (adaptation of the aperture ratios is required; see the paragraph on imaging optics before). In Fig. 4.3, we have shown a Czerny-Turner system. One should use proper order sorting filters for the grating monochromator. These filters are long-pass filters. Their purpose is to suppress higher (mainly second) order PL contributions, which otherwise would fake spectral features at twice the wavelength of the real contributions. The use of such filters is crucial if extended spectral ranges are analyzed or if the excitation of the sample provides several spectrally separated contributions, e.g. from substrate and epitaxial layers.

The use of prism monochromators has become rare for several reasons. Systems which allow the exchange between gratings and prisms, however, are utmost flexible if changes from a high sensitivity (and low spectral resolution) to high spectral resolution are necessary. Such a measuring scenario is not unlikely, for instance when new samples are first inspected in order to get an overview and then are eventually analyzed in detail.

An alternative to the use of a monochromator is to analyze the PL signal with an interferometer. This approach, which is predominantly used if PL in the IR spectral range is to be analyzed, is called Fourier-transform (FT) PL and is often

accomplished by the use of commercial FT-spectrometers; see also Sect. 2.2.3. Some FT-spectrometer vendors offer complete PL-extensions. This technique will be addressed in detail in Sect. 4.5.4.

Filter: A second set of filters might be introduced into the optical path of the PL signal either before or after the monochromator. They are not shown in Fig. 4.3, thy serve for the separation of residual excitation laser light, in particular stray light. If the excitation laser beam hits the sample surface perpendicularly, this filter serves to suppress the directly reflected laser emission.

Detector: There is a wide variety of detectors available for PL measurements. While in the past single-element detectors have been used exclusively, nowadays, detector arrays such as CCD-cameras are wide-spread. If CCD-cameras are used, the monochromator is often used as polychromator. In this case, the exit slit of the monochromator is largely widened or removed and the image from the monochromator's exit slit plane is imaged to the surface of the CCD-camera. In this situation, the spectral resolution is not determined by the slit width of the monochromator anymore, but rather by the pixel dimensions of the CCD-camera. The exit slit width, if there still is an exit slit, determines the spectral range that is monitored by the camera only.

The right choice of the detector is a key issue when constructing a PL setup. PL signals are typically small, and therefore the detector should be sensitive. This is ensured by using quantum detectors rather than thermal detectors. Their sensitivity is characterized in terms of responsivity or sensitivity. Important parameters are the dark signal (i.e. the signal when the light entrance is blocked) as well as the noise. A key parameter, which must be chosen according to the expected emission from the samples that will be analyzed, is the wavelength range of operation.

The 'classical' detector for PL spectroscopy is the photomultiplier tube (PMT). The operation principle relies on the external photoelectric effect at an alkali metal (or GaAs) electrode with subsequent amplification by cascaded electrodes (dynodes). PMTs cover the entire range from the UV to the NIR. Their drawback, however, is that they might be destroyed, if they are excessively exposed by light, while the dynodes are biased. Cooling of PMTs is an option for noise reduction. PMTs are suited for single-photon counting.

Semiconductor detectors, photodiodes, and photoconductors are state-of-the-art complements, in part even alternatives to the PMT. Their working principle is the internal photoelectric effect. In contrast to the external photoelectric effect, the quasi-free carriers generated by light absorption lower the resistance of the detector material or generate an electrical signal without physically leaving the absorbing material. Typical detector materials are, from the VIS to the IR, Silicon, Germanium, InGaAs, InSb, $Hg_{1-x}Cd_xTe$ (often called MCT) and III-V-based QW Infrared Photodetectors (QWIP).

Semiconductor detectors, such as avalanche photodiodes (APD) have internal amplification schemes. The detectors based on these semiconductor materials are available as single detectors as well as arrays (mostly CCD-cameras) as cooled or as uncooled modules. Cooling implements noise reduction. Most detector vendors

offer comparison charts, where the detectors responsivities or sensitivities are displayed versus the wavelength.

Amplifier: In Fig. 4.3 we placed an amplifier between the detector and the control computer. The term 'amplifier' does not only stand for an actual pre-amplifier here, but for the whole electronics supporting the detector. It highly differs depending on the type of detector and the detection technique chosen. While PMTs need an additional high-voltage supply, most photon detectors are used together with analog pre-amplifiers (or impedance converters). The detector signal subsequently reaches the computer via an A/D-converter or a frame grabber card.

Another important option for signal acquisition, which is used in many PL setups, is lock-in amplification. It relies on phase sensitive rectification of an AC PL signal into the DC output, according to a reference signal. This approach allows for an increase of the signal-to-noise ratio of PL measurements by orders of magnitude. The AC PL signal is commonly produced by modulating the excitation laser with a mechanical chopper. When choosing the chopper frequency, the time constant of the detector-pre-amplifier combination must be taken into account. Typically, the chopper provides the reference signal depending on which the phase sensitive rectification of the PL signal is carried out. The instruments, often called *lock-in amplifier*, are typically available as digital stand-alone devices or computer cards. Analog 'lock-in' devices are still available and in use.

Computer control: The computer control of the setup is not directly related to the actual spectroscopic experiment. However, it will finally decide about its success, as well. One key question that is to be answered before constructing the setup is the 'degree of automatization'. This means, that one should reflect on which components should be controlled by the computer keyboard and which by power buttons, switches, and alignment screws.

The definition of the 'degree of automatization' will depend on many additional factors that are not directly related to science, e.g., the number samples (sequence of measurements), the qualification of the operators, etc. A high-degree of automatization makes routine measurements more convenient but may reduce the flexibility of the setup. The minimum in computer control is embedding the monochromator (parameter: wavelength) and the detector (parameter: PL signal) into the software, so that during a measurement, the PL spectrum (PL signal vs. wavelength) is accumulated and stored. In our experience it is advantageous to have this spectrum displayed real-time on the computer screen during the measurement.

From a practical point of view, it is important to have a real-time PL signal available, i.e. a direct display of the actual PL signal magnitude (at a given wavelength), which is visible from all locations of the setup, where optical alignments will be done.

In Sect. 4.1, we mentioned already the fact that PL signals are often presented (and published) as measured. Actually, it should be divided by the spectral transmission curve of the entire setup between the sample and (including) the detector. We refer to this curve as *instrument function*. Even if one is convinced that the spectral characteristics of all optical elements (including the air in between them) are smooth in the considered spectral range, a test with a small light bulb

(or another continuum source) in the sample position makes sense, because unexpected effects such as absorption lines in air or window materials, ghosts (from the grating), higher orders of laser or plasma lines, etc. might produce residual contributions to the spectra.

If the PL signal is not visible to the naked eye (and unfortunately this is frequently the case) mechanical alignment aids can be helpful. This can be for instance a small light bulb or an isotropic emitting LED (sometime the sealing must be removed) that is placed at an alternative detector port at the monochromator (if available at the particular instrument) or at another image plane within the optical system. Now, its light can be tracked back through the monochromator and optics towards the sample and it should be visible at the sample surface as a tiny spot. If the excitation spot and this light spot fall together, the setup should be well pre-aligned. At this point, one should start with a known sample and complete the alignment by maximizing the PL signal. After this, one can check the overlap of excitation light spot and the spot from the alignment aid again. If they largely overlap everything seems to be correct and further alignment could be performed along the actual PL-signal detected.

The motivation to add these remarks was to provide something like a raw guideline on, how to design a PL-setup. A suggestion how to assemble the 'best PL setup' can not be given here, since there are too many contradicting scientific, economic, and planning requirements that have to be included. In any case, it might be advantageous to have an open architecture of the setup, which allows adding further options, if required. This involves, e.g., multiple detector ports at the monochromator as well as the option to change the gratings, either to switch to another wavelength range or to modify the spectral resolution.

It should be mentioned that many vendors of the equipment, which has been mentioned in this subsection, have web-sites with plenty of useful information on those components that have been introduced here only briefly.

4.3.2 Resonantly Excited PL

So far we considered the excitation laser photons $\hbar\omega_{\mathrm{exc}}$ in PL experiments exclusively as suppliers of energy for the creation of carrier pairs $\delta n = \delta p$. Obviously, a variation of the excitation wavelength for photon energies above the bandgap allows a variation of the penetration depth; see (4.1) and (4.3). Such a variation is very useful in order to investigate gradients within a structure or to make estimates on the influence of the surface.

There is, however, another important use of the parameter $\hbar\omega_{\mathrm{exc}}$: In contrast, e.g., to CL experiments with electron beam excitation, optical excitation allows for *selective excitation*. In case of a QW-structure, it could be worthwhile to analyze the QW emission for two different types of excitation: first for excitation with photons larger than E_g of the barrier, and second for excitation with photons smaller than E_g of the barrier, but sufficiently large to excite at least the QW ground state. In the first

case, the population of the QW is expected to take place predominantly indirectly via the barrier, whereas the latter case allows for direct and exclusive excitation of the QW. This approach allows us to distinguish between effects related to the barrier and the QW, but also estimating carrier transfer processes in the structure, even from a steady-state experiment.

This approach works for all types of structures, in which a narrow gap material is buried in a wider bandgap material as it is typical for many types of device structures.

Furthermore, resonant excitation spectrally close to strong resonances such as exciton lines, can create additional features in PL spectra [7]. Under such conditions, even spectral features caused, e.g., by Raman scattering (i.e. not by radiative recombination), can be introduced into PL spectra. Therefore, one should be cautious when interpreting spectra measured for situations, where holds $\hbar\omega_{\mathrm{exc}} \sim E_g$.

4.3.3 PL Excitation Spectroscopy

PL excitation (PLE) spectroscopy is one example for PL spectroscopy, which is based on resonant excitation tuned continuously. A PLE spectrum, often only called *excitation spectrum*, gives the PL signal at a fixed wavelength, called *monitor wavelength*, versus excitation wavelength. The key element for a PLE setup is a tunable light source, while the rest of the PL-setup remains (almost) unchanged; see e.g. Fig. 4.3. This is also true for the monochromator, which is often used to define the monitor wavelength window like a tunable bandpass filter. If the signals are very weak, appropriate filters must serve for this purpose.

The requirements to the tunable source are quite demanding:

- The excitation light beam should be spectrally narrow because this determines the spectral resolution of the PLE spectrum.
- The excitation wavelength should be known and fed into the computer, because this represents the abscissa of the PLE spectrum.
- The excitation power should be constant within the entire wavelength range covered and high enough to generate a sufficient PL signal at the monitor wavelength.

So far, there has been no ideal PLE source. Relevant technical approaches to meet these requirements are:

- The use of a continuum light source such as lamps and spectral selection, e.g. by a second monochromator that provides the *excitation wavelength*. With the emergence of powerful *white light sources*, this approach (i.e. the combination of broad-band light sources with monochromator) is expected to become more relevant.
- The use of tunable lasers such as Dye- or Ti:Sapphire lasers. In this case, the *excitation wavelength*-value is mostly determined by a wavemeter.
- Combinations of both approaches are used as well.

In either case, the need for the attenuation of the excitation light to constant power level remains. Here the use of a computer controlled gray wedge is very useful.

Figure 4.4 show PLE spectra. Figure 4.4a points to an important ability of PLE, namely monitoring absorption properties [8]. The spectrum on top represents a calculated absorption spectrum, while PLE data are given at the bottom. Obviously most of the theoretically expected absorption features of the multiple QW structure analyzed by the authors, are well resolved in the PLE spectrum. Thus, in scientific lines of arguments absorption data are often replaced by PLE spectra in order to avoid the effort necessary for the preparation of ultrathin samples for a transmittance measurement or for the analysis of transmittance data, which are frequently troubled by interferences. If one is interested, e.g., in the absorption properties of a

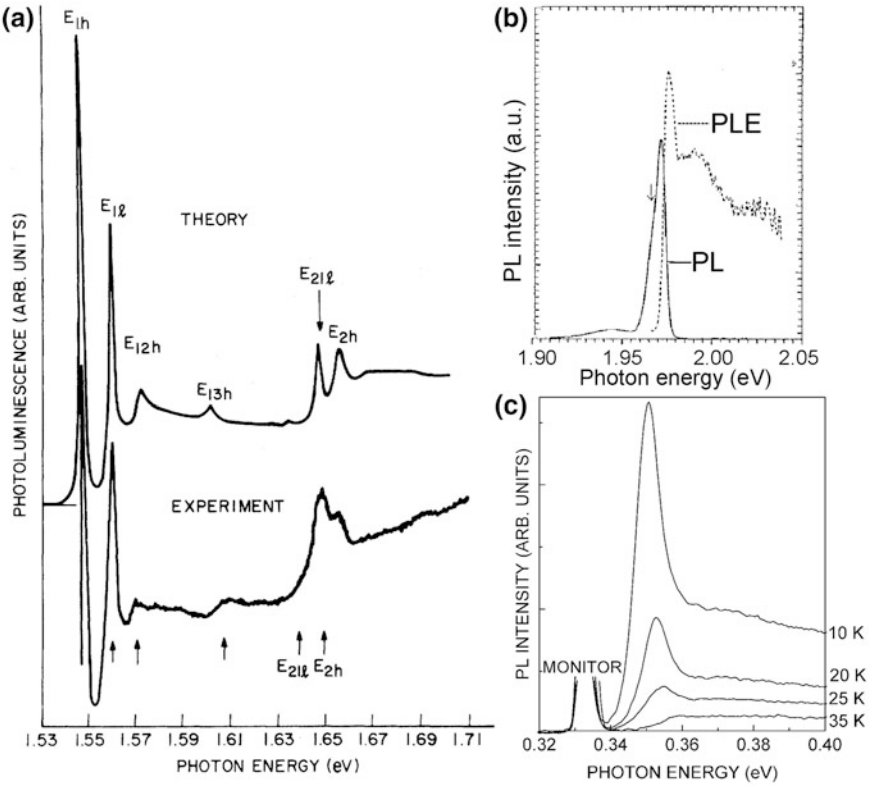

Fig. 4.4 PLE spectra from different samples. **a** Theoretically modelled and measured PLE spectra from an GaAs multiple QW sample [8]. **b** PL and PLE spectra from $Ga_{0.52}In_{0.48}P$ at T = 4.2 K [9]. **c** PLE spectra at various temperatures from narrow-gap $Hg_{0.651}Cd_{0.335}Mn_{0.014}Te$ at T = 10 K [10]

single QD, PLE remains as an unique option because they could hardly be accessed by a standard transmittance measurement [11].

Figure 4.4b shows PL and PLE spectra from $Ga_{0.52}In_{0.48}P$ [9]. The most striking feature is the 4.5 meV energetic difference between PL and PLE peak. Such shifts are referred to as *Stokes shift* and they are often identified as localization energies of excitons. In either case a large Stokes shift between the excitonic peak in PL and PLE is an indication of a levelled interband density of states that might indicate poorer material quality.

Figure 4.4c shows temperature-dependent PLE data of the excitonic transition from a bulk narrow-gap HgCdMnTe-sample [10]. Obviously, the sharp PLE (absorption) resonance vanishes with increasing temperature, which points to thermal delocalization and subsequent dissociation of the intrinsic excitons.[5]

In general, the shapes of the PLE spectra tell us how much the excitation at an arbitrary wavelength (typically shorter than the monitor wavelength) contributes to the PL-signal at the monitor wavelength. There are two processes involved, firstly absorption, and secondly a transfer towards lower lying states, which are involved in the recombination process that generates the PL at the monitor wavelength. Consequently, the shape of a PLE spectrum depends on the monitor wavelength chosen, as well. Sometimes, this makes interpretations more complicated, but also offers chances to quantify, e.g., the transfer towards lower lying states. If one is mainly interested in absorption properties, one should select a monitor wavelength far away from any resonance, e.g. at a defect-related transition.

Therefore, taking PLE spectra is often considered a way to get qualitative insight into the absorption spectrum.

4.4 Mechanisms Contributing to the PL Spectrum

4.4.1 Introduction

The PL spectrum is expected to actually represent the spontaneous emission spectrum according to (1.70). Thus, its shape is clearly predicted for an ideal direct semiconductor with two parabolic bands, namely valence and conduction band, and absence of any many particle effects; see Fig. 4.5a. Although these assumptions do not completely match reality, (1.70) contains already important information.

At the *lower energy side*, the spectrum is determined by the combined density of states of the bands involved in the process. It is expected to stop at E_g and provides information about the energetic band structure of the material, in practice mostly about deviations from the ideal band structure. The *high energy side* of the spectrum is determined by the distribution functions of the carriers. Thus there is

[5]Therefore, when considering the energy of free excitons, a kinetic energy term should be added to the exciton energy. In the preceding considerations we omitted this.

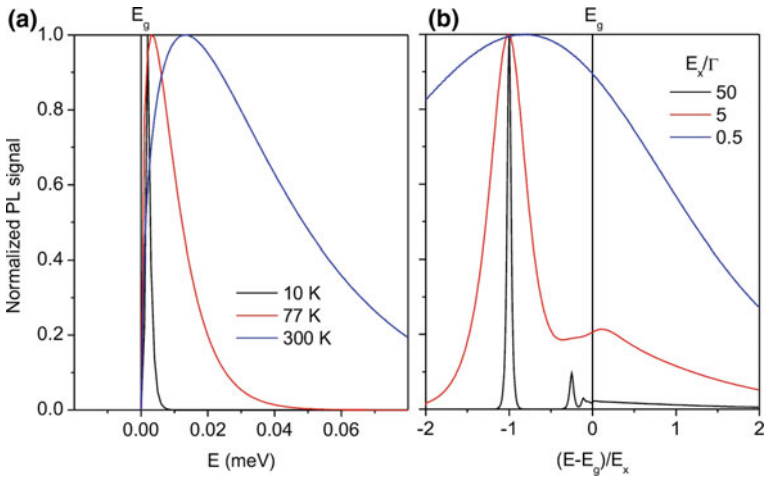

Fig. 4.5 Calculated PL spectra. The left part shows spectra at different temperatures, assuming a pure spontaneous band-to-band recombination according to (1.70). The value of E_g was set to zero. The right part shows excitonic spectra. Again the value of E_g was set to zero, while Γ represents broadening parameter

information about equilibrium (n_0 and p_0) and non-equilibrium (δn and δp) carrier concentrations and their (effective) temperature T. Even for an idealized crystal structure, deviations from the simple view on the PL spectrum above given become relevant:

- The band-structure of an (ideal) Zincblende structure contains four instead of two bands, which are non-parabolic, i.e. the effective masses are energy-dependent. Moreover, the three valence bands are degenerated.
- PL requires the generation of non-equilibrium carriers. Typically, this is accomplished by optical excitation with photon energies above E_g, resulting in bipolar generation of carrier pairs $\delta n = \delta p$. In this situation, Coulomb attraction often prevents electrons and holes to become fully spatially separated. This type of binding allows electron-hole pairs to release energy, in contrast to free electrons and holes. The couples are called *excitons*, and energy that gets released is referred to as the exciton *binding energy* (E_x).
- Finite temperatures cause lattice vibrations with repercussions to the electronic band structure but with direct impact to the shape of PL lines, as well. Furthermore, extra lines created by phonon-assisted transitions may appear, which are called *phonon replica*.

Notice that these effects are already relevant in an idealized material. Taking into account the only presence of point defects (which are e.g. a result of intentional and unintentional doping) there are further potential valleys that create additional localized electronic energy levels. Here additional optical transitions (with or without participation of extended states) might take place.

In the following, we will briefly review the transitions which potentially contribute to a PL spectrum in the sequence of their appearance from higher to lower photon energies.

4.4.2 Band-to-Band Transitions

Spontaneous emission via band-to-band transitions represents the fundamental intrinsic emission process in semiconductors in the single-particle image, which is the outcome of bandstructure calculations. Sometimes this process is also called *electron-hole plasma transitions* or short *plasma transitions*. This is because the *exciton* generation is considered the fundamental excitation process in particular in materials with high E_x-values, and 'ionized' or 'dissociated' excitons (i.e. free electrons and holes) are considered to represent a 'plasma'. The spectral shape of band-to-band recombination is described by (1.70) and is depicted in Fig. 4.5a. On the energy scale, they start exactly at E_g and form a homogeneously broadened PL line. The broadening parameter addressed in this Fig. is the temperature. For a non-degenerated material, this line peaks at $\sim E_g + 1/2 \times kT$ and is extended towards higher photon energies with a FWHM of $\sim 2kT$. These statements only hold when we assume the idealized square-root shaped $\alpha(\hbar\omega)$-dependence.

4.4.3 Free Excitons

Above all, exciton formation allows free carriers to reach a lower overall energy by binding them. Free excitons can be illustrated as *hydrogen atoms* consisting of an electron-hole pair which is traveling free through the semiconductor lattice. In most inorganic semiconductors, the exciton dimensions are large compared to the lattice constants of the crystals. In contrast to the localized *Frenkel-exciton*, this type of 'outstretched' exciton is called *Wannier-Mott exciton* and its binding energy amounts to

$$E_x = -\frac{\mu}{m_0}\frac{1}{\varepsilon_r^2}R \tag{4.6}$$

in bulk material. R = 13.6 eV is the Rydberg energy. Therefore E_x is sometimes also called the *Exciton Rydberg*. The free electron mass is m_0, $1/\mu = 1/m_e + 1/m_h$ is the exciton's reduced mass, and ε_r is the dielectric constant. m_e and m_h are effective masses of electron (e) and hole (h), respectively. Since there are two types of holes in Zincblende semiconductors, namely heavy (hh) and light (lh) ones, also two kinds of excitons, namely hh- and lh-excitons can be observed. In GaAs, the bulk hh-exciton binding energy is equal to 4.8 meV with a Bohr radius of 11.6 nm. In CdTe, it is equal to 10.0 meV and the Bohr radius is 6.8 nm, whereas in wide

bandgap ZnO E_x equals 59 meV and the Bohr radius is 1.8–2.0 nm. Following further the analogy to the Hydrogen atom, excitons are expected to display excited states, which form a series of emission lines as known from the Lyman series of the Hydrogen atom. These lines are spectrally located at

$$E(n) = E_g - \frac{1}{n^2} E_x, \tag{4.7}$$

with n being the principal quantum number (n = 1, 2, 3, …). Figure 4.5b depicts such a series of emission lines converging to a continuum beyond E_g. The broadening energy Γ here describes all potential broadening mechanisms. Obviously the overall-shape of the free exciton PL lines depends immensely on the ratio Γ/E_x. A value of $\Gamma/E_x = 0.50$ is representative for high-quality wide-bandgap materials such as ZnO, whereas $\Gamma/E_x = 50$ rather describes the situation in a narrow-bandgap mixed crystal system as $Hg_{0.3}Cd_{0.7}Te$.

In the case of bulk GaAs, the free exciton ground state is spectrally located at $E(n = 1) = E_g - E_x = 1.519 - 0.0048$ eV $\sim$ 1.514 eV followed by the first excited state at 1.5178 eV. Notice that these numbers refer to E_g at low temperatures.

In lower-dimensional systems such as QWs and QDs, the actual exciton dimensions are reduced due to the presence of the barriers. This situation is called *confinement* or *quantum-confinement*. The spatial shrink (reduction of the effective Bohr-radius) is accompanied by an increase in exciton binding energy. There is an upper E_x-limit for the hh-exciton ground state in QWs, namely the one for the 'infinitely thin QW' with $E_x(\text{QW}) = 4\ E_x(\text{bulk})$. Thus, $E_x(\text{QW})$-values are expected in the range $E_x(\text{bulk}) < E_x(\text{QW}) < 4\ E_x(\text{bulk})$ with typical enhancement factors between 2 and 3. Their determination requires numerical calculations, *excitonic corrections*, for all states. The increase of the exciton's binding energy by restricting the propagation of the free excitons from the 3-dimensional space to a plane is the result of a kind of localization. In Sect. 4.4.5, we will show that further confinement (localization) will lead to *localized excitons*, which allow the carrier pairs to reach states at even lower energies.

We advise caution not to mix the principal quantum number n of the exciton with the principal quantum number n representing the numbering of the quantized levels within a QW. Both types of series can appear even together. This means that each single transition in a QW can be 'decorated' by an exciton series; see [12]. Since we will not go further into these details, we will continue to use the letter n for both sets of quantum numbers.

Direct exciton recombination without any phonon participation leads to the appearance of a *zero-phonon line* in the PL spectra. Sometimes the corresponding transition is also called no-phonon (NP) transition. If excitonic recombination is assisted by phonons, additional satellites appear which are called *phonon replica*. In polar materials, the most dominant phonon-assisted process is related to LO phonons. The coupling to LO-phonons is quantified by the *Huang-Rhys parameter* which stands for the intensity ratio of subsequent phonon replica.

Free exciton lines are denoted by X, X^0, or sometimes also X^{NP}. The index NP stands for no-phonon. Phonon replica of the X-transitions are frequently denoted as X′, X″, … or X^{TO}, X^{2TO}; the latter in case the interaction with the lattice takes place via transversal optical phonons.

Free excitons can merge with electrons and holes and can form so called *charged excitons* or *trions*, which are denoted X^- or X^+. Charged excitons show up in the PL as a sharp line at energies below the X line. The binding of two free excitons results in formation of *biexcitons* denoted by XX. All these processes entail an effective energy loss of the system compared to the quasi-particles when separated. In PL spectra this energy loss always results in a red-shift of the related line. Notice, that the term *biexciton* is also used in order to describe the situation when two electron hole pairs are generated in a single QD [13, 14].

4.4.4 Band-to-Band Transitions Versus Excitonic Transitions

Obviously, the two models, namely the single-particle image and the excitonic one (that involves multiple particles in a non-equilibrium situation) are somewhat contradictory; see also Fig. 4.5a, b. In fact, both models represent border cases, those of completely bound and completely dissociated electron-hole pairs. Which case better describes an actual PL spectrum certainly depends on the investigated semiconductor material or the structure itself and on many additional factors such as temperature, doping, disorder, interface roughness, the presence of defects, etc.

As a rule of thumb it is fair to presume that wider bandgaps, large E_x-values, low doping, and low temperatures are in favor of the applicability of the excitonic model, whereas smaller bandgaps, lower E_x-values, higher doping, and increased temperatures lead to a situation, which is frequently well-described within the model of band-to-band transitions.

Quantitative indicators are e.g.

- the ratio E_x/kT for the estimation of the influence of the temperature (thermal dissociation of the excitons)
- the Mott-density for the description of the increasing impact of n_0 and or δn. Elevated carrier concentrations result in screening and phase-space filling that reduces E_x. If excitonic contributions become reduced at elevated non-equilibrium carrier densities, this is referred to as *bleaching* of the excitons.

As an example, Fig. 4.6 shows PL spectra from GaAs [15]. The authors separated the contributions of excitions and dissociated electron-hole pairs. The increasing contribution of dissociated electron-hole pairs with temperature illustrates the effect of the thermal dissociation of excitons.

Many-body effects, however, can remain effective even at very high carrier concentrations. In degenerated material, they might manifest themselves as *Fermi-edge singularity*, an excitonic PL feature at the Fermi-edge. Owing to favorable

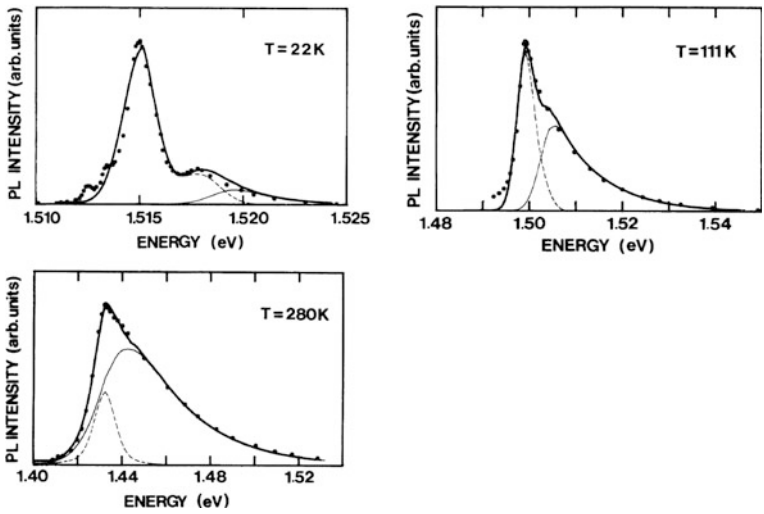

Fig. 4.6 PL spectra from GaAs at different temperatures (*full circles*). The full line shows fits to the data, comprising the contributions of bound and dissociated electron-hole pairs: Excitonic PL and PL due to dissociated excitons (free carrier pairs) are indicated by *thin dashed an full lines*, respectively [15]

circumstances, even distinct PL lines can be observed near the Fermi-edge. This is sometimes called *Mahan exciton*. Notice that in addition to the increased E_x-values in QWs and QDs compared to bulk, the lowered efficiency of screening also works in favor of excitonic effects even at elevated carrier densities.

The contribution of the bound electron-hole pairs to the *oscillator strength* of the edge emission remains significant, even if the identification of pronounced exitonic lines is hindered by broadening effects.

A comprehensive description of the contributions of bound and dissociated electron-hole pairs, which goes beyond the limiting cases, requires theoretical considerations. We refer here to the work by Haug and Koch [16].

4.4.5 Bound Excitons

Free excitons propagate through the crystal lattice.[6] Point defects, other kinds of lattice defects, QWs, and QDs form potential wells that present potential trapping sites for them. This trapping process is rather fast and takes place on a ps-timescale or even faster. When we take typical excitonic lifetimes on the order of ns into account, the free excitons might be localized before a substantial part of them

[6]Therefore, when considering the energy of free excitons, a kinetic energy term should be added to the exciton energy. In the preceding considerations we omitted this.

recombines, thus producing X-emission. As a result, no or only weak X-emission is observed, while the trapped excitions produce emission lines energetically below X. This type of excitons is called *bound excitons* (BE).

The situation of excitons that are confined by a QW within one dimension has already been discussed in Sect. 5.4.3. Historically, BEs trapped in 'natural valleys' in bulk materials have been investigated long before QWs and QD were available. The 'natural valleys' in bulk materials are for instance point defects or alloy fluctuations. Effectively they are representing three-dimensional potential valleys. Since different kinds of localization sites are expected to create differently shaped potential valleys within a given semiconductor material, the efficiency of exciton localization is expected to be different, as well. Of course, this results in different localization energies for different dopants or types of defects to which the trapping of free excitons takes place. Therefore, BE PL emission appears as a set of more or less sharply pronounced lines spectrally located at slightly lower photon energies than the X line, the ground-state emission of the free exciton.

If the nature of the defects to which the excitons are bound is known, e.g. from PL experiments with intentionally foreign-doped materials, one can specify the observed PL lines as neutral donor bound exciton (D^0, X) or ionized donor bound exciton (D^+, X). Analog denotations are used for acceptor bound excitons with (A^0, X) and (A^-, X). PL lines that are caused by recombination of 'defect-induced BE' lines are denoted as (d, X) and have been reported for instance as a result of exciton binding to defects incorporated during epitaxial growth [17]. Excitons may also be attracted by surfaces (SX) [18, 19].

If BEs are located at donors or acceptors, their localization energies (i.e. the red-shifts with respect to X) typically amounts to only a fraction of the donor-or acceptor binding energies. The ratio between binding and localization energies usually amounts to 0.1–0.3. It remains constant in a given material. The corresponding linear relation is called *Haynes rule*.

The interaction between the binding center and the excition bound to it can go so far that BE recombination leaves the binding center itself in an excited state. Since two electrons are involved in such a process, one from the exciton and one in the defect center, these transitions are called *two-electron-transitions*. The resulting spectral features are called *two-electron-satellites* (TES). The spectral separation between BE and corresponding TES represents the energy needed to push an electron from its ground state in the defect to its first excited state. If shallow defects are considered, this energy is ¾ of the defects binding energy (see hydrogen model). Thus a given center can be probed by analysis of its BE- and TES-lines BE emission may be accompanied by phonon replica as well.

4.4.6 Defect Related Transitions

We mentioned potential valleys as localization sites for excitons. Point defects, such as foreign dopant atoms, form energetic valleys as well, which allow the trapping of

unbound free electrons and holes. This trapping process could also be called 'ionization', since the charge state of the defect site is changed. The electronic eigenstates within the defect potential are located (on the energy scale) mostly within the energy gap of the material, i.e. between valence and conduction band. The depth of the energetic levels, i.e. their distance from valence or conduction band edge (also called *activation* energy or *ionization energy*), depends on the microscopic structure of the defects that are considered. Giving a classification for the defects in semiconductors is beyond the scope of this introductory guide for spectroscopists. We will only distinguish between shallow and deep level defects.

Shallow defects are described by the effective mass approximation in a very similar way to the (free) Wannier exciton. Therefore, shallow defects are often called *hydrogen-like defects*. Typical ionization energies of ground states are ~ 6 meV for donor and some 30 meV for acceptor levels in bulk GaAs.

Deep level defects are spatially strongly localized and therefore not described by the effective mass approximation that supposes the extension of the electronic wavefunctions across several lattice constants. This situation reminds us of the Frenkel exciton.

While transitions between energy levels of the same defect (intra-defect-transitions) result in photons of extremely low energies that are typically not detected by standard PL experiments, transitions between band states and defect states (energetically located close to the opposite band) feature photon energies, which correspond to E_g diminished by the ionization energy of the defect (at least in direct semiconductors). Therefore, they are typically below the different excitonic transitions located on the energy scale. Such transitions between band states and defect states are called 'free-to-bound transitions' and denoted, e.g. as (e, A^0) in case of a band-to-(neutral) acceptor transition. If there is more detailed knowledge about the nature of the defect, this is reflected in the naming the defect. For instance, the acronym (e, C^0_{As}) stands for a transition of a free electron to a neutral carbon acceptor that is located on an arsenic lattice site within a GaAs crystal.

Donor-acceptor-pair transitions (DAP) are transitions between defect states of physically different defects, which are naturally located at different sites within the crystal lattice. DAPs belong to the bound-to-bound transitions and typically involve states in the vicinity of valence and conduction bands. The acronym is (D^0, A^0) in case of neutral donors and acceptors involved. $\left(D^0,\ C^0_{As}\right)$ stands for a transition of an electron from a neutral donor to a neutral carbon acceptor on an arsenic site. The strength of the Coulomb interaction between the localized electron- and hole-states depends on the distance between the particular donor and acceptor sites. Therefore, the transition energies of DAPs created by recombination via different distant donors and acceptors become different, as well. This is described by the so called 'Coulomb-term'. The recombination of carriers trapped in adjacent donor and acceptor sites creates the largest photon energies, while the involvement of defects far apart from each other located defects causes emission at longer wavelengths.

An experimental consequence of this is, e.g. that the spectral position of DAP PL depends on the excitation density. Higher excitation densities populate more states

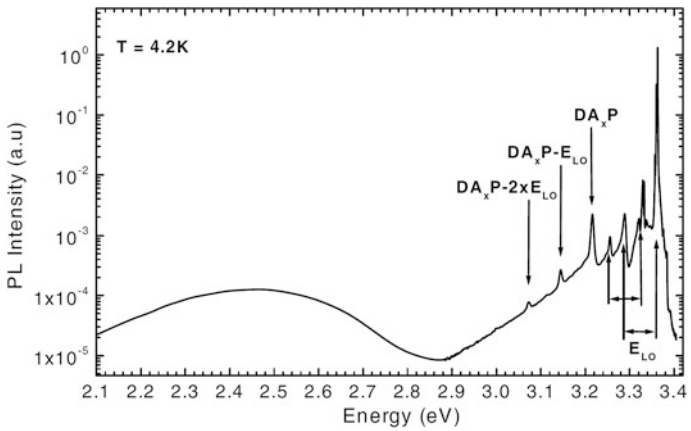

Fig. 4.7 Overview PL spectrum of bulk ZnO showing excitonic, donor acceptor pair (labelled her with DA_xP), and deep level emission. Phonon replica with longitudinal optical phonons (E_{LO}) are indicated [20]

and consequently, there is a higher probability of having close-by recombination partners. This results in a 'bluer' PL.

DAPs typically show series of phonon replica. The strength of the electron-phonon coupling for this type of optical transitions is described by a Huang-Rhys parameter, as well.

Together with transitions via deep centers, the PL lines generated by DAPs are at low photon energies.

Another type of PL lines at low photon energies might be created by inter-subband transitions in QWs. These are relaxation processes between the minibands within the conduction or the valence band. With standard PL setups such transitions, which are typically spectrally located in the mid IR, are not expected to be detected. In so called quantum-cascade diode lasers (QCL), however, such transitions are even used to create IR laser emission. Quantum well infrared photodetectors (QWIP) in turn use these transitions in order to detect IR radiation.

Finally, Fig. 4.7 shows a variety of optical transitions in an overview-PL-spectrum as they were discussed in the preceding sections. The material ZnO represents a typical wide-bandgap semiconductor. Although the details, in particular the relative strength of the PL lines, depend very much on the chosen experimental parameters chosen, the sequence of lines is universal and valid for most semiconductors.

4.4.7 PL Contributions at Energies Larger Than E_g

At the beginning of this section, we mentioned that we will discuss the relevant transitions according to the sequence of their appearance, from higher to lower photon energies. For methodical reasons, however, we waived any discussion of PL

contributions at energies higher than E_g so far, and it should be mentioned as well that most spectroscopists do not even look whether there is PL at photon energies > E_g or not. If present, this type of PL could be subdivided into two groups, into PL spectrally located between the excitation photon energy $\hbar\omega_{\mathrm{exc}}$ and E_g, and such whose energy is not only larger than E_g but *even larger* than $\hbar\omega_{\mathrm{exc}}$.

The latter case is indeed exotic, but may absolutely appear in PL experiments. Non-linear two photon absorption, cascaded absorption via real intermediate levels within the gap, or Auger-processes can provide non-equilibrium carriers with energies that allow them to recombine in a way that high-energy PL photons are created. In most cases, two excitation photons are required to generate a single photon of such 'high-energy' PL emission. There are, however, also reports where the necessary energy for forming the high-energy photons is not provided by two photons but by a single photon together with phonons, i.e. by thermal energy [21, 22].

Sometimes this type of PL is called *upconversion PL*, but this term is also used in a completely other context as we will discuss later.

Although PL lines that are spectrally located *between* $\hbar\omega_{\mathrm{exc}}$ and E_g also do not represent a standard situation, this is a more likely situation than the aforementioned. Mechanisms potentially responsible for such PL will be addressed now:

Hot-carrier PL: In a standard PL experiment, $\hbar\omega_{\mathrm{exc}}$ exceeds E_g. Consequently, the excess energy $\hbar\omega_{\mathrm{exc}}$-$E_g$, which is sometimes called the *quantum defect,* gets initially transmitted to the created electron-hole pair as kinetic energy ($\boldsymbol{k} > 0$). In fact, this means that both carriers (or the exciton) are pushed into the bands. Their energetic relaxation within the band (intraband relaxation) takes place on a ps timescale, eventually resulting in lattice heating. However, a small fraction of non-equilibrium carriers also recombines at high k-values, before a Fermi-distribution is established. This results in *hot PL* from the non-thermal regime.

In addition, after thermalization of the electron-hole plasma (or the excitons) might still have a higher temperature than the semiconductor lattice. According to Fig. 4.5a, this impacts mainly the high-energy side of the interband PL. In fact, the emission is extended to higher photon energies, and its slope in a semi-logarithmic plot allows extracting the *effective carrier temperature*. Consistently, in the excitonic model, see Fig. 4.5b, a larger Γ-value (e.g. caused by an increased effective carrier temperature) also causes an extension of the PL spectrum towards higher photon energies.

PL from higher transition within the intrinsic bandstructure: Considering the intrinsic bandstructure of a bulk Zincblende semiconductor, the resonance at Γ is the one at lowest photon energies of $\sim E_g$. Therefore, it is also called the E_0-transition. In Zincblende material, however, there is a third valence band, namely the split-off band that is separated from the other two (hh and lh) by the energy amount Δ. Exciting such materials with high-energy photons also causes transitions from split-off band to the conduction band. Most of the free holes created in the split-off band relax into the hh and lh valence bands within ps, however, a smaller fraction can recombine radiatively, causing a PL 'edge emission' at higher photon energies, namely at $E_g + \Delta$. This 'edge' is referred to as the $E_0 + \Delta_0$-transition. But there are even higher transitions away from the Γ-point of the Brillouin-zone, which are

named E_1, $E_1 + \Delta_1$, etc.[7] The analysis of the PL via higher transitions is a technique for probing PL properties of narrow-gap semiconductors in order to circumvent the difficulties accompanied with IR PL.

Resonant levels: Defects not only create energy levels within the energy gap, but so-called resonant levels, as well. The term 'resonant' stems from their energetic position that is resonant to either the valence or the conduction band. The presence of such defect levels *within a band* can give rise to optical transitions which involve this level and the opposite band. This results in PL lines which are spectrally blue-shifted beyond E_g.

There are further effects, but also artifacts, which produce or fake additional PL contributions energetically above E_g and elsewhere. A recipe of how to identify artifacts can not be given here. It is always good to know the peculiarities of the PL setup. This includes knowledge about the instrument function, see Sect. 4.3, but also knowledge about additional lines from the excitation laser (e.g. plasma lines) and the spectral position of their second and higher orders after having been diffracted by the grating of the monochromator. Further identification steps for unexpected PL contributions involve a systematic parameter variation, e.g. of excitation density, temperature, or the application of an additional independent spectroscopic technique. This is what makes the distinction of a good spectroscopist. However, the identification of the nature of PL lines in semiconductor materials is always a demanding challenge.

4.4.8 The Impact of the Parameter Excitation Density

In the preceding paragraphs of Sect. 4.4, we addressed the variety of optical transitions in semiconductors. We learned that the semiconductor material or the epitaxial structure determine the appearance of the PL spectrum, but there are also experimental parameters which influence how the PL spectrum looks like. In Sect. 4.4.4, e.g., we addressed how the parameters temperature and carrier concentration can act either in favor of band-to-band- or excitonic transitions as dominating *edge emission* mechanisms.

The parameter *excitation density* is a fundamental external parameter, which can determine the shape of PL spectra. Figures 4.8 show excitation dependent spectra for various materials and structures. Something that is observed in almost all PL experiments is shown in Fig. 4.8a for nominally undoped GaN: [23] While transitions related to extrinsic defects, such as DAP, (e, A), and transitions involving deep level defects dominate the spectrum at very low densities, edge emission features like the (D,X) at 3.475 eV dominate at elevated excitation densities. This evolution can be understood as a kind of 'filling of the available states'; starting

[7]Do not mix this denotation with the naming of the excited states in QWs, where the allowed optical transition energies are sometimes numbered in the same way, namely E_1, E_2, … .

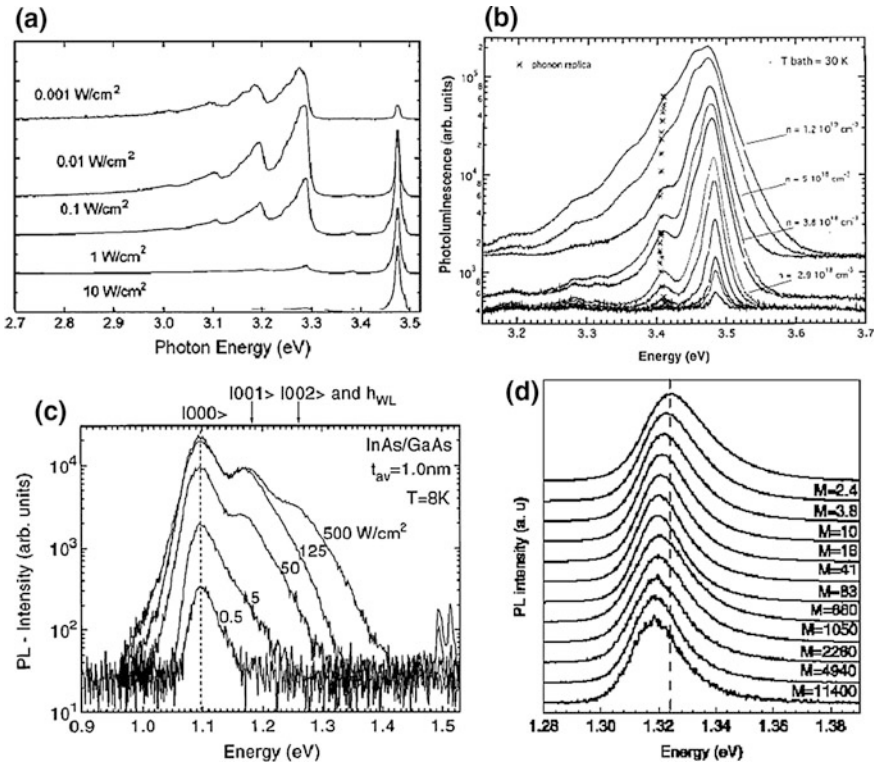

Fig. 4.8 PL spectra monitored at different excitation densities: **a**, **b** GaN [23, 24] **c** InAs/GaAs QDs [25] **d** hexagonal nanopillars containing a single InGaAs/GaAs QW [26]

with defect-related transitions at lowest energies and ending with the edge emission at highest energies. Sometimes this is called 'global state filling'. For further increased densities, the bands are filled and the carrier ensemble is heated. This is very nicely visible in Fig. 4.8b, where an increasing 'high-energy tail' of 'hot carriers' from the edge emission (above 3.5 eV) is revealed [24]. For a lattice temperature of 30 K, the authors find for increasing densities of 1.4–16 MW cm^{-2} effective carrier temperatures of 123–228 K for increasing densities of 1.4–16 MW cm^{-2}, respectively.

Figure 4.8c, d show excitation dependent spectra from highly-confined electron-hole pairs, namely in QDs and single QW layers in nanopillars. For the InAs/GaAs QDs, see Fig. 4.8c, the tendencies are very similar to those in the wide-gap bulk material as discussed in Fig. 4.8a: with increasing excitation density, higher-energy states are filled and hence higher-energy optical transitions become dominant. In case of this particular nanostructure, the higher energy states are formed by the excited QD states [25]. Even PL contributions from wetting layers become visible in such structures.

In Fig. 4.8d, excitation dependent spectra from single QW layers in nanopillars are shown, while the density is increased by about four orders of magnitude [26]. Here, the modifications in terms of PL lineshape and peak position are rather small. The slight blue shift of the spectra can be explained by effects of piezoelectricity, photon screening, and band filling.

4.5 Applications of Steady-State Photoluminescence

Although it was not explicitly expressed, all preceding sections in chapter 4 dealt with steady-state PL, i.e. with PL excited by cw lasers. Indeed, this represents a standard PL approach. What information can we actually extract from steady-state PL spectra?

The answer is rather simple: if we analyze the edge emission, we can obtain exactly those parameters which go into (1.70), at least as long as the band-to-band model is still applicable; see Sect. 4.4.2. Correspondingly, the same holds for the excitonic model; see Sects. 4.4.3 and 4.4.5. Obviously, these 'true' answers are not very helpful and therefore we will present examples, in which steady-state PL is used as a tool.

The following list is not exhaustive, but it represents the subjectively biased view of the author on experiments that demonstrate the power of the steady-state PL technique.

4.5.1 Analysis of E_g Shifts

The determination of E_g of a 'new' or 'unknown' material by PL measurements alone is not feasible. Too many parameters go into PL lineshapes and often the assignment of the lines in observed spectra is not unambiguous. Moreover, E_g-values of elementary semiconductors and binary alloys, such as GaAs or ZnO, are well known. On the other hand, E_g is a parameter which is clearly related to many optical transitions, in particular to those of the edge emission. For ideal band-to-band transitions, E_g represents the low-energy limit of the spectrum. In contrast, the X transition peaks at an energy that is red-shifted by the amount of E_x with respect to E_g; see Sect. 4.4. Shallow levels are closely coupled to E_g, as well. Thus, the edge PL is, if well understood, an utmost sensitive tool for the determination of even very small *E_g-shifts*.

We will start our survey with *bulk material*. Here, E_g-shifts can be caused by the application of 'external forces' such as mechanical stress, electric, or magnetic fields. Elevated carrier concentrations can also shift actual E_g-values via the mechanism of band gap renormalization. In such situations, PL can be an utmost precise tool for the determination of the expected E_g-shifts.

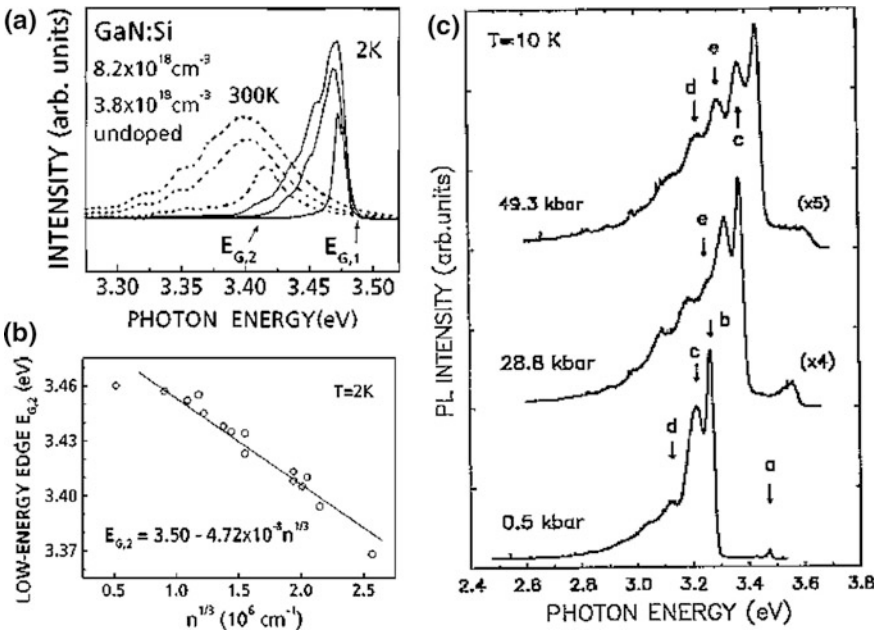

Fig. 4.9 Bandgap shifts deduced from PL spectra from GaN samples. **a**, **b** The influence of carrier concentration according to Yoshikawa et al. [27]. **c** The influence of external pressure according to Hwang et al. [28]

Figures 4.9 show the effects of elevated equilibrium carrier concentrations (a, b) and stress (c) on PL spectra of GaN. Figure 4.9a shows the red-shift of PL spectra with increasing carrier concentrations at 2 K and ambient temperature [27]. This shift is quantified in Fig. 4.9b, in which it is plotted versus $n_0^{1/3}$, resulting in a linear relationship as already known from other materials such as GaAs. In this particular case, n_0 is determined by the extrinsic Si-doping level. Figure 4.9c shows how a reduction of the lattice constant of GaN impacts on the PL spectrum [28]. The blue shift of the PL indicates an E_g-shift towards larger values. In this particular case, the reduction of the lattice constant is implemented by hydrostatic pressure, whose values are indicated in the figure, as well. Blue shifts of PL spectra can also be caused by E_g-shifts in magnetic fields B.

Figure 4.10 shows PL spectra from GaAs monitored for increasing B-values. Full circles give the spectral position of the X line vs. B [29]. These examples illustrate a cardinal condition for the application of this type of 'E_g-shift analysis': *E_g should be the one and only parameter to be modified by the external force.* However, this is mostly not the case. Since the exciton binding energy also depends on the magnetic field, i.e. $E_x = E_x(B)$ the observed shift of the X line is determined by both $E_x(B)$ and $E_g(B)$, resulting in the so-called *diamagnetic shift* of the exciton at smaller B-values as indicated in Fig. 4.10. For larger B-values, the shift of the

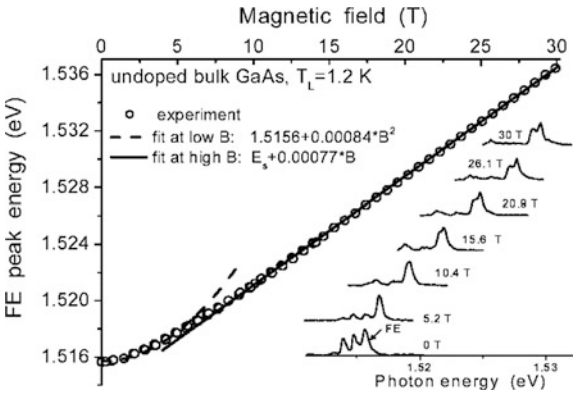

Fig. 4.10 Bandgap shifts deduced from PL spectra from GaAs samples in an external magnetic field according to Ashkinadze et al. [29]

X line (as given in the figure) is expected to show the genuine almost linear $E_g(B)$-shift.

After having discussed the impact of 'cautious' doping during growth to the PL spectra, we will now come to a rather 'harsh' way of modifying the carrier concentration, ion implantation. Figure 4.11a, b show the effect on the PL spectra, caused by Cd^+ and Cd^+, N^+ ion implantation, respectively. While the reference spectra from un-implanted material, labeled in both plots as (A), are dominated by edge emission, increasing implantation doses shift the spectrum more and more to lower energies, indicating the increasing relevance of recombination via extrinsic defects [30]. Notice that except for the 'doping effect' of the implanted atoms, the structural damage caused by the implantation process itself represents a major source for the creation of defect centers and resulting doping effects.

Except for 'external forces', alloying results in E_g-shifts, as well. Alloying here means proceeding from a binary semiconductor such as GaAs or CdTe with a very well-known bandstructure to a mixed crystal system such as $Ga_{1-x}Al_xAs$ or $Hg_{1-x}Cd_xTe$ in which E_g is determined by the *mole fraction* (x) that is often alternatively called 'composition'. Figure 4.12 shows PL spectra obtained from a set of $Ga_{1-x}Al_xAs$-samples with different x-values, which are given on top of the PL lines [31]. Obviously, in this x-range, the PL lineshape does not undergo substantial modifications. This makes it likely that we do indeed see E_g-shifts here. Therefore, this data has been used by the authors for calibration purposes. Thus, this is an application of PL as a tool for the determination of mole fractions x in mixed crystal systems. In [32] this topic is addressed in great detail. Overall, PL offers a very elegant way for monitoring x-trends in structures.

Turning our discussion from bulk semiconductor material towards micro- or nanostructures, the same tendencies basically remain effective. However, the term 'E_g' must now be replaced by 'lowest quantum-confined optical transition' or 'ground-state transition'. Figure 4.13a shows a QW structure that features a lateral

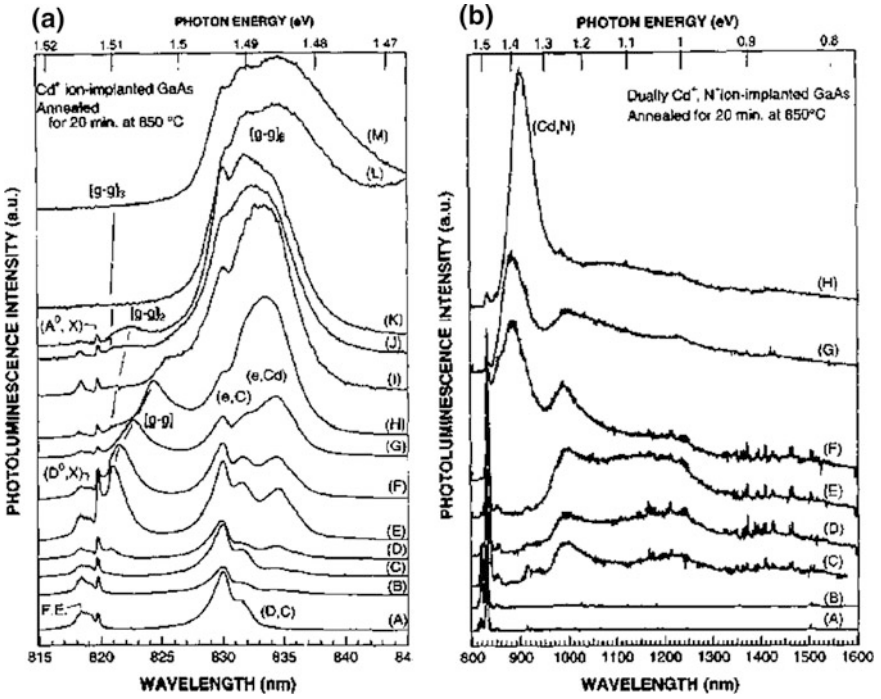

Fig. 4.11 Evolution of PL spectra from GaAs in dependence on the concentration of implanted atoms according to Kotani et al. [30]. **a** Cd concentration increasing from 10^{16} to 3×10^{21} cm^{-3} [from (B) to (M)]. **b** Cd + N concentration increasing from 10^{17} to 10^{20} cm^{-3} [from (B) to (H)]

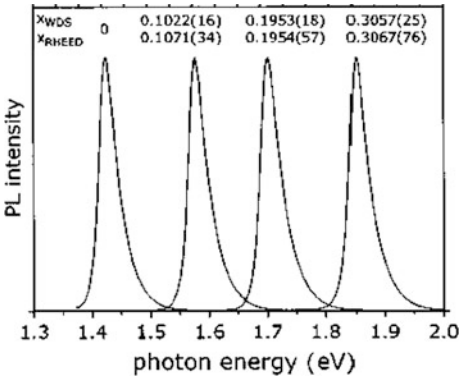

Fig. 4.12 Room-temperature PL spectra from $Al_xGa_{1-x}As$ films with differing mole fractions; see labels on *top* of the spectra [31]

modification of the band-structure. An InGaAs QW is overgrown by an InGaP 'stressor' layer, which compresses the QW thanks to its smaller lattice constant. After removing stripes of stressor material, an additional lateral modification of the band-structure is achieved; see results of modelling work and PL data given in Fig. 4.13b, c, respectively [33].

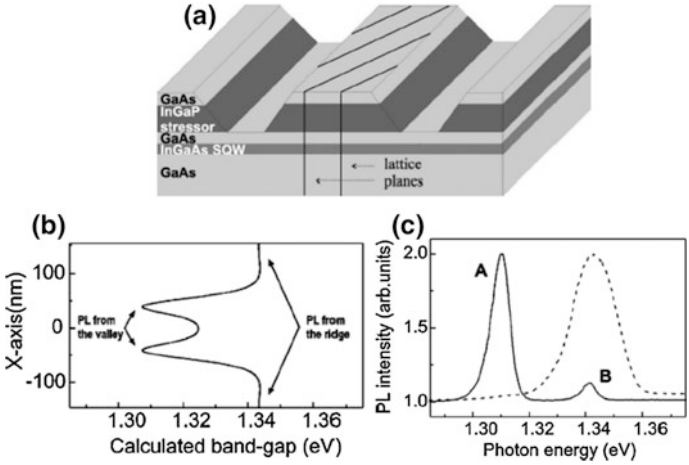

Fig. 4.13 **a** QW structure with a subsequently introduced lateral band-structure modification. **b** Calculated lateral band-structure modification. **c** PL spectra from such a structure with (*full line*) and without (*dashed line*) subsequently introduced lateral band-structure modification [33]

The bandstructure of this compressed QW without any lateral modification is probed by PL; see the dashed spectrum in Fig. 4.13c consisting of one single line labelled B. The PL from the modified QW structure shows two contributions, one from the compressed (B) and another red-shifted one from the relaxed parts of the QW (A); see full line in Fig. 4.13c. At first glance, one might be surprised why the PL line from the strained QW is that drastically reduced. This finding becomes clear when we bear in mind that the width of the removed stripes is smaller than L_D, and therefore an effective carrier drift (field-enhanced diffusion) takes place towards the narrower-gap strain-relaxed stripes of the QW. In Sect. 4.6.3, we will show for this type of samples, how our present tentatively given assignment of the PL spectra is confirmed by time-resolved PL.

4.5.2 Surface Recombination Velocity

Since PL is implemented by external laser excitation in a semiconductor, this kind of spectroscopy inherently involves effects related to the surface, where the laser beam 'intrudes' into the material and has the highest intensity. In Sect. 4.2.1, we introduced the parameter surface recombination velocity s. The model calculation presented in Fig. 4.2a has demonstrated the impact of the surface recombination to the carrier distribution and hence the total number of steady-state nonequilibrium carriers δn for a given excitation density. According to $I_{PL} \propto \delta n$, this directly affects the PL signal. In fact, samples with poorer surface quality show poorer PL signals, as well.

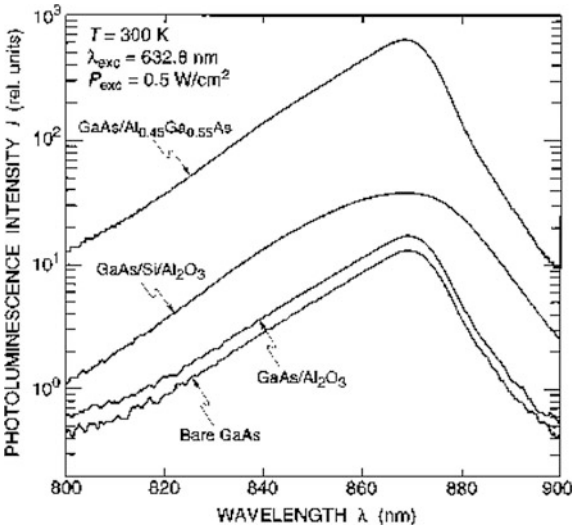

Fig. 4.14 Room temperature PL spectra of GaAs samples with no coating (*bottom spectrum*) and several different coatings [34]

Figure 4.14 illustrates this for the PL of differently treated *n*-GaAs surfaces [34]. These surfaces have been prepared while advanced methods for the fabrication of diode laser facets were developed. Out-coupling facets of diode lasers are indeed semiconductor surfaces that have to withstand very high optical loads on the order of several 10 MW cm^{-2} even during long-term operation of several thousand hours. Thus the achievement of low *s*-values is crucial. In this example, regular cw-PL represents the tool that allows us to compare the effects of surface treatments. The comparison of *s*-values is valid as long as all other parameters are kept constant. However, true *s*-measurements are not possible with a standard PL experiment. In Sect. 4.6.3, we will address this topic again and show how time-resolved PL helps to come closer to accomplishing this goal.

4.5.3 Rare Earth or Transition Metal Atoms in Semiconductors

So far we focused our discussion on PL from semiconductors to optical transitions within bandstructures of the materials. However, there are inner-atomic transitions that could provide PL lines, as well: while the electronic states of the valence electrons of the atoms merge into bands when the atoms are chemically bound to form the semiconductor lattice, *inner atomic shells* remain unaffected. The inner-atomic shells of transition metals such as Cr, Mn or Fe and rare earths such as Eu, Er, or Yb are not completely occupied. This allows *internal transitions* within the incompletely occupied 3d- and 4f-shells in transition metals and rare earths, respectively. Such *luminescent atoms* frequently maintain, at least in part, their

ability to emit light via inner-shell-transitions even if involved into a crystal lattice either as dopand or even as 'regular ingredient' in mixed crystal lattices such as $Cd_{1-x}Mn_xTe$ or Pb_{1-x} Eu_xTe.

Figure 4.15 show PL caused by inner-shell-transitions in (a) the $Zn_{1-x}Mn_{1-x}Te$ mixed crystal system, in (b) InP:Yb, and in (c, d) diluted $Ga_{0.99}Mn_{0.01}N$. In the two top Figs., both types of transitions are shown, the intra-3d- and intra-4f-shell

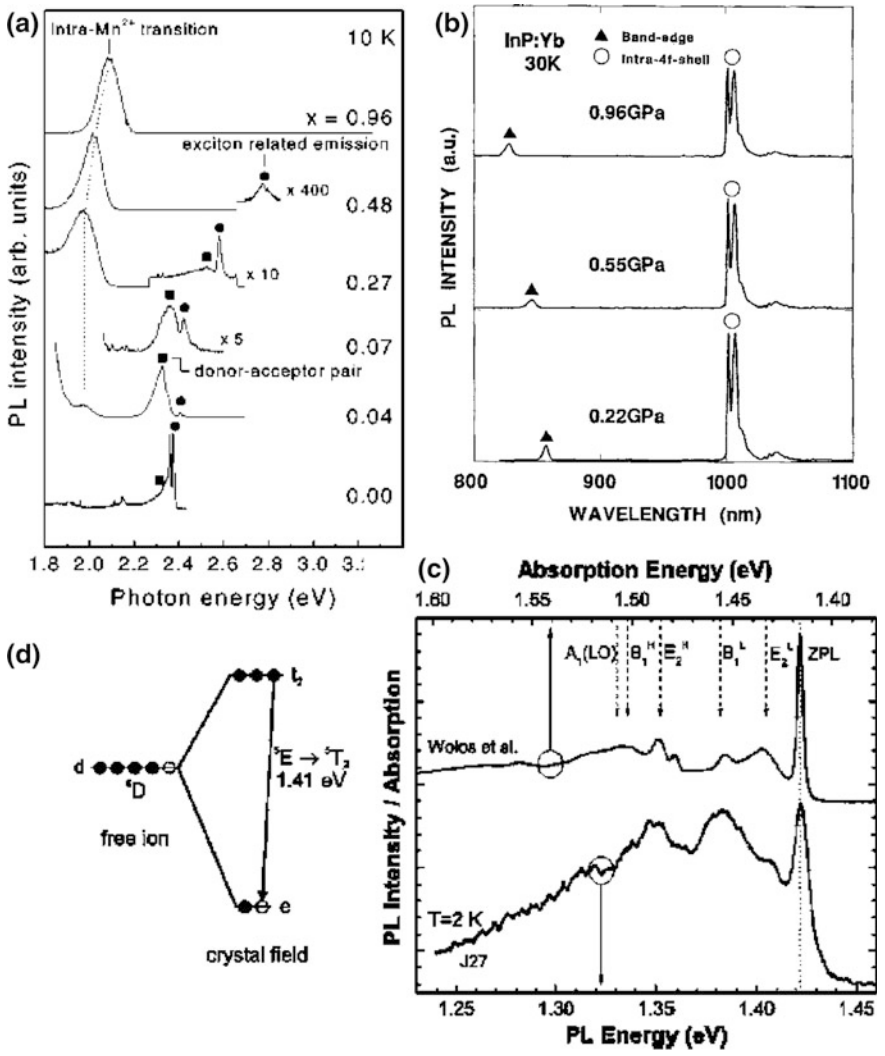

Fig. 4.15 **a** Dependence of the PL spectra on the Mn-content of $Zn_{1-x}Mn_xTe$ epilayers at 10 K. The *dots* refer to the excitonic transitions in the mixed crystal system [35]. **b** Dependence of the PL spectra of InP:Yb on the hydrostatic pressure. The triangles refer to the excitonic transitions. [36]. **c** PL from GaMnN with a Mn content of about 0.5 %; see lower spectrum. **d** Proposed transition scheme [37]

transitions at lower photon energies, and the edge emissions from the $Zn_{1-x}Mn_{1-x}Te$ and InP hosts at larger photon energies. In (a), the parameter is the Mn-content of the mixed crystal [35]. This is particularly notable because two modifications are achieved by the Mn alloying at the same time: first, by the nature of the 'host material', e.g. the E_g-value is modified, and secondly because the concentration of the Mn 'luminescent atoms' is changed. Both effects are visible in the spectra. In (b), the lattice constant of the host is tuned by the application of hydrostatic pressure [36]. While the expected E_g-tuning of the host PL (see triangles) is well visible, the inner-shell-transition PL remains nearly unaffected (see open circles). In (c), a completely different example of inner-shell PL is presented, an infrared emission out of wide-bandgap $Ga_{0.99}Mn_{0.01}N$ [37]. In this particular case, the states that are involved in the PL generation are not created until the Mn-ions becomes are into the GaN-matrix, i.e. feel the impact of the crystal field of the host; see scheme in (d).

These examples demonstrate the multifaceted character of what is achieved by the introduction of rare earth or transition metal 'luminescent atoms' into semiconductors.

- For instance, they can be alloyed into other materials which results in the formation of mixed crystal systems. This leads to a modification of the edge PL by an E_g-shift, broadening effects, etc.
- If 'luminescent atoms' are introduced into a host, they modify its potential. Thus they might act as 'defects' and create defect states, which can be involved into extra optical transitions that appear as extra PL lines or as sites for exciton localization.
- The 'luminescent atoms' frequently maintain their ability to perform inner-shell-transitions after having been excited. Their excitation typically takes place via the host semiconductor material.
- Thus there might be two types of PL, one from the host and one from the 'luminescent atoms'. Typically the presence of 'luminescent atoms' also impacts to the host PL, and the presence of a host material modifies the inner-shell-transitions PL.
- If 'external forces' are applied, the two types of PL emission often react very much different, because of their completely different physical origins.

Notice that the analysis of the PL from 'luminescent atoms' also represents an important *analytical PL tool* for investigations of the incorporation of atoms into a host lattice. Modifications of the inner-shell-transitions PL which is caused by the host's crystal potential allow us to analyze the incorporation and to provide the so-called *crystal corrections*. In this way, 'luminescent atoms' became a type of 'nanoprobes' reporting with their PL out of semiconductor crystal lattices long before genuine nanostructures entered the agenda of optical spectroscopy.

4.5.4 Infrared Fourier-Transform Photoluminescence

The extension of all PL methodology, see Sect. 4.3, towards the NIR is rather straightforward.

- The first severe barrier towards the MIR is reached, however, when optical elements made of fused silica become opaque at ~2.4 μm wavelength. Thus, they must be replaced either by IR-grade lenses made of semiconductor materials such as ZnSe, Ge, chalcogenide glasses, or mirrors. In many cases, mirrors represent an excellent choice because of their wavelength-independent foci.
- A second severe barrier in the MIR is approached, when the signal merges into the 300 K thermal background of Planck's radiation.

In either case, MIR PL spectroscopy is struggling with small signals, partly because the signals are indeed very small, and partly because of the limited performance of the typical IR detectors made of Ge, InGaAs, InSb, $Hg_{1-x}Cd_xTe$, or QWIP's. This sad statement is true, at least if one compares these detectors to single-photon counting systems, which are available for the VIS-NIR. Maximization of the light throughput towards the detector becomes very important. In this situation, FT-spectrometer with their *throughput- or Jacquinot-advantage* came into play; see Sect. 2.2.3. Originally, they had been developed for transmittance and reflectance spectroscopy in the IR. But after they became equipped with cooled MIR detectors, they became important tools for IR PL spectroscopy, as well. Since the measurement procedure in FT-spectrometers is essentially a DC measurement, the need to eliminate the thermal background became urgent. Either a double modulation technique (look-in measurement for very-slow interferometer mirror motion velocities or even step-scan-operation) or phase selective excitation [38] (phase locking of PL excitation and interferometer mirror motion) provide experimental solutions.

Figure 4.16 show excitation-dependent FT PL spectra from bulk narrow-gap semiconductors $Hg_{0.78}Cd_{0.22}Te$ [39] and InSb [40] at low temperatures as examples for MIR PL.

The main reason to use Fourier spectrometers for PL spectroscopy is the inherent *Jacquinot-advantage*, while the *Fellgett-advantage* is less important due to the typically relatively small bandwidths of PL spectra in general. The same holds for the *Connes-advantage* and high spectral resolution. It is convenient to have them but they are not important for PL spectroscopy of semiconductors. However, in the next subsections we will provide at least one exception in which even PL lines from bulk materials might be narrower that resolvable by FT PL.

Take note of several papers which stress that FT PL spectra may be affected by artifacts produced by the sampling, [41] computing, [42] alignment, etc. Therefore, if 'novel' PL lines are observed by FT PL, in particular if they are spectrally located at multiple wavelengths of a known emissions such as the excitation laser (second-harmonic artifact), [43] one should be very cautious with further interpretations. Insertion of appropriate edge filters is one methodological approach that

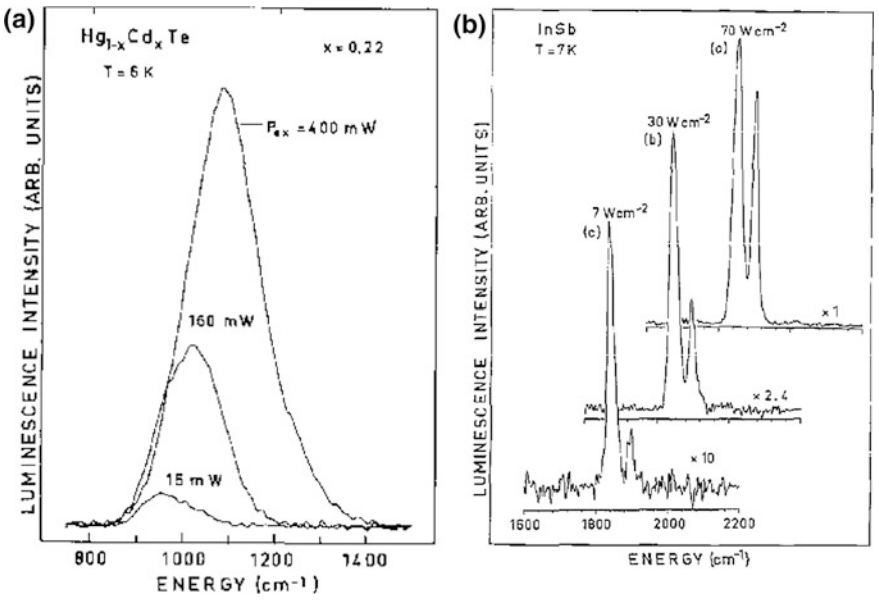

Fig. 4.16 FT PL spectra from $Hg_{0.78}Cd_{0.22}Te$ [39] (**a**) and InSb (**b**) [40]

helps to identify the nature of such make-believe PL contributions. Alternatively, cross-checking with monochromator-based setups can provide clarity.

4.5.5 Photoluminescence from Indirect Materials

By far the most important semiconducting material, silicon, is an *indirect* semiconductor. Nevertheless, it is of utmost importance for optoelectronics as well, because it is a major detector material. In addition, Si is the best-mastered semiconductor with respect to purity, crystal perfection, and technology. Thus, Si has always been an attractive material for basic studies, and this statement holds despite the low PL signals. From the point of view of emitter applications, a cardinal goal since decades is to 'make Si a luminescent material'. The tool to check the success of such approaches is, of course, PL again. In this subsection, we will address exclusively PL on Si which is representative for all other indirect semiconductors, in particular also Germanium.

In an indirect material, radiative recombination requires the participation of additional quasiparticles in order to match both energy and momentum conservation at the same time. In this respect, phonons with their large quasi-momentums and rather small energies perfectly match to photons and therefore, most PL lines observed in Si are created by so-called *phonon assisted* transitions; i.e. transitions under participation of one or more phonons. This statement holds for (almost) all

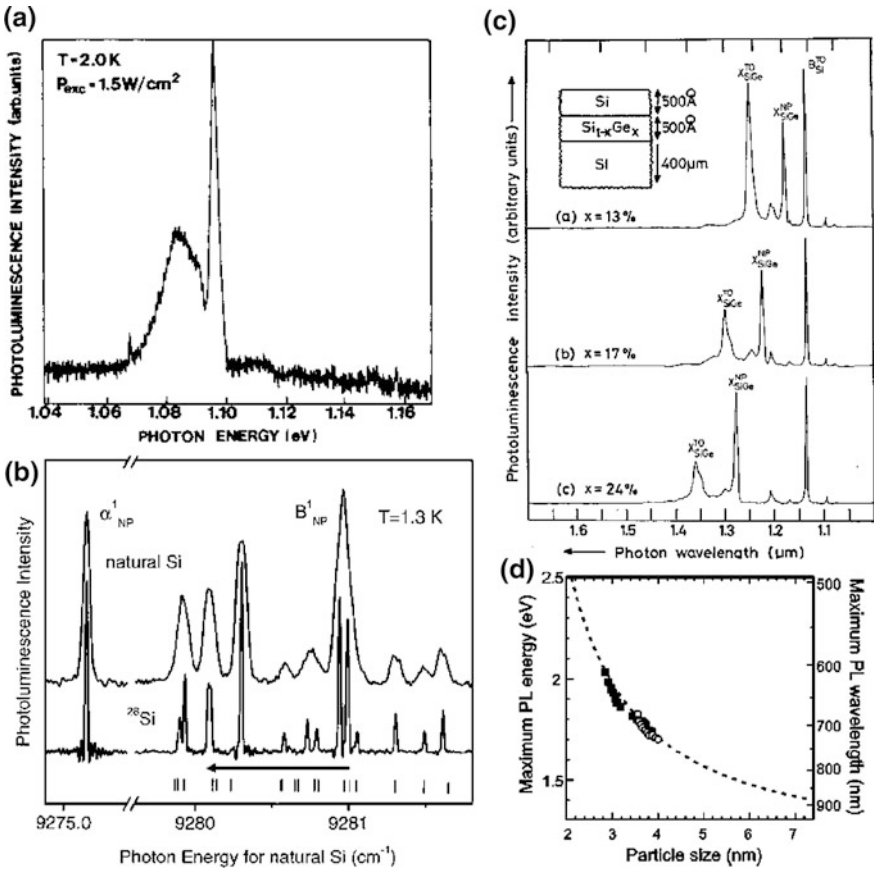

Fig. 4.17 **a** PL spectrum from a Si-crystal [44]. **b** PL spectra from natural (*top*) and monoisotopic Si (*bottom*) [45]. **c** PL spectra from $Si_{1-x}Ge_x$-alloys [46]. **d** PL peak position versus Si-QD size [47]

types of transitions which have been discussed in previous sections for direct materials.

Figure 4.17a shows a low-temperature PL spectrum of a high-quality float-zone Si crystal [44]. There are two PL lines, namely X^{LO}, i.e. the first LO-phonon phonon replica of the X-line at 1.097 eV, and the first LO-phonon phonon replica of the electron-hole-droplet (EHD) emission.[8] The presence of an EHD is a peculiarity of excitons in indirect materials, and has therefore not been addressed

[8]EHD emission appears, for energetic reasons, at elevated exciton densities (but below the Mott-density) and at low temperatures and can be illustrated in analogy to the nucleation of water droplets. Relevant parameters for Silicon are: stabilization energy ~8 meV, exciton density 3.3×10^{18} cm^{-3}, and temperature <24 K.

before. We do not see any PL contribution at X because emission without participation of phonons is forbidden in the indirect material. This strict rule is relaxed for localized excitations such as BEs, or in materials with broken symmetry such as alloys or nanostructures, which we will address now. Figure 4.17b shows such PL from zero- or no-phonon lines. Here, Phosphorus and Boron BE emission from 'natural' Si is monitored and denoted as α^1_{NP} and B^1_{NP}, respectively; see the upper spectrum [45]. By using ultrahigh spectral resolution PL with an energy resolution as low as $\sim$1.7 μeV (as achieved by FT PL), the authors demonstrate that the BE PL shows a fine structure in monoisotopic Si. This finding reveals isotopic randomness as the main broadening mechanism for the considered BE PL in 'natural' Si.

Figure 4.17c, d show PL data from heterostructures containing $Si_{1-x}Ge_x$-alloys and Si-QDs, respectively. The PL spectra from the structures, see Fig. 4.17c, shows a set of excitonic lines that stem from the narrower-gap $Si_{1-x}Ge_x$ alloys and the Si-layers that clad it [46]. While the cladding contribution, the first TO phonon replica of the Boron BE in Silicon (denoted by the authors as B^{TO}_{Si}), stands constant in all spectra, the lines from the alloy shift with changing x- and E_g-values. Both the X-line from the alloy and its first TO phonon replicas are visible. Again, the presence of the original X-line from an indirect material is surprising but can be explained by the broken symmetry in the alloy. Figure 4.17d shows PL peak positions from Si-QDs [47]. The corresponding PL spectra consist of one band only and shift, driven by quantum size effect, for small QDs well into the VIS. The PL efficiencies of such QDs are much higher than in bulk silicon and such results certainly arise hopes to find ways preparing Si-based nanostructures light emitting materials.

4.6 Time-Resolved Photoluminescence (TR PL)

4.6.1 Introduction

We have shown that steady-state carrier concentration as well as the information depth in a cw PL experiment are determined by the parameter of *non-equilibrium carrier recombination lifetime* τ*;* see also (4.3). τ is often only called *lifetime*. It describes the kinetics of a non-equilibrium population decay $\delta n(t) = \delta p(t)$, provided that the number of recombining carriers pairs is proportional to the total number of excited carrier pairs $\delta n = \delta p$. This situation is called *linear recombination* and is described by an exponential, in which τ is the *decay time constant*. In fact, the independence of τ on δn is given in limited intervals, at best. Thus *non-linear* recombination is an issue which must be addressed. Auger-recombination, for

instance, is well-known as an intrinsic process that results in non-linear recombination, at least at high δn. Many other effects such as carrier transport [see (4.2)] and recombination including excitonic and defect-related processes cause non-linearities of the carrier decay as well. Naturally, the same holds for stimulated emission at high δn.

There is another type of linearity, whose existence is of crucial importance for all TR PL analysis: it is the assumption that the radiative recombination mechanism, which creates the PL signal that is analyzed, is proportional to δn, i.e.

$$I_{\mathrm{PL}}(t) \propto \delta n \qquad or \qquad I_{\mathrm{PL}}(t) \propto \delta p. \tag{4.8}$$

In other words: The PL signal, which is picked up, is assumed to be proportional to the non-equilibrium carrier population $\delta n(t) = \delta p(t)$ that decays. This is the link between all types of TR PL experiments and the conclusions regarding carrier kinetics. The assumption is valid in wide ranges, but it is invalid if the *radiative recombination* mechanism becomes non-linearly dependent on δn.

TR PL setups typically employ a pulsed laser as an excitation source and a fast detection system which is able to monitor the PL transient $I_{\mathrm{PL}}(t)$. The choice of laser and detector are determined by the required time resolution.

What time constants can we expect? Obviously, this depends on the processes which one intends to investigate:

- For characterization purposes, the *lifetime* τ is often needed. If interband recombination in direct materials is considered, the range 10^{-9}–10^{-7} can be expected.
- Trapping into QWs, a process which even involves carrier transport, takes place on a scale of several 10 ps [48]. The same scale is relevant for *carrier (excitation) transfer* between different nanostructures, e.g. between QW and QDs.
- Trapping into defects often takes place on a ps range, as well [5]. If the capture of formerly free electrons from one band into a defect center is substantially more efficient than the emission (or recombination) into the other band, these defect centers are called *traps*. In some cases, the capture into 'traps' takes place even on a sub-ps-scale [4]
- As already mentioned when addressing cw PL, the relaxation of carriers within a band is accomplished on a ps-timescale. The range, before a Fermi-distribution is established, is called the *non-thermal regime*. Inter-miniband-transitions, i.e. transitions between different sub-bands within either the valence or conduction band, take place on a comparable timescale.
- Ultrafast processes on a fs-timescale, such as the coherence decay by *dephasing* (mainly scattering processes), can be addressed by PL, as well, although on this timescale, other experimental approaches, such as pump-probe-spectroscopy, are more relevant.

4.6.2 TR PL: Experimental

The photons, which are collected, transmitted, and focused by the optics of a cw PL setup, see Fig. 4.3, could have traveled along slightly different tracks. Some of them might have been transmitted close to the optical axis, some of them a little off. When we take the velocity of light into account, a 30 mm optical path difference which might have been be accumulated in a standard cw PL setup, creates almost 0.1 ns temporal broadening of any PL signal. In other words: *the wavefront of the PL signal which was created by a short pulse, is deformed by the optics.* The good news from this estimate is that TR PL can be easily accomplished with standard TR PL setups, by following the guidelines as they were given in Sect. 4.3, even down to the sub-ns resolution range.

Additionally, the time resolution of a standard TR PL setup is limited by both the excitation laser pulse width and the time resolution of the detection system. Both should complement each other and meet the time resolution required for solving the spectroscopic task. It is also possible that one of them is better; however, such a solution will probably not be the most economic one.

Lasers: Pulsed lasers can be gain-switched, Q-switched, or mode-locked. Externally modulated cw lasers are less common.

- A typical standard pulse source for TR PL is the frequency doubled (532 nm) or tripled (355 nm) Q-switched Nd:YAG laser, which provides pulse-length in the ns range.
- Mode-locked lasers reach the sub ps-range. Here, either YAG-based lasers or the Ti:Sapphire (750–1000 nm) are representative for usual hardware. Although being able to provide extremely short pulses, these systems have fixed repetition rates in the region of 76–82 MHz. In other words: the time between subsequent pulses is, e.g. $\sim$12 ns in case of 82 MHz. If the PL decay has a time constant reaching this order (or even longer), there will definitely be carrier accumulation. Lowering the repetition rate in mode-locked systems is only possible by using *pulse pickers*.
- In TR PL, semiconductor lasers take a larger part than in cw PL. The simplest way of producing pulses is to drive them with current pulses (gain switching). Pulses with widths on the order of ns- are obtained in this way.
  Q-switched semiconductor laser allow pulsed operation with pulse lengths down to about 50 ps. Often passive Q-switching (using saturable absorber facets) is combined with gain switching by the laser driver.
  The typically very high repetition rates (GHz) of mode-locked diode lasers make them less suitable for PL applications; see points above.

The choice of the 'right' repetition rate is crucial. A high repetition rate allows us to reduce the required measuring (averaging) time. If long time constants are involved into the recombination, however, an elevated repetition rates carrier accumulation will take place. This leads to a quasi-steady state situation not

necessarily close to the equilibrium case, when a subsequent excitation pulse begins. Whether this is the case or not can be tested experimentally by varying the repetition rate in a wider range.

The pulsed excitation laser and detector have to be synchronized, and the temporally resolved detector signal, often called *PL transient*, is monitored. Pulsed operation allows averaging over many pulses, for instance by using the box-car technique or a sampling oscilloscope.

Detectors: PL detection can be accomplished, e.g., by fast Si-photodiodes (*pn*-, *pin*-, or Schottky-type) which reach the sub-ns response time range. Even temporal resolutions down to 10 ps are possible at the expense of sensitivity, which is, on the other hand, another urgent requirement in PL spectroscopy.

In this situation, *avalanche photodiodes* (APD) represent an excellent trade-off. Thanks to internal amplification, APDs offer the advantage that the detection limit can be improved substantially, typically by two to four orders of magnitude compared to standard photodiodes, while response times of 100 ps are maintained.

Time-correlated single photon counting is another option to reach ps-time resolution, even if the PL signals are very weak. Here PL transients are reconstructed out of multiple measurements of the time between excitation laser pulse and the arrival of a single photon at the detector (e.g. a PMT). Climactic summation of the data from many PL pulses allows the reconstruction of PL transients as a histogram. Time resolutions on the order of 10 ps are reached.

Streak-cameras represent another option for accomplishing TR PL with ps- and even sub-ps time resolution. Photons create free electrons at a photocathode, which are accelerated in an electric field. A perpendicular applied AC field[9] deflects them in a defined way, so that the temporal profile of the PL signal becomes transformed into a spatial profile, just similar to an oscilloscope. After passing an electron amplifier, called multi-channel plate, the electrons hit a phosphor screen. The image at the screen is then imaged by a CCD camera.

Which of these options finally will be chosen depends on the desired time resolution and 'non-scientific' boundary conditions such as equipment that is already available, organization of the work (throughput), etc. Figure 4.18a shows a TR PL setup which involves a mode-locked Ti:Sapphire laser, an optical parametric oscillator (providing NIR pulses) and frequency-doubling for both, as well as a synchro-scan streak-camera for detection; see [49].

For the sake of completeness, we would also like to mention a special type of TR PL which is called *phase fluorimetry*. It relies on analysis of the phase shift between a sinusoidal excitation of the frequency f and the subsequent PL signal. This method works best if $1/f$ is on the order of τ. Typically, a cw excitation laser beam is modulated by a sinusoidal or rectangular function, e.g. by electro-optical modulators or fast mechanical choppers. The same type of excitation and phase-sensitive analysis is used in photocurrent spectroscopy, as well. Analysis of

[9]This AC field must be synchronized with the excitation laser's repetition rate.

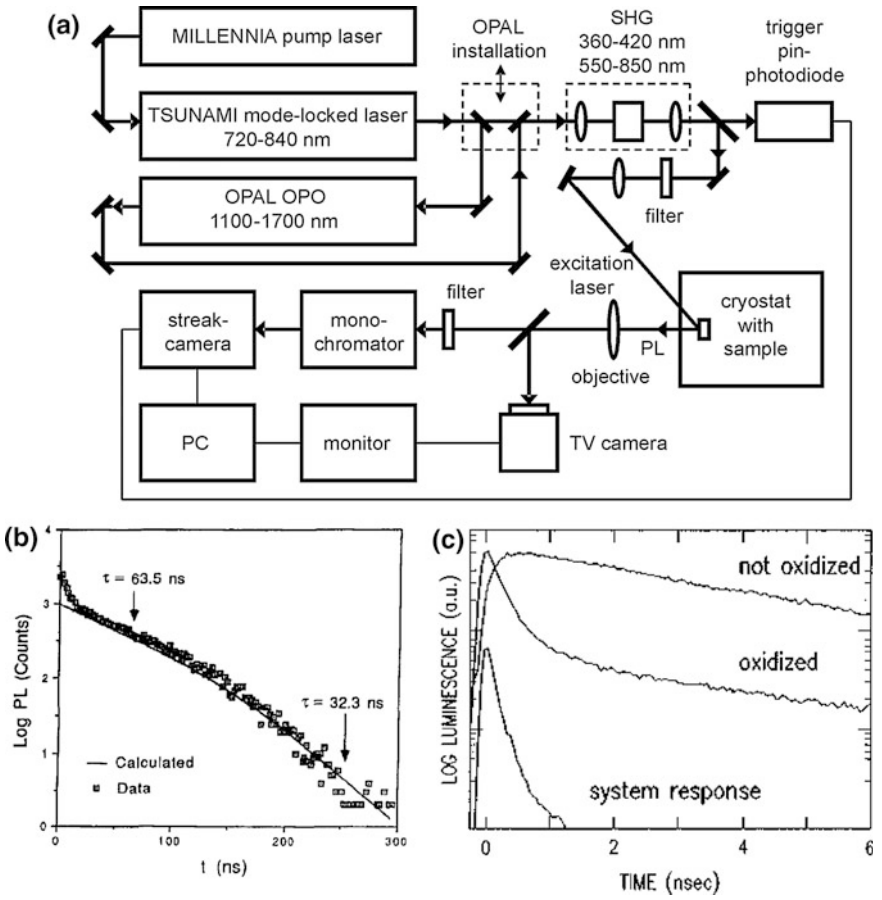

Fig. 4.18 **a** Schematic of a TR PL setup. **b** PL decay from an AlGaAs double heterostructure with a non-exponential decay. The characteristic downturn of the decay-curve points to dominating non-radiative Shockley-Read-Hall recombination [50]. **c** TR PL transients from a GaAs surface before and after oxidation [51]

such PL and photocurrent data is made in exactly the same way and will be addressed in Chap. 6. The basic assumption is that only one single τ-value determines the phase. This is not necessarily valid. Thus, its application to semiconductor analysis is less straight forward, compared to direct monitoring of PL transients after short impulsive excitation. Phase fluorimetry has been applied to the determination of τ in GaAs/AlGaAs QWs [52]. This method is applied to minerals or bio-samples more frequently than to semiconductors.

4.6.3 TR PL: Practical Examples

It is assumed that the PL transient $I_{PL}(t)$ is represents the $\delta n(t) = \delta p(t)$-decay within the probed sample region. In Sect. 4.2.1, we have already shown that diffusion and surface recombination impact to δn for the steady-state case. This holds also for $\delta n(t)$ within a transient. Thus the time constant of any $\delta n(t)$-decay, namely τ_{PL}, is not identical with τ and therefore a separation of effects caused by surfaces and diffusion is still required. One standard approach is to use a set of double-hetero-structures, where a narrower-gap material with the thickness d is clad by wider-gap barriers. For such a set, TR PL is measured and τ_{PL} is extracted from the (hopefully almost) exponential PL transient $I_{PL}(t)$. By using

$$\frac{1}{\tau_{PL}} = \frac{1}{\tau} + \frac{2s}{d}. \tag{4.9}$$

one can extract both the genuine τ -value[10] for bulk material and the interface recombination velocity s from a plot $\tau_{PL}^{-1}(2/d)$. Obviously, this approach requires samples which differ exclusively by d. Details on the approach and its limits are provided in a series of studies by Ahrenkiel; see e.g. [50]. If we now recall Sect. 4.5.2, which dealt with surface recombination estimations by cw PL, we can state that TR PL allows even quantitative s-analysis.

An example of, how TR PL can help us understand technological issues, is provided in Fig. 4.18c. Here, PL transients are given for a GaAs surface before and after oxidation. The authors interpret the presence of the fast transient to be caused by increased recombination via surface states [51].

With the results presented in Fig. 4.19a, b and c, we will now come back to structures whose cw PL data have already been discussed in Sect. 4.5.1; see Fig. 4.19a, b, namely laterally strain-modulated QWs [49]. Figure 4.19a, b show streak-camera images of the original QW (a) emitting at 922 nm, and of the same QW after the etching procedure was applied that causes the lateral strain-modulation; see again the original emission as well as an additional one at 947 nm in (b). Figure 4.19c shows selected spectra taken as cuts out of maps as shown before. The one at the bottom is representative for the initial population of the two relevant regions, original QW and strain-relaxed QW; see scheme in Fig. 4.13. Obviously in Fig. 4.13b, the PL of the QW areas decays very quickly due to two different mechanisms, 'regular' recombination and carrier transport towards the strain-relaxed QW. By applying a rate-equation model, lifetimes and transport time

[10]Actually, this τ-value might still be impacted on by 'photon recycling', in particular, if material with a high internal quantum efficiency is analyzed. The term 'photon recycling' describes the re-absorption of PL-photons followed by radiative recombination. Eventually, this results in seemingly enhanced diffusion constants and τ -values. The latter could interfere with the approach described above.

constants are determined to 180, 190, and 28 ps for QW, strain-relaxed QW, and transfer, respectively.

Figure 4.19d shows a PL spectrum from $GaAs_{0.899}N_{0.111}$ (inset) and PL transients for different probe photon energies [54]. The transitions that are probed are band-to-band, (e, C^0), and two transitions related to N-clusters, which are relevant in this material system. The very different time constants are interpreted in terms of different degrees of localization of the carriers involved in the optical transitions. These are free carriers in the case of band-to-band transitions, a free electron and a localized hole in case of (e, C^0), and strongly localized carriers at the N-clusters.

Figure 4.19e, f and g show a streak-camera image (g) and cuts out of it, namely spectra (e) and transients (f). Here, PL from *single QDs* is analyzed and exciton

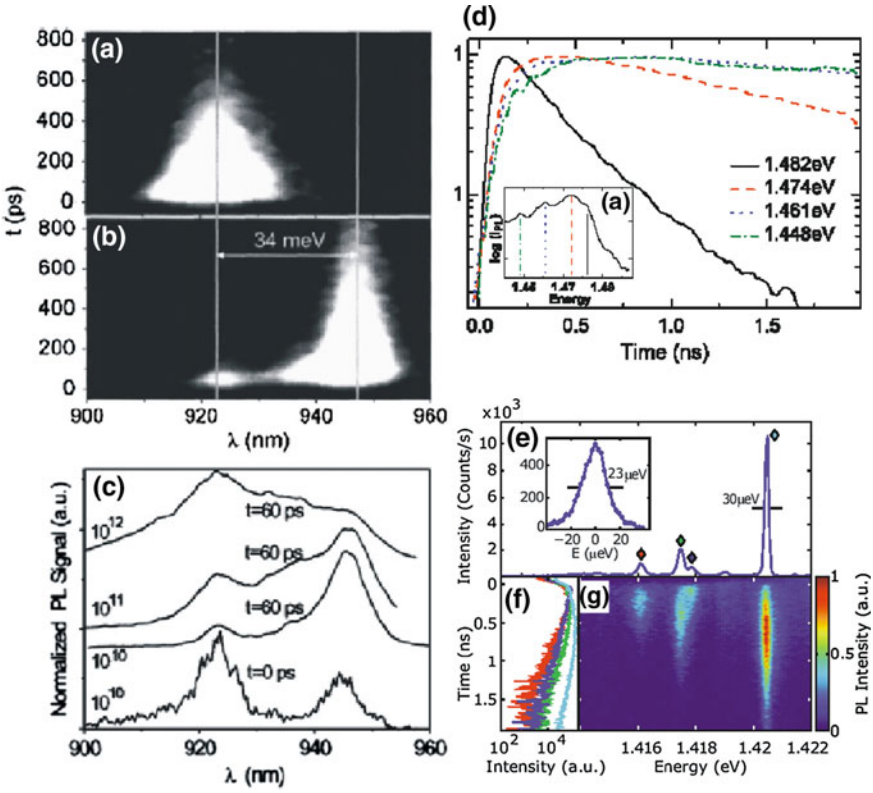

Fig. 4.19 **a** TR PL data from the unpatterned reference QW and **b** from the laterally strain-modulated QWs. **c** PL spectra for increasing excitation flux per pulse photons/cm^2. The reference spectrum at the *bottom* is representative for the initial population [53]. **d** TR PL for different detection energies marked by lines in the *inset* showing the time-integrated PL spectrum from $GaAs_{0.899}N_{0.111}$ [54]. **e** Steady-state PL, **f** TR PL transients, and **g** a transient PL map from a single InAs QD on GaAs [55]

lifetimes of 500 ps are found [55]. PL of excitons and charged excitons is detected and a PL linewidth as narrow as 23 μeV is observed.

Material scientists often ask spectroscopists 'whether the lifetime has improved or not' in their samples. This leads to the question, *how to interpret lifetime reductions or increases*, e.g., if data from two samples that differ by one parameter are compared. A general answer can't be given here. A lifetime change can be caused, e.g. by a modified recombination rate of defect-related transitions. This could be caused by adding or removing defects. Here an increased lifetime is good news if one is interested in efficient radiative recombination, e.g. in an emitter structure. If on the other hand, a lifetime increase is observed, this could pinpoint a reduced wavefunction overlap of electrons and holes in a QW or nanostructure, as well. This would be rather bad news for an emitter structure, at least if electron-hole separation is not especially desired.

Notice, that analysis of TR PL data frequently relies on the existence of exponential $I_{PL}(t)$-transients, as seen in Fig. 4.19d. In practice, however, non-exponential behavior is frequently observed; see Fig. 4.18b, c [50, 51]. The author of [50], for instance, approximated the observed transient by two exponentials; see Fig. 4.18b. The additional downturn at the end of the transient is interpreted as caused by the density dependence of Shockley-Read-Hall recombination (non-radiative recombination via mid-gap levels).

There are some general rules which help to observe exponential $I_{PL}(t)$-transients. Their identification is useful because they often (not always) point to the desired τ-value.

- Fast trapping into defects, e.g. at surfaces, causes fast components at the beginning of transients; see e.g. Figure 4.18c. This particularly appears at low excitation densities and ambient temperature. Such effects can be often reduced by saturating the traps with elevated excitation densities.
- High densities can lead to the onset of faster recombination mechanisms, e.g. by increasing impact of Auger processes. The shapes of the transients look very similar to what was mentioned before, but now elevated densities rather lead to an enhancement of a fast component at the beginning of the $I_{PL}(t)$-transients.
- τ_{PL} can depend on the probe wavelength $\hbar\omega$, as well. This might not be surprising if different PL lines are considered; see Fig. 4.19d. However, spectral dependences $\tau_{PL}(\hbar\omega)$ are observed *even within single PL lines*. If for instance edge emission is probed, carrier (pair) localization can increase τ_{PL} at $\sim E_g$ when probing at lower energy $\hbar\omega$-values [56]. For probing τ, in general, a probe wavelength well above E_g is recommended, provided that there is any PL contribution.

To summarize, the results of TR PL measurements depend on the experimental conditions chosen even more than in cw PL. Thus the demands to the experimentalist to make the right choice are even higher. Comparisons of PL transients

from different samples should always be based on experiments which have been performed with the same setup under well-defined conditions. The use of *test samples* with known carrier kinetics is highly recommended.

4.6.4 Ultrafast TR PL

If ps temporal resolutions are required, one can not use standard cw PL setups without modification anymore. There are some guidelines for reducing wavefront distortions in a PL setup:

- Reduce the number of optical elements to a minimum and avoid the use of dispersive elements such as lenses as much as possible.
- If dispersive elements such as filters or cryostat windows are used, it is a good choice to place them at a position where the PL signal is transferred in a parallel beam.
- Confine the lateral spatial spread of the PL light by apertures. This will reduce the signal but might help to achieve improved temporal resolutions.

Vendors of streak cameras provide adapted monochromators, where the optical path length for different wavelength is balanced, or offer special software tools to implement spectro-temporal corrections.

PL-upconversion is an elegant way to perform PL spectroscopy even on a fs-timescale. The idea of this approach relies on sum-frequency generation: the PL signal and the radiation from a fs-laser are combined in a non-linear crystal. Since the presence of the sum-frequency necessarily requires both contributions *at the same time*, the sum-frequency will be created during the fs-laser pulse only. By using a mechanical delay stage, the laser pulse can be tuned on the timescale through the PL transient. Thus, the PL signal is sampled with a time-resolution set by the pulse length of the fs-laser. Moreover, in this approach, slow and sensitive detectors can be used.

Naturally, the sum-frequency approach offers another useful option. The PL transients are converted into *another spectral range* and this can be very useful, for instance, if IR PL from narrow-gap materials is to be analyzed [57].

Figure 4.20a shows a scheme of a PL upconversion setup. Key elements are the excitation laser that creates the PL and a second synchronized laser (or laser beam). In this particular case, the second laser source is an optical parametric oscillator which is also pumped by the excitation laser. The PL signal and the radiation of the second laser are combined and the sum frequency is detected by the PMT. The delay stage allows to shift the pulse of the second laser temporally across the PL transient.

Figure 4.20b shows PL transients from a narrow gap PbTe QW (emission spectrum, see inset) [57]. In this example, the use of the PL upconversion technique allowed a detailed analysis of MIR PL transients.

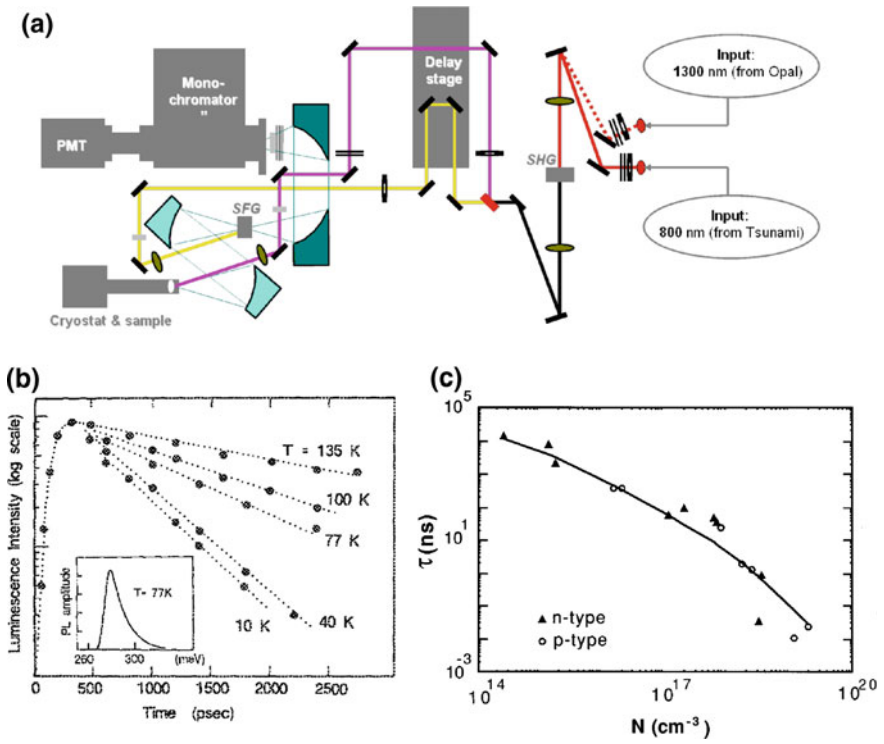

Fig. 4.20 **a** Schematic diagram of a PL upconversion setup. **b** TR PL decays from narrow-gap PbTe/PbEuTe QWs emitting at ~5 μm wavelength [57]. **c** TR PL decays versus carrier concentration of $In_{0.53}Ga_{0.47}As$ [58]

In Fig. 4.20c lifetimes in $In_{0.53}Ga_{0.47}As$ are presented versus carrier concentration [58]. A PL upconversion technique has been successfully applied, as well, in order to analyze PL transients that take place in the IR at about 1.7 μm wavelength. Analysis of such data sets allows to draw conclusions regarding the acting recombination mechanisms in different doping regimes for this important material.

The application of PL-upconversion which has proven to reach time resolutions of ~50 fs represents an experimental challenge:

- Both PL and sum-frequency generation are not very effective processes. Therefore, one has to deal with very small amounts of light.
- There are limits for the collection of PL because often the desired time resolution forbids the use of large apertures which potentially allow the efficient collection of PL light.

Thus, if the ultrashort timescale is addressed, one should always consider the option of performing pump-probe instead of PL-upconversion spectroscopy.

[59] gives an overview on ultrafast dynamics of excitation in semiconductors and involves a special section on ultrafast TR PL.

4.7 Photoluminescence Mapping

4.7.1 PL Mapping: Experimental

When we discussed the applications of cw PL in Sect. 4.5, we already compared PL spectra measured at *different locations* of a sample. It suggests itself to extend this type of analysis to a mapping approach. Another origin of PL mapping is *fluorescence microscopy*. These two roots of PL mapping also represent the two main technical solutions which are sometimes called 'PL topography' and 'PL microscopy'; see [60]. The first could alternatively be called 'scanning approach', 'point-by-point-measurement' or 'serial approach', while the second rather represents an 'imaging approach' or a 'parallel measurement'. For the scanning approach, each location is *individually excited*, and the signal (either a scalar like the total PL signal magnitude or even a complete spectrum) is stored. For the imaging approach, the whole area that will be imaged to a camera has to be *homogeneously excited*, and the image of the PL pattern is taken with the camera.

These two approaches represent not only two different technical solutions, but differ in terms of PL generation, as well: for the scanning approach, the excitation spot is surrounded by unexcited material, while for the imaging approach homogeneous excitation of all imaged area is an intrinsic demand. Thus, if spatial resolutions on the µm scale are desired, excitation spot size diameters arrive at the order of L_D for the scanning approach. This leads to substantial impacts of diffusion on the PL signal as addressed in Sect. 4.2.2. Naturally, at least the lateral diffusion impact is substantially lowered for the imaging approach.

Figure 4.21a shows a setup which is representative for the scanning approach [61]. The peculiarity of this setup is the ability to scan full ∅ = 300 mm wafers but also the zooming which helps to achieve a spatial resolution of 1 µm. This is demonstrated by the data presented in Fig. 4.21b, c, d and e, in which a defective area is traced from the macro- to the micro-scale.

This example leads us to an estimate: assuming a 'dwell time'[11] per measured location of 10 ms only, the measurement of a whole ∅ = 300 mm wafer with the highest spatial resolution of 1 µm would last more than 20 years. This illustrates a cardinal problem related to mapping. One has to make sure that the *spatial resolution of the map matches the scientific question*, which should be answered. Be cautious not to mix this everlasting principal problem with pure technical limitations related to, e.g., computer memory.

[11]The term *dwell time* stands for the total of exposure time plus the time required for the mechanical alignment; i.e. the total time needed to produce one data point in a PL map.

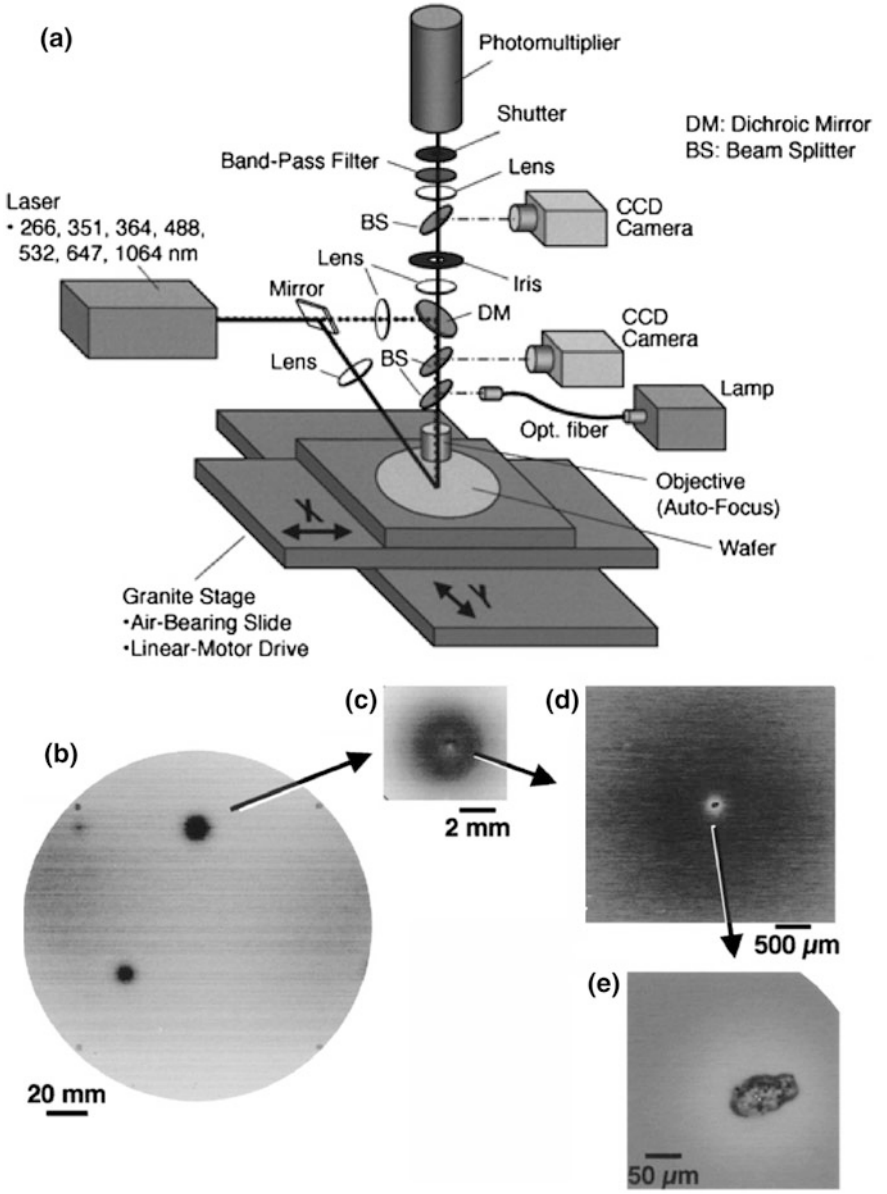

Fig. 4.21 Schematic diagram of intensity mappings of band-edge emission from top Si layer of a silicon-on-insulator-wafer, 200 mm in diameter, excited by UV light [61]. **b** Full wafer mapping and (**c**, **e**) microscopic mapping. Brighter regions indicate a higher intensity

For the imaging approach, the number of acquired data points is determined by the camera array used for PL detection. Here the magnification of the objective will control the trade-off between spatial resolution and inspected area. Although spectral discrimination is possible by inserting appropriate (even tunable) filters as well, the main strength of this approach is the shorter measuring time and its flexibility. On the other hand, this kind of setup will not be able to produce a PL line-scan with a number of data points larger than the camera pixel number along this direction.

Other important questions related to PL mapping experiments are

- What semiconductor material that will be mapped? An indirect material like Silicon will require more sensitive PL detection compared to GaAs.
- Which PL contributions should be monitored? This decision determines the requirements to the setup (e.g. detectors or cameras) as outlined in Sect. 4.3 for regular PL spectroscopy.
- Which parameters should actually be mapped? This could either be the integrated PL signal or the PL signal within a certain spectral channel (e.g. a selected PL line). Both tasks can be accomplished either by using the scanning approach or the imaging approach. Monitoring complete spectra at locations set by a customized grid employing a camera is another option. It implies the application of the scanning approach and requires a software tool for a detailed analysis of the massive expected data amounts.
- What excitation laser(s) should be used? Selective or resonant excitation by choosing an excitation wavelength that reveals those PL features one is actually looking for is an important opportunity.
- Should the measurement be cw or transient? Indeed, there are special setups, where mapping is combined, with TR-PL. This allows for *PL lifetime mapping* [62].
- At which temperature should the PL mapping carried out? There are cryostats available that allow to map of even 6-in. wafers at liquid Helium temperature.

Complete PL mapping setups are commercially available. Mostly, they are designed according to the needs of semiconductor industry.

4.7.2 PL Mapping: Practical Examples

Figure 4.22a, b show PL intensity maps from 2-in. semi-insulating GaAs-wafers [63]. Both wafers stem from the same crystal but have been cut close to the seed (a) and from the middle part (b). Obviously, the PL pattern looks very different. This can be assigned to the cellular structure that is typical for LEC[12]-grown bulk

[12]LEC stands for *Liquid Encapsulated Czochralski* what represents a growth technique for GaAs bulk crystals.

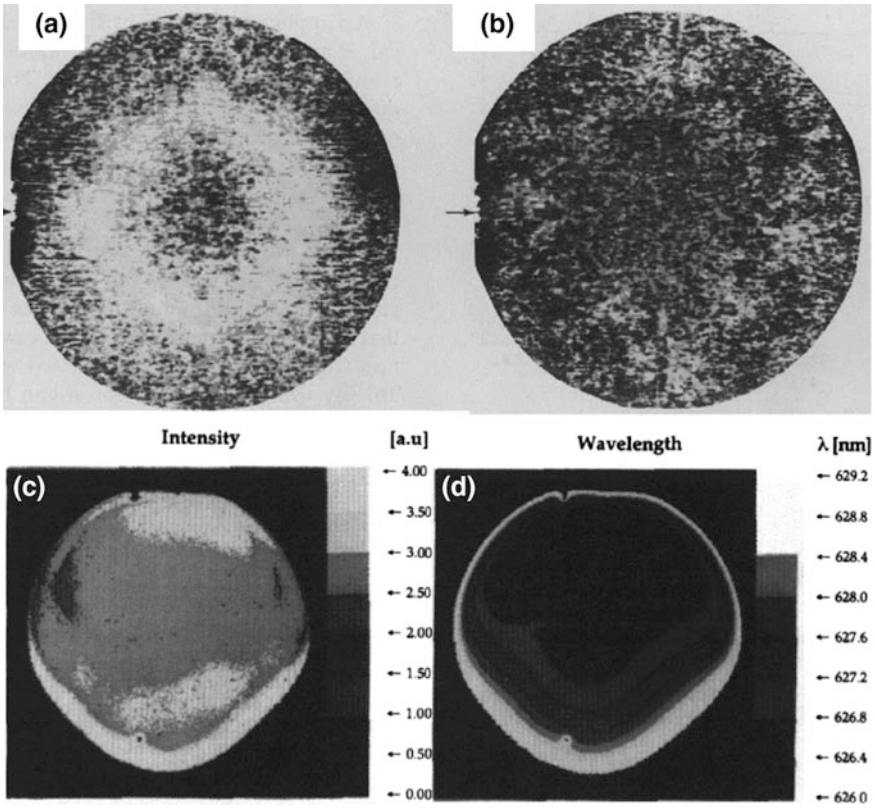

Fig. 4.22 (**a**, **b**) PL intensity maps from 2-in. semi-insulating GaAs-wafers recorded at ambient temperature with the scanning approach [63]. Intensity-map (**c**) and peak-wavelength-map (**d**) of an $In_{1-x}Ga_xP$-layer. The data shown in (**c**–**d**) are extracted from full spectra [64]

GaAs. This cell structure which is formed by dislocations, makes the existing defects and consequently the non-radiative recombination centers spread inhomogeneously across the wafer, resulting in an inhomogeneous band-edge PL pattern. Such measurements represent routine analysis for wafer manufacturers.

Figure 4.22c, d shows PL maps of MOCVD[13]-grown $In_{1-x}Ga_xP$ layers, which are (almost) lattice matched to their GaAs substrate [64]. This data is extracted from experiments which are again based on the scanning approach. In this case, however, complete spectra are recorded. This allows for a subsequent extraction of parameters such as peak intensity (c) or peak wavelength (d). The latter map could potentially tell a device manufacturer, e.g. about the expected emission wavelengths of devices. In this particular case, the wavelength homogeneity informs us about the

[13]MOCVD stands for *Metal Organic Chemical Vapor Deposition* which is a deposition technique for the growth of epitaxial layers.

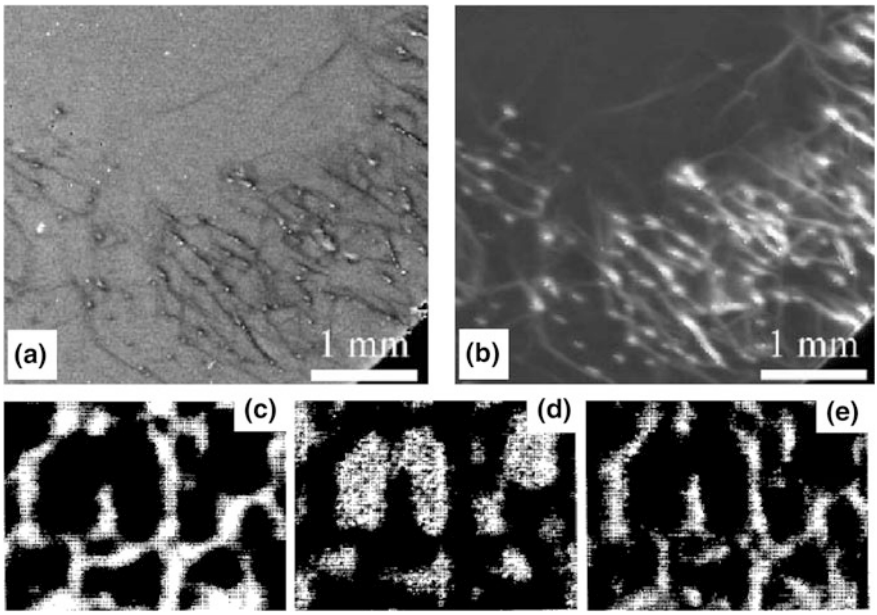

Fig. 4.23 PL intensity mapping of (**a**) the 1.8 eV band, and (**b**) the 1.1 eV band on p-type 4H–SiC [65]. PL maps from semi-insulating GaAs: (**c**) PL intensity map (**d**) PL effective-carrier-temperature-map (**e**) non-equilibrium-carrier lifetime map calculated from (**d**) [66]

mole fraction x and eventually about the 'degree' of lattice matching that is achieved with this not completely homogeneous $In_{1-x}Ga_xP$ layer.

Figure 4.23a, b show two PL maps taken from the same parts of a wide-bandgap 4H-SiC wafer[14] at the emission energies of 1.8 eV (a) and 1.1 eV (b), which have been selected by filters [65]. Since the E_g-value of 4H-SiC amounts to 3.25 eV, the mapped PL bands clearly correspond to transitions via deep level defects. While the 1.8 eV band decreases around dislocations, the 1.1 eV band shows there a clear enhancement. The resulting *inverse contrast* of the two maps shows the competition of the two defect-related recombination paths. As shown above for LEC GaAs, the SiC dislocations are visible in PL maps because they tend to getter point defects and become 'decorated' in this way. Such a behavior is known for several other semiconductors, as well.

Figure 4.23c, d and e again show PL maps from semi-insulating GaAs [66]. Complete spectra have been recorded, in this case at T = 2 K, and analyzed in detail. These maps are examples of what information becomes extractable from complete spectra. While Fig. 4.23c gives the total PL signal (at 817 nm,

[14]The term 4H indicates a special polytype of SiC. Different polytypes of SiC, with distinctly different electronic properties are formed by different stacking plane offsets between Si- and C-planes in this hexagonal crystal structure.

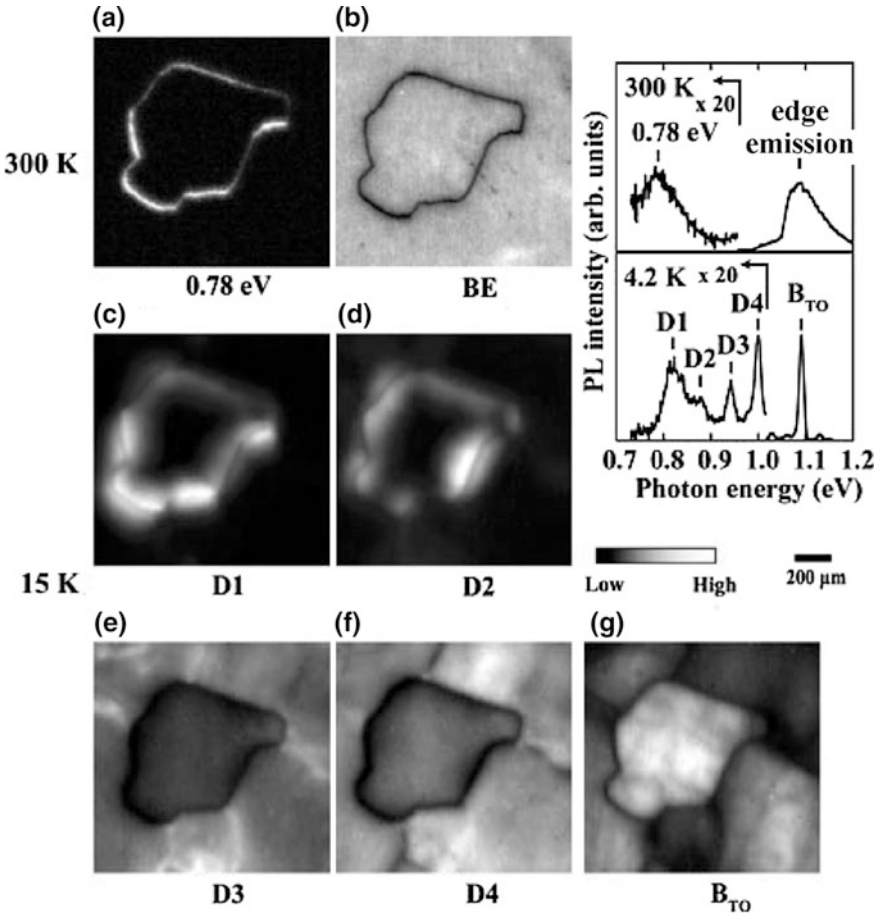

Fig. 4.24 PL spectra at 300 K and 4.2 K; see right top and center, respectively. The maps displayed in (**a**–**g**) are taken in different spectral channels. Detection energies are (**a**) 0.78 eV band, (**b**) band-edge emission (**c**) D1, (**d**) D2, (**e**) D3, (**f**) D4 and (**g**) B_{TO} emission [67]

corresponding to band edge emission), in Fig. 4.23d the effective carrier temperature is given. It is determined from the high-energy tail of the edge emission as described in Sect. 4.4.7. Finally, in Fig. 4.23e even a lifetime estimate is derived from the data. From the fact that PL signal (c) and lifetime (e) correlate, the authors conclude that a non-uniform non-radiative recombination causes the observed contrasts. The opposite option, namely a fluctuating radiative recombination rate, would be expected to have an anti-correlation; see discussion in Sect. 4.6.3.

With Fig. 4.24, we arrive at the topic of PL mapping of multi-crystalline Si wafers [67]. PL spectra are recorded for 4.2 K (bottom) and ambient temperature (top). The observed PL bands are assigned and labeled. For room-temperature, band edge emission and an emission at 0.78 eV are observed. The latter is assigned to

transitions via deep levels that are formed by Oxygen precipitates. The corresponding maps from a crystallite show very nicely that this deep level band stems from the grain boundary (a), while the inner part of the grain shows the same homogeneous band-edge-emission as the surrounding material (b). Substantially more details are derived from the low temperature data. The bandedge emission band mutates into a single line assigned to a TO-replica of a BE bound to Boron, labeled B_{TO}.[15] The lines labeled D1-4 are assigned to be related to dislocations, i.e. to recombination via defect levels. It is revealed that D1 (a) and D2 (b), whose PL magnitudes complement each other at the grain boundary, are caused by point defects in the strain field of dislocations, while D3 and D4 show substructures within the grain stem from intrinsic dislocations. The PL map at the BE line reveals even more structures within and outside the grain.

With the solar industries emerging, large-area wafer screening is increasing attracting attention, in particular as an analytical tool for process control. By using the imaging approach and cameras consisting of multiple CCD-sensor chips, mapping times on the order of a second for a 6 inch Si wafer became possible. From these PL maps, special software tools extract information on lifetime (*lifetime mapping*) or special foreign impurities such as Copper or Iron (*Iron mapping*). These software tools are utmost useful for process control in a production line. For a scientific analysis, however, it should always be checked carefully if all assumptions about the given algorithms are indeed justified. As it derives from any cw PL map, a 'lifetime map' requires the assumption that all parameters except for lifetime stay constant.

Since PL mapping is frequently used by people who grow semiconductors, it has a certain taste of 'applied PL spectroscopy', on one side. On the other side, it is very important for every spectroscopist to know that the appearance of different lines in a PL spectrum may simply reflect the presence of different spatial origins within the excitation spot. Experimentalists know that a sample showing absolutely the same PL spectrum from all locations rather represents the exception than the rule.

Even if PL mapping is not the goal of a particular study, it is always worthwhile checking spectra from various sample locations and thinking about the origins of differences if they are observed.

4.7.3 Ring-Shaped PL Pattern in Biased Quantum Wells

When combining focused excitation, as typical for the scanning approach, with PL imaging of the area around this excitation spot, new phenomena have been discovered. Several groups detected macroscopic ring-shaped PL pattern in biased QWs.

[15]Notice this labeling to be not consistent with the denotation we have introduced in Sect. 4.4.5 and the one used in the discussion of Si PL in Sect. 4.5.5. There are no effectively accepted standards for PL-line labeling.

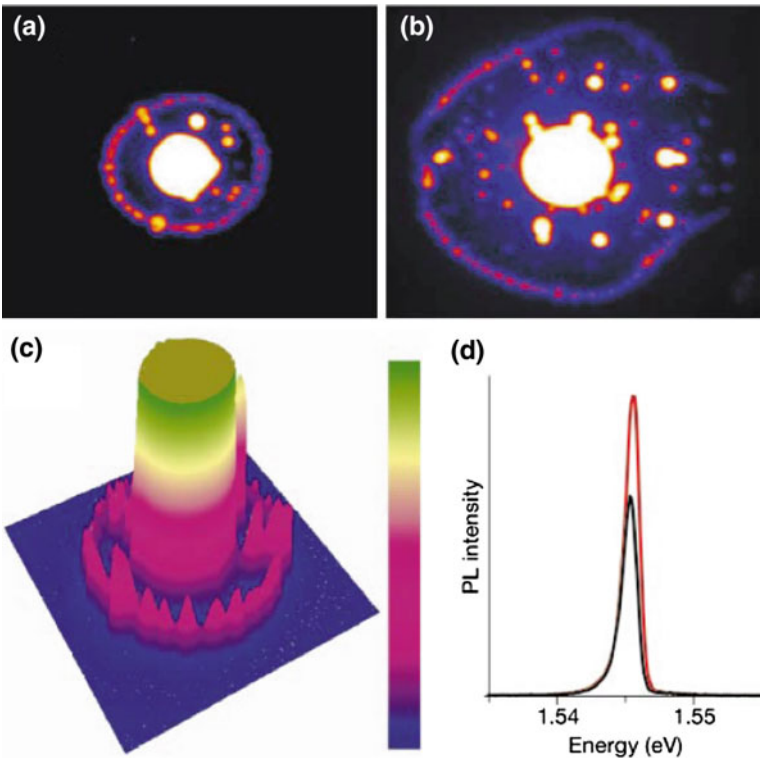

Fig. 4.25 PL maps of biased GaAs/AlGaAs coupled QW monitored for 0.39 **a** and 1.03 mW **b** excitation [68] **c** contour plot of the data shown in (**a**). The color bar starts at zero (*blue*) and presents a linear scale in arbitrary units **d** indirect exciton PL spectrum (*red*) and the adjacent pass (*black*) on the fragment chain along the ring

Figure 4.25a, b shows such images [68]. Notice that the imaged area is with 0.53×0.44 mm^2 of *macroscopic* size.

Figure 4.25c shows a contour map (linear scale) of the data given in (a). In (d) spectra are shown in a peak (red) and in an adjacent pass (black) on the fragmented chain along the ring. The presence of such rings is classically explained by charge separation by diffusion of electrons and holes in the biased QWs [6]. This PL has been reported in 2002, after more than two decades of intense spectroscopic research on QWs in labs across the world. Thus, this example shows that even a well-known technique applied to well-known structures sometimes reveals surprises for thoughtful spectroscopists.

4.7.4 Near-Field Scanning Optical Microscope Based PL

When we addressed absorption mapping in Sect. 2.5.3, we pointed to the option of accomplishing absorption mapping with a spatial resolution beyond the diffraction limit by using a near-field scanning optical microscope (NSOM). In PL spectroscopy, this demanding technique found a variety of very successful applications.

Figure 4.26a shows a micrograph of a coated fiber tip, which is the key element of the NSOM technique. The tip serves as the citation source and/or detector. Such fiber tips scan in a controlled way very closely to the surface of samples (typical distance 5–10 nm) like the tip of an atomic force microscope. In this situation, the evanescent light, emerging from the probe, interacts with the sample and allows for the high spatial resolution on the order of 100 nm. Alternatively, uncoated fiber tips with an intrinsically poorer spatial resolution can also be used. Typically, they have a transmittance by 3 orders of magnitude higher compared to coated tips.

Figure 4.26b, c and d show results from a GaAs/AlGaAs-nanostructure consisting of quantum wires and QDs as obtained by Intonti et al. [69] using NSOM PL. (b) gives a schematic top view of the structure. Lithographic patterning of the substrate gives rise to the formation of quantum wires with a QD at the corner of two intersecting wires. (c) shows a far-field PL spectrum, while (d) displays NSOM PL maps recorded at the detection energies of the three peaks shown in (c). Obviously, the three species QD, wire, and substrate cause the three lines visible in the far-field spectrum; see (c).

In Sects. 4.2.2 and 4.7.1, we stressed that for excitation spots diameters that are small compared to L_D, the transport of non-equilibrium carriers out of the excitation spot substantially influences the micro-PL data. The situation in NSOM-based PL is even more extreme. We will now present two examples how to employ the situation when L_D exceeds the size of the excitation spot. In this situation, NSOM-based *optical transport measurements* become possible.

- Malyarchuk et al. reported on NSOM-based PL measurements at diode laser structures by analyzing the edge area of the QW [70]. Near the surface, the surface recombination velocity s gives rise to a gradual variation of the PL signal on a micrometer length scale. From this data, D and s are independently determined. Moreover, it has been shown that s decreases with increasing intensity due to the saturation of surface states, which cause non-radiative recombination. Figure 4.26e presents this result.
- Friede et al. [71] investigated the lateral in-plane transport of surface excitons in ZnO structures by time-resolved NSOM-based PL. Comparative analysis of the PL transients in near- and far-field geometry, i.e. with excitation spots smaller and larger than LD, allowed for experimental separation of the diffusion contribution to the PL-decay. This allowed them to determine the in-plane diffusion coefficients of surface excitons in ZnO to $D_{SX}(T < 10\ K) = 0.30\ cm^2/s$. The results prove that this kind excitons are confined in a potential valley (along the growth axis) near the semiconductor surface but remain mobile within the lateral direction.

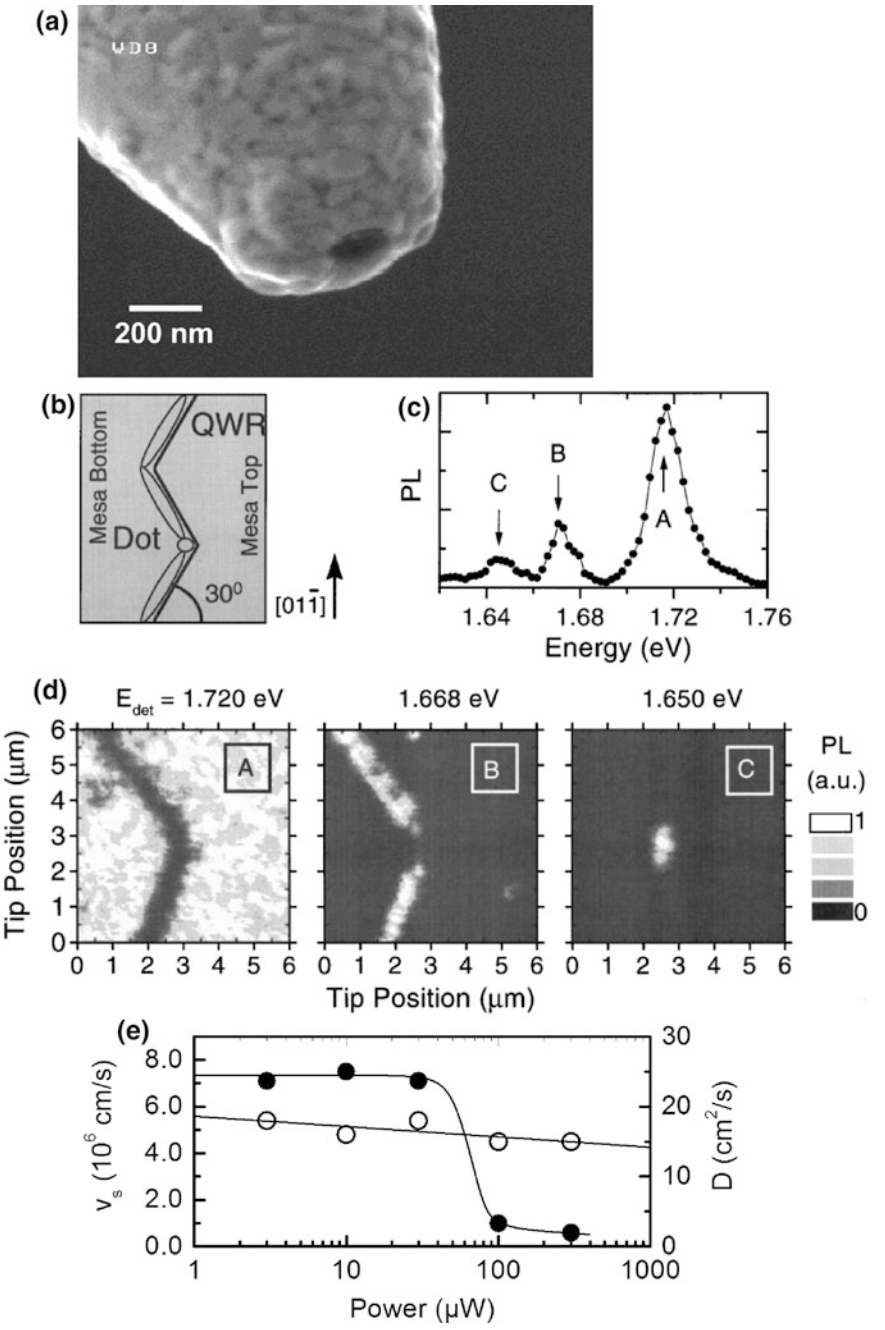
(a)
200 nm
(b)
Mesa Bottom
QWR
Mesa Top
Dot
30⁰
[01$\bar{1}$]
(c)
PL
C
B
A
1.64
1.68
1.72
1.76
Energy (eV)
(d)
E_{det} = 1.720 eV
1.668 eV
1.650 eV
Tip Position (μm)
PL
(a.u.)
1
0
(e)
v_s (10^6 cm/s)
D (cm^2/s)
Power (μW)

◀ **Fig. 4.26** **a** Scanning electron micrograph of a coated fiber tip as used for NSOM experiments. **b**–**d** NSOM-based PL analysis of localized and delocalized excitons in a single GaAs quantum wire [69]. **b** Schematic top view of the structure. The lithographic patterning of the substrate gives rise to the formation of a quantum wire with a QD at the corner of two intersecting sidewalls. **c** PL spectrum recorded near the QD position. **d** NSOM PL maps recorded at the detection energies of the three peaks (A, B, C) shown in (**c**). **e** Surface recombination velocity (*full circles*, *left scale*) and diffusion coefficient (*open circles*, *right scale*) determined from NSOM PL experiments at a QW [70]

The combination of NSOM with ultrafast spectroscopy represents an interesting option, in particular for the investigation of nanostructures. A detailed review on this topic has been given by Vasa et al. [72].

4.8 Photoluminescence at Devices

4.8.1 Introduction

There is no principal difference between PL at semiconductor materials and PL in devices, which are made from these materials. Many studies, even in basic research, are done with device structures. There are, however, also two technical aspects that cause severe difficulties.

- Due to the presence of sealing, metallization, housings, etc. the optical access to important parts of the device may be hindered. If one removes them, however, the original state of the device is modified. Therefore, often only device parts, such as the facet of edge-emitting lasers, can be examined by PL.
- PL at devices is often done at ambient temperature. On the one hand, this is because they are typically operated at this temperature and therefore, the PL information is frequently needed for room-temperature. On the other hand, substantial cooling (e.g. to 77 or 4.2 K) is frequently expected to cause irreversible damage to packaged devices. This is due to mismatch of coefficients of thermal expansion between semiconductors, metallizations, and heat sinks, which are tolerated by the semiconductor chips only within a limited temperature region around ambient temperature.

Therefore, PL at devices involves additional challenges for the spectroscopist. In the following, we will give a non-exhaustive list of examples, which span an overview on chances and limitations of PL in devices.

4.8.2 Strain Analysis in Devices by Means of PL Scanning

In order to reduce the cost per Watt of emission power, extended arrays of high-power diode lasers have been created, so-called 'cm-bars'. Figure 4.27a shows a schematic of the front of such an array, which brings out why the name was chosen: the width of the array is 1 cm. When producing such a device, the challenge is to keep the stress introduced into the extended semiconductor chip as small as possible. Problematic processes are the metallizations and the soldering of the chip to a metallic heatsink. This calls for means to measure the *packaging-induced strains*. Micro-PL inspection at the substrate along the facets of cm-bars at least allows to monitor spatial modifications of the bandstructure, which are likely to be introduced by the packaging process [73].

Figure 4.27b shows the PL peak position along two traces across the substrate. One of them has been taken across the center of the substrate (dotted line), see dotted line in Fig. 4.27a, whereas a second one (full black line) was made about 10 µm off the active region; i.e. closer to the solder interface. Notice that the grind lines in Fig. 4.27b are located between the emitters of the array. The distinct PL peak shifts at exactly these positions are caused by grooves which are etched a couple of microns into the active region for the purpose of side-mode suppression.

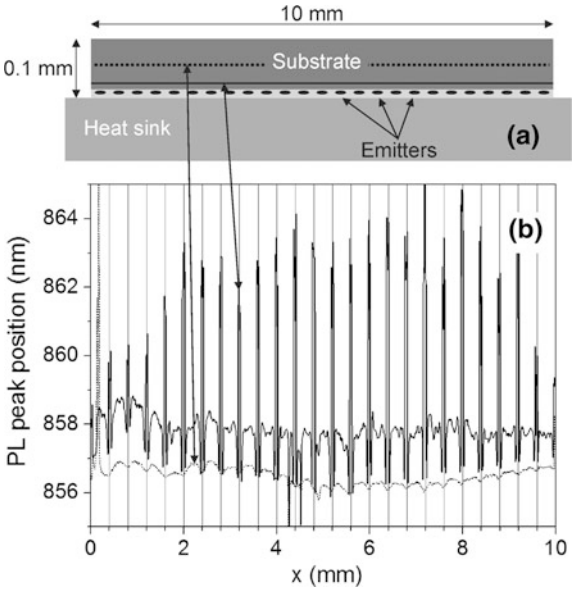

Fig. 4.27 **a** Schematic of the front facet of a monolithic high-power diode laser array of a width of 1 cm. *Two lines* are indicated at the substrate of the epi-down-packaged device, namely a *dotted one* in center of the substrate and a full one about 10 µm off the position of the emitters. **b** PL peak positions as determined from lineshape fits of the PL spectra taken along the *two lines* at ambient temperature

Their impact is still visible even in the center of the substrate; see slight modulation of the dotted line in Fig. 4.27b. Of course, this example does not represent a 'strain measurement', only an 'E_g-shift analysis' as addressed in Sect. 4.5.1. Nevertheless, this analysis allows device manufacturers to optimize their packaging processes and thus to improve their products, see also [74, 75].

4.8.3 Temperature Measurements at Operating Devices

Since at least the edge PL emission from semiconductors is closely linked to E_g of the material, any type of PL line shifts potentially point to E_g-shifts. If PL is measured at a fixed position on a device, and the temperature of the devices is changed, it suggests itself to assign the PL line shift to the temperature change. Of course, it must be checked that the temperature change does not affect PL properties indirectly, e.g., substantial lineshape changes due to temperature or via thermally-induced strain. Once such indirect effects are excluded, PL can be employed as a sensitive 'thermometer', which probes a rather thin layer at a device surface.[16] An example are facet temperature measurements at the front facets of diode lasers [76, 77]. Figure 4.28a present such data. In Fig. 4.28a, PL spectra from the $Ga_{0.4}Al_{0.6}As$ *p*-cladding layer of a QW laser are shown at three different injection currents. The facet temperatures (circles) in Fig. 4.28b are derived from a calibration based on temperature dependent PL measurements and represent the actual cladding layer surface temperatures. This temperature is probably not exactly the same as at the active region (QW and waveguide), but since the claddings are expected to be heated by the active region, its temperatures are excellent indicators for active region temperatures, as well. Such work allows device manufacturers to optimize their laser facet processes.

4.8.4 TR PL at Devices

Figure 4.29 present PL experiments carried out with InGaN/AlGaN/GaN light emitting diodes [78]. The device architecture is given in Fig. 4.29a. Since the excitation light can pass through the semitransparent AuNi-electrode on top, the PL spectrum, see Fig. 4.29b, is mainly created in the *p*-type epitaxial layers. The two PL bands labeled A and B are assigned to impurity-related PL in the active region and band-edge emission in *p*-GaN layers, respectively. Figure 4.29 present the TR PL data of band A (c) and B (d). The results are interpreted within a saturable

[16]The term 'thin' is addressed in detail in Sect. 4.2. The typical information depth at ambient temperature is on the order of a few μm. Notice that this approach addresses a substantially thicker surface layer compared to micro Raman experiments; see Chap. 3.

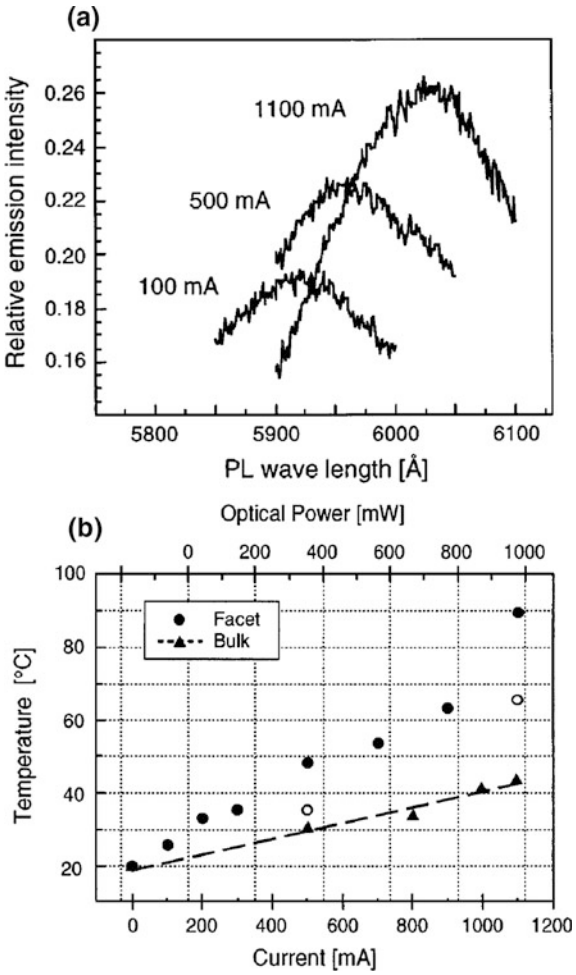

Fig. 4.28 Facet temperatures as determined by PL spectroscopy at the cladding layers of operating diode lasers [76]. **a** PL spectra taken at different operation currents. **b** Facet temperatures versus operation current (*circles*). The average bulk temperatures determined from the wavelength shift of the device emission are added (*triangles*)

three-level model; see scheme in Fig. 4.29d. The behavior of line B reveals stimulated emission as dominating carrier recombination mechanism at high densities.

TR PL data have been used in order to estimate surface recombination velocities s at GaAs-laser facets, which experienced different surface treatments; see in Fig. 4.30a, b device A and B, respectively [79]. For this purpose, TR PL measurements for two different excitation wavelengths, namely 395 and 790 nm, have been performed for each device. Due to the very different absorption coefficients at these wavelengths, the excited carrier clouds are located at different depths,

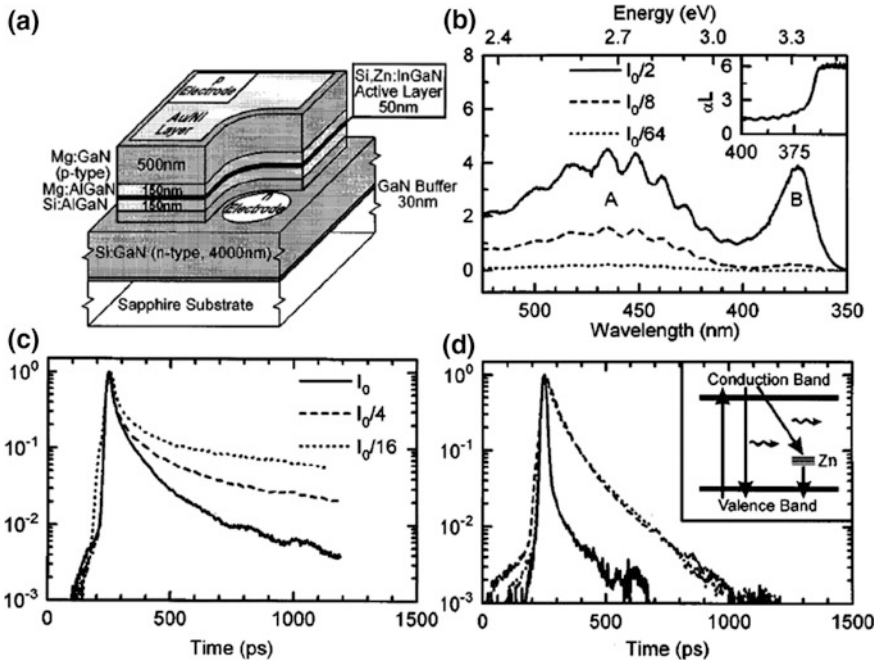

Fig. 4.29 TR PL at an $In_{0.06}Ga_{0.94}N$-based light-emitting diode [78]. **a** Schematic of the device architecture. **b** Pump power dependence of the steady-state PL at ambient temperature. Impurity related emission is labeled A, and band-edge emission is labeled B. The *inset* shows the linear absorption spectrum. **c**, **d** Normalized, time-resolved A- and B-band TR PL, respectively. The *inset* in (**d**) shows a schematic of the proposed recombination model

see discussion in Sect. 4.2.1. Consequently, the carrier clouds are affected by surface recombination in very different ways. Thus, *s* is the parameter that causes the two PL transients (full circles and open squares) in each of the Fig. 4.30a, b to look different. The PL transients are modeled based on a rate equation approach by Ahrenkiel, [80, 81]. In Fig. 4.30c, the ratios of the transients are plotted together with modeled PL transients with the parameter *s*. This allows an estimation of *s* for differently treated surfaces. In this particular example, the *s*-values are compared with diode laser properties. This helps to correlate device properties with technological treatments such as front facet coatings.

4.8.5 PL Mapping at Opened Devices

If devices as a diode laser fail, manufacturers are interested in a root cause analysis. In singular cases, the reason is obvious or can by directly identified, e.g. by microscopy, scanning electron microscopy, etc., i.e. by appearance. As shown in the preceding paragraphs, even PL spectroscopy at accessible surfaces can be used

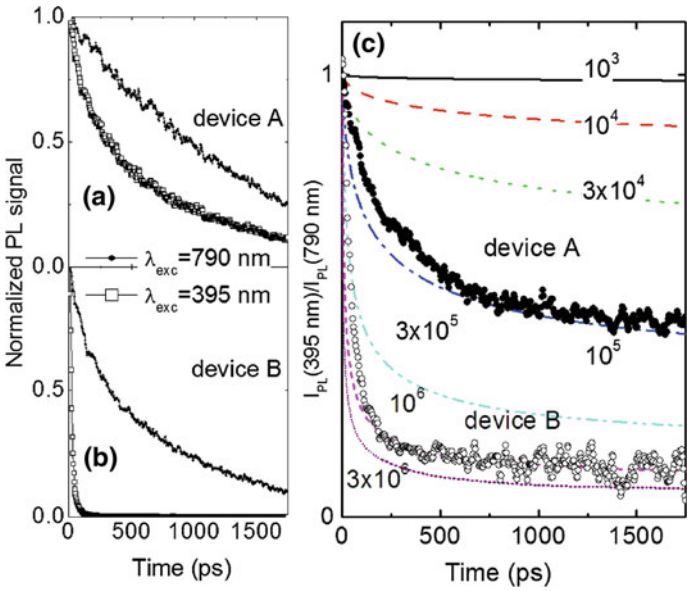

Fig. 4.30 **a**, **b** Normalized TR PL data from the font facets of two device devices, named A and B, excited with 790 and 395 nm wavelength. **c** Ratios the PL-transients (data taken at 395 nm by data taken at 790 nm) of device A (*solid symbols*) and B (*open symbols*). The fan chart of lines is calculated with the surface recombination velocity as a parameter: $s = 10^3$ (full), 10^4 (*dashed line*), 3×10^4 (*dotted line*), 10^5 (*dash-dotted line*), 3×10^5 (*dash-dot-dotted line*), 10^6 (*short-dashed line*), 3×10^6 cm/s (*short-dotted line*); from *top* to *bottom* [79]

in order to find clarification. However, the starting points of degradation might also be located inside the devices. In such cases, the device must be opened. Techniques, which enable opening of devices, have been developed for the GaAs-material system and typically involve several preparation steps including selective etching [82]. Figure 4.31 shows PL maps of the front part of the QW plane of two different high-power diode laser arrays [82]. In case of these originally epi-side down packaged devices, preparation involved the removal of the top *n*-contact and of the entire substrate. In this way, only the epilayer system remains and the active region plane is uncovered for PL inspection. The maps represent the QW emission intensity within 200 µm wide emitting stripe (see white bars on top of the maps), which is subdivided again into 20 parallel emitters. The front facets of the devices are indicated. Notice that the two failed devices have experienced quite different operation conditions.

The device which PL map is shown in Fig. 4.31a, failed after having been subjected to long term operation. The other has failed in a so-called COD-test,[17]

[17]COD stands for *catastrophic optical damage*. This effect represents a sudden diode laser failure mechanism that is related to an overheating, and subsequent physical destruction of the front facet of a diode laser.

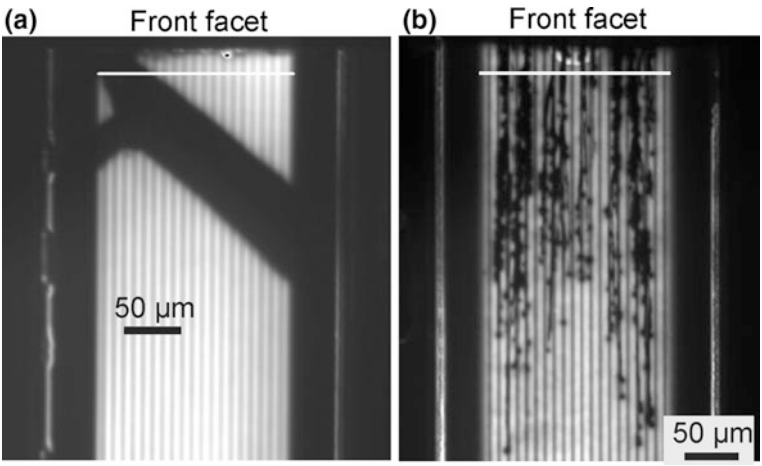

Fig. 4.31 PL maps of the QW emission from two failed and subsequently opened devices [82, 83]. While (**a**) shows the defect signatures of a device that failed during long-term aging, PL map (**b**) shows defect pattern as formed during a short overheating known as COD.[q]

i.e. a short and strong overheating. Obviously, the resulting PL maps differ very much. In Fig. 4.31a, there is one distinct 'dark band' extended along the <100> crystallographic direction. This 'dark band' indicates a lack of QW PL, which is most likely due to non-radiative recombination at extended defects such as dislocations. In Fig. 4.31b, there are 'dark bands' starting at the facet and spread along the propagation direction of the laser light (laser axis). This signature indicates QW destruction which begins at the front facet and is extended into the cavity by melting. Thus, PL mapping offers chances to distinguish between different degradation modes of optoelectronic devices.

References

1. L. Schrottke, H.T. Grahn, K. Fujiwara, Phys. Rev. B **56**, 13321 (1997)
2. U. Jahn, K. Fujiwara, J. Menniger, R. Hey, H.T. Grahn, J. Appl. Phys. **77**, 1211 (1995)
3. G. Duggan, G.B. Scott, J. Appl. Phys. **52**, 407 (1981)
4. J. Kuhl, E.O. Gobel, T. Pfeiffer, A. Jonietz, Appl. Phys. A-Mater. Sci. Process. **34**, 105 (1984)
5. A.J. Lochtefeld, M.R. Melloch, J.C.P. Chang, E.S. Harmon, Appl. Phys. Lett. **69**, 1465 (1996)
6. M. Haque, Physical Review E (Statistical, Nonlinear, and Soft Matter Physics) **73,** 066207 (2006)
7. D. M. Graham, P. Dawson, M. J. Godfrey, M. J. Kappers, J. S. Barnard, C. J. Humphreys, E. J. Thrush, physica status solidi (c) **3,** 2001 (2006)
8. R.C. Miller, A.C. Gossard, G.D. Sanders, Y.-C. Chang, J.N. Schulman, Phys. Rev. B **32**, 8452 (1985)
9. M.C. DeLong, D.J. Mowbray, R.A. Hogg, M.S. Skolnick, M. Hopkinson, J.P.R. David, P.C. Taylor, S.R. Kurtz, J.M. Olson, J. Appl. Phys. **73**, 5163 (1993)

10. J.W. Tomm, Y.I. Mazur, M.P. Lisitsa, G.G. Tarasov, F. Fuchs, Semiconductor Science and Technology, 148 (1999)
11. H. Htoon, P.J. Cox, V.I. Klimov, Phys. Rev. Lett. **93**, 187402 (2004)
12. S. Schmitt-Rink, D.S. Chemla, D.A.B. Miller, Adv. Phys. **38**, 89 (1989)
13. V. Klimov, S. Hunsche, H. Kurz, Phys. Rev. B **50**, 8110 (1994)
14. S.L. Sewall, R.R. Cooney, K.E.H. Anderson, E.A. Dias, D.M. Sagar, P. Kambhampati, J. Chem. Phys. **129**, 084701 (2008)
15. E. Grilli, M. Guzzi, R. Zamboni, L. Pavesi, Phys. Rev. B **45**, 1638 (1992)
16. H. Haug, S.W. Koch, in *Quantum Theory of the Optical and Electronic Properties of Semiconductors*, 5 ed. (World Scientific Publishing Co Pte Ltd, 2009)
17. H. Kunzel, K. Ploog, Appl. Phys. Lett. **37**, 416 (1980)
18. V.V. Travnikov, A. Freiberg, S.F. Savikhin, J. Lumin. **47**, 107 (1990)
19. S. Kuehn, S. Friede, S. Sadofev, S. Blumstengel, F. Henneberger, T. Elsaesser, Appl. Phys. Lett. **103**, 191909 (2013)
20. B.K. Meyer, H. Alves, D.M. Hofmann, W. Kriegseis, D. Forster, F. Bertram, J. Christen, A. Hoffmann, M. Strassburg, M. Dworzak, U. Haboeck, A.V. Rodina, Physica Status Solidi B-Basic Res. **241**, 231 (2004)
21. E. Finkeißen, M. Potemski, P. Wyder, L. Vina, G. Weimann, Appl. Phys. Lett. **75**, 3 (1999)
22. S. Eshlaghi, W. Worthoff, A.D. Wieck, D. Suter, Phys. Rev. B (Condens. Matter Mater. Phys.) **77**, 245317 (2008)
23. E. Oh, H. Park, Y. Park, Appl. Phys. Lett. **72**, 70 (1998)
24. F. Binet, J.Y. Duboz, J. Off, F. Scholz, Phys. Rev. B **60**, 4715 (1999)
25. M. Grundmann, N.N. Ledentsov, O. Stier, D. Bimberg, V.M. Ustinov, P.S. Kop'ev, Z.I. Alferov, Appl. Phys. Lett. **68**, 979 (1996)
26. L. Yang, J. Motohisa, K. Tomioka, J. Takeda, T. Fukui, M. M. Geng, L. X. Jia, L. Zhang, Y.L. Liu, Nanotechnology, 275304 (2008)
27. M. Yoshikawa, M. Kunzer, J. Wagner, H. Obloh, P. Schlotter, R. Schmidt, N. Herres, U. Kaufmann, J. Appl. Phys. **86**, 4400 (1999)
28. S.J. Hwang, W. Shan, R.J. Hauenstein, J.J. Song, M.-E. Lin, S. Strite, B.N. Sverdlov, H. Morkoc, Appl. Phys. Lett. **64**, 2928 (1994)
29. B.M. Ashkinadze, E. Cohen, V.V. Rudenkov, P.C.M. Christianen, J.C. Maan, L.N. Pfeiffer, Phys. Rev. B (Condens. Matter Mater. Phys.) **76**, 075344 (2007)
30. M. Kotani, T. Iida, Y. Makita, Y. Kawasumi, X.H. Fang, S. Kimura, D.S. Jiang, H. Shibata, T. Shima, T. Tsukamoto, N. Koura, Nucl. Instrum. Methods Phys. Res., Sect. B **121**, 302 (1997)
31. L.H. Robins, J.T. Armstrong, R.B. Marinenko, A.J. Paul, J.G. Pellegrino, K.A. Bertness, J. Appl. Phys. **93**, 3747 (2003)
32. B. Monemar, J. Appl. Phys. **49**, 2922 (1978)
33. J. Grenzer, U. Zeimer, S.A. Grigorian, S. Feranchuk, U. Pietsch, J. Fricke, H. Kissel, A. Knauer, M. Weyers, Phys. Rev. B **69**, 125316 (2004)
34. L.W. Tu, E.F. Schubert, M. Hong, G.J. Zydzik, J. Appl. Phys. **80**, 6448 (1996)
35. Y.-M. Yu, B.O, M.-Y. Yoon, J.Bae Kim, Y. Dae Choi, Thin Solid Films **426,** 265 (2003)
36. K. Takarabe, physica status solidi (b) **198,** 211 (1996)
37. J. Zenneck, T. Niermann, D. Mai, M. Roever, M. Kocan, J. Malindretos, M. Seibt, A. Rizzi, N. Kaluza, H. Hardtdegen, J. Appl. Phys. **101**, 063504 (2007)
38. F. Fuchs, A. Lusson, J. Wagner, P. Koidl, Proc. SPIE **1145**, 323 (1989)
39. F. Fuchs, A. Lusson, P. Koidl, R. Triboulet, J. Cryst. Growth **101**, 722 (1990)
40. F. Fuchs, K. Kheng, K. Schwarz, P. Koidl, Semicond. Sci. Technol. **8**, S75 (1993)
41. C. Lamberti, A. Antolini, 8th International Conference on Fourier Transform Spectroscopy **1575,** 497 (1992)
42. A. Antolini, C. Lamberti, Appl. Surf. Sci. **50**, 212 (1991)
43. A. Bignazzi, E. Grilli, M. Radice, M. Guzzi, E. Castiglioni, Rev. Sci. Instrum. **67**, 666 (1996)
44. Q.X. Zhao, H. Weman, B. Monemar, Phys. Rev. B **38**, 8529 (1988)
45. D. Karaiskaj, M.L.W. Thewalt, T. Ruf, M. Cardona, H.J. Pohl, G.G. Deviatych, P.G. Sennikov, H. Riemann, Phys. Rev. Lett. **86**, 6010 (2001)

46. D.J. Robbins, L.T. Canham, S.J. Barnett, A.D. Pitt, P. Calcott, J. Appl. Phys. **71**, 1407 (1992)
47. G. Ledoux, O. Guillois, D. Porterat, C. Reynaud, F. Huisken, B. Kohn, V. Paillard, Phys. Rev. B **62**, 15942 (2000)
48. J. Hader, J.V. Moloney, S.W. Koch, Appl. Phys. Lett. **85**, 369 (2004)
49. V. Talalaev, J.W. Tomm, T. Elsaesser, U. Zeimer, J. Fricke, A. Knauer, H. Kissel, M. Weyers, G.G. Tarasov, J. Grenzer, U. Pietsch, Appl. Phys. Lett. **87** (2005)
50. R.K. Ahrenkiel, Solid-State Electron. **35**, 239 (1992)
51. J.A. Kash, B. Pezeshki, F. Agahi, N.A. Bojarczuk, Appl. Phys. Lett. **67**, 2022 (1995)
52. Y. Arakawa, H. Sakaki, M. Nishioka, J. Yoshino, T. Kamiya, Appl. Phys. Lett. **46**, 519 (1985)
53. V. Talalaev, J.W. Tomm, T. Elsaesser, U. Zeimer, J. Fricke, A. Knauer, H. Kissel, M. Weyers, G.G. Tarasov, J. Grenzer, U. Pietsch, Appl. Phys. Lett. **87**, 262103 (2005)
54. K. Hantke, S. Horst, S. Chatterjee, P.J. Klar, K. Volz, W. Stolz, W.W. Ruhle, F. Masia, G. Pettinari, A. Polimeni, M. Capizzi, J. Mater. Sci. **43**, 4344 (2008)
55. U. Perinetti, N. Akopian, Y.B. Samsonenko, A.D. Bouravleuv, G.E. Cirlin, V. Zwiller, Appl. Phys. Lett. **94**, 163114 (2009)
56. A. Maassdorf, S. Gramlich, E. Richter, F. Brunner, M. Weyers, G. Trankle, J.W. Tomm, Y.I. Mazur, D. Nickel, V. Malyarchuk, T. Gunther, C. Lienau, A. Bärwolff, T. Elsaesser, J. Appl. Phys. **91**, 5072 (2002)
57. E.T. Heyen, M. Hagerott, A.V. Nurmikko, D.L. Partin, Appl. Phys. Lett. **54**, 653 (1989)
58. R.K. Ahrenkiel, R. Ellingson, S. Johnston, M. Wanlass, Appl. Phys. Lett. **72**, 3470 (1998)
59. A. Othonos, J. Appl. Phys. **83**, 1789 (1998)
60. M. Baeumler, C. Fitz, U. Weinberg, J. Wagner, W. Jantz, Mater. Sci. Eng. B **66**, 131 (1999)
61. M. Tajima, Z.Q. Li, R. Shimidzu, Japan. J. Appl. Phys. Part 2-Lett. **41**, L1505 (2002)
62. T. Katsumata, H. Imagawa, M. Watanabe, H. Zuzuki, M. Koishi, J. Cryst. Growth **103**, 14 (1990)
63. Z.M. Wang, J. Windscheif, D.J. As, W. Jantz, Appl. Surf. Sci. **50**, 228 (1991)
64. D.J. As, S. Korf, Z.M. Wang, J. Windscheif, K.H. Bachem, W. Jantz, Semicond. Sci. Technol. **7**, A27 (1992)
65. E. Higashi, M. Tajima, N. Hoshino, T. Hayashi, H. Kinoshita, H. Shiomi, S. Matsumoto, Mater. Sci. Semicond. Process. **9**, 53 (2006)
66. Z.M. Wang, J. Windscheif, D.J. As, W. Jantz, J. Appl. Phys. **73**, 1430 (1993)
67. M. Inoue, H. Sugimoto, M. Tajima, Y. Ohshita, A. Ogura, J. Mater. Sci.-Mater. Electron. **19**, S132 (2008)
68. L.V. Butov, A.C. Gossard, D.S. Chemla, Nature **418**, 751 (2002)
69. F. Intonti, V. Emiliani, C. Lienau, T. Elsaesser, R. Nötzel, K. H. Ploog, Phys. Rev. B **63**, 075313 1 (2001)
70. V. Malyarchuk, J.W. Tomm, V. Talalaev, C. Lienau, F. Rinner, M. Baeumler, Appl. Phys. Lett. **81**, 346 (2002)
71. S. Friede, S. Kuehn, S. Sadofev, S. Blumstengel, F. Henneberger, T. Elsaesser, Phys. Rev. B **91**, 121415 R1 (2015)
72. P. Vasa, C. Ropers, R. Pomraenke, C. Lienau, Laser Photonics Rev. **3**, 483 (2009)
73. E. Martin, J.P. Landesman, J.P. Hirtz, A. Fily, Appl. Phys. Lett. **75**, 2521 (1999)
74. *Quantum-Well Laser Array Packaging*; *Vol.*, edited by J. W. Tomm and J. Jiménez (McGraw-Hill, New York, 2007)
75. M. Hempel, M. Ziegler, S. Schwirzke-Schaaf, J. Tomm, D. Jankowski, D. Schröder, Appl. Phys. A Mater. Sci. Process. **107**, 371 (2012)
76. J.M. Rommel, P. Gavrilovic, F.P. Dabkowski, J. Appl. Phys. **80**, 6547 (1996)
77. A. Chavan, R. Radionova, G.W. Charache, R.J. Menna, H. Schluter, J.L. Hostetler, IEEE J. Quantum Electron. **41**, 630 (2005)
78. G. Mohs, B. Fluegel, H. Giessen, H. Tajalli, N. Peyghambarian, P.C. Chiu, B.S. Phillips, M. Osinski, Appl. Phys. Lett. **67**, 1515 (1995)
79. M. Ziegler, V. Talalaev, J.W. Tomm, T. Elsaesser, P. Ressel, B. Sumpf, G. Erbert, Appl. Phys. Lett. **92**, 203506 (2008)

80. *Minority Carriers in III-V Semiconductors Physics and Applications*; *Vol. 39*, edited by R.K. Ahrenkiel and M.S. Lundstrom (Academic Press Inc., Boston, San Diego, New York, London, Sidney Tokyo, Toronto, 1993)
81. *Minority Carrier Lifetime in Compound Semiconductors*; *Vol. 3*, edited by T.J. Coutts and J.D. Meakin (Academic Press, 1988)
82. M. Baeumler, J.L. Weyher, S. Muller, W. Jantz, R. Stibal, G. Herrmann, J. Luft, K. Sporrer, W. Spath, Defect Recogn. Image Process. Semiconductors DRIP VII **1997**(160), 467 (1998)
83. C. Frigeri, M. Baeumler, A. Migliori, S. Muller, J.L. Weyher, W. Jantz, Mater. Sci. Eng. B-Solid State Mater. Adv. Technol. **66**, 209 (1999)

Chapter 5
Cathodoluminescence

Abstract This chapter deals with a technique combining the optical spectroscopy with the high spatial resolution of the electron microscopes, *cathodoluminescence* (CL). This chapter is tightly related to Chap. 4, in the sense that the light emission mechanisms are similar, but the main difference lies in the excitation source. We present in this chapter the main experimental issues of this technique. First, the excitation of the luminescence emission with an electron beam is carefully described, looking at both the "information depth" and the lateral spread, both of them governed by the energy of the electrons. The main experimental issues, and the imaging procedures are analyzed. A series of case applications, in which the CL technique provides a plus of analytical possibilities, is presented, and applied to either bulk semiconductors, devices, and nanostructures.

5.1 Introduction

The electronic and optical properties of semiconductors are often characterized by spectroscopic methods. In particular, luminescence in its diverse forms is a powerful spectroscopic characterization tool for as grown semiconductors, but also for semiconductors at different stages of processing. The reduced dimension of the semiconductor devices requires of the control of the local parameters at the submicrometer scale. In this context, there is an increasing demand for probes allowing the study of the local properties of semiconductors. The study of individual nanostructures requires of very high spatial resolution probes in order to extract information of single objects instead of the properties averaged over a finite number of nanosized objects. Also, layer by layer characterization of multilayer structures is a relevant problem, which can be afforded with luminescence techniques.

The currently existing local luminescence techniques are:
Micro-photoluminescence (μ-PL), in which the excitation laser beam is focused with an optical microscope objective in a similar way as it was described for micro-Raman spectroscopy; in this case the size of the laser beam at focus is diffraction limited, therefore it is of the order of the laser wavelength. An alternative

J. Jimenez and J.W. Tomm, *Spectroscopic Analysis of Optoelectronic Semiconductors*, Springer Series in Optical Sciences 202,
DOI 10.1007/978-3-319-42349-4_5

approach uses holes on photolithographic masks, superposed to the sample, the excitation is done through one of such holes, and the emission light is collected as well through it; thus, the spatial resolution is determined by the hole diameter. An advanced variant of this is the near field scanning optical microscopy (NSOM) [1–3]. When the object is closer than the wavelength (near field) to the light beam the lateral resolution is not diffraction limited, but is determined by the size of the beam. Nevertheless, the very low signal characteristic of this technique makes difficult to apply it in a systematic way for many problems; normally, it presents a high cost in terms of experimentation time.

Other excitation sources can be used, in particular, electron beams. The most commonly used of them is Cathodoluminescence (CL), which consists of the luminescence emission under the excitation with energetic electrons arising from an electron gun; this will be the subject of this chapter.

Scanning tunnelling luminescence (STL), where, at difference with CL, low energy electrons are injected/extracted with the tip of a scanning tunnelling microscope (STM) [4].

Among these methods, CL is very useful, because of its high lateral and depth resolution possibilities; also, because it is fast and easy to handle, and last but not least, because of its powerful imaging capabilities when associated with an scanning electron microscope (SEM) or a transmission electron microscope (TEM).

CL concerns the emission of light by solids under the excitation with an electron beam (4–6). It works as follows, when the incident e-beam (primary electrons) impacts onto the semiconductor surface, excess e-h pairs are generated. The luminescence signal generated by the recombination of those e-h pairs constitutes the CL emission [5]. The radiative recombination generates photons in a similar way to that described in Chap. 4 for PL. What makes the difference with the other luminescence techniques is the excitation. The use of energetic electrons with energies ranging from hundreds of eVs to tens of KeVs as the excitation source, presents some remarkable differences with respect to the excitation with light of the PL experiments. Among other, it is very suitable for the study of wide band gap semiconductors, because the excitation is independent of the bandgap. In fact, it is largely used for the characterization of AlN, GaN, ZnO, diamond [6–13] …. On the other hand, the CL apparatus is usually attached to an electron microscope, either SEM or TEM, which permits combining the small beam size and the scanning capability of these instruments with the great potential of the luminescence spectroscopy.

In μ-PL experiments the laser beam is focused with a microscope objective being its size diffraction limited, therefore, the excitation beam has a diameter around 1 μm at the focus, which is not enough small for allowing the assessment of local properties at the nanometer scale. The μ-PL systems average the luminescence signal over relatively extended areas, and over several members of a community of structures with submicrometric dimension, e.g. nanocrystals, nanowires …. In contrast, higher spatial resolution can be achieved with CL permitting the assessment the local properties of single semiconductor structures. In this context, CL appears as a powerful technique for the characterization of the local properties of

semiconductors, and specifically for low dimensional structures, for which the optical properties are highly localized and require high spatial resolution, which cannot always be individually reached with the optical beams. On the other hand, the use of SEMs and TEMs allows to benefiting from other structural and analytical capabilities associated with these instruments, which are complementary to the CL measurements; e.g. crystalographic analysis, electron beam induced current (EBIC), energy-dispersive X-ray spectroscopy analysis (EDX) …. For all these reasons CL is nowadays a major characterization tool for semiconductor materials, nanostructures, and devices. Several excellent monographies devoted to the CL applications to semiconductor characterization are available [5, 14–17].

In this chapter, we will overview the CL technique as a semiconductor characterization tool, highlighting the main differences with PL, and emphasizing the practical aspects that help to perform the experiments, and to understand the results. A few application cases, where the use of the CL technique presents added value with respect to the use of other characterization methods, namely, μ-PL, shall be presented. For these purposes, we will highlight the main aspects that make CL a powerful characterization tool. Concerning the comparison with PL, once the e-h pairs are generated by the e-beam, the recombination mechanisms leading to the luminescence emission are similar to those described for PL. Therefore, we will not supply herein additional description of the recombination mechanisms involved in the luminescence emission; e.g. see the excellent review about the PL techniques applied to nitride semiconductors by Reschikov [18], other excellent reviews are those of Gillian [19], and Pavesi for the AlGaAs alloy system [20], and Chap. 4 of this volume.

The CL spectra are treated in a similar way as in the PL technique. As already mentioned, the main difference with PL concerns the excitation mechanism, and how this excitation determines the luminescence emission, the formation of images, and the spatial resolution, both lateral and in depth.

One of the assets of CL is the use of the imaging methods associated with the scanning of the excitation source. The formation of CL images is based on the competitiveness between the different e-h recombination paths operating in the material under study, which determines the contrast in the CL images. For a quantitative interpretation of the CL data one needs a precise modelling of the e-h pair generation and the mechanisms for the CL signal formation, for which is necessary to consider some physical parameters, as the carrier diffusion lengths, the absorption coefficient for the emitted photons, the internal reflection, the role of the surface states …; all of them being relevant to the formation of the CL signal [21]. On the other hand, other aspects plague the use of the CL; in particular, one has to consider charge effects on the sample during the e-beam exposure [22]. All those physical aspects can be studied by observing the dependence of the CL signal with the electron beam energy [23].

We will discuss about the configuration of a CL apparatus, the detectors, the operation modes, the spatial resolution, the probe depth, and other aspects relevant to the analysis of semiconductors by CL. Finally, we will present a few case applications, regarding aspects specific of the CL technique. Among other, the

estimation of the carrier diffusion length making use of the electron beam scanning [24], the study of multilayer structures based on the penetration depth of the electron beam, in particular we will study the problem of the degradation of high power laser diodes, and other devices [25], the analysis of surfaces and interfaces using low e-beam energies [26], the spectral image as a powerful tool for the study of different inhomogeneities, in particular, the orientation patterned GaAs crystals (OP-GaAs) [27], the dislocations in GaAs [28], also, we will present some examples of the characterization of nanoscaled structures, e.g. the ZnO nanowires [29]. Obviously, this list is by no means exhaustive, many other examples might have been selected, however, they permit to illustrate the capabilities of the CL technique as an advanced characterization tool of semiconductors at the submicrometric scale.

5.2 e-Beam Excitation. The Generation Function

5.2.1 Excitation with an e-Beam

The PL and CL excitation sources are very different; indeed, they constitute the main, but not minor, difference between the two methods. We have to focus our analysis on two aspects, the mechanism of e-h generation under e-beam irradiation, and the mechanism of the CL signal formation.

Different primary electron energy loss mechanisms take place when the e-beam (primary electrons) impacts onto the semiconductor surface. The generation of excess e-h pairs can be done by band to band excitation of the valence band electrons, by decay of plasmons, and by X-rays arising from the de-excitation of core shell electrons. The Coulombian interaction between the primary electrons and the plasmons presents low relevance for semiconductors, because of the low concentration of free electrons in the conduction band. The electrons generated close to the surface and with energy high enough to overcome the work function are emitted out of the semiconductor. These electrons are the secondary electrons and are responsible for the electron microscopy image. In our context, we are interested in the generation of e-h pairs, which later on shall participate in the recombination responsible for the CL emission. The interaction between the e-beam and the sample is schematically summarized in Fig. 5.1, where the different processes are represented.

The energy of the electrons is much higher than the energy of the photons exciting the PL, therefore, one electron can generate many e-h pairs, contrarily to the laser excitation of the PL experiments, where one photon generates one e-h pair. Also, the penetration of the electrons into the target (electron range, R_e) can be varied by means of the electron energy allowing a true in depth analysis. In PL measurements the probe depth is governed by the absorption coefficient, which gives a shorter range of penetration depths, even using tunable lasers, because the excitation is done with above band gap energy, which is strongly absorbed. The

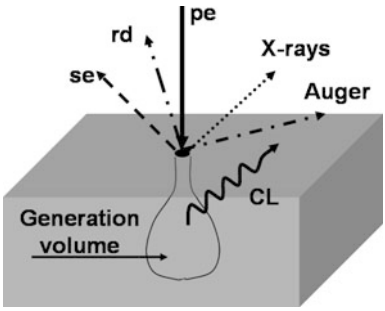

Fig. 5.1 Scheme representing the different electron solid interactions. *Pe* primary electrons, *rd* retrodispersed electrons, *se* secondary electrons

penetration depth of the excitation laser beams does not exceed a few hundred nms, while up to 2–3 μms can be reached with the e-beam. This is very useful for certain applications, as the multilayer structures, where one can access to the different layers by varying the electron beam energy.

Under electron irradiation the effective ionization energy, E_i, representing the average energy loss per created e-h pair is related to the band gap energy by the following empiric relation [30, 31]:

$$E_i = 2.8\,E_g + C \tag{5.1}$$

where C, represents the energy spent for purposes other than ionization, this wasted energy is predominantly transferred to the lattice; it is related to the phonon energy; therefore, it depends on the target composition; its value ranges from 0 to 1 eV [30]. According to this, the number of e-h pairs generated under electron excitation depends on the energy of the primary electrons. Figure 5.2 represents the energy necessary for creating an e-h pair in different semiconductor materials [31].

5.2.2 *The Generation Function*

If one excites with primary electrons of E_p energy, which is determined by the acceleration voltage applied to the electrons, usually ranging from 0 to 30 kV in SEMs, the generation factor is given by the following expression:

$$G = E_p(1 - R)/E_i \tag{5.2}$$

where R is the fraction of the energy of the primary electrons lost in electron backscattering processes; e.g. 0.25 for GaAs [21].

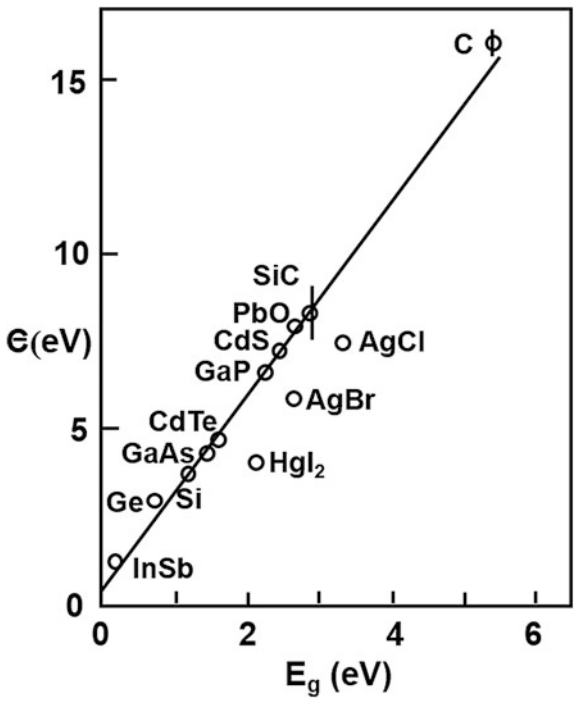

Fig. 5.2 Measured e-h pair creation creation energies for different semiconductors as a function of the band gap [31]

Because of the progressive energy loss the generation of e-h pairs is not uniformly distributed over the generation volume, but its spatial distribution obeys the following relationship:

$$N_{e-h} = G\, I_b \frac{g(r,z)}{e} = \frac{E_p(1-R)\, I_b}{e\, E_i} g(r,z) \tag{5.3}$$

where g(r, z) (cm^{-3} s^{-1}) is the normalized energy loss function, which represents the e-h pair generation rate per unit volume, taken over the primary electron penetration range, R_e, with I_b the e-beam current.

The form of the generation function has a strong influence on the CL signal. The use of analytical generation functions is a step towards the complex problem of the quantitative CL measurements, for which one needs using Monte Carlo simulations for the e-h pair generation, the resulting three dimensional distribution of the excess minority carriers, the internal optical absorption and reflection, and the Fresnel losses at the surface [5]. Note that the large probe depth that can be reached with high acceleration voltages implies that photons can be generated a few micrometers below the surface; these photons have to travel to the surface to leave the semiconductor to be detected; therefore, a significant internal self-absorption can take place for the high energy photons, which can change the shape of the spectrum in the high energy side. Figure 5.3a presents the near band edge (NBE) part of the CL

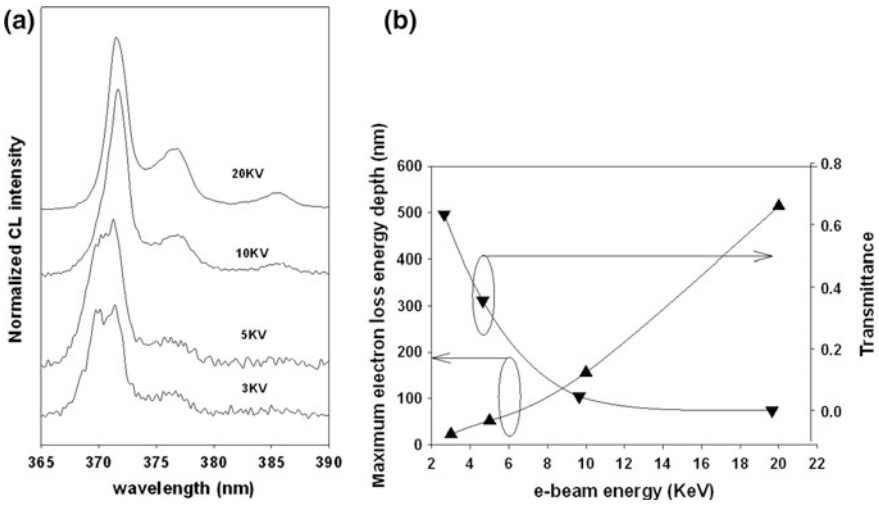

Fig. 5.3 CL spectra of ZnO crystals for different e-beam acceleration voltages **a** maximum energy loss depth as a function of the e-beam energy. **b** The right axis scales the transmittance

spectra of a ZnO crystal for different e-beam energies showing the shift of the onset of the high energy side of the spectrum to lower energies because of the self-absorption of the most energetic photons generated at a depth $\geq$150 nm ($\geq$10 keV electrons excitation). The maximum electron energy loss depth and the transmittance of 367 nm photons are plotted in Fig. 5.3b, the absorption coefficient was taken from [32]; there is a drastic reduction of the transmittance for e-beam energies >10 keV.

The energy loss function is usually calculated applying the Rutherford cross section for electron scattering deflections, and the Bethe energy loss equation [33]. Kilovolt electrons penetrating a solid target are elastically and inelastically scattered, primarily by collisions with shielded nuclei. The path followed by the electrons after successive collisions can be approximated by a series of straight line segments. A statistical summation of the energy losses over many of such segments would provide the curve of the energy loss versus depth. Electron stopping concerns the inelastic scattering with bonded electrons, in which the incident electrons (primary electrons) excite or eject electrons with the corresponding energy loss of the primary electrons. The in-depth generation rate function is crucial for the interpretation of the CL data.

One of the most widely used generation rate functions, G(z), is the Everhart-Hoff function [34, 35]:

$$G(z) = \frac{0.6}{R_e} + 6.21\left(\frac{z}{R_e}\right) - 12.4\left(\frac{z}{R_e}\right)^2 + 5.69\left(\frac{z}{R_e}\right)^3 \tag{5.4}$$

for $0 \leq z \leq 1.1R_e$

$$G(z > 1.1R_e) = 0$$

The maximum electron range is derived from the energy loss equation.

The Grun range [36] gives a simplified primary electron range, which depends on the density of the target and the energy, E_b, of the primary electrons [34]

$$R_e = (0.0398/\rho)E_b^{1.75}(\mu m) \tag{5.5}$$

The density, ρ, is expressed in g/cm^3, and E_b in KeV.

A more detailed estimation of the electron range was given by Kanaya and Okayama [37]:

$$R_e = (0.0276/\rho Z^{0.889})E_b^{1.67}(\mu m) \tag{5.6}$$

where, Z is the average atomic number.

The ranges estimated by the Kanaya-Okayama method are longer than those calculated by the Eberhart-Hoff formula.

The primary electron range is the penetration depth of the electron beam. It depends on the energy of the electrons; this dependence is used for the CL in depth analysis. On the other hand, from (5.4) one can see that the distribution of the e-h pairs generated by the e-beam has a maximum at $\approx R_e/3$, which corresponds to the depth of maximum electron loss energy, which will be taken as the CL probe depth. Therefore, by varying the acceleration voltage one can tune the penetration depth of the primary electrons, and thereafter the CL probe depth.

Other approaches to the analytical generation function, taking account of both in depth and lateral extension of the generation volume, have been done. One of the most used ones was provided by Donolato [38, 39] and consists of the product of an exponential, accounting for the depth profile, and a gaussian distribution accounting for the lateral extension:

$$g(r, z, R_e) \approx \Gamma\left(\frac{z}{R_e}\right) \exp\left[-\frac{r^2}{2\,\sigma^2(z, R_e)}\right] \Big/ \left[R_e\,\sigma^2(z, R_e)\right] \tag{5.7}$$

$$\Gamma\left(\frac{z}{R_e}\right) \approx \exp\left[-7.5\left(\frac{z}{R_e} - 0.3\right)^2\right] \tag{5.8}$$

$$\sigma^2(z, R_e) = 0.36\,d^2 + 0.11\frac{z^3}{R_e} \tag{5.9}$$

Other approaches are available [31, 34, 40–45], showing discrepancies concerning both the penetration depth and the lateral extension of the generation volume.

Bonard et al. [46] used an exponential function multiplied by a parabola for the depth distribution of the generation rate:

$$G(z) = \frac{\exp\left[\frac{2\Lambda - z_0}{\Lambda}\right]}{\Lambda^2}(z + z_0)^2 \exp\left(-\frac{z}{\Lambda}\right) \tag{5.10}$$

$$\Lambda = 0.03 + 0.0015 * E_b{}^{1.68} \tag{5.11}$$

$$z_0 = 0.002 * \exp(E_b/12.6) \tag{5.12}$$

Equation (5.10) was compared with the experimental results obtained in a series of samples specifically designed to minimize the carrier diffusion (three GaAs QWs 6 nm thick, separated by 10 nm thick AlAs spacers, all buried below a 5 μm thick layer of $Al_{0.4}Ga_{0.6}$ As), the depth dependence was analyzed in samples with a lap angle, for more details see [31]. The agreement between the experimental and calculated values was very satisfactory, Fig. 5.4.

The maximum generation occurs at:

$$z_{\max\,gen} = 2\Lambda - z_0 \tag{5.13}$$

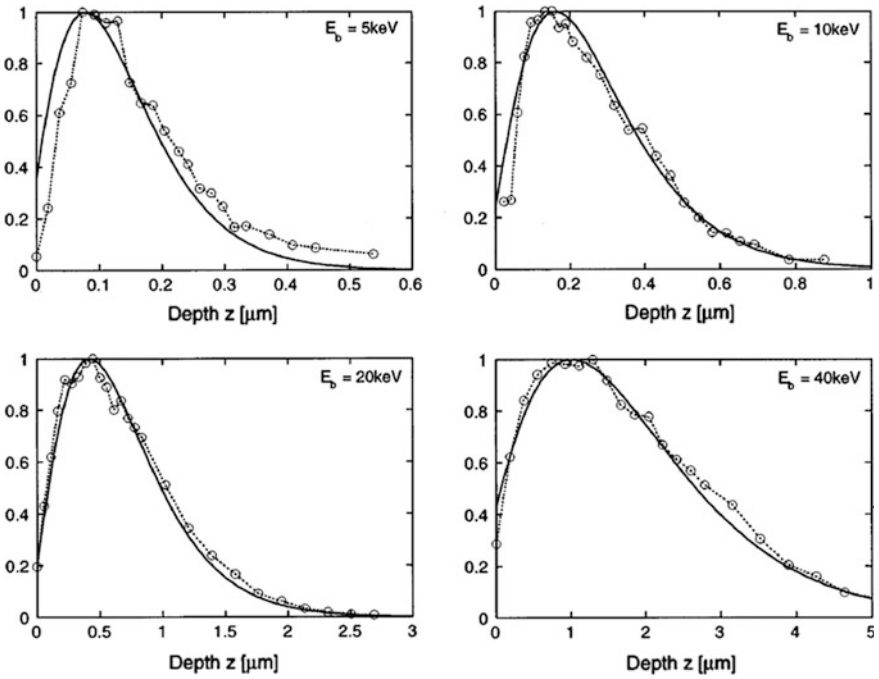

Fig. 5.4 Normalized energy loss versus depth at different e beam energies. The symbols are the experimental data and the lines are the calculated energy loss depths using (5.10) [46]

and the electron range is given by:

$$R_e = 10\Lambda - z_0 \tag{5.14}$$

The lateral dispersion was also modelled using the sum of two gaussian functions, which gave the best fitting to the CL measurements:

$$G(x) = A * \exp\left(-\frac{x^2}{2\sigma_1^2}\right) + (1 - A) * \exp\left(-\frac{x^2}{2\sigma_2^2}\right) \tag{5.15}$$

σ_1 and σ_2 are the widths of the two functions and the amplitude A was written as:

$$A = 1.07 - 0.093 * E_b + 3.55 * 10^{-3} * {E_b}^2 - 4.01 * 10^{-5} * {E_b}^3 \tag{5.16}$$

The Gaussian widths were found to obey the following expressions:

$$\sigma_i = a_i + b_i * {E_b}^{ci} \tag{5.17}$$

E_b is the beam energy in keV ($a_1 = 0.1$, $b_1 = 0.0035$, $c_1 = 1.25$, $a_2 = 0.32$, $b_2 = 0.0004$, $c_1 = 2.25$).

The lateral dependence of the e-h pair generation compared to the experimental data for different E_b values is shown in Fig. 5.5, showing an excellent agreement.

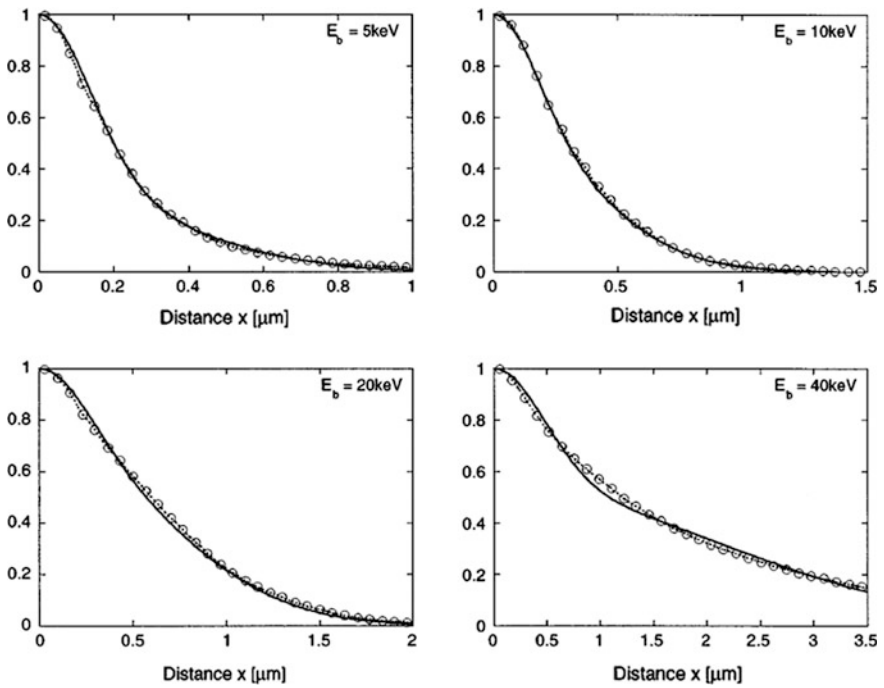

Fig. 5.5 Normalized lateral energy dispersion for different e-beam energies. Symbols correspond to experimental data, and lines are the calculated values using (5.15) [46]

5.3 Monte Carlo Simulation

Monte Carlo simulations allow obtaining the excitation shape by calculating the trajectories of the PEs, taking account of the continuous energy loss function for inelastic scattering, and the angle dispersion for elastic scattering.

The penetration depth calculated by the Monte Carlo method was contrasted with CL measurements at different voltages on a sample composed of stacked QWs of different emission energy. The authors used the intensity emissions from the different QWs, getting a good agreement with the Monte Carlo simulation of the depth generation function [47].

These simulations allow to appreciate the influence of the beam current and electron energy on the e-h generation volume.

Monte Carlo simulations using the free software package CASINO [48] permit to reproduce the shape of the e-h generation volume. Figure 5.6 shows the dispersion effect for different numbers of incident electrons (beam current) and a constant acceleration voltage (20 kV) in GaAs, revealing that the number of electrons (beam current) has not a great influence on the generation volume, but it mainly affects the concentration of generated e-h pairs, equivalent to the role of the incident laser intensity in PL measurements. Figure 5.7 presents the dispersion effect in GaAs at different acceleration voltages, and a number of 200 incident electrons, showing a significant increase of the generation volume by increasing the acceleration voltage. The optimisation of the spatial resolution requires the adequate choice of the excitation conditions to each case.

The calculations show, that the electron range in semiconductors for the conventional acceleration voltages of the SEM (up to 30 kV) scales up to a few μms, which is far beyond the typical 100–200 nm depth probed by excitation laser beams

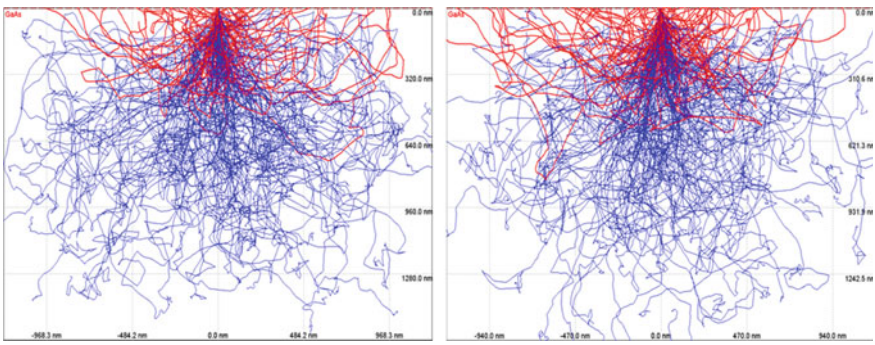

Fig. 5.6 Monte Carlo simulation of the electron trajectories in GaAs for 20 keV electrons and different numbers of electrons

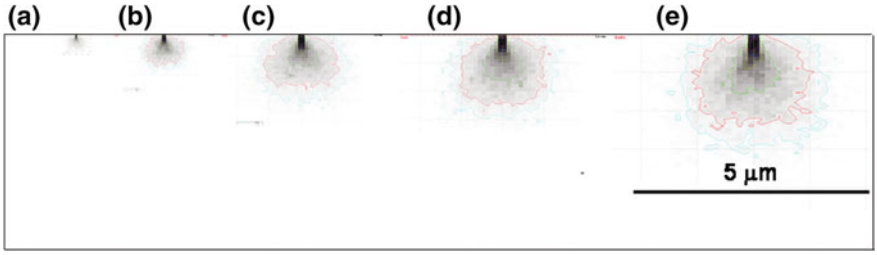

Fig. 5.7 e-h generation volume in GaAs calculated by Monte Carlo simulation for different e-beam energies and constant number of electrons (e-beam current). **a** 10 keV, **b**15 keV, **c** 20 keV, **d** 25 keV, **e** 30 keV [48]

Table 5.1 Calculated energy loss depth for different semiconductors and e-beam energies

e-Energy (keV)	maximum energy loss depth (μm)				
	Si	GaAs	GaN	ZnO	InP
5	0.13	0.042	0.1	0.096	0.082
10	0.43	0.22	0.33	0.3	0.27
15	0.87	0.4	0.63	0.57	0.55
20	1.47	0.73	1.03	0.93	0.87
25	3.2	0.97	1.5	1.4	1.33
30	3	1.4	2.7	1.93	1.73

in PL experiments [49]. As an example, CL measurements allow probing depths from a few nms to a few microns, see Table 5.1; while in PL the probe depths with usual excitation sources (Ar^+ laser at 514.5 nm for GaAs, and HeCd laser at 325 nm for ZnO) are ≈110 and ≈ 60 nm, respectively. By tuning the acceleration voltage the electron range can be varied from 0 to the maximum R_e allowed by the available maximum acceleration voltage provided by the e-gun. The maximum energy loss depth calculated for different semiconductors and acceleration voltages are shown in Table 5.1

The normalized energy loss per unit length in GaAs for different acceleration voltages is represented in Fig. 5.8. The maximum of each curve determines the depth of maximum energy loss (≈Re/3).

The generation depth calculated by Monte Carlo simulation in a 75 nm thick InGaN layer on a GaN buffer layer is shown in Fig. 5.9 [50]. For low voltages one excites only the InGaN layer, while by increasing the voltage the GaN buffer layer is also excited.

The probe depth of CL provides access to some problems that are difficult to analyze by PL; e.g. the study of multilayer structures; the deepest layers can be buried several hundreds of nms, or even micrometers, however their CL response can be detected using high KeV electrons, at the expense of the lateral resolution. Using photon excitation one probes the upper layers, which in many cases prevents the study of the active layers, e.g. the QWs in laser diodes in top view observation. The e-beam with selected acceleration voltage can cross the full multilayer

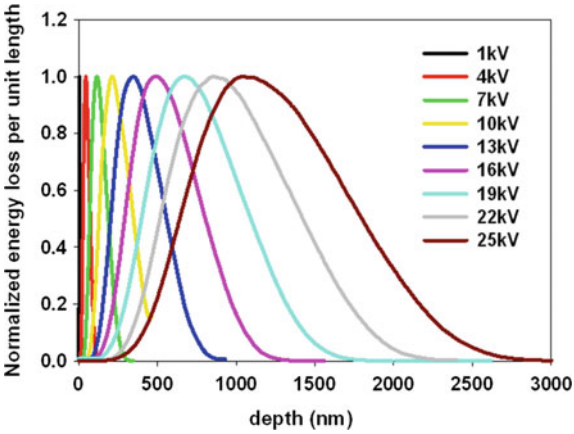

Fig. 5.8 Normalized energy loss versus depth in GaAs calculated by Monte Carlo method

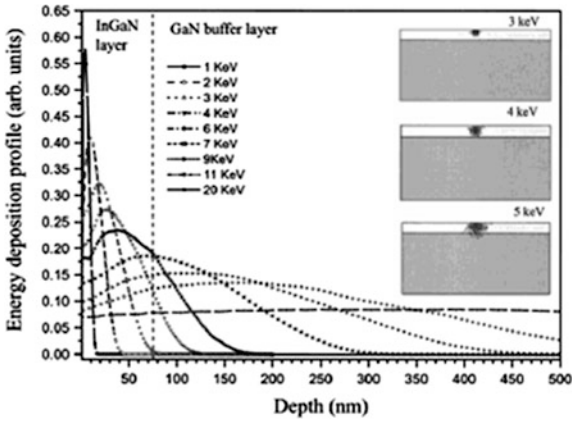

Fig. 5.9 Energy deposition (energy loss in the text) calculated by Monte carlo simulations on a 75 nm thick InGaN layer on a thisk GaN buffer layer, one starts to reach the GaN layer for 5 keV electrons [50]

structure, allowing the analysis of the different layers; which are identified because they emit in different spectral windows due to their different compositions. We will argue later on about the importance of the CL technique, when studying the laser diode cavities, which are fully accessible to the e-beam. Furthermore, as shown in the previous paragraph the CL study of multi-quantum well (MQW) structures, with different spacer barriers separating the QWs, was used to check the analytical generation functions, because such structures allow to neglect carrier or exciton diffusion between the different QWs [46], it was also used to study the inductively coupled plasma (ICP) etching of a series of InAsP QWs of different compositions placed at different depths and spaced by InP barriers [51], Fig. 5.10.

In summary, depth profiling can be achieved by varying the e-beam energy; however, increasing the e-beam energy also increases the e-h generation rate. In order to keep constant the generation rate, one adjust the beam current, I_b, keeping constant the power of the e-beam, $I_b * V_b$, which permits to vary the penetration

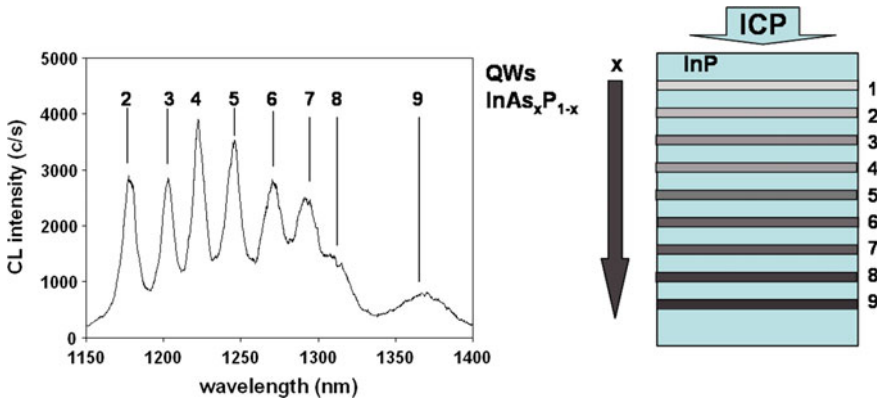

Fig. 5.10 CL spectrum of a series of 9 buried InAsP QWs of variable composition with InP spacers, submitted to ICP plasma etching. The emission from QW #1 is not observed because the QW was removed by the ICP etching

depth with constant e-h pair generation rate over the e-beam voltage range used for the profiling measurements.

The variable penetration depth of the e-beam permits to study the distribution of defects and impurities [52–54]. Figure 5.11 shows the CL spectra of ZnO crystals at different e-beam energies. One observes relevant changes in the spectra with the e-energy, which reveals in-depth defect distribution [55]. On the other hand, the onset of the high energy side of the NBE emission is shifted to the red for increasing e-beam energy due to the self absorption of the high energy photons for high penetration depths, as it was previously described, the free exciton lines are usually not observed for high e-beam energies.

5.4 Charge Effects. The Dead Layer

A severe reduction of the CL efficiency has been reported to occur in phosphors for low e-beam energies [56, 57]. This effect is also observed in semiconductors. It has been phenomenologically described in terms of a generic surface dead layer. The dead layer is responsible for the anomalous CL signal at low e-beam acceleration voltages, resulting in a finite threshold voltage for the CL signal observation [58]. The existence of such a dead layer on the top surface of the samples studied by CL is generally assumed; the e-h pairs recombine non-radiatively within this layer, which makes the dead layer naturally non radiative. The dead layer was also described by Wittry and Kyser [40] as a space charge region, where e-h pairs are depleted due to Fermi level pinning by surface states. Generically, one can say that the dead layer is the region adjacent to the surface in which all the recombination is non radiative, or the e-h pairs are depleted. Therefore, one cannot observe CL

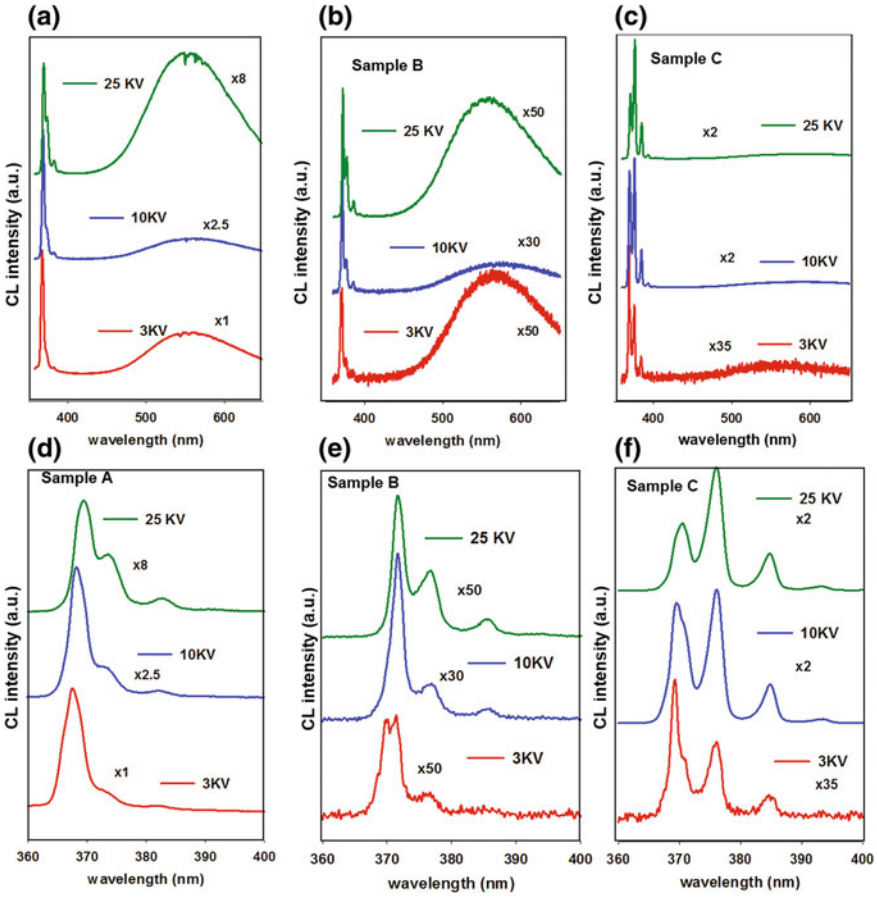

Fig. 5.11 CL spectra of ZnO crystals from different growers showing the influence of the e-beam keV in the spectrum shape. The spectrum shape depends on the growth conditions. At low KeV there is a clear dependence with the surface polishing, which was specific of each crystal (T = 80 K) [55]

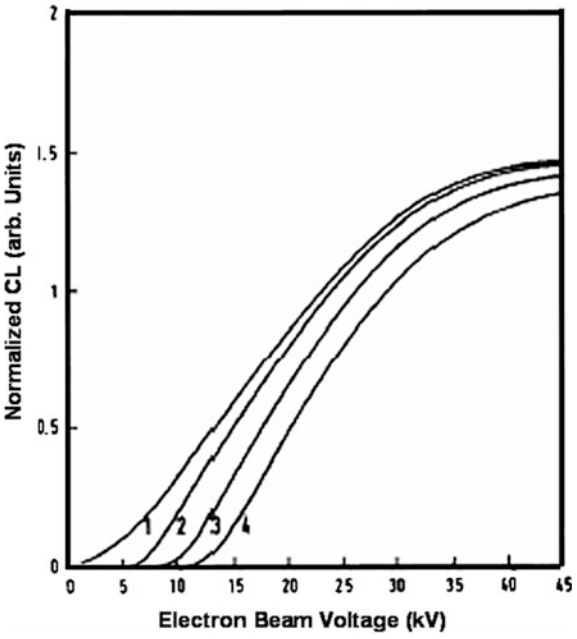

Fig. 5.12 CL intensity versus e-beam acceleration voltage for different dead layer thicknesses in GaAs. (*1*) 0 μm, (*2*) 0.2 μm, (*3*) 0.4 μm, (*4*) 0.6 μm [5]

emission if the electron range is shorter than the thickness of the dead layer; Fig. 5.12 plots the CL signal as a function of the e-beam energy for different dead layer depths in GaAs, showing the CL emission threshold shifting towards the high beam energies for increasing dead layer thickness [5]; this fact determines the conditions at which the CL spectra can be acquired with low energy primary electrons.

The dead layer thickness depends on different factors, as the sample doping, and the existence of surface states, which are tightly related to the surface reactivity, and the surface treatment undergone by the sample. The beam voltage emission threshold of ZnO was shown to be sensitive to the surface preparation and doping [59, 60].

It should be noted that the dead layer is not merely determined by the surface recombination velocity, S, since the PL signal is much less sensitive to the surface than the CL signal in similar probe depth conditions. Also, different voltage thresholds were observed in ZnO for the different crystallographic planes and different surface preparation [59]. The CL and PL signals obtained with similar probe depths (electron range equivalent to $1/\alpha$, where α is the absorption coefficient for the excitation photons in PL—325 nm from a He-Cd laser) present differences in the emitted signal in the presence of a dead layer, while PL gives a well defined spectrum, the CL spectrum presents a poor resolution and a strong dependence with the acceleration voltage of the e-beam; which, according to Witry and Kyser [40], suggests that the saturation of surface states can play an important role in the

formation of the dead layer because of the formation of a space charge region, which is almost negligible for laser excitation, bur relevant for e-beam excitation.

Surface recombination removes carriers with an efficiency that increases linearly with S/(S + 1), and decreases exponentially with the ratio source depth/diffusion length, where the source depth can be considered to be the depth of the maximum energy loss. Therefore, the CL signal will increase with the electron energy [40, 61].

Nouiri et al. [21, 62–65] proposed the existence of a charge depletion region induced by the surface charges. This is in good agreement with the above discussion about the dead layer in highly reactive surfaces. ZnO crystals are very useful for studying the influence of the surface on the CL intensity at low acceleration voltages. Surface states can have a crucial relevance for the properties of metallic contacts on those surfaces. Brillson et al. studied the surface states in relation to the lattice defects, the impurities, and the surface reactions. They observed significant changes in the CL spectra, depending on the characteristics of the ZnO crystals, the metallic contacts and the treatments applied, using depth resolved cathodoluminescence spectroscopy (DRCLS) [66, 67]. Nouiri et al. made a study of the influence of the surface charge on the CL signal [65]. The charge trapped at surface states is responsible for the depletion region, which removes the generated e-h pairs avoiding the recombination inside the space charge region, with the result of a sharp decrease of the CL signal for low acceleration voltages. They made estimations of the CL intensity with the acceleration voltage for donor and/or acceptor states located at different energies in the band gap in GaAs, showing that the CL quenching at low voltage is enhanced in the presence of midgap surface states.

5.5 The CL Signal

The luminescence signal arises from the recombination of the e-h pairs generated by the electron beam. The recombination can be either radiative, or non-radiative. Furthermore, different recombination centers, which the relative concentrations and recombination efficiencies contribute to the intensity of the different luminescence emissions, can be involved. Their relative spatial distribution is responsible for the contrast of the CL images, either panchromatic, or monochromatic.

The recombination centers are characterized by their recombination rates, which are inversely proportional to the recombination times, τ_r, for the radiative recombination, and τ_{nr} for non radiative recombination. The recombination time is characteristic of each recombination center. In the presence of both radiative and non radiative recombination centers the carrier lifetime is related to the recombination times by the following expression:

$$\frac{1}{\tau} = \frac{1}{\tau_r} + \frac{1}{\tau_{nr}} \tag{5.18}$$

Both, τ_r and τ_{nr}, can be the result of different recombination centers:

$$\begin{aligned} \tau_r^{-1} &= \sum_i \tau_{ri}^{-1} \\ \tau_{nr}^{-1} &= \sum_j \tau_{nrj}^{-1} \end{aligned} \tag{5.19}$$

The internal quantum efficiency (IQE) defined by the ratio of the radiative to the total recombination rates can be expressed as:

$$\eta = \left(1 + \frac{\tau_r}{\tau_{nr}}\right)^{-1} \tag{5.20}$$

The IQE is enhanced at low temperature, therefore; the CL signal is notably improved at low temperature.

One of the strengths of CL is its imaging capability. Conventional CL images can be either panchromatic or monochromatic. In the panchromatic images the contrast is determined by the local fluctuations of the IQE, i.e. the ratio between the radiative and non-radiative recombination rates, within the spectral sensitivity range of the detector. In monochromatic images one selects a narrow spectral window corresponding to a particular CL band and the image of such emission is collected. One can define the internal quantum efficiency for that monochromatic emission arising from a particular recombination center, with a recombination time τ_{rl}:

$$\eta_l = \frac{\tau}{\tau_{rl}} = \frac{1}{1 + \frac{\tau_{rl}}{\tau_{nr} + \tau_r}} \tag{5.21}$$

in this case the image contrast is determined by the ratio between the recombination rate responsible for that emission, and the recombination rate of all the recombination paths, both radiative and non radiative.

SEM and monochromatic images of shell Mg-doped GaN nanorods are shown in Fig. 5.13 [68]. The monochromatic images correspond to the near band edge (NBE) emission, the DAP transition associated with Mg acceptors [69], and the YL band associated with Ga vacancy complexes [18]. The monochromatic images reveal the distribution of the different emissions over the nanorods.

Taking into account that the recombination rates, either $1/\tau_{ri}$ or $1/\tau_{nrj}$, are proportional to $(N_{ri}\sigma_{ri}v_{th})$ and $(N_{nrj}\sigma_{nrj}v_{th})$ respectively; where N_r (N_{nr}) is the concentration of radiative (non radiative) recombination centers, σ_r (σ_{nr}) the capture cross section, and v_{th} the thermal velocity of minority carriers, the image contrast is governed by the concentrations of the recombination centers and their corresponding capture cross sections.

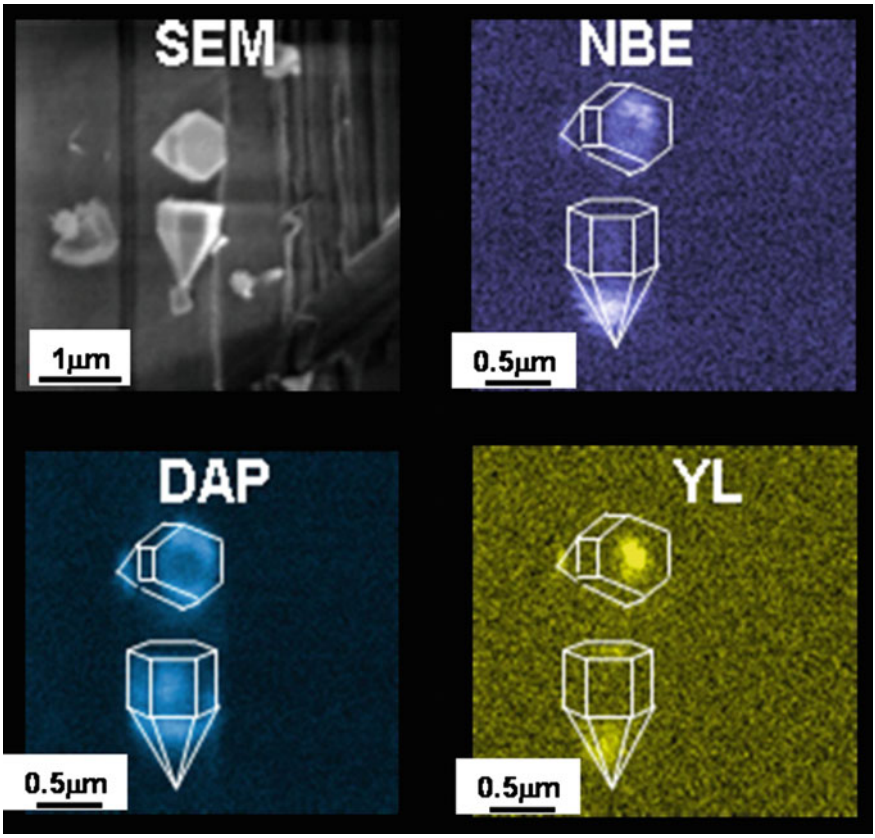

Fig. 5.13 SEM, NBE monochromatic image, DAP monochromatic image, YL monochromatic image of Mg shell doped GaN nanorods [68]

The CL signal has to take account of the three processes: generation, diffusion and recombination; but also, one has to consider pure optical effects as self-absorption of the emitted photons, internal total reflection and Fresnel losses at the surface [5]. These factors determine the external quantum efficiency (EQE). The internal absorption of photons is more important in CL than in PL, because in CL, especially for high voltages, the photons are generated deeper in the sample than in PL measurements, therefore, they have to travel a long way before being extracted; the result is a decrease of the CL intensity, mainly for the high energy photons of the band edge (NBE) emission; eventually, the most energetic emissions associated with free excitons cannot be observed. Yacobi and Holt [15] derived a factor accounting for the internal absorption losses:

$$f_A = \frac{1}{1 + \alpha L_d} \tag{5.22}$$

where α is the absorption coefficient and L_d is the free carrier diffusion length, which accounts for the additional depth due to the diffusion of the generated carriers before they recombine. Remember that the carriers, or excitons, can move away before recombining, what means that the recombination can occur out of the generation volume. The diffusion of the free carriers and/or the excitons reshapes the N_{eh} (r, z) function, affecting the spatial resolution of the luminescence probes, and in particular of the CL. The CL experiments record the radiative recombination emissions as a function of the primary electron beam position; but because of the carrier diffusion it does not record the real location of the recombination centers. Usually, the minority carrier diffusion length is the dominant parameter; however, contrarily to the PL measurements, in CL one can also excite a relevant population of majority carriers; therefore, under high excitation conditions, with respect to the equilibrium free carrier concentration, one should take account of the ambipolar diffusion lengths.

The exponential decay of the free carrier concentration limits the spreading of the CL source due to carrier diffusion to the diffusion length. This means that the experimental resolution of the CL depends on both the generation range, R_e, and the diffusion length, L_{diff}, accordingly, the minimum diameter that can be resolved by CL, D_{CL} is [70]:

$$D_{CL} = \sqrt{R_e^2 + L_{diff}^2} \tag{5.23}$$

Therefore, it depends on the e-beam energy, but also on L_{diff}. By reducing the electron range, Re, one can expect to work with a CL probe in pure diffusive regime; in other words, under such specific experimental conditions the e beam constitutes a punctual e-h pair source; this approximation is possible, because of the high current beams of the field emission SEMs, which can supply very high current beams of nanometric lateral dimension with low voltages. In fact, at very low voltage (<1 kV) with very small beam size (≈2 nm), the effective generation volume was only a few tens of cubic nm, which permits to assume that the generation source is punctual, and the spatial resolution in such experimental circumstances would be mainly determined by the carrier diffusion length.

The use of low acceleration voltages (1 kV), in field emission SEM allowed Pauc et al. [24] the study of pure and doped GaN crystals aiming to the estimation of a reliable value for the carrier diffusion length in GaN. We will come back to this point.

One can obtain CL images of defective areas with high spatial resolution, in which the IQE changes with respect to the surrounding areas, although, sometimes they present a fuzzy aspect due to the capture of the carriers generated within diffusion length distance from the defect. Imaging dislocations and other extended

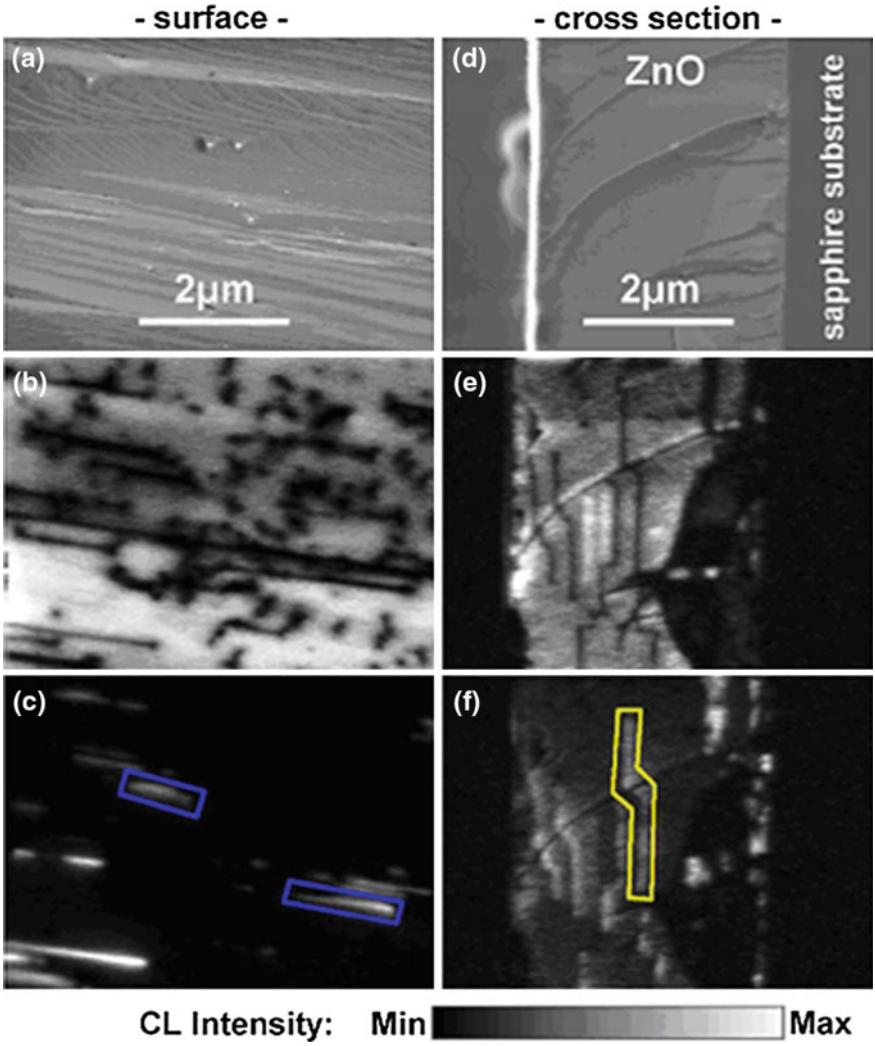

Fig. 5.14 **a** SEM image of the sample surface, **b** near band gap CL image (3.349–3.379 eV spectral window), **c** (eA^0) CL image (3.296–3.325 eV spectral window), **d** SEM image of the sample cross section, **e** monochromatic CL image in the band gap range as **b**, **e** monochromatic CL image in the eA^0 spectral range as **c** [83]

defects has been achieved by CL [71–86]. CL images obtained in different faces of ZnO are shown in Fig. 5.14 [83].

In low dimensional structures, the diffusion can be limited by the dimension of the structure, as in NWs or QDs [87]. Multilayer structures can be studied because of the confinement of the generated carriers in the different layers. For example,

laser diode structures are very well characterized, allowing a layered CL image, because of the limited interlayer diffusion of the generated carriers and the different emission spectral windows of the different layers.

In regions close to defects, e.g. dislocations, which are non radiative recombination sites [72, 81, 88], the weight of τ_{nr} is increased, and therefore the diffusion length is substantially reduced, improving the spatial resolution with respect to the defect free regions, where the carrier diffusion spreads out the volume of light generation.

Note that the presence of defects can induce strain fields which can have a non negligible influence on the band gap of the material, which depending on the sign, can stimulate the carrier diffusion towards or away the defect with the result of reverse contrast for the two cases. The in plane diffusion length can be very large in QWs; however, the QW thickness and/or compositional fluctuations generate local potential wells that constitute barriers to the in plane carrier diffusion, especially for narrow QWs, with thickness of the order of the exciton radius [16, 77, 89]. This permits to image the fluctuations in terms of the CL spectral changes [90], Fig. 5.15.

The CL intensity is defined as the number of photons emitted per unit time. It can be expressed for a point electron excitation source as [15]:

$$I_{CL} = f_D f_A f_R \eta \frac{G I_b}{e} \tag{5.24}$$

$$f_R = \frac{n - \sqrt{n^2 - 1}}{2n} \left[1 - \left(\frac{n-1}{n+1} \right)^2 \right] \tag{5.25}$$

where, f_D is a constant dependent on the efficiency of the detector. f_R is related to the optical losses due to total reflection because of the large refractive index of the semiconductor. n is the refractive index.

The CL signal depends on the e-beam parameters, but also on different materials parameters, as S (SRV), the diffusion length, the optical absorption coefficient, the dead layer thickness, and also the charging of the sample under the e-beam exposure. The relation between all these parameters and the CL signal is not simple, but generally presents non linear dependence, for more information see [5].

The study of the variation of the CL signal with the primary beam energy can be used to estimate semiconductor parameters as the absorption coefficient, the diffusion length, the dead layer thickness, the surface recombination velocity, and the quantum efficiency [23, 91].

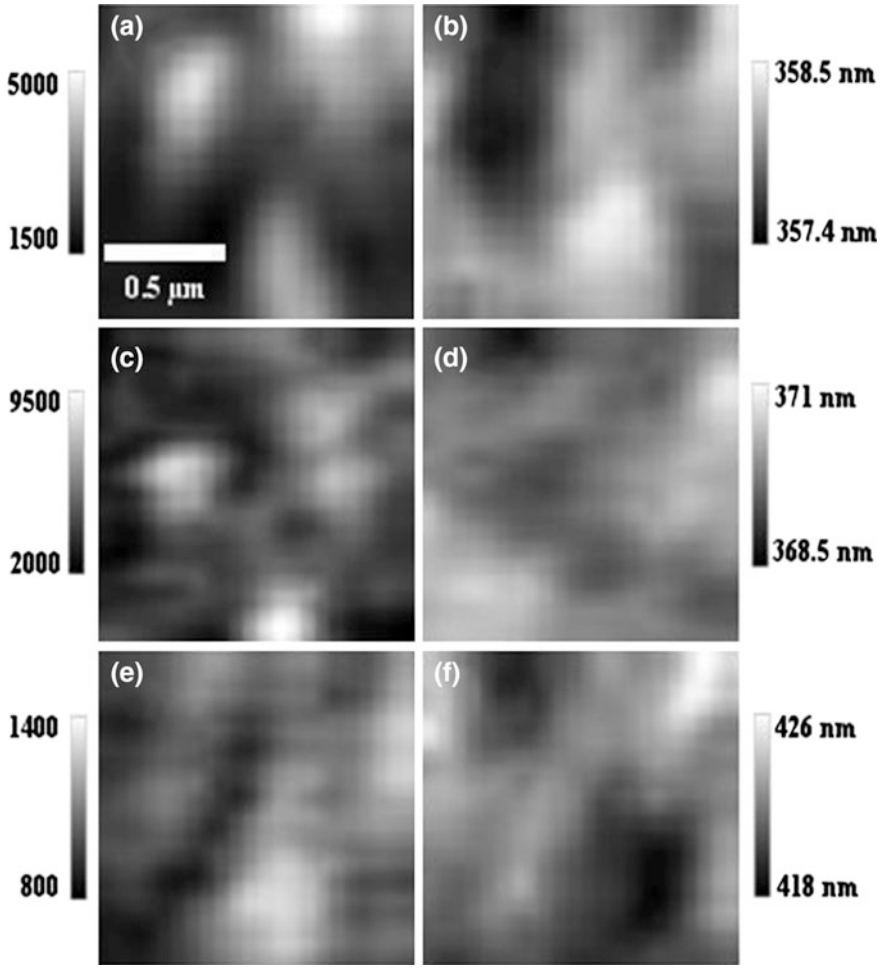

Fig. 5.15 CL intensity and peak wavelength distribution of capping GaN layer (**a**, **b** respectively), InGaN barrier (**c**, **d**), and InGaN QW (**e**, **f**). Note that the peak wavelength fluctuations scale from 1 nm for the GaN capping layer, through 2.5 nm for the barriers, to 8 nm for the QW, due to fluctuations of composition and the piezoelectric field [90]

5.6 Experimental Set-Up

CL experiments are carried out with an electron gun as the excitation source, the electrons are focused on the sample surface. Usually, CL experiments are carried out in vacuum chambers, generally in a SEM, but also CL set-ups are mounted in TEMs; with the improvement of the detectors sensitivity the CL TEM option is increasingly reclaimed [92, 93].

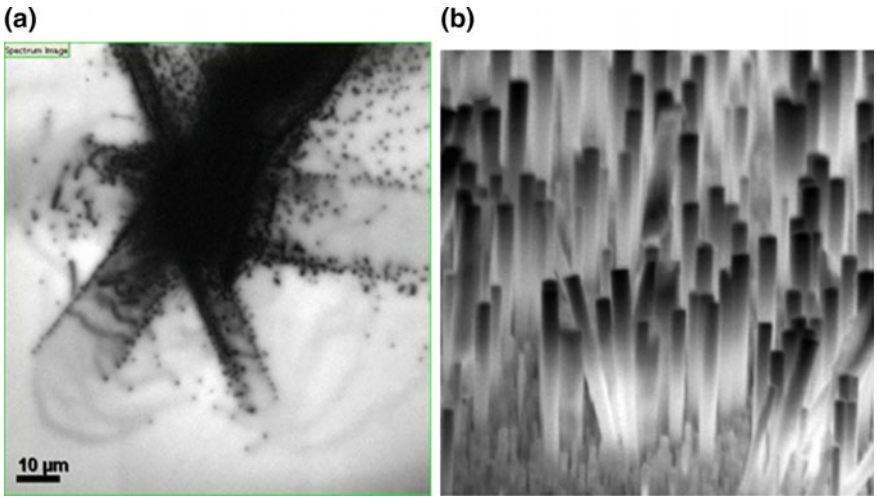

Fig. 5.16 Panchromatic images of indented ZnO crystal (**a**), ZnO NWs (**b**)

The CL systems were initially conceived for the acquisition of luminescence spectra in geologic samples, because of the large band gap of the geological materials, e.g. quartz. Later on, the CL parts were attached to the SEMs, which added the high spatial resolution imaging capability to the CL technique. Pioneer SEM_CL set-ups allowed the acquisition of luminescence images. In these images, the light emitted is collected by the optics, and transferred to the detector, which records indistinctly all the photons within its spectral window of sensitivity. Normally, the detector is a photomultiplier (PMT) for visible emission, and a Ge detector for infrared emission; actually, the Ge detectors are being replaced by InGaAs detectors. These images are contrast images, which reveal local changes in the CL signal, mainly because of the local changes in the IQE due to the spatial fluctuations of the recombination centers concentration, either radiative or non-radiative. This kind of image is named as a panchromatic image. Some panchromatic images are shown in Fig. 5.16.

One observes dark and bright regions associated with spatial variations of the IQE, note that generally CL is revealing structures that are not observed in the secondary electron image. In early CL setups, a photodiode was inserted inside the microscope chamber, very close to the sample, and the light emitted was collected by a lens and focused in the photodiode, which was coupled to the e-beam scanning, forming the CL image. Obviously, this arrangement is not ideal, because of the low angle of light collection, and the lack of spectroscopic capability.

The CL emission from the interior of the sample emerging to the surface is dispersed because of the large refractive index of semiconductors, which makes that the emerging light rays deviate from the normal; this dispersion, together with the weak signal demands highly efficient collecting optics. In this context, the core of the modern CL set-ups is the collecting optics, and its coupling to the spectroscopic

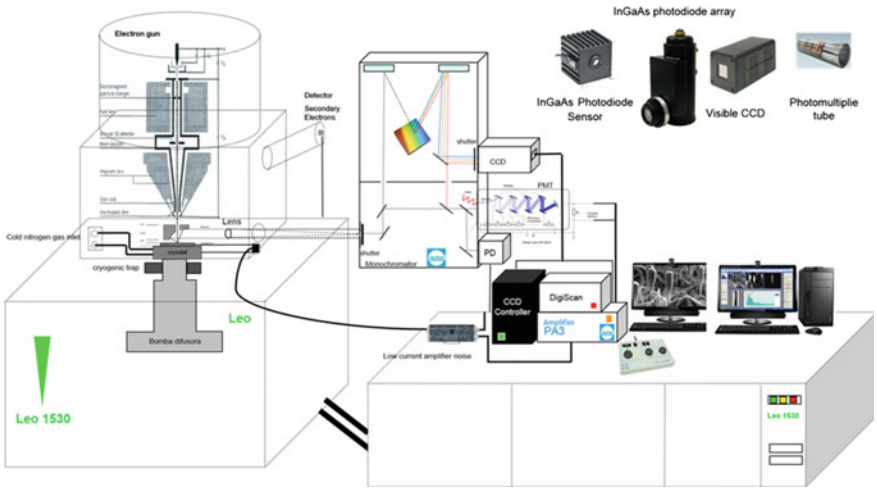

Fig. 5.17 CL set-up

and detection stages. Therefore, a CL set-up attached to the microscope consists of the collecting optics, the parts guiding the light to the spectrometer, the spectrometer itself, and the detector. Optionally, one can also include a cryogenic stage for low temperature measurements, and an electrostatic beam blanking for time resolved CL measurements (TRCL). A scheme of a CL system is shown in Fig. 5.17.

The light collection system is crucial, because of the very small generation volumes and the weak luminescence emission, especially if one desires working with low electron energies for high spatial resolution applications. One needs to collect all the available photons in order to improve the signal to noise ratio. The light collection systems have evolved from the early ones reported by Steyn et al. [94]. Mirrors with large solid angles are the ones with the best collecting efficiency; among them, parabolic and elliptic mirrors are the ones usually mounted on the CL systems. These mirrors permit collecting most of the light emitted and emerging from the surface of the sample. The mirrors have a hole aperture on the top aligned with the microscope column allowing the e-beam to go across the mirror reaching the sample; the e-beam must strike the sample on the mirror focus. In the parabolic mirror the collected light is directed parallel to the paraboloide axis, then guided through an evacuated tube, or an optic fibre, into the spectrometer for serial detection (spectrally resolved CL), or directly into the detector for parallel detection (panchromatic CL). In the elliptic mirror, the e-beam strikes the sample in one of the focus and the collected light is concentrated in the other focus of the elipse where the light guide must be placed in order to drive the light to the spectrometer and detection stages as described for the parabolic mirror; this arrangement is very well adapted to optic fiber coupling. A new CL concept has been recently developed called quantitative CL [95], which integrates a SEM with an optical

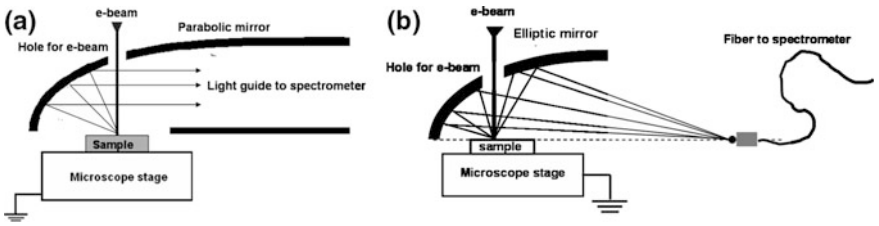

Fig. 5.18 Parabolic mirror (**a**), elliptic mirror (**b**)

microscope, formed by aspheric reflective surfaces in the polar piece of the SEM optimized for photon collection. This concept should eliminate some of the distortions introduced by the parabolic and ellipsoidal mirrors when recording CL spectrum images at low magnification, since it works with a focal plane instead of a focal point. Both the parabolic and elliptic arrangements are shown in Fig. 5.18.

Once the light arrives into the entrance slit of the spectrograph, it can follow different paths depending on the operation mode, either serial or parallel. It can bypass the monochromator gratings entering directly onto the detector; this is the parallel detection mode, in which the panchromatic images are recorded; or, the light beam enters the monochromator and is dispersed for spectral detection, which is known as the serial detection mode, which is the mode used for spectrally resolved CL. The diffraction grating can be placed in zero order, where there is not spectral dispersion obtaining the zero order image, which is similar to the panchromatic image, but with the light following a different path; the zero order operation is practical for the alignment of the system for spectroscopic CL, because the optical path is the same as the one used for the spectroscopic mode. With the monochromator in dispersive mode, one can select a narrow spectral window for obtaining a monochromatic image, i.e. images revealing the spatial distribution of a particular luminescence emission, see Fig. 5.13, where different monochromatic images of GaN nanorods were shown. The CL spectrum can be recorded either local, or global. If one scans over a sampling area (global spectrum), one can obtain a CL spectrum averaged over the sampling surface.

The detectors are essential to the CL capabilities, both imaging and spectral. The modern CL apparatus are equipped with several detectors; which can cover different spectral ranges, and also can be either single channel, or multichannel detectors. Actually, single channel detectors are used for acquiring panchromatic and/or monochromatic images, however, they are less useful for spectroscopic analysis, because the acquisition of a spectrum with a single channel spectrum, e.g. a PMT, is time consuming, and only a few local spectra can be acquired in a reasonable time. The single channel detectors are selected by their spectral window of sensitivity; usually, the PMTs are used for UV and visible detection. Nowadays, InP/InGaAs photocatode PMTs are sensitive to a broad spectral range, from 300 nm to 1700 nm, suitable for most of the semiconductor emissions. Otherwise, InGaAs

and/or Ge detectors are used for the infrared spectral range; they can extend the detection from the upper limits of the PMTs up to 2100 and 1800 nm respectively.

The last generation of CL setups allows for fast spectrum acquisition by using multichannel detectors, e.g. CCDs, or Vidicons, which enable spectral imaging to the CL technique. By using these detectors the local full spectral information over the scanned area can be acquired. This gives a superior dimension to the CL technique. This operation mode is called the spectral image mode, or hyperspectral mode. In this mode the region of interest (ROI) is scanned, and the spectrum is recorded for each pixel according to a defined frame. The result is an image where each couple of spatial coordinates is associated with a spectrum. The spectrum imaging permits the acquisition of a high amount of data in a very short time. The scanning speed is fast, then, the time of image acquisition is mainly determined by the detector integration time. In the case of micro-PL images, the time is longer because of the step by step motion of the sample; however, it permits mapping large surfaces, which is not possible with the CL set-up. The use of fitting routines permits the conversion of these images into images of different spectral parameters, as well as the revelation of a continuous range of monochromatic images.

The core of the spectral imaging mode is the multichannel detector. The CCD detectors must have low noise, high sensitivity, excellent linearity, and no etaloning. The low noise is achieved by CCD cooling, using either a Peltier, or a dewar for liquid nitrogen cooling; the last solution is better in terms of lower noise, but also because of the absence of the vibrations produced by the fan in Peltier cooled CCDs. Another important aspect is the speed of acquisition. When using CCD detectors signals can be enhanced by increasing the integration time. However, typical spectral images can consist of a few thousand pixels with full spectral information, which makes non sense the use of long integration times; therefore, the acquisition of images in a reasonable time, demands integration times ranging from the milliseconds to tens of milliseconds. It means that the quantum efficiency of the detector is crucial for the reduction of the integration time. One can use thinned back illuminated CCDs, and front illuminated CCDs. The back illuminated CCDs present a higher quantum efficiency, approaching 90% at the peak wavelength, and a very good response in the UV and visible ranges, while the QE is reduced in the red and near IR. The front illuminated CCDs have half QE at the visible range, and much lower in the UV. The problem with back illuminated CCDs is etaloning, which consists of an interference fringe pattern in the spectral response, especially in the red and near IR spectral regions. Therefore, the back illuminated CCDs are preferred for UV and visible detection, while the front illuminated CCDs are more suitable for the red and near IR spectral windows. Actually, back illuminated CCDs enhanced in the IR spectral range are available, with QE around 50%. Furthermore, back illuminated cameras with reduced etaloning, up to a factor 5 reduction, are also available. See the discussion of Chap. 3 about the detectors.

Figure 5.19 shows a CL spectral image of a glided dislocation revealed by selective etching in Si-doped GaAs; each pixel contains the full spectrum information; a few spectra corresponding to specific areas of the image, the core of the dislocation (1), the unperturbed matrix (2), the glide trail (3), the dislocation site

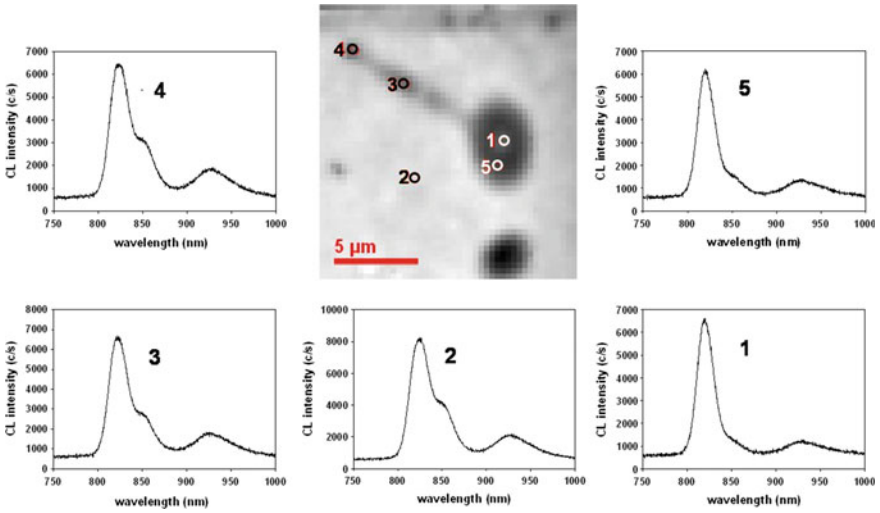

Fig. 5.19 CL spectral image of a glided dislocation in GaAs revealed by selective chemical etching. Each pixel carries the complete spectral information. The sampled spectra are the spectra corresponding to the points numbered in the image [28]

before gliding (4), and the area surrounding the dislocation core (5), are shown evidencing significant changes in the spectra depending on the position, which reveal changes in the doping and point defect distribution under the influence of the dislocation [82]. A detailed description of the results obtained by the spectral images will be presented as a case application concerning the characterization of orientation patterned GaAs (OP-GaAs) crystals, and the dislocation of Fig. 5.19.

SEM/STEM systems provide accurate scanning of the excitation beam which permits a very good spatial stability, unless charge effects, discussed in the next paragraph, occur.

5.7 Electrostatic Charge

Electron beam bombarding an insulating surface can induce electrostatic charge and the corresponding electrostatic field [96, 97]. This field can contribute to the dead layer, but also is responsible for the presence of electrostatic forces that can move the sample during the CL measurement, making difficult the focus and deforming the images. In the most insulating samples one can deposit a transparent metal layer, which permits grounding the sample removing the charges, and allowing the luminescence emission going through.

The electrostatic force induced by the electrostatic charge is responsible for the deformed CL images often obtained with NWs and other reduced dimension

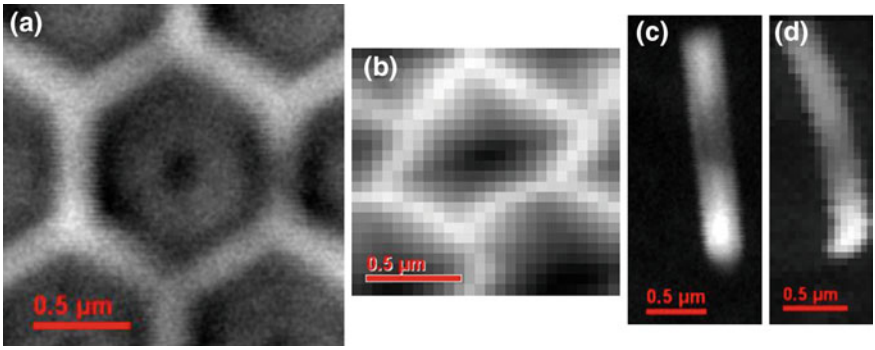

Fig. 5.20 Top view CL images of GaN nanorods, **a** panchromatic image, **b** spectral image. *Side view* CL images of GaN nanorods, **c** panchromatic, **d** spectral image. The longer e-beam exposure of the spectral images produces distortions due to charge effects

structures, in particular NWs are bent under the effect of the electrostatic charges [98], this effect can be mitigated by optimizing the experimental conditions.

The charging effects make difficult the operation of focusing the image. Even if one arrives to obtain a satisfactory panchromatic CL image, the charge effects are most critical for the spectral images. Usually, spectral images require of prolonged e-beam exposition, which magnifies the electrostatic charge, and can introduce in reduced dimension structures distortions of the image, Fig. 5.20 shows panchromatic, and spectral images, respectively of a shell Mg-doped GaN nanorod in top view and side view; the spectral images present a strong distorsion with respect to the conventional panchromatic images.

5.8 Case Applications

5.8.1 Carrier Diffusion Length

The diffusion length of carriers, and excitons, is a major parameter for optoelectronic devices. On the other hand, as mentioned above it plays a major role in the spatial resolution of luminescence based techniques, namely in the CL spatial resolution.

Generally, one refers to the diffusion of the minority carriers, though in CL experiments, under high generation rates, one can also generate majority carriers in excess. Therefore, one has to consider ambipolar diffusion. If one considers a local carrier source the density profile is governed by the diffusion of the generated carriers following the relation:

$$n(r) \sim (1/r)\exp - (r/L_{diff}) \tag{5.26}$$

L_{diff} depends on the mobility, μ, of the diffusing carriers, the lattice temperature, T, the carrier electric charge, q, and the lifetime, τ [96]:

$$L_{diff} = (k_B \mu T \tau / qe)^{1/2} = (D\tau)^{1/2} \tag{5.27}$$

Being D the diffusion coefficient. Note that differences in such coefficient must be considered when one deals with 1D, 2D or 3D structures. The type of confinement determines the direction over which the generated carriers can diffuse. When the carrier generation occurs close to the surface, closer than the diffusion length, a significant amount of the generated carriers can diffuse towards the surface recombining non radiatively. This is very important for CL measurements under ultralow acceleration voltages, it was already discussed in relation to the dead layer.

We deal here with the use of the CL for the estimation of the carrier diffusion length. There are different ways to determine the diffusion length using CL. Zarem et al. [99, 100] used a mask made of an opaque 75 nm thick Al layer, deposited on the semiconductor surface. When the e-beam is over the mask it can excite the semiconductor underneath the metal layer generating e-h pairs, but the metal layer does not permit the CL emission to emerge out. The diffusion length is measured by scanning the e-beam across the edge of the metal mask, if the volume generation is at diffusion length distance of the metal layer edge, the emitted light should emerge out through the unmasked surface, so it can be collected by the mirror. The ambipolar diffusion lengths of different materials have been measured at 300 K following this procedure [99–101]. Another method for the assessment of the diffusion length, consists of the measurement of the CL intensity profile across a discontinuity, e.g. a dislocation, a local potential barrier. Usually, dislocations act as non radiative recombination centers (NRRCs); therefore, the intensity profile around them is governed by the diffusion of the generated carriers towards the dislocation where they recombine non radiatively. Using the CL emission around a decorated threading dislocation, a diffusion length of 1.5 μm was obtained in GaAs QW, for both normal excitonic CL, and donor-acceptor-pair (DAP) CL [77, 89].

The minority carrier diffusion length in GaN is a very relevant parameter, because the threading dislocations (TDs) are admitted to be non radiative recombination channels. In spite of the huge concentration of TDs the emission efficiency is high, allowing the fabrication of high performance light emitting devices. This suggests that the minority carrier diffusion length must be very short, thus minimizing the detrimental influence of the dislocations in the IQE of GaN. Several attempts have been carried out to study the recombination activity around TDs in GaN. CL was used for this purpose. Earlier results reported an upper limit of 0.25 μm for the minority carrier diffusion length, which was mainly determined by the radius of the primary electrons excitation volume, as a consequence of the use of a high acceleration voltage (10 kV); lower voltages were used for achieving reliable measurements of the diffusion length in GaN [102].

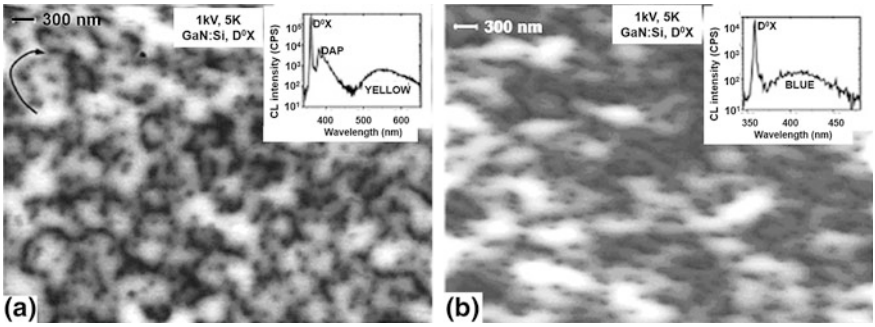

Fig. 5.21 CL image obtained at very low e-beam energy (1 keV), in Si-doped GaN (**a**), and undoped GaN (**b**), showing very tiny dark spots associated with the non radiative recombination of the TDs [24]

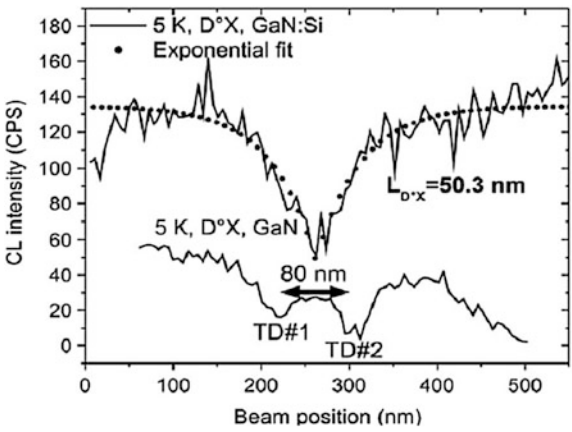

Fig. 5.22 CL intensity profiles across the dark spots of Fig. 5.20. The diffusion length is calculated by exponential fitting of the intensity profiles [24]

Pauc et al. [24] studied undoped and Si-doped GaN using very low voltages (1 kV). The CL images were similar to those reported elsewhere [103, 104]; however, the lower acceleration voltage permits a higher spatial localization by working in pure diffusive mode (see Sect. 5.5). This permits the observation of well contrasted tiny dark spots with dimension below 100 nm. These dark spots are associated with the TDs, Fig. 5.21.

The intensity profile around the dark spot was used for measuring the diffusion length, see Fig. 5.22. The diffusion lengths at 100 K, averaging free and bound excitons, and DAP emission, were extracted from the corresponding monochromatic CL intensity profiles, resulting in 56 ± 14 nm and 74 ± 27 nm respectively. The longer diffusion length measured for the DAP emission band is consistent with the more fuzzy aspect of the DAP monochromatic image than the excitonic

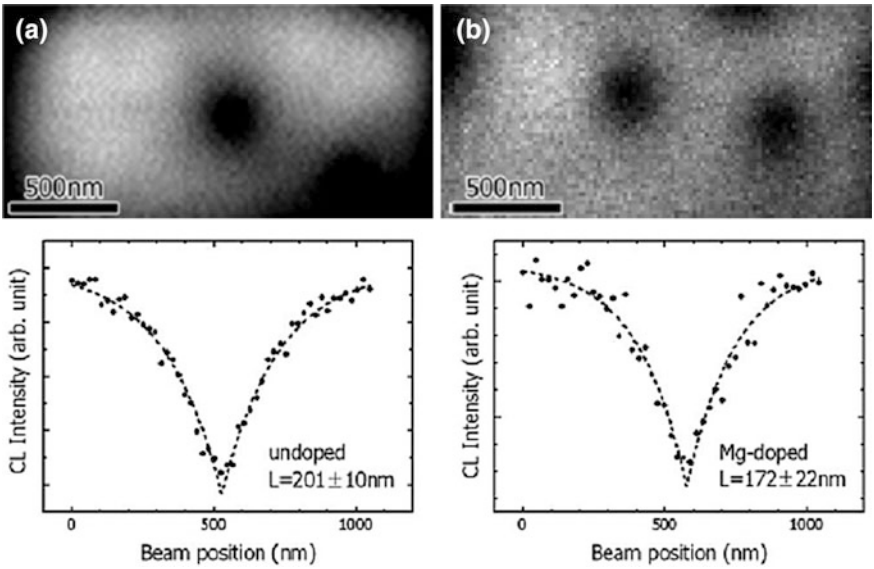

Fig. 5.23 Monochromatic CL images of GaN dislocations obtained from the excitonic emission, **a** undoped GaN, **b** Mg doped GaN. The *lower panels* show the respective exponential fits of the intensity profiles across the dark spots revealed in the CL images [105]

monochromatic image. For more details concerning the validity of the experimental conditions for the estimation of the diffusion length the reader is addressed to [24].

Ino et al. [105] studied the influence of doping and temperature on the carrier diffusion length in GaN using TEM CL, Fig. 5.23. The diffusion length deduced from the free exciton emission was shorter in the doped sample than in the undoped sample for the full temperature range, consequence of the impurity scattering. The authors claim that the diffusion lengths measured may be mediated by the surface recombination.

The discrepancy in the diffusion lengths reported in the literature can arise from the different nature of the samples, but also from the diffusion model used, and the size of the generation volume, for more details about this see [24, 106].

5.8.2 *In-Depth Analysis: Multilayer Structures. Laser Diodes and AlGaN/GaN HEMTS*

One of the main strengths of the CL technique is the capacity of carrying out a true in depth analysis, allowing a sufficient penetration of the electron beam in contrast to the reduced penetration capacity of the laser beams. This is very suitable for the study of multilayer structures, since the successive layers can be reached by varying the acceleration voltage of the electrons. One of the problems for which successful

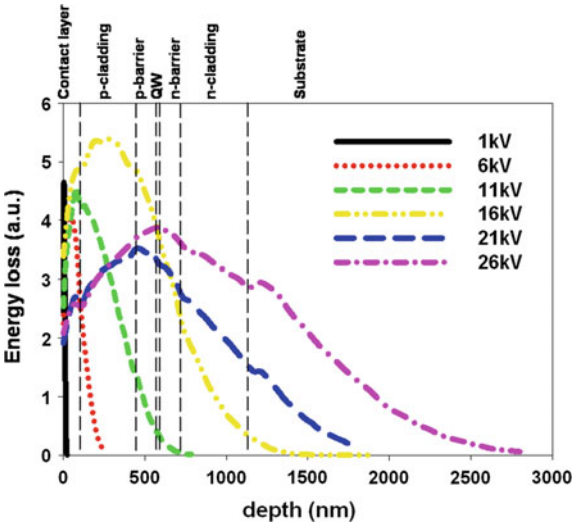

Fig. 5.24 Calculated loss energy versus depth for different e-beam energies of a typical QW laser structure

application of the CL technique has been demonstrated concerns the study of degraded laser diodes [103–108]. Also, recent studies have been carried out on AlGaN/GaN HEMTS [109]. Measurements with high spatial accuracy are crucial for device modelling and failure predictions.

The degradation of laser diodes is related to the formation of defects in the active parts of the device. Among the laser failure modes one can distinguish wear-out and catastrophic failures [110]. Wear out failures are associated with the generation of point defects that progressively decrease the laser power efficiency. Catastrophic failures are associated with the generation of extended defects leading to the sudden end of the laser life. Those defects may be localized at the front facet, but can also occur inside the cavity far from the mirror facets. When using PL some of the layers are beneath the penetration depth of the laser beam; therefore, the PL study of those layers demands of the thinning of the laser structure in order to make the active parts accessible to the excitation laser beam [111]. This is overcome using the electron beam as the excitation source, since it can cross the full multilayer structure by varying the acceleration voltage. Figure 5.24 shows the maximum electron energy loss for different e-beam energies, calculated by Monte-carlo simulations, in a 808 nm laser structure composed of the following layers (contact layer (GaAs)/ p-cladding ($Al_{0.6}Ga_{0.4}As$)/ p-barrier ($Al_{0.3}Ga_{0.7}As$)/ QW ($Al_{0.1}Ga_{0.9}As$)/n-barrier ($Al_{0.3}Ga_{0.7}As$)/n-cladding ($Al_{0.6}Ga_{0.4}As$)/substrate (GaAs). The CL signal from the different layers can be extracted by varying the e-beam energy, or using an e-beam energy that crosses the structure, because of the different composition of the layers they can be distinguished by its different emission spectral windows.

In the case of broad emitter lasers after degradation, the front facet presents defects with dark contrast in the CL image of the QW, Fig. 5.25. The degree of degradation is not the same for all of the dark zones, but some of them are still

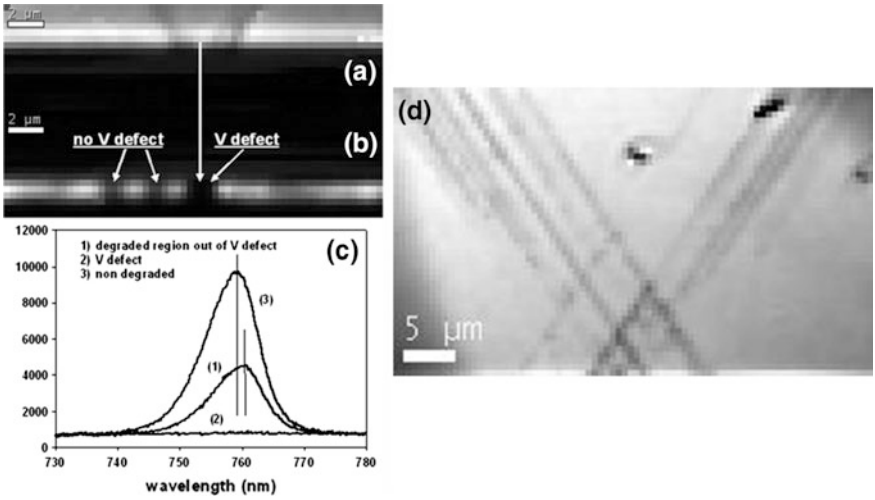

Fig. 5.25 Front facet CL image of a broad area emitter 808 nm laser. **a** Cladding layer and substrate where one can appreciate the V-shaped defect. **b** QW and waveguide. The defects are localized in the QW. These "dark" defects correspond to different levels of degradation. The local spectra at different positions of the QW are shown in **c**, the defect indicated by V is fully dark, while the other defects labeled as no V defect are still emitting light. The *right panel* **d** shows an array of V defects in the front facet of a laser [113]

emitting light, while others are fully dark, indicating the destruction of the QW. The darkest regions can develop dark contrast branches forming a V shape with an angle of 70° in between the two arms of the V; this V is generated in the active zone of the laser and can extend far away inside the substrate. The dark lines form an angle of 55° with the [112] epitaxial plane. This means that they follow the intersection of [108, 109] crystal planes [113].

The problem with the observation of the front facet is that the volume of observation is restricted to the region close to the mirror, less than ~ 2 µms depth, losing thus the information about the damage inside the cavity. The observation of the cavity can be achieved by CL if one removes the metallization layers, allowing the access of the e-beam to the inner laser cavity. Top-view panchromatic CL images of broad emitter lasers reveal the presence of dark spots (DSDs) distributed over the cavity, and also dark line defects (DLDs) propagating along the cavity, Fig. 5.26. The defects can be completely dark, or they can still emit under the excitation with the e-beam, which corresponds to different stages of degradation. The DSDs are not fully dark, but they still emit, while the DLDs along the cavity are fully dark, which points to the destruction of the QW.

Monochromatic images evidence that the damage is concentrated in the active part of the laser structure, QW and waveguides, while the contact layers are free of defects, in fact, the damage pattern is only observed in the image corresponding to the QW emission, while the monochromatic image corresponding to the contact layer is free of dark defects, Fig. 5.26. In these laser structures the guides and the

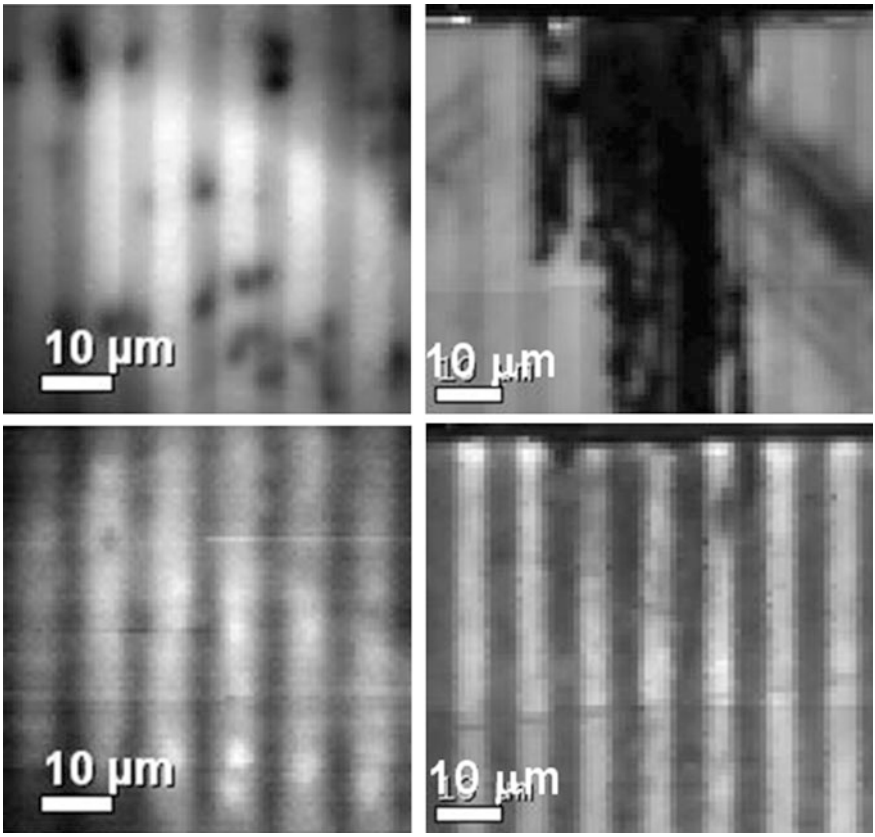

Fig. 5.26 Monochromatic CL images ot two broad area emitter 808 nm lasers, showing partially degradation, with DSDs, and full degradation with DLDs. The *upper panel* corresponds to the QW emission, while the *lower panels* are the contact layer emission images. The damage is localized in the QW

claddings are AlGaAs with Al concentration above the crossover from direct to indirect band gap, therefore, they do not emit luminescence, and one cannot acquire information about the stage of degradation of the guide layers.

The study of the CL parameters can help to study the evolution of the QW structure during degradation. The luminescence parameters of the QW were estimated from CL spectral images. The images representing the distribution of the peak intensity, peak wavelength and full width at half maximum (FWHM) of the QW CL emission are shown in Fig. 5.27; local CL spectra obtained at points with different levels of degradation are also shown. As a general trend one observes anticorrelation contrast between intensity and FWHM, and between intensity and peak wavelength. The most general trend in the degraded zones is the redshift and broadening of the QW emission luminescence band. However, one can observe degraded zones that do not follow such a trend, but blue shift and strong broadening

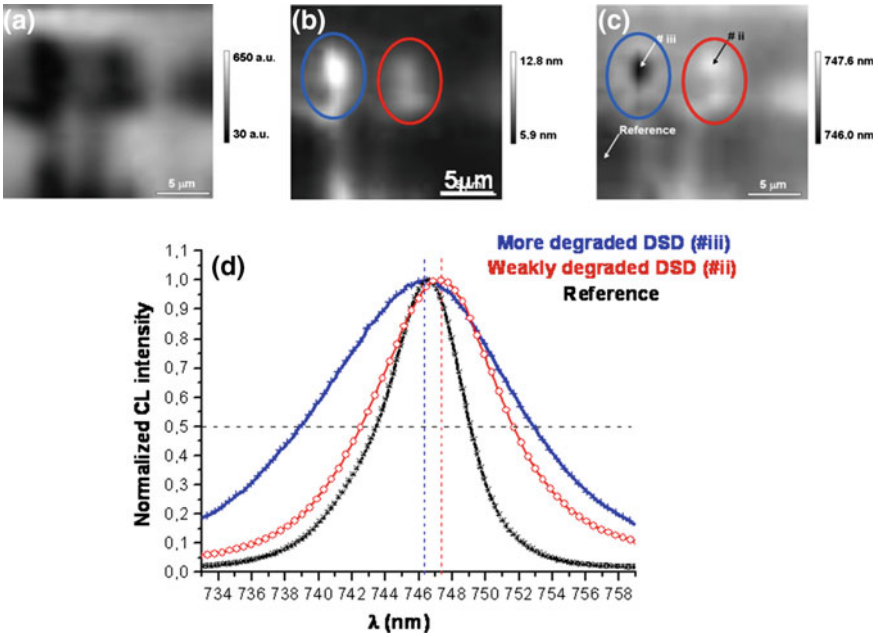

Fig. 5.27 Spectral images obtained in *top view* in a degraded laser, **a** QW emission intensity, **b** peak wavelength of the QW emission, **c** FWHM of the QW emission. The spectra in undamaged (reference), and two zones with different degree of degradation are plotted in **d**. Note that the more degraded region shows *blue* shift and broadening of the QW emission, evidencing intermixing [114]

of the QW emission are observed, which correspond to the cation intermixing between the QW and the guides [114, 115].

In 980 nm monomode lasers one can study the evolution of the InGaAs QW and the barrier layers. The CL spectrum reveals the emission arising from all of these layers, the p-guide, the n-guide and the QW. The degradation appears as a DLD along the laser cavity. The monochromatic images reveal that in the zones neighboring the heaviest degradation of the QW the two adjacent AlGaAs guide layers can also be degraded (Fig. 5.28).

Another example of the capacity of the CL technique for device failure analysis has been recently reported in the study of high frequency, high power AlGaN/GaN high electron mobility transistors (HEMTs) [116]. The high current density in the gate channel can induce a relevant Joule heating, reducing the carrier mobility and ending by the device degradation. There is a great interest in understanding the physical mechanisms leading to the loss of performance of these devices. The temperature during operation has been measured by micro-Raman spectroscopy, with a spatial resolution limited by the laser beam diameter (slightly submicrometric) [117]. Because of the structure of the HEMTs the characterization demands a high lateral resolution, as well as in depth capabilities. By varying the beam

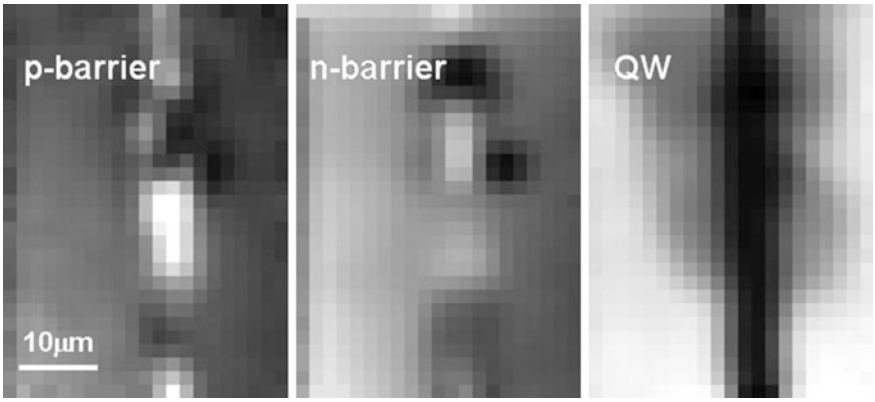

Fig. 5.28 Monochromatic emission of the p-barrier layer, the n-barrier layer and the QW in a monomode InGaAs QW pump laser (980 nm)

energy one can study different layers, e.g. the unpassivated extrinsic drain and source regions, and the regions shadowed by the gate overhang, or coated with dielectrics. Temperature can be also measured by CL from the shift of the near band edge emission (NBE) according to [118]

$$E_g(T) = E_g(0) - \left(5.98 + 0.12 \times 10^{-4} eV/K\right) \tag{5.28}$$

It should be noted that the beam current is negligible with respect to the device operation current; therefore, during the CL measurements the operation of the device is not distorted by the electron beam.

The temperature was measured around the channel, see Fig. 5.29, with results comparable to those obtained by micro-Raman spectroscopy [118] but with a significantly higher spatial resolution.

Furthermore, one can visualize damaged areas, which appear with dark contrast in the CL image, Fig. 5.30 shows a clear correlation between the hot zones revealed by Kelvin probe force microscopy (KPFM) and the dark areas in the CL images. On the other hand, local CL spectra reveal the formation of point defects, in particular the degraded areas present an increase of the deep level luminescence, the so-called yellow luminescence (YL) associated with Ga vacancy complexes [18], at the expense of the NBE emission, establishing an unambiguous relation between degradation and the defects responsible for the YL.

5.8.3 Low Electron Energy Cathodoluminescence

We have already discussed the high capacity of CL for in-depth analysis. However, one can imagine several characterization situations in which one needs to adjust the

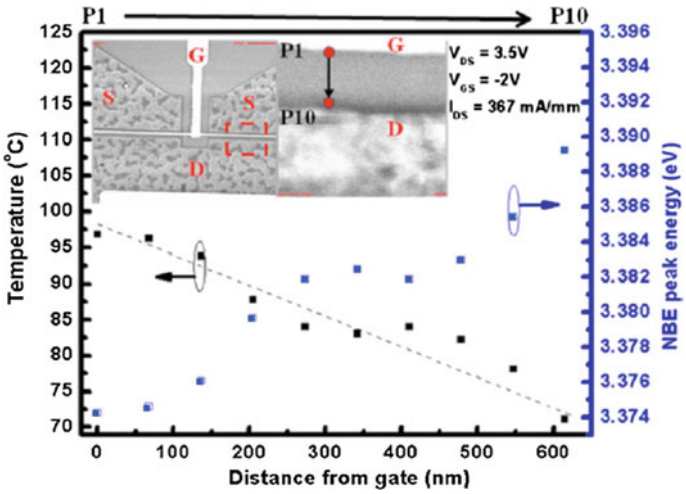

Fig. 5.29 Temperature as a function of the distance from the gate in an AlGaN/GaN HEMT. The symbols correspond to the measured points along the line P1-P10 from gate to drain [116]

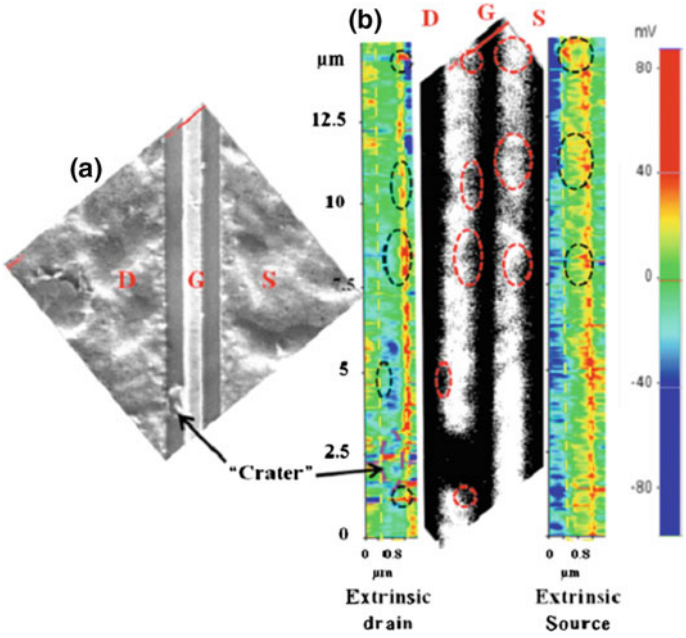

Fig. 5.30 **a** SEM image showing a defect between D and G in a HEMT operated to failure. **b** CL map of the NBE emission (central image), and KPFM images of the extrinsic drain and extrinsic source regions (side images). The zones with lower emission are zones with defects, highlighted by *dashed circles* in the image, that partially or fully quench the NBE emission. The KPFM maps show non uniform potential distribution correlated to the CL image [116]

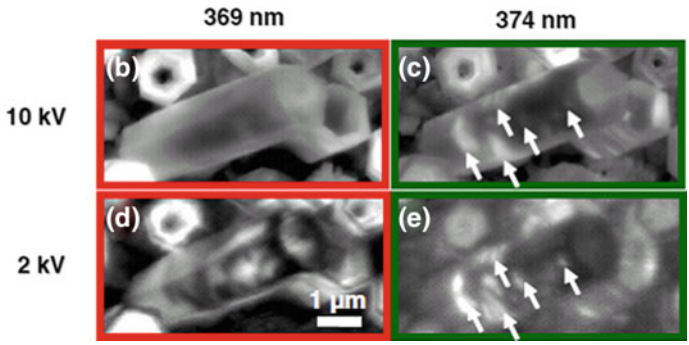

Fig. 5.31 Monochromatic images of ZnO nanotubes at two different electron acceleration voltages. Note the richer details of the low voltage images [22]

probe depth to very short dimensions, such as the case of nanostructures with dimensions of a few nm, but also, one can include the study of surfaces and interfaces by finely adjusting the variation of the e-beam energy.

Figure 5.31 shows monochromatic CL images of ZnO nanotubes obtained at 2 and 10 kV respectively [22]. The penetration depth of 10 kV electrons in ZnO is ≈790 nm, with maximum energy loss at 270 nm; while for 2 kV the penetration depth is 50 nm with maximum energy loss at 17 nm. At 2 kV one images the outer shell of the nanotube wall (≅150 nm), while the 10 kV images are averaging the emission over the full nanotube. The main differences appear in the 369 nm image revealing irregular donor distribution over the nanotube surface, meanwhile the 374 nm image, corresponding to DAP transitions, presents a similar pattern for both 2 and 10 kV. Therefore, the use of low energy electrons permits to reveal inhomogeneities in the distribution of defects and impurities that might not be resolved using higher energy electrons. This is clearly appreciated in Fig. 5.31, where the images acquired at 2 kV are much more detailed tan the images acquired at 10 kV.

Brillson has carried out studies of the CL emission in GaN and ZnO at very low voltages [26, 67]. Those experiments evidenced that CL at very low voltage can reveal electronic and chemical properties of surfaces and interfaces at the nanoscale. This application of CL to surface science is carried out at very low e-beam energy, and needs very clean surfaces and ultrahigh vacuum. In fact, the electron beam exposure over prolonged time at conventional vacuum levels in SEM chambers (10^{-6} Torr) can result in carbon deposits that quench the luminescence emission at low voltages [57]. The carbon deposit is formed by the splitting of CO molecules by the electron beam; it can be avoided by working in ultrahigh vacuum chambers [67].

Low keV CL permits the study of different properties of surfaces and interfaces; in particular, interfacial states, interdiffusion, formation of dielectric phases because of the interface reactivity, at metal/GaN schottky barriers, GaN/InGaN QWs, or AlGaN/GaN pseudomorphic structures. The study of surfaces has to be done at very lowe-beam energy, this method was called low energy electron excited nano

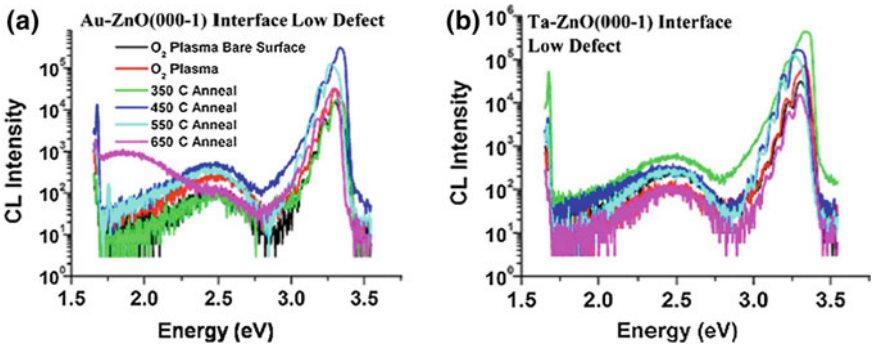

Fig. 5.32 5 kV CL spectra of the metal/ZnO interface at different annealing temperatures, **a** Au/ZnO, **b** Ta/ZnO [121]

luminescence (LEEN) spectroscopy [26, 119, 120]. As an example, the use of low energy electrons allowed to achieve the characterization of surfaces and interfaces. Au/ZnO, and Ta/ZnO interfaces treated under different annealing conditions were studied by depth resolved CL (DRCL) at 5 kV; the results are shown in Fig. 5.32. Note the presence of a red band below 2 eV formed when the Au/ZnO contact is annealed at 650 °C [121].

5.8.4 Spectral Images: Orientation Patterned GaAs Crystals

An example of the use of the spectrum images is the study of the orientation patterned GaAs (OP-GaAs) crystals. Infrared (IR) and terahertz (THz) frequency generation presents a high potential for applications in IR spectroscopy and THz imaging. For these purposes one needs compact and efficient tunable laser sources operating at room temperature. Those specifications can be met by using nonlinear optical materials for frequency conversion. In particular, GaAs presents a high potential because of several properties, as its large second order optical susceptibility, the high transparency in a broad IR spectral range (0.9–18 μm), and its excellent thermal properties. However, GaAs is not birrefringent so that phase matching is not possible. Instead, one can built up structures alternating the sign of the second order optical susceptibility to produce IR and THz sources based on the quasi phase matching principle [122]. These structures can be prepared by growing a grating of GaAs crystals with alternating orientation, the so-called OP-GaAs crystals [123–125], which are periodic gratings of alternate [001] oriented domains and [00-1]inversion domains separated by antiphase boundaries (APBs). These crystals are optically pumped inside of an optical parametric oscillator (OPO), generating laser sources with wavelengths ranging from 2 μm to the THz range. The signal wavelength range is determined by the choice of the pump laser wavelength, and the period of the OP-GaAs grating. Hydride vapour phase epitaxy

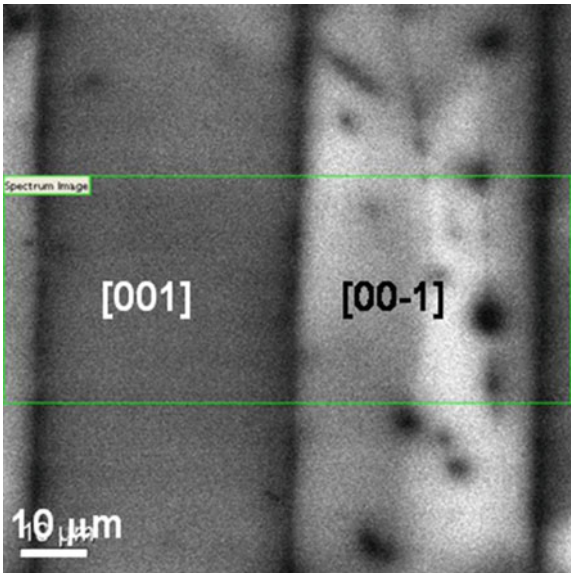

Fig. 5.33 Panchromatic CL image of an OP-GaAs crystal, *side view*. CL contrast between the two domain orientations is observed, as well as along the domain walls

(HVPE) is the technique used for growing thick gratings of periodic $[001]/[00\bar{1}]$ oriented GaAs domain structures. The bottlenecks to achieve high conversion efficiency are the fabrication of high quality crystals in order to minimize the optical losses, and the preservation of the grating period all over the crystal, in order to maintain the efficiency of the nonlinear interaction [108] antiphase boundaries (APBs) are formed formed by As–As and Ga–Ga antibonds, which behave as non radiative recombination centers. The control of defects with electro-optical signature [126–131], either point defects or extended defects is crucial to minimize the optical losses. To study the grating structure the crystals are cleaved in order to expose the lateral facet of the OP-GaAs crystal. This cleaved surface consists of the $(1\bar{1}0)/(\bar{1}10)$ planes of the alternated $[001]/[00\bar{1}]$ domain orientations, as shown in Fig. 5.33, the domain structure is revealed in the CL image. The two domain orientations show different CL brightness, in general the CL of $[00\bar{1}]$ domains look brighter than the [001] domains, which is the consequence of the different incorporation rate of residual impurities and defects in the two domains, because of their different growth faceting [27].

Once the panchromatic CL image is acquired one selects a region of interest and one acquires the spectal image of that region. The spectral image opening the spectral window to the full spectral range covered by the optical system (monochromator + CCD) detector is shown in Fig. 5.34a. This image is equivalent to the panchromatic image, as observed when comparing the images of Figs. 5.33 and 5.34a. It should be noted that the CL image can be blurred by the detection dark level; in Fig. 5.34b we present the same image after the spectral baseline correction, showing some areas with enhanced contrast with respect to the raw spectral image and the panchromatic image.

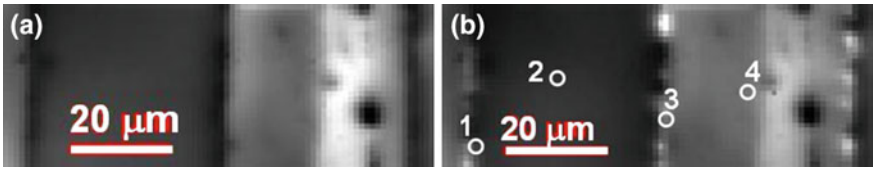

Fig. 5.34 **a** Spectral image encompassing the full spectral range; this image is equivalent to the panchromatic image. **b** Same as **a** but after spectral baseline substraction

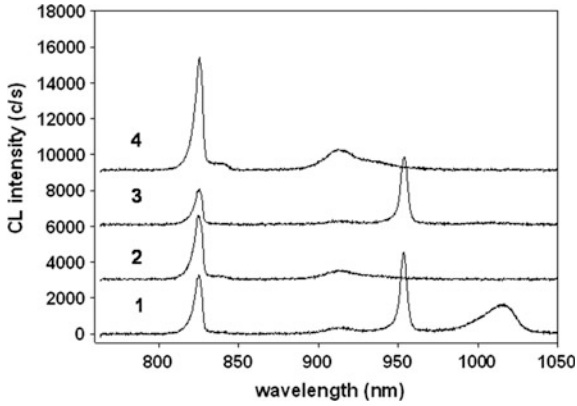

Fig. 5.35 CL spectra of the points numbered in Fig. 5.33b

Typical spectra recorded on the points marked in the image of Fig. 5.34b are shown in Fig. 5.35.

The near band edge (NBE) emission consists of an asymmetric band peaking at ≈822 nm (1.508 eV), which corresponds to a bound exciton overlapping the band to band transition [132]. Several defect related bands are observed at 910 nm (1.36 eV), 927 nm (1.337 eV), 950 nm (1.31 eV), and 1010 nm (1.22 eV). The bands at 910 and 927 nm, are an eA^0 transition, and its phonon replica respectively, with V_{Ga} as the acceptor [133]; the band peaking at 950 nm is not identified, it is specific of these crystals, it is worthnoting the anomalously narrow shape of this band associated with a deep level transition; finally, the band at 1010 nm is associated with V_{Ga}-Si_{Ga} complexes [134].

Once the spectral image is recorded and the baseline is substrated, the spectra are fitted and the corresponding images of amplitudes, peak wavelengths and FWHMs, are obtained. The amplitudes of the NBE, 910, 950 and 1010 nm emission bands, normalized to the total emission in order to remove the influence of the NRRCs, are shown in Fig. 5.36.

The NBE emission and the 910 nm band associated with $V_{Ga,}$ present similar distributions along the domain walls. The distribution of both emissions in the body

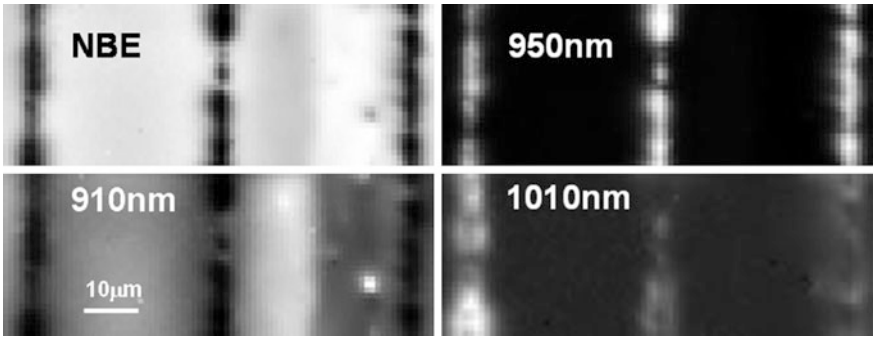

Fig. 5.36 Amplitudes of the NBE, 910, 950 and 1010 nm emission bands deduced by fitting the raw spectral image. The amplitudes are normalized to the total amplitude

Fig. 5.37 Distribution of NRRCs deduced from the inverse of the image suma of the four emission bands

of the domains presents reverse contrast. The two other bands, 950 nm and 1010 nm appear clearly localized along the domain walls, which supports the role of the domain walls as centers gettering impurities and point defects. The NBE and 910 nm emissions along the domain walls are anticorrelated to the 950 nm band, and in a minor extent to the 1010 nm band.

Summing the four images of Fig. 5.36 one obtains the overall radiative emission distribution, the inverse of that image gives a picture of the distribution of the NRRCs, Fig. 5.37, which shows its different incorporation to the two domain orientations, and the role of the impurities along the domain walls inhibiting the non radiative activity of the antibonds, As–As and/or Ga–Ga.

5.8.5 Dislocations in Si-Doped GaAs

This is an instructive example of the use of the fitting routines for the treatment of the spectrum images. If we come back to the CL image of Fig. 5.19, which represents the spectral image of a glided dislocation in Si-doped GaAs crystals, and proceed to fitting the different bands appearing in the spectra, one obtains a series of

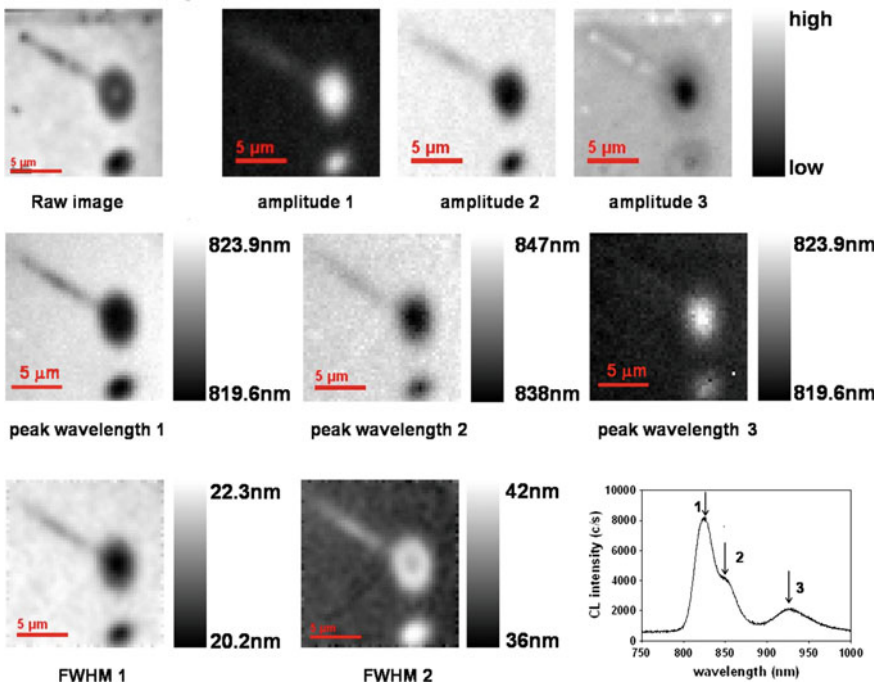

Fig. 5.38 Spectral data images extracted from the raw image. Note the different contrast observed for the images representing the different spectral parameters, and the rich information contained in the raw image. The three bands are indicated in the spectrum of the right lower corner

images corresponding to the different spectral parameters of those bands. These images are shown in Fig. 5.38.

The raw image shows the overall emission within the spectral sensitivity of the CCD detector, giving an image equivalent to the corresponding panchromatic image, but keeping the full spectral information. The main luminescence bands observed in Si-doped GaAs are the band labelled 1, which is associated with an (eA^0) transition with the acceptor being Si_{As} or C_{As}; the peak energy of the band ($\approx$1.496 eV) suggests that the main contribution is due to C_{As} [135], which is also consistent with the fact that a significant concentration of Si_{As} can be hardly justified at the Si doping level of these samples. Nevertheless, it is difficult to distinguish between both acceptors, because their luminescence parameters are very close. Bands 2 and 3 are close to the bands corresponding to either boron acceptors, B_{As} [136], or gallium antisites, Ga_{As} [137], which have been claimed to give a

couple of bands at 1.441 eV (λ = 859.8 nm) and 1.316 eV (λ = 941.5 nm) respectively. However, the energies of bands 2 and 3 do not exactly match these values. A band at 1.36 eV has been associated with Ga vacancies [138], however, it does not match the shape of band 3. It should be noted that the almost unobservable band at 1.25 eV is associated with Si_{Ga}-V_{Ga} complexes [139]; this band is intense for high Si doping concentrations, which is not our case. According to this, the most reliable hypothesis regarding bands 2 and 3 is that they arise from complexes involving impurities and native defects [138–140].

The images of the amplitudes of the three bands permit to observe the different distribution of the three CL bands; one can see the bright contrast of band 1, and the dark contrast of bands 1 and 2 around the dislocation core. Contrarilly, the trace give bright contrast for bands 1 and 3, while band 2 gives dark contrast. Furthermore, significant changes in the lineshape, peak wavelength and FWHM are observed in the corresponding images. The large peak shifts observed cannot be accounted for only by strain, but one can assume that the complexes are modified under the influence of the dislocation, for most information about this the reader is addressed to [28, 141, 142].

5.8.6 Nanostructures

The study of nanostructures is one of the most interesting applications of the CL technique. It has the advantage of the high spatial resolution and the acquisition of microscopy images allowing a one to one correlation between the CL emission and the morphology. This is especially useful for studying NWs, nanorods, nanoparticles, QWs …. We present here some examples regarding the CL emission in nanostructures.

Figure 5.39 shows the panchromatic, and monochromatic (3.34 and 1.75 eV) CL images of catalyst free ZnO nanorods [7, 29]. One can observe the progressive CL quenching from tail to tip. The CL intensity distribution was compared with the intensity of a defect related Raman band (275 cm^{-1}). The Raman spectra were recorded along the nanorod [7], and the intensity of this Raman band normalized to the intensity of the non polar phonon band E2 was plotted along the nanorod, and compared to the CL intensity profile. Spatial anticorrelation between both was observed, Fig. 5.40. One can argue that the defects responsible for the 275 cm^{-1} Raman band are the NRRCs in ZnO [7]. These defects are associated with Zn_i complexes [143], which is consistent with the increasing Zn precursor flow rate during growth.

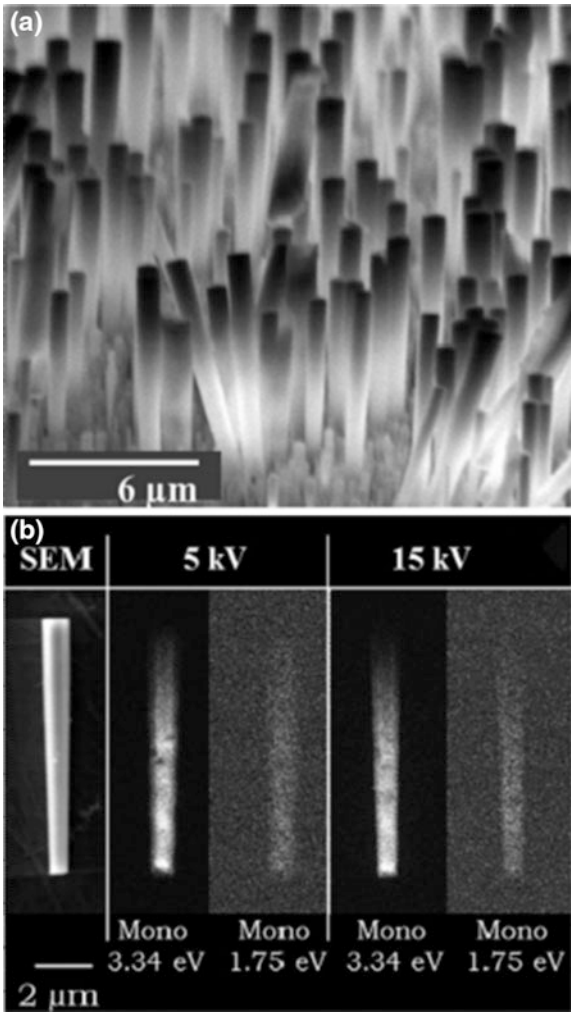

Fig. 5.39 Panchromatic CL image of catalyst free ZnO nanorods. **a** SEM image and monochromatic CL images (3.34 eV and 1.75 eV) at 5 and 15 kV acceleration voltage of the electrons of a single nanorod (**b**) [29]

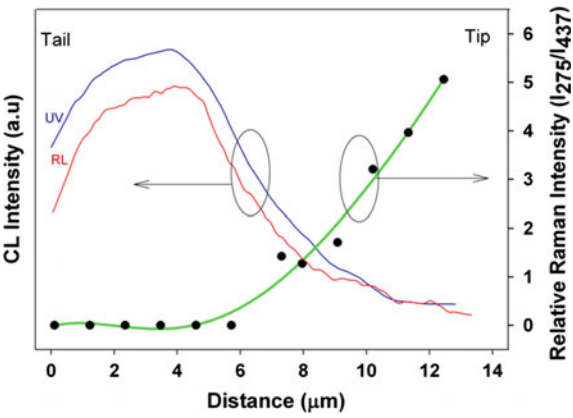

Fig. 5.40 UV (3.34 eV band), and RL (1.75 eV band) intensities along the nanorod, and relative intensity of the 275 cm^{-1} Raman band showing spatial anticorrelation [7]

Table 5.2 Comparative CL-PL

	SEM-CL	PL
Lateral resolution	50 nm. Improved in a TEM Influence of L_{diff}	Diffraction limited ($\approx\lambda_{exc}$) Improved in NSOM Influence of L_{diff}
Penetration depth	From a few nm to 2 μm	$1/\alpha$ (absorption coefficient)
Images	Panchromatic Monochromatic	Global illumination Using filters
Spectral images	Yes (scanning e-beam, fast)	Yes (point bay point, slow)
Charge effects	Yes	No
Image size	From $<\mu m^2$ to a few hundred μm^2 (pan-CL)	From a few μm^2 to full wafer
Spectral resolution	Determined by the spectrometer and the detection	Determined by the spectrometer and the detection
Photon recycling	Significant at high KeV	Low
Time resolved	Yes (beam blanker)	Yes (pulsed laser)

5.9 PL and CL: A Comparative

A comparative between PL and CL is summarized in Table 5.2.

References

1. J.W.P. Hsu, Mater. Sci. Eng. R **33**, 1 (2001)
2. K. Matsuda, S.V. Nair, H.E. Ruda, Y. Sugimoto, T. Sarki, K. Yamaguchi, Appl. Phys. Lett. **90**, 013101 (2007)
3. M.J. Romero, A.J. Morfa, T.H. Reilly, J. Vande Langemaat, M. Al Jassim, Nano Lett. **9**, 3904 (2009)
4. A. Gustaffson, M.E. Pistol, L. Montelius, L. Samuelson, J. Appl. Phys. **84**, 1715 (1998)
5. J.C.H. Phang, K.L. Pey, D.S.H. Chan, IEEE Trans. Electron Dev. **39**, 782 (1992)
6. M. Avella, J. Jiménez, F. Pommereau, J.P. Landesman, A. Rhallabi, Appl. Phys. Lett. **93**, 131913 (2008)
7. D.N. Montenegro, V. Hortelano, O. Martínez, M.C. Martínez-Tomas, V. Sallet, V. Muñoz-Sanjosé, J. Jiménez, J. Phys. D Appl. Phys. **46**, 235302 (2013)
8. H.C. Ong, A.S.K. Li, G.T. Du, Appl. Phys. Lett. **78**, 2667 (2001)
9. M.J. Wallace, P.R. Edwards, M.J. Kappers, M.A. Hopkins, F. Oehler, S. Sivaraya, D.W.E. Allsopp, R.A. Oliver, C.J. Humphreys, R.W. Martin, J. Appl. Phys. **116**, 033105 (2014)
10. O. Martínez, M. Avella, J. Jiménez, B. Gerard, R. Cuscó, L. Artús, J. Appl. Phys. **96**, 3639 (2004)

11. Y. Ohno, Y. Tokumoto, I. Yonenaga, K. Fujii, T. Yao, N. Yamamoto, Phys. B **407**, 2886 (2012)
12. J. Mass, M. Avella, J. Jiménez, M. Callahan, D. Bliss, B. Wang, J. Mater. Res. **22**, 3526 (2007)
13. A.M. Fischer, S. Srinivasan, F.A. Ponce, B. Monemar, F. Bertram, J. Christen, Appl. Phys. Lett. **93**, 151901 (2008)
14. B.G. Yacobi, D.B. Holt, J. Appl. Phys. **59**, R1 (1986)
15. B.G. Yacobi, D.B. Holt, *Cathodoluminescence Microscopy of Inorganic Solids*. (Plenum Press, New York, 1990)
16. M.A. Herman, D. Bimberg, J. Christen, J. Appl. Phys. **70**, R1 (1991)
17. A. Gustafson, L. Samuelson, *Microprobe characterization of semiconductors*, ed. by J. Jiménez (Taylor and Francis, New York, 2002), Chapter 6
18. M. Reschikov, H. Morkoc, J. Appl. Phys. **97**, 061301 (2005)
19. G.D. Gillian, Mater. Sci. Eng. R **18**, 99 (1997)
20. L. Pavesi, M. Guzzi, J. Appl. Phys. **75**, 4779 (1994)
21. A. Nouiri, A. Djemel, R.J. Tarento, Microelectron. Eng. **51–52**, 151 (2000)
22. B. Dierre, X. Yuan, T. Sekiguchi, Sci. Technol. Adv. Mater. **11**, 043001 (2010)
23. D.S.H. Chan, K.L. Pey, J.C.H. Phang, I.E.E.E. Trans, Electron Dev. **40**, 1417 (1993)
24. N. Pauc, M.R. Phillips, V. Aimez, D. Drouin, Appl. Phys. Lett. **89**, 161905 (2006); **97**, 166102 (2010)
25. V. Hortelano, J. Anaya, J. Souto, J. Jiménez, J. Perinet, F. Laruelle, Microelectr. Rel. **53**, 1501 (2013)
26. L.J. Brillson, J. Vac. Sci. Technol. B **19**, 1762 (2001)
27. D. Faye, A. Grisard, E. Lallier, B. Gérard, M. Avella, J. Jimenez, Appl. Phys. Lett. **93**, 151115 (2008)
28. M.A. González, O. Martínez, J. Jiménez, C. Frigeri, J.L. Weyher, J. Electron. Mater. **39**, 781 (2010)
29. D.N. Montenegro, V. Hortelano, O. Martínez, M.C. Martínez-Tomas, V. Sallet, V. Muñoz-Sanjosé, J. Jiménez, J. Appl. Phys. **113**, 143513 (2013)
30. A.C. Klein, J. Appl. Phys. **39**, 2029 (1968)
31. R.C. Aling, S. Bloom, Phys. Rev. Lett. **35**, 1522 (1975)
32. V. Skirant, D.R. Clarke, J. Appl. Phys. **81**, 6357 (1997)
33. D.B. Holt, E. Napchan, Scanning **16**, 78 (1994)
34. T.E. Everhart, P.H. Hoff; J. Appl. Phys. **42**, 5837 (1971)
35. M. Godlewski, E.M. Goldys, M.R. Phillips, R. Langer, A. Barski, J. Mater. Sci. **15**, 495 (2000)
36. A.E. Grun, Z. Naturforch A **129**, 89 (1957)
37. K. Kanaya, S. Okayama, J. Phys. D Appl. Phys. **5**, 43 (1972)
38. C. Donolato, Phys. Stat. Sol. A **65**, 649 (1981)
39. C. Donolato, P. Venturi, Phys. Stat. Sol. a **73**, 377 (1982)
40. D.B. Wittry, D.F. Kayser, J. Appl. Phys. **36**, 1387 (1971)
41. C.J. Wu, D.B. Wittry, J. Appl. Phys. **49**, 2827 (1978)
42. H.J. Fitting, H. Glaefeke, W. Wild, Phys. Stat. Sol. **43**, 185 (1977)
43. U. Werner, F. Koch, G. Oelgart, J. Physique D **21**, 116 (1988)
44. S.G. Konnikov, V.A. Solevev, V.E. Umanskii, V.M. Chystakov, Sov. Phys. Semicond. **21**, 1229 (1988)
45. M.J. Romero, D. Araújo, R. García, Mater. Sci. Eng. B **42**, 168 (1996)
46. J.M. Bonard, J.D. Ganière, B. Akamatsu, D. Araújo, F.K. Reinhart, J. Appl. Phys. **79**, 8693 (1996)
47. C. Trager-Cowan, A. Kean, F. Yang, B. Henderson, K.P. O'Donnell, Phys. B **185**, 319 (1993)
48. D. Drouin, A.R. Coutre, R. Gauvin, P. Hovington, P. Horny, H. Demers, *Montecarlo Simulation of Electron Trajectories in Solids (CASINO)*. (University of Sherbrooke, Quebec, Canada). http://www.gel.usherbrooke.ca/casino/What.html

49. D. Apsnes, M. Studna, Phys. Rev. B **27**, 985 (1983)
50. S. Pereira, M.R. Correia, E. Pereira, K.P. O'Donnell, C. Trager-Cowan, F. Sweeney, E. Alves, Phys. Rev. B **64**, 205311 (2001)
51. J.P. Landesman, C. Levallois, J. Jiménez, F. Pommereau, Y. Léger, A. Beck, T. Delhaye, A. Torres, C. Frigeri, A. Rhallabi, Microelectr. Rel. **55**, 1750 (2015)
52. X.L. Sun, S.H. Goss, L.J. Brillson, D.C. Look, R.J. Molnar, J. Appl, Phys. **91**, 6729 (2002)
53. M. Godlewski, T. Wojtowicz, E.M. Goldys, M.R. Phillips, R. Czernecki, P. Prystawko, M. Leszcynski, R. Perlin, I. Grzegory, S. Porowski, T. Böttcher, S. Fige, D. Hommel, Opto-Electron. Rev. **12**, 353 (2004)
54. L.J. Brillson, J. Phys. D Appl. Phys. **45**, 183001 (2012)
55. M.C. Martínez-Tomás, C.V. Hortelano, J. Jiménez, B. Wang, V. Muñoz-Sanjosé, Cryst. Eng. Commun. **15**, 3951 (2013)
56. L. Ozawa, *Cathodoluminescence* (Kodansha, Tokyo, 1990)
57. C.H. Seager, D.T. Tallant, W.L. Warren, J. Appl. Phys. **82**, 4515 (1997)
58. F. Ishikawa, H. Hasegawa, Appl. Surf. Sci. **212–213**, 885 (2003)
59. C. Ton-That, M.R. Phillips, M. Foley, S.J. Moody, A.P.J. Stampfl, Appl. Phys. Lett. **92**, 261916 (2008)
60. Y.H. Choo, J.Y. Kim, H.S. Kwack, B.J. Kwon, L.S. Dang, H.J. Ko, T. Yao, Appl. Phys. Lett. **89**, 201903 (2006)
61. W. Van Roosbroeck, J. Appl. Phys. **26**, 380 (1955)
62. A. Nouiri, A. Djemel, R.J. Tarento, J. Algerian, J. Adv. Mater. **3**, 27 (1999)
63. A. Nouiri, A. Hadef, A. Djemel, R.J. Tarento, J. Maghr. Phys. **1**, 39 (2000)
64. A. Nouiri, R.J. Tarento, J. Phys. C **12**, 10343 (2000)
65. A. Nouiri, Z. Elateche, R. Aouati, N. Belabed, Surf. Interface. Anal. **39**, 752 (2007)
66. L.J. Brillson, H.L. Mosbacker, M.J. Hetzer, Y. Strzhemechny, G.H. Jessen, D.C. Look, G. Cantwell, J. Zhang, J.J. Song, Appl. Phys. Lett. **90**, 102116 (2007)
67. L.J. Brillson, H.L. Mosbacker, D.L. Doutt, Y. Dong, Z.Q. Fang, D.C. Look, G. Cantwell, J. Zhang, J.J. Song, Superlatt. Microstruc. **45**, 206 (2009)
68. V. Hortelano, O. Martinez, R. Cuscó, L. Artús, J. Jimenez, Nanotechnol. (to be published)
69. G. Callsen, M.R. Wagner, T. Kure, J.S. Reparaz, M. Bügler, J. Brunnmeier, C. Nenstiel, A. Hoffmann, M. Hoffmann, J. Tweedie, Z. Bryan, S. Aygun, R. Kirste, R. Collazo, Z. Zitar, Phys. Rev. B **86**, 075207 (2012)
70. S.M. Davidson, J. Microsc. **110**, 177 (1977)
71. K. Maeda, S. Takeuchi, Jpn. J. Appl. Phys. **20**, L165 (1981)
72. E.A. Fitzgerald, Y. Ashizawa, L.F. Eastman, D.G. Ast, J. Appl. Phys. **63**, 4925 (1988)
73. S. Myhajlenko, J.L. Batsone, H.J. Hutchinson, J.W. Steeds, J. Phys. C **17**, 6477 (1984)
74. K. Maeda, M. Sato, A. Kubo, S. Takeuchi, J. Appl. Phys. **54**, 161 (1983)
75. J. Schreiber, S. Hildebrandt, H. Uniewski, V. Bechstein, Mater. Sci. Eng., B **42**, 24 (1996)
76. R.J. Tarento, Y. Marfaing, J. Appl. Phys. **71**, 4997 (1992)
77. D. Araújo, G. Oelgart, J.D. Ganière, F.K. Reinhart, Appl. Phys. Lett. **62**, 2992 (1993)
78. J.C. Brooksby, J. Mei, F.A. Ponce, Appl. Phys. Lett. **90**, 231901 (2007)
79. S.F. Chichibu, T. Onuma, T. Hashimoto, K. Fujito, F. Wu, J.S. Speck, S. Nakamura, J. Appl. Phys. **91**, 251911 (2007)
80. M. Albrecht, J.L. Weyher, B. Lucznik, I. Grzegory, S. Porowski, Appl. Phys. Lett. **92**, 231909 (2008)
81. P.M. Petroff, R.A. Logan, A. Savage, Phys. Rev. Lett. **44**, 287 (1980)
82. V.A. Coleman, J.E. Bradby, C. Jagadish, M.R. Phillips, Appl. Phys. Lett. **89**, 082102 (2006)
83. M. Schirra, R. Schneider, A. Reiser, G.M. Prinz, M. Feneberg, J. Biskupek, U. Kaiser, C.E. Krill, R. Sauer, K. Thonke, Phys. B **401–402**, 362 (2007)
84. M. Schirra, R. Schneider, A. Reiser, G.M. Prinz, M. Feneberg, J. Biskupek, U. Kaiser, C.E. Krill, K. Thonke, R. Sauer, Phys. Rev. B **77**, 125215 (2008)
85. K. Thonke, M. Schirra, R. Schneider, A. Reiser, G.M. Prinz, M. Feneberg, J. Biskupek, U. Kaiser, R. Sauer, Microelectron. J. **40**, 210 (2009)

86. S. Khromov, C.G. Hemmingsson, H. Amano, B. Monemar, L. Hultman, G. Pozina, Phys. Rev. B **84**, 075234 (2011)
87. A. Gustafsson, E. Kapon, Scanning Microsc. **12**, 285 (1998)
88. A. Jakubowicz, J. Appl. Phys. **59**, 2205 (1986)
89. D. Araújo, G. Oelgart, J.D. Ganière, F.K. Reinhart, J. Appl. Phys. **76**, 2992 (1994)
90. O. Martínez, M. Avella, J. Jiménez, M. Bosi, R. Fornari, Phys. Stat. Sol. C **7**, 68 (2010)
91. W. Hergert, P. Reck, L. Paseman, J. Schreiber, Phys. Stat. Sol. A **101**, 611 (1987)
92. N. Yamamoto, H. Itoh, V. Grillo, S.F. Chichibu, S. Keller, J.S. Speck, S.P. DenBaars, U.K. Mishra, S. Nakamura, G. Salviatti, J. Appl. Phys. **94**, 4315 (2003)
93. S.K. Lim, M. Brewster, F. Qian, Y. Li, C.M. Lieber, S. Gradecak, Nano Lett. **9**, 3940 (2009)
94. J.B. Steyn, P. Giles, D.B. Holt, J. Microscopy **107**, 107 (1976)
95. Atto Light, http://www.attolight.com
96. J. Cazaux, J. Appl. Phys. **59**, 1418 (1988)
97. J. Cazaux, Nuc. Instr. Methods Phys. Res. B **244**, 307 (2006)
98. A. Seminara, B. Pokroy, S.H. Kang, M.P. Brenner, J. Aizenberg, Phys. Rev. B **83**, 235438 (2011)
99. H.A. Zarem, P.C. Sercel, J.A. Lebens, L.E. Eng, A. Yariv, K.J. Vahala, Appl. Phys. Lett. **55**, 1647 (1989)
100. H.A. Zarem, J.A. Lebens, K.B. Nordstrom, P.C. Sercel, S. Sanders, L.E. Eng, A. Yariv, K.J. Vahala, Appl. Phys. Lett. **55**, 2622 (1989)
101. R.B. Lee, K.J. Vahala, C.E. Zah, R. Bhat, Appl. Phys. Lett. **62**, 2411 (1993)
102. S.J. Rosner, E.C. Carr, M.J. Ludowise, G. Girolami, H.I. Erikson, Appl. Phys. Lett. **70**, 420 (1996)
103. E.B. Yakimov, J. Phys. C: Cond. Matter **14**, 13069 (2002)
104. M. Avella, E. Puente, J. Jiménez, L. Polenta, A. Castaldini, A. Cavallini, J. Cryst. Growth **210**, 220 (2000)
105. N. Ino, N. Yamamoto, Appl. Phys. Lett. **93**, 232103 (2008)
106. A. Jakubowicz, J. Appl. Phys. **57**, 1194 (1985)
107. A. Martín-Martín, M. Avella, M.P. Iñiguez, J. Jiménez, M. Oudart, J. Nagle, J. Appl. Phys. **106**, 173105 (2009)
108. J.W. Tomm, M. Ziegler, M. Oudart, J. Nagle, J. Jimenez, Phys. Stat. Sol. A **206**, 1912 (2009)
109. A. Martín-Martín, M. Avella, M.P. Iñiguez, J. Jiménez, M. Oudart, J. Nagle, Appl. Phys. Lett. **93**, 171106 (2008)
110. T.Q. Tien, A. Gerhardt, S. Schwirzke-Schaaf, J.W. Tomm, M. Pommiès, M. Avella, J. Jiménez, M. Oudart, J. Nagle, Appl. Phys. Lett. **87**, 211110 (2005)
111. M. Avella, M. Pommiés, J. Jiménez, M. Betiatti, G. Hallais, V. Lemonon, Mater. Sci. Semicond. Process. **9**, 204 (2006)
112. N.W. Ashcroft, N.D. Mermin, *Solid State Physics* (Holt-Saunders International Editions, Philadelphia, 1976)
113. A. Martín-Martín, M. Avella, M. Pommies, M.P. Iñiguez, J. Jiménez, M. Oudart, J. Nagle, J. Mater. Sci: Mater. Electron. **19**, S140 (2008)
114. M. Pommiès, M. Avella, E. Cánovas, J. Jiménez, T. Fillardet, M. Oudart, J. Nagle, Appl. Phys. Lett. **86**, 131103 (2005)
115. D.G. Deppe, N. Holonyak Jr., J. Appl. Phys. **64**, 93 (1988)
116. C.H. Lin, T.A. Merz, D.R. Doutt, M.J. Hetzer, J. Joh, J.A. del Alamo, U.K. Mishra, L.J. Brillson, Appl. Phys. Lett. **95**, 033510 (2009)
117. J.W. Pomeroy, M. Kuball, M.J. Uren, K.P. Hilton, R.S. Balmer, T. Martin, Appl. Phys. Lett. **88**, 023507 (2006)
118. A.P. Young, L.J. Brillson, Appl. Phys. Lett. **77**, 699 (2000)
119. L.J. Brillson, R.E. Viturro, Scanning Microsc. **2**, 789 (1988)
120. L.J. Brillson, H.W. Richter, M.L. Slade, B.A. Weinstein, Y. Shapira, J. Vac. Sci. Technol. A **3**, 1011 (1985)
121. H. Mosbacker, C. Zgrabik, C. Swain, S. Hage, M. Hetzer, D.C. Look, G. Cantwell, J. Zhang, J.J. Song, L.J. Brillson, Appl. Phys. Lett. **91**, 072102 (2007)

122. D.S. Hum, M.M. Fejer, C.R. Physique **8**, 180 (2007)
123. L.A. Eyres, P.J. Tourreau, T.J. Pinguet, C.B. Ebert, J.S. Harris, M.M. Fejer, L. Becouarn, B. Gérard, E. Lallier, Appl. Phys. Lett. **79**, 904 (2001)
124. E. Schaar, K.L. Vodopyanov, P.S. Kuo, M.M. Fejer, X. Yu, A. Lin, J.S. Harris, D. Bliss, C. Lynch, V.G. Kozlov, W. Hurlbut, IEEE J. Sel. Top. Quant. Electron. **14**, 35 (2008)
125. A. Grisard, E. Lallier, B. Gerard, Opt. Express Mater. **2**, 1020 (2012)
126. D. Bliss, C. Lynch, D. Weyburne, K. O'Hearn, J.S. Bailey, J. Cryst. Growth **287**, 673 (2006)
127. O. Martínez, M. Avella, H. Angulo, J. Jimenez, C. Lynch, D. Bliss, Superlatt. Microstr. **45**, 337 (2009)
128. O. Martínez, M. Avella, V. Hortelano, J. Jiménez, CLynch. D. Bliss: J. Electron. Mater. **39**, 805 (2010)
129. A. Grisard, F. Gutty, E. Lallier, B. Gérard, J. Jimenez, Phys. St. Sol. C **9**, 1651 (2012)
130. V. Hortelano, O. Martínez, J. Jiménez, C. Lynch, M. Snure, D. Bliss; Phys. St. Sol. C **9**, 1674 (2012)
131. M. Snure, V. Hortelano, J. Jiménez, S. Swider, M. Mann, V. Tassev, C. Lynch, D. Bliss, J. Cryst. Growth **352**, 258 (2012)
132. G. Brammertz, Y. Mols, S. Degroote, V. Motsnyi, M. Leys, G. Borghs, M. Caymax, J. Appl. Phys. **99**, 093514 (2006)
133. I. Harrison, L. Pavesi, M. Henini, D. Johnston, J. Appl. Phys. **75**, 3151 (1994)
134. K.C. Shin, M.H. Kwark, M.H. Choi, M.H. Oh, Y.B. Tak, J. Appl. Phys. **65**, 736 (1989)
135. P.W. Yu, W.C. Mitchel, M.G. Mier, S.S. Li, W.L. Wang, Appl. Phys. Lett. **41**, 532 (1982)
136. F.M. Kessling, M. Albrecht, K. Irmscher, R. Krause-Rehberg, W. Ulrici, P. Rudolph, J. Cryst. Growth **310**, 1418 (2008)
137. J.C. Bourgoin, H.J. Bardeleben, D. Stievenard, J. Appl. Phys. **64**, R65 (1988)
138. L. Pavesi, N. Hong Ky, J.D. Granière, J.D. Granière, F.K. Reindhart, J. Appl. Phys. **71**, 2225 (1992)
139. J.T. Schick, C.G. Morgan, P. Papoulias, Phys. Rev. B **66**, 195302 (2002)
140. H. Overhoff, J.M. Spaeth, Phys. Rev. B **72**, 115205 (2005)
141. C. Frigeri, J.L. Weyher, J. Appl. Phys. **65**, 4646 (1989)
142. J.L. Weyher, J. Van der Well, C. Frigeri, Semicond. Sci. Technol. **7**, A294 (1992)
143. F. Friedrich, M.A. Gluba, N.H. Nickel, Appl. Phys. Lett. **95**, 141903 (2009)
144. J. Mass, M. Avella, J. Jiménez, M. Callahan, E. Grant, K. Rakes, D. Bliss, B. Wang, Appl. Phys. A **88**, 95 (2007)
145. J. Jiménez, C. R. Phys. **4**, 663 (2003)
146. M.Baeumler, W.Jantz; Microprobe characterization of semiconductors, ch.1, J.Jiménez editor (Taylor and Francis New York 2002)

Chapter 6
Photoelectrical Spectroscopy

Abstract This chapter introduces *photocurrent* (PC) spectroscopy. Although PCs are extensively employed in everyday live, e.g. in solar cells and photodetectors, their use as an analytical tool is less wide spread. We will discuss the topic of homebuilt spectroscopic apparatus and methodology such as steady-state, transient, and modulation approaches. Suitable sample geometries are addressed, since they are crucial for PC analysis. Then, the features that are observed in PC spectra are systematically described and their microscopic nature is addressed. This also includes related photoelectric effects and the results one can expect from PC analysis. Applications such as laser beam induced current are addressed. This includes case studies, as well.

6.1 Introduction

The *photoelectrical* properties of semiconductors are widely used in practice, for instance in many kinds of photodetectors or solar cells. But except for these well-known and extremely important applications, analysis of photoelectrical properties can also be used as a *tool* that helps to learn more about semiconductor materials or devices. This will be the topic of this chapter.

Photoconductivity (PC) involves two fundamental processes, the generation of free charge carriers by *absorption* and the subsequent motion of them, i.e. *carrier transport*. That two different basic processes take place represents an advantage and a drawback at the same time: on the one hand, more details can be investigated within one single experiment; on the other hand, there are also parameters, some of which are often not exactly known. Therefore, PC analysis is *less straightforward* than the analysis of a transmittance measurement or Hall-effect analysis, which represent typical absorption and transport measurements, respectively.

But then why use PC analysis? *What are the advantages of PC spectroscopy*?

- The technique possesses unsurpassed sensitivity, in particular to species, which show *weak absorbance* only. This can be, among others defects: assume that foreign defects are introduced into a material by doping. They might cause an

J. Jimenez and J.W. Tomm, *Spectroscopic Analysis of Optoelectronic Semiconductors*, Springer Series in Optical Sciences 202,
DOI 10.1007/978-3-319-42349-4_6

absorption coefficient of 5 cm^{-1}. If they are to be detected in a 1 µm thick epitaxial layer, a 0.05% reduction of the absolute transmittance has to be detected. This can hardly be achieved in a standard transmittance measurement. However, a PC measurement might be more successful.

- The PC is somewhat complementary to a transmittance measurement: the effects of the photons, which *remain in the sample* are monitored, while the photons that *pass through the sample* are monitored in the transmittance measurement by an external detector. Thus, PC can provide completely independent information on shapes of absorption spectra. As mentioned in Sect. 2.5.1, this is similar to photoacoustic spectroscopy.
- In contrast to transmittance spectra, PC spectra of thin layers or cavities are typically not affected by spectral interference patterns.
- There are samples, in which the parts that should be analyzed are embedded into other layers. This could hold for heterostructures but, also for the active regions of diode lasers. If the access to the 'interesting' parts of semiconductor structures is not possible with a transmittance measurement, a PC measurement could help to record absorption properties by using the sample itself as the detector.
- When forming lines of scientific arguments, e.g. in a scientific paper, it is often useful to present additional data that *independently* reveal the results of the original finding. Sometimes, PC spectroscopy can provide this type of experimental cross-check.

The presence of both fundamental processes involved in PC generation, namely generation of free carriers by absorption of photons and charge transport, are *necessary conditions*.

The *absorption processes* are primary all those, which we have discussed in the preceding chapters. In the following, we will consider their ability to create freely moving carriers and thus eventually implement PC generation.

The driving forces for charge carrier *transport* are electric fields which are caused by potential gradients. Such fields can be either

- provided by an externally applied voltage, or
- caused by any type of built-in potential gradients, e.g., by *pn*-or *pin*-junctions, at hetero-junctions, graded-gap structures, doping gradients, at contact metallizations (*Schottky* contact), etc.

Figure 6.1a, b show PC spectra and a simplified schematic diagram of a PC setup, respectively. The circuit in (b) includes two resistors, one of them representing the sample that is the subject of the PC analysis. The PC is detected as the voltage drop across the reference resistor R_{ref}. In practice, this resistor could also represent the input resistance of the instrument. This scheme also illustrates that whether one calls such a photoelectric measurement photo*current* or photo*voltage* spectroscopy mainly depends on the value of R_{ref} with respect to the resistance of the investigated sample. One often uses R_{ref}-values close to the sample resistance in order to achieve the best sensitivity (impedance matching). For simplicity, however, we will exclusively use the term 'PC' for all types of photoelectrical measurements.

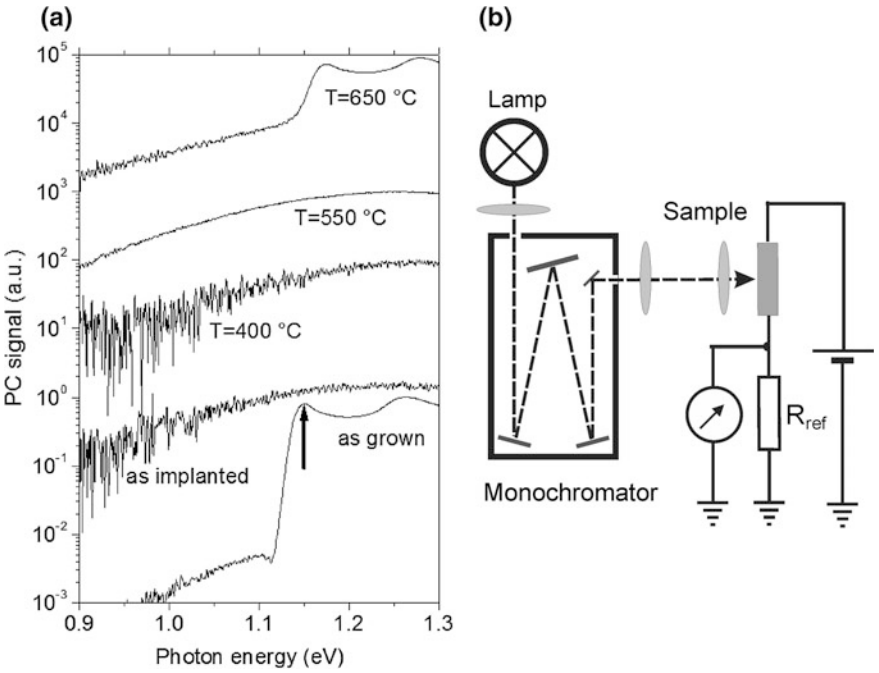

Fig. 6.1 **a** PC spectra from as-grown, as-implanted, implanted, and annealed parts of an $In_{0.253}Ga_{0.747}As$ QW [1]. The annealing temperatures (T) are indicated. The main structure at 1.136 eV (see *arrow*) is caused by the onset of the QW-transitions. **b** Schematic of a PC setup

The PC spectra shown in Fig. 6.1a are taken from an InGaAs QW sample [1]. The abscissa represents the photon energy of the excitation light beam. The ordinate is the PC, measured for constant photon flux, i.e. for a constant number of photons per spectral interval and area. A PC spectrum from the fresh sample is shown at the bottom. The energetically lowest QW transition is marked by an arrow. Obviously, the shape of the spectrum resembles the spectral absorption behavior of the QW. Energetically below the QW 'edge' at $\sim$1.13 eV, there is a shoulder, likely caused by defect-related transitions. Notice that this shoulder is weaker in amplitude by two orders of magnitude than the QW PC. The second spectrum from the bottom has been obtained from the same sample after ion implantation. Ion implantation, i.e. bombarding a material with a flux of accelerated ions, is known to be a process that substantially increases the defect concentration within semiconductors. Obviously, in this particular case, the process completely quenches the QW PC. However, boosted annealing, i.e. keeping the material temporally at an elevated temperature, (see successive spectra from the bottom to the top) allowed the QW PC almost to recover. Annealing is a process that is expected to reduce the number of active defects in a material and it is exactly what happens here with those defects initially introduced by the ion implantation process. For clarity, the spectra are shifted along the ordinate scale. This example serves here exemplarily to

introduce what PC measurements can deliver. Moreover, this result already points to the substantial impact of defects to PC spectra and to the capability of PC spectroscopy to put defect analysis into practice.

Notice that there are many further analytical techniques, which employ photoelectrical properties, as well. This includes defect spectroscopy such as photo-DLTS,[1] PITS,[2] or related PC-based techniques, such as the 'modulated photoconductivity' technique, which will be addressed briefly in a later section.

In this chapter, we will mainly address *PC spectra* as shown in Fig. 6.1a, which are measured by tuning the excitation (or probe) photon energy and monitoring the *extra current* generated within the sample by this illumination. As mentioned, this type of approach provides a kind of complement to the spectroscopic techniques, which were addressed in preceding chapters.

6.2 Generation of Photocurrents

6.2.1 Conductivity and Photoconductivity

Photoconductivity comprises two fundamental processes, namely *absorption* and *carrier transport*.

Figure 6.2a shows an electric circuit again. A cuboid-shaped PC sample with the length L, the height h, and the thickness d is shown. The equilibrium carrier concentration $n_0 p_0 = n_i^2$ is represented by a number of open and full circles which stand for holes and electrons, respectively. Here, n_i is the intrinsic carrier concentration which is independent of doping. Since there are more full than open circles, one would call this material a n-type semiconductor. When we consider the steady-state situation and applying to this circuit an external voltage U_{constant} to this circuit, this voltage will split into the voltage drop at the sample $U = E \cdot L$ and the one at the reference resistor U_{ref}. According to Ohm's law, the current density j_0 passing through the sample is

$$j_0 = \sigma_0 \cdot E. \tag{6.1}$$

When we insert the contributions of electron and holes to the conductivity σ_0, we get

$$j_0 = e \cdot (\mu_n \cdot n_0 + \mu_p \cdot p_0) \cdot E, \tag{6.2}$$

where μ_n and μ_p are the mobilities of electrons and holes. Conductivity σ_0 and current density j_0 are indicative for the situation in the sample without any extra

[1] DLTS stands for *Deep Level Transient Spectroscopy*.

[2] PITS stands for *Photo-Induced Transient Spectroscopy*.

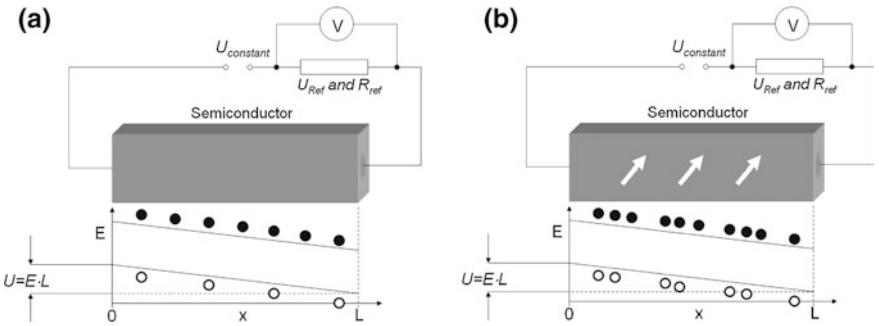

Fig. 6.2 The sample, the electric circuitry, and a bandgap diagram without (*left*) and with external illumination (*right*)

illumination. Therefore, we will call them *dark conductivity* and *dark current* density, respectively.

If a constant flux of light with a photon energy larger than E_g is now directed onto the sample, see arrows in (b), interband absorption generates additional free electrons and holes $\delta n = \delta p$ and the actual current becomes

$$j = e[\mu_n \cdot (n + \delta n) + \mu_p \cdot (p + \delta p)] \cdot E. \tag{6.3}$$

With (6.2) we get

$$j = j_0 + e(\mu_n \cdot \delta n + \mu_p \cdot \delta p) \cdot E, \tag{6.4}$$

and call the extra current in excess of j_0

$$j_{PC} = e(\mu_n \cdot \delta n + \mu_p \cdot \delta p) \cdot E, \tag{6.5}$$

the *photocurrent* density j_{PC}. It can be measured practically as an increased voltage drop at R_{ref} during illumination.

The photocurrent I_{PC} is easily obtained by integrating (6.5) along the cross-section $h \cdot d$ of the sample

$$I_{PC} = e \int_0^h \int_0^d dydz(\mu_n \cdot \delta n + \mu_p \cdot \delta p) \cdot E. \tag{6.6}$$

This expression is still of restricted practical value, since δn and δp are not known. Now, we will employ our knowledge from Sect. 4.2.1, where we have shown, how to calculate $\delta p(z)$ via a rate equation model. There, the starting point (6.2) was

$$0 = g(z) - \frac{\delta n(z)}{\tau} + D\frac{\partial^2 \delta n(z)}{\partial z^2}. \tag{6.7}$$

Equation (6.7) can be simplified since carriers which diffuse (described by the third term on the right) are not lost for PC generation, independent of their actual location along the z-direction

$$g(z) = \frac{\delta n(z)}{\tau}. \tag{6.8}$$

Notice that this approach presumes the absence of any surface recombination. By assuming lateral sample homogeneity, we waive the integration along the y-direction and put (6.6) and (6.8) together

$$I_{PC} = e \cdot h \cdot E \int_0^d dz\left[\mu_n \cdot g(z) \cdot \tau + \mu_p \cdot g(z) \cdot \tau\right]. \tag{6.9}$$

This way, we obtain the contributions of electron and holes to the total PC. The appropriate generation term $g(z)$ has already been given in Sect. 4.2.1 by (4.3).

Notice that τ stands here for the entire recombination behavior of the sample and is assumed to be independent of δn. Often, this is not valid in wide δn-ranges, since even intrinsic recombination, such as Auger recombination, does not fulfill this requisite.

6.2.2 *Intrinsic Photocurrent Spectra* $I_{\mathrm{PC}}(\hbar\omega)$

In Sect. 4.4, we explained how to describe PL spectra within the frame of different basic concepts, such as band-to-band transitions (Sect. 4.4.2) and exciton recombination (Sect. 4.4.3). Eventually it turned out that each of these models describes important features well, depending on the investigated material and the experimental conditions that were chosen. Thus, both alternative models have certain areas of validity.

With the description of PC spectra, which is now desired, we are in a very similar situation. Therefore, we will start again with modeling PC spectra $I_{\mathrm{PC}}(\hbar\omega)$, generated by band-to-band transitions in homogeneous bulk material. For this purpose, we use (6.9). For the optical generation rate, we apply what has been used to describe PL generation, see (4.3), including all involved dependencies on $\hbar\omega$.

$$g(z, \hbar\omega) = \frac{I_0}{\hbar\omega}\eta_{exc}(\hbar\omega) \cdot \alpha(\hbar\omega) \cdot [1 - R(\hbar\omega)] \cdot e^{-\alpha(\hbar\omega)\cdot z}. \tag{6.10}$$

Without loss of generality, we apply (6.9) and (6.10) to one carrier type (n) only and get

$$I_{PC} = \frac{I_0 \cdot e \cdot h \cdot E \cdot \mu_n \cdot \tau}{\hbar\omega} \eta_{exc}(\hbar\omega) \cdot \alpha(\hbar\omega) \cdot [1 - R(\hbar\omega)] \cdot \int_0^d dz e^{-\alpha(\hbar\omega)\cdot z}. \quad (6.11)$$

The integration results in

$$I_{PC} = \frac{I_0 \cdot e \cdot h \cdot E \cdot \mu_n \cdot \tau}{\hbar\omega} \eta_{exc}(\hbar\omega) \cdot [1 - R(\hbar\omega)] \cdot (1 - e^{-\alpha(\hbar\omega)\cdot d}). \quad (6.12)$$

The last term illustrates the statement given in the introduction already: In contrast to a transmittance measurement, PC registers the effect of the photons that are *absorbed* within the investigated sample of the thickness d. Thus, complementary things are probed.

Furthermore, we can expand the exponential for $\alpha(\hbar\omega) \cdot d < 1$ and get

$$I_{PC} = \frac{I_0 \cdot e \cdot h \cdot E \cdot \mu_n \cdot \tau}{\hbar\omega} \eta_{exc}(\hbar\omega) \cdot [1 - R(\hbar\omega)] \cdot \alpha(\hbar\omega) \cdot d. \quad (6.13)$$

In the spectral region close to E_g, $\alpha(\hbar\omega)$ is changing with $\hbar\omega$ more than all other parameters do in (6.13). Thus, we get as rule of thumb

$$I_{PC} \propto \alpha(\hbar\omega) \quad \text{as long as} \quad \alpha(\hbar\omega) \cdot d < 1. \quad (6.14)$$

This proportionality is frequently used in practice, since in this way, *PC spectroscopy can substitute an absorption measurement*. For transmission measurements, see Sect. 2.2.1, the scope of the application of (6.14) can be extended by measuring sets of samples with different thicknesses d. This is confirmed by calculations in which (6.12) was used.

Figure 6.3a shows PC spectra of GaAs as calculated for constant photon flux ($I_0/\hbar\omega$ = constant). For the absorption coefficient, a square-root-law, corresponding to a parabolic bandstructure, has been assumed. Two very different sample thicknesses have been chosen. While the 0.5-mm sample represents a typical wafer thickness (a sample like this might have been cut from a wafer for standard characterization), the 2 µm thick layer represents an epitaxial layer. Figure 6.3b shows the same as (a) but with a more realistic absorption coefficient, consisting of an Urbach tail, see (1.75) with E_u = 10 meV, below E_g, which merges into a square-root-dependence. We can conclude:

- For the 2 µm thick sample, the PC spectrum images $\sim\alpha(\hbar\omega)$, although the prerequisite $\alpha(\hbar\omega) \cdot d < 1$ gets lost already $\sim$30 meV above E_g.
- For the 500 µm thick sample, $\alpha(\hbar\omega) \cdot d = 1$ is reached about 45 meV *below* E_g at $\sim$1.38 eV. For even lower photon energies, $\alpha(\hbar\omega)$ is also well-reproduced

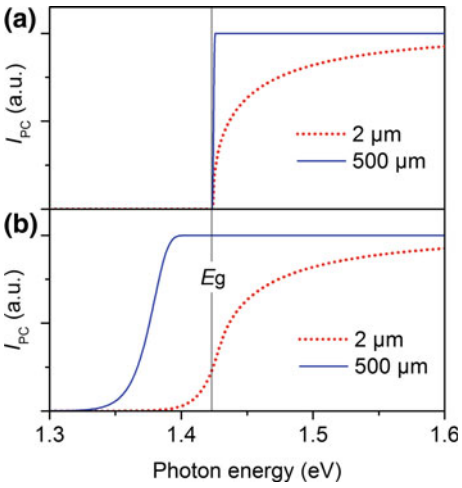

Fig. 6.3 Calculated PC spectra from GaAs at ambient temperature. The vertical line in both subfigures indicates the energy gap of GaAs at 1.424 eV. No surface recombination has been taken into account. **a** PC spectra for two samples of different thicknesses assuming the absorption follows a square-root law. **b** PC spectra for two samples of different thicknesses assuming the absorption follows an exponential dependence below 1.43 eV and a square-root law above. In order to describe the exponential tail, the Urbach parameter E_u has was set to 10 meV, which corresponds to a doping concentration of $\sim 1.5 \times 10^{18}$ cm^{-3}

and provides information about the Urbach tail. Actually, Urbach tails are often determined by monitoring PC spectra in this range and plotting them in a logarithmic display. For photon energies above $\sim$1.38 eV, however, the PC saturates and no further information may be derived.

- The 'determination' of E_g from PC spectra of 'thin' samples is feasible in the same way as described in Sect. 2.2.1 for absorption measurements. Notice that PC spectra from 'thick' samples *do not allow to draw any conclusion with respect to* E_g.
- These considerations still do not include the presence of any defects or excitons, which are likely to modify the shape of the absorption coefficient further and make quantitative conclusions even more difficult.

There is another conclusion that may be drawn from (6.13): For a given excitation wavelength, the PC which is provided by a single band (either valence or conduction band) is

$$I_{PC} \propto \mu \cdot \tau. \tag{6.15}$$

We will use this finding later as rule of thumb and even extend its validity.

6.2.3 Intrinsic PC Spectra in Presence of Surface Recombination

Surface recombination is a major effect that reduces PCs and also substantially impacts the shape of PC spectra. As mentioned, the considerations in Sect. 6.2.2 are made wile assuming a surface recombination velocity of $s = 0$. Although the conclusions involved in (6.14) and (6.15) still hold to a large extent for $s > 0$, as well, the handy *proportionalities do not strictly apply* anymore.

The calculation of I_{PC} in presence of surface recombination can be performed by using the results obtained in Sect. 4.2.1 for PL. There, the concentration profiles $\delta n(z)$ have been calculated along the sample thickness d for a given excitation photon energy $\hbar\omega_{exc}$, based on the work by Duggan and Scott [2] see Fig. 4.2. For a given PL measurement, $\hbar\omega_{exc}$ is fixed, of course. We also learned that the carrier distribution, e.g. its 'center of gravity' considerably depends on $\hbar\omega_{exc}$, if one changes the excitation laser wavelength; see Fig. 4.2b. Since $\hbar\omega$ varies in a PC measurement,[3] each data point in a PC spectrum represents PCs, which originate from different locations along the z-axis of the sample. Therefore, it becomes clear right away that the size of the probed sample region depends on the photon energy. For a capable analytical technique, this statement does not sound very promising. However, as long as samples are homogeneous along z and $I_{PC} \propto g$, this will not matter at all.

By using (6.7) and (6.10) and the boundary conditions [(4.4) and (4.5) Sect. 4.2.1], it is even possible to calculate carrier profiles $\delta n(z, \hbar\omega)$ analytically. Integrating these profiles along the sample thickness d, an analytical expression for $\delta n(\hbar\omega)$ is provided; see [2]. The photocurrent spectrum can be calculated by using a modified version of (6.6):

$$I_{PC}(\hbar\omega) = e \int_0^h \int_0^d dydz(\mu_n \cdot \delta n(\hbar\omega) + \mu_p \cdot \delta p(\hbar\omega) \cdot E. \tag{6.16}$$

Figure 6.4 shows PC spectra from a $d = 500$ µm thick peace of 'bulk' GaAs, as calculated from (6.16) for constant photon flux, i.e. $I_0/\hbar\omega$ = constant. The same absorption coefficient as in Fig. 6.3b is used, namely a square-root dependence and an Urbach parameter of $E_u = 10$ meV. The other parameters are listed in the caption. The main parameter s is varied between 5×10^4 and 10^6 cm/s which

[3] In case of PL, the use of the terms 'excitation photon energy' for the photons that generate the non-equilibrium carriers and 'photon energy' for the abscissa of the monitored spectrum are self evident. When dealing with PC, this distinction is not required because the 'excitation photon energy' and denotation of the abscissa are identical. Therefore, we use the term 'photon energy' only when dealing with PC spectroscopy.

represent typical surface recombination velocities for doped GaAs. Compared to the case $s = 0$, see Fig. 6.3b, the PC in a spectral region energetically above ~ 1.4 eV is substantially reduced, while in the region below this photon energy the PC remains almost unaffected. This can be understood along these lines:

- The impact of the surface recombination on the PC spectra depends on the number of carriers that are close to the surface. For small $\alpha(\hbar\omega)$, the carrier cloud is predominantly generated in the bulk, whereas for high absorption coefficients the carrier cloud is generated close to the surface; compare Fig. 4.2.
- Since $\alpha(\hbar\omega)$ is monotonically increasing with $\hbar\omega$, these *two contradicting tendencies* form a 'PC peak' at about 1.397 eV, i.e. 27 meV below the known $E_g = 1.424$ eV of GaAs. The spectral position of the 'PC peak' is determined by the Urbach parameter of $E_u = 10$ meV. Large E_u-values create 'PC peaks' at lower photon energies. Whenever the E_u-values and carrier concentrations are small, the 'PC peak' blue-shifts closer to E_g, while the absence of any Urbach tail (this is, of course, an impractical assumption) would shift the 'PC peak' to an energy slightly above E_g.
- Thus, the spectral position of the 'PC peak' in Fig. 6.4 is determined by an *extrinsic parameter* here. Therefore the 'PC peak' position does *not allow the determination of* E_g. Notice that other material parameters such as L_D and τ also impact on the 'PC peak' position. Shifts between 'PC peaks', however, could well indicate E_g-shifts, at least if no other parameters change at the same time.
- Notice that Fig. 6.4 has been calculated without taking any excitonic effects into account. Obviously, there is a high risk to misinterpret such 'PC peaks' as excitonic PC resonance; see also the following section.

The reduction of the PC at photon energies above E_g with increasing s, see chart above 1.45 eV in Fig. 6.4, is used as a practical method for the estimation of surface recombination velocities.

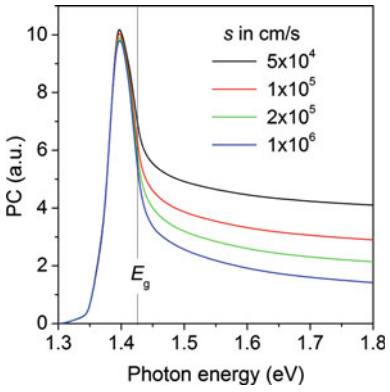

Fig. 6.4 Calculated photocurrent spectra for bulk GaAs according to Duggan and Scott [2]. The parameter is the surface recombination velocity further material parameters are $L_d = 4$ µm and $\tau = 20$ ns

6.2.4 *Photoconductivity from QWs, Quantum Dots, and Excitonic Photoconductivity*

Interband PCs from QWs: Let us assume a QW is populated by non-equilibrium carriers that have been generated by photoexcitation resonant to the lowest quantum-confined transition. Whenever PC is considered, one has to distinguish between two cases, namely *lateral* transport, i.e. within the QW plane, and *vertical* transport, i.e. along growth direction; see also Sect. 6.3. While the presence of a lateral QW PC is plausible after applying a bias to the selectively contacted QW (i.e. it should not be short-linked by the barrier), the option of vertical transport is not self-evident. Electrons and holes are captured in the potential valleys of valence and conduction bands, respectively, and there is actually no reason for them to get spatially separated even if moderately[4] biased. Consequently, no vertical PCs can actually be expected. But there are mechanisms that free the confined carriers and thus allow for vertical current transport.

- There is *thermionic emission* of carriers which are trapped in QWs. Schneider and von Klitzing quantified this mechanism for QWs [3], (see Footnote 4). For the case of holes in a multiple QW structure, the electric field strength and temperature dependencies of the effective barrier height have been determined.
- *Tunneling* represents another mechanism which supports freeing carriers and eventually can result in a vertical current transport, in particular for elevated electric fields.
- The *Schottky effect* leads to an effective lowering of barriers heights due to the action of an electric field at a *pn*-junction or surface. Emission rates are potentially increased by this mechanism, as well.

Fox et al. [4] studied the effects of barrier design (width, height), external fields, temperature, and population on QW photocurrents. Furthermore, the authors experimentally determined the *carrier sweep out time* (τ_{so}) to a range between 10 and several 100 ps. Thus, there is another, very effective depopulation mechanism for QWs that we have not considered so far. If we include this mechanism, the non-equilibrium lifetime of carriers within a QW τ can be written as

$$\frac{1}{\tau} = \frac{1}{\tau_r} + \frac{1}{\tau_{so}}, \tag{6.17}$$

where (τ_r) represents the recombination lifetime, which we simply identified as τ up to now. If we take into account typical τ_r-values of QWs on the order of ns, it turns

[4]The term 'moderate bias' refers to an external electric field, which would be sufficient for separating electrons and holes in bulk material. On the other hand, potential shape and energetic structure of the QW should remain (almost) unaffected. Thus, tunneling or the quantum-confined Stark effect are not considered.

out that carrier sweep out is frequently a *more efficient mechanism for QW depopulation by far than recombination*.

But why we have not considered such a basic process in preceding chapters when considering carrier balances, e.g., for QW PL? The answer is simple: Carriers that left the QW by thermionic emission (and they do it, of course, also in PL experiments, as well) are highly likely to be re-trapped by the QW if they do not get spatially separated by a potential gradient or a bias and removed by a closed electric circuit. Since regular PL experiments do not involve this, the swept-out carriers are not lost for recombination. They recombine either from the barrier or get re-trapped by the QW. Therefore, in PL experiments, charge separation (another word for 'photocurrent generation') must be considered, if they are carried out in regions with potential gradients; see [5].

Knowledge about these processes is widely used in order to model the properties of QW-based devices, which rely on vertical current transport, such as QW based detectors or solar cells [6].

Intersubband transitions in QWs are employed in quantum well infrared photodetectors (QWIP) [7].

Interband PCs from QDs are created in a similar way as they are created in QWs: Carrier pairs are generated by absorption via quantum-confined states. Freeing them, however, requires a secondary process such as thermionic emission.

Excitonic photoconductivity: As neutral quasi-particles, excitons can not contribute directly to PCs because their motion will not result in any net charge transport. Clear excitonic lines have been observed in PC spectra, however, and sometimes excitons even govern PC spectra. They are particularly well detectable in materials with very high exciton binding energies such as Cu_2O [8, 9], in wide-gap semiconductors such as ZnO [10], but also in GaAs-based QWs even at ambient temperature; see Fig. 6.5. How do these two facts go together?

Of course, excitonic transitions create utmost efficient absorption features, fulfilling one necessary condition for PC generation. The second one, namely spatial separation of electron and hole, can only be achieved if the excitons undergo scattering processes, e.g. with other excitons, defects, or become thermally dissociated. Such processes, however, are not unlikely, and therefore, PC spectra often show excitonic features.

- For *vertical QW PC*, *QD PC*, and *excitonic PC* holds: They require the presence of a secondary mechanism that frees the carrier pairs and allows their separation within an electric field. The presence of such mechanisms in practical experiments is highly likely. A clear identification and quantification of these processes is, however, often very difficult.
- Quantum-confinement increases exciton binding energies by reducing the exciton's Bohr radius. Therefore, PC spectra from QWs often display pronounced excitonic effects, as well; see Fig. 6.5.

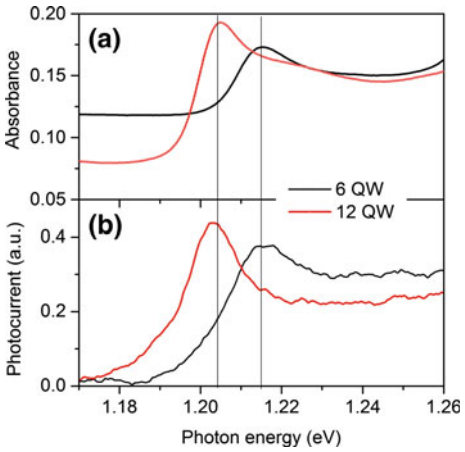

Fig. 6.5 Comparison of the excitonic absorption spectra **a** and excitonic PC spectra **b** from two different InGaAs/GaAs-QW structures at ambient temperature

6.2.5 *Extrinsic Photoconductivity*

We have stressed already the affinity of the PC technique to defects, i.e. *extrinsic* PC contributions. Moreover, there are carrier exchange processes between bands and defect levels, i.e. there is interplay between *intrinsic* and *extrinsic* PC.

In Sect. 4.6.1, we addressed the *temporal hierarchy* of the processes after an optical excitation. Now we recall those as they are of particular relevance for PC generation.

- After carrier pairs are generated, their relaxation is mainly determined by two, at least initially, competitive processes, namely recombination and trapping. Recombination includes both intrinsic and extrinsic mechanisms, trapping is a pure extrinsic process.[5] When *recombination* of the carrier pair takes place, no matter if it is radiative or non-radiative, the carriers are lost for PC generation. Thus, recombination is expected to quench PCs, e.g., in direct semiconductors on a timescale of ns. The term *trapping* refers to a special type of defect-related recombination, namely the capture of charge carriers by defects [*traps* (see Footnote 5)]. Typically, only one carrier type is involved in this process, either

[5]A *trap* is an electronic level in within E_g with a substantially higher *capture rate* than *emission rate*. Traps attract only one carrier type, either electrons or holes, for a certain time, which is typically long compared to the intrinsic non-equilibrium carrier lifetime τ of the material. Since traps are caused by defects within the semiconductor lattice, their number is finite. Thus, their ability for *trapping* carriers becomes saturated at elevated excitation levels. Traps become either depopulated by re-emission into the band from where they originally come from or into the opposite one. In the first case, they act like a type of carrier storage, while in the latter case their behavior is the one of a a non-radiative recombination center.

the electron or the hole. Trapping into defects can be more efficient even than intrinsic recombination, since it takes place on a ps- or even fs-timescale [11]. As the number of defects sites in a semiconductor crystal is finite, trapping is likely to saturate.

- Under certain circumstances, PCs can last extremely long, e.g. seconds, hours, or even longer. This effect is well-known, e.g. from wide-bandgap II–VI semiconductors, and is called *persistent* PC [12–14]. It is caused by free non-equilibrium carriers which do not find partners for recombination. Such a situation may occur after bipolar generation by trapping of one type of carriers into defects or by any other type of spatial carrier separation; e.g. in potential fluctuations [15].
- After the recombination is essentially completed, the PC is actually expected to be terminated. In practice, however, carrier release, e.g. out of traps into band states, can provide additional contributions to the PC. Since the duration during which the carriers are trapped might be long compared to τ, these PC contributions might be relevant even a long time after photoexcitation has ended. Such a behavior is shown in Fig. 6.6a [16], where the temporal behavior of the PC due to a change in $\hbar\omega$ from 1.10 to 1.15 eV is plotted.

Notice that these effects are relevant to semiconductors in general and not exclusively related to the PC technique.

But why we have not discussed them in preceding chapters, when we addressed CL or PL?

- Extrinsic effects such as trapping are *less relevant* (not irrelevant) to the results obtained by Raman-, PL-, or CL-spectroscopy. This is because the impact of traps saturates at elevated excitation densities as it is typical for the other techniques. PC measurements are typically performed at lower excitation densities than necessary for the other techniques.
- Furthermore, PC detection does not provide any straightforward selectivity with respect to the mechanisms that are generating the current. In contrast to PL, CL or Raman, the *spectral selectivity of the technique does not unambiguously pinpoint the mechanism of current transport for PC.*
  In other words: while measuring, e.g. a particular peak in a PC spectrum, one can not directly detect which current transport mechanism is actually creating this particular feature. This is due to the aforementioned carrier re-distribution processes between band(s) and defects.
- If long PC time-constants are effective, see Fig. 6.6a, it requires measuring times of the same order for *one single data point* in a PC spectrum. This might become impractical.

The impact of these specific characteristics ton PC experiments will be discussed in detail in Sect. 6.3.

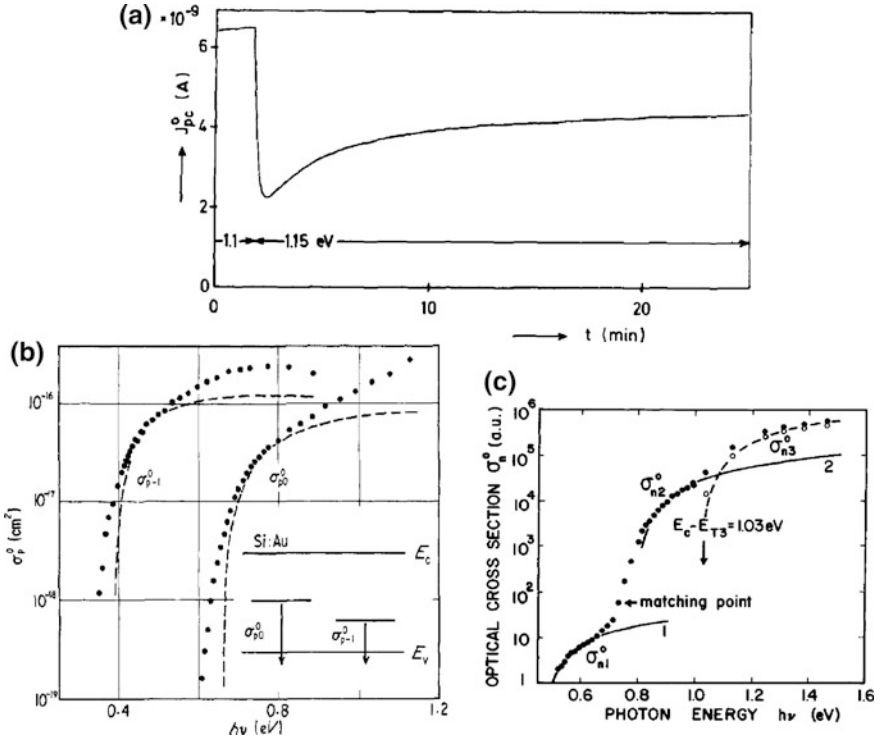

Fig. 6.6 Extrinsic PCs in GaAs and Si. **a** Change of the PC from GaAs:O due to a change in photon energy from 1.10 to 1.15 eV [16]. **b** Below bandgap PC spectra (absorption cross sections) from Si [16]. The *curves* represent fits according to the theory by Lucovsky [17]. The inset shows the energetic position of the deep levels and the optical hole transitions responsible for forming the observed two PC bands [18, 19]. **c** Below bandgap PC spectra (absorption cross sections) from high-resistivity GaAs:O [16]. Cross sections were measured for three different deep states in high-resistivity *n*-type O-doped GaAs. Energy positions of the three levels at 77 K are ∼0.46, ∼0.79, and ∼1.03 eV below the conduction band

The spectral shape of extrinsic PC spectra: Fig. 6.6b, c show absorption cross sections $\sigma(\hbar\omega)$ that are derived directly from extrinsic PC spectra,[6] [20], which are monitored at photon energies below E_g [18–20]. Such PCs are caused by transitions which involve deep-level defects. While the full circles in (b) show data from Si:Au, the data points in (c) represent spectra obtained from high-resistivity *n*-GaAs:O.

[6]The spectral shape of the absorption cross section σ in a given spectral range is obtained by plotting the inverse of the photon flux that needed to keep the photocurrent constant in this range. This approach, named *constant photoconductivity technique*, will be addressed in detail in Sect. 6.3.

The inset in (b) gives a scheme showing the energetic position of the deep levels within the forbidden gap and the two optical hole transitions (see arrows) responsible for forming the observed below-bandgap PCs. In (c), even three deep levels are detected, which are located at 0.46, 0.79, and 1.03 eV below the conduction band of the GaAs (E_g = 1.508 eV at T = 77 K).

The full curves in (b) and (c) represent fits according to early calculations by Lucovski [17].

$$\sigma(\hbar\omega) \propto \frac{\sqrt{E_i}}{(\hbar\omega)^3} \cdot (\hbar\omega - E_i)^{\frac{3}{2}}. \tag{6.18}$$

E_i is the ionization energy of the defect level. This estimate assumes parabolic bands and a δ-potential for the deep level. Refined calculations are provided by Grimmeiss [18]. An extension of this which describes $\sigma(\hbar\omega)$ for transitions related to deep traps in AlGaAs/GaAs-QW-structures is provided by Takikawa et al. [21].

Extrinsic PC contributions: In Zincblende semiconductors, i.e. in most important optoelectronic materials, μ_n and μ_p are intrinsically different due to their asymmetric bandstructure. For extrinsic reasons (trapping), the temporal evolutions $\delta n(t)$ and $\delta p(t)$ differ as well. Thus it is adequate to introduce 'effective lifetimes' of electrons and holes, τ_e and τ_p, respectively. According to (6.15), μ_n, μ_p,τ_e, and τ_p are weight factors for the contributions of non-equilibrium electrons and holes to the I_{PC} that is eventually measured.

$$I_{PC} \propto \sum_i \mu_i \cdot \tau_i. \tag{6.19}$$

The index i stands for electrons and holes in the conduction and valence bands here. Sometimes the product of *effective lifetime* and *effective mobility* is used to quantify and compare extrinsic PC contributions.

Extra PC contributions via defects or defect bands are sometimes also quantified by using (6.19). This kind of PC is often called *hopping* PC and includes contributions by long living carriers with rather low mobilities ('hoping mobility') compared to the mobilities within the bands. Conductivity via localized defect states is explained microscopically either by tunneling from one defect site to adjacent ones or by successive thermionic emission, short-range transport ('hopping'), and re-trapping. Alternatively, there might be a defect band which is degenerated with band states. In this context, the term *mobility edge* is frequently used. Although E_g and *mobility edge* are typically not separated by far, both edges refer to different effects. While E_g is a parameter that describes the intrinsic bandstructure of a material, the mobility edge separates between extended (high mobility band-like) and localized (low mobility) states. This concept is also applied to model the behavior of disordered or amorphous materials.

6.2.6 Other Photoelectrical Effects

Photo electromagnetic effect: The (PEM) effect is an effect related to PC if carried out in presence of a *magnetic field*.

If one implements surface excitation to a cuboid-shaped PC sample, see Fig. 6.2a, by using high-energy photons, carriers will diffuse to the opposite side of the crystal. The Lorentz-force, which is caused by a magnetic field perpendicular to this diffusion current, will create a voltage (current) along the third orthogonal direction. This is called the PEM-effect and it results in a special type of photocurrent.

Dember effect: The Dember effect is closely related to PC generation, as well. The starting point is again the surface excitation at a PC sample. If the generated excitons start diffusing (driven by the concentration gradient), they will not cause any net charge transport. They are likely become, at least partly dissociated into free electrons and holes depending very much on the particular conditions. The diffusion coefficients of free electrons $D_e = \frac{kT}{e} \cdot \mu_e$ and holes $D_h = \frac{kT}{e} \cdot \mu_h$ in Zincblende semiconductors differ due to the different mobilities μ_e and μ_h, which are caused by the asymmetric bandstructure of valence and conduction bands. Therefore, electrons and holes will diffuse with different speeds, leading to charge separation. This results in an electric field, the *Dember field*, which slows down the diffusion of the electrons, and eventually leads to a more uniform diffusion behavior of both carrier types called *ambipolar diffusion*. The afore-given scenario describes the *longitudinal* Dember-effect, which is measurable by very specialized setups only. A *lateral* Dember effect may appear as a result of the presence of fields or in electrically anisotropic semiconductor materials.

In combination with the PEM effect, the lateral Dember effect allows the independent *determination of components of the mobility tensors* of electrons and holes, μ_n and μ_p respectively [22].

Mobility-photoconductivity (μ-PC): Notice that the letter μ stands for mobility here and not for micro. If carriers are excited within a band, e.g., by intraband absorption, they might reach final states, where μ has another value compared to the initial state. This can be accomplished by excitation with photons $\hbar\omega < E_\mathrm{g}$. According to (6.15), a change in μ is expected to cause a modification of the PC [23]. Indeed, PC saturation has been assigned to μ-PC [24].

Since such PCs typically appear for $\hbar\omega < E_\mathrm{g}$, they might be mixed with extrinsic, bolometric, or other types of residual PCs. Applications of μ-PC include far-infrared and THz detection.

Photo-Hall effect: The modification of a Hall-voltage by extra illumination is called photo-Hall voltage. The resulting current can be used for analytical purposes, e.g., in order to decide whether a photocurrent is caused by μ-PC only or by a de facto change in δn.

Negative photoconductivity: The term *negative PC* refers to a situation, in which photoexcitation results in a *reduction* of the actual conductivity, at least in a certain spectral range. Explanations for this phenomenon typically point to a

situation, where photoexcitation brings carriers from conducting bands into less conducting bands or states. 'Free-to-bound' transitions potentially create this effect.

The presence of negative PC is indicated by a 180° phase shift, if a look-in based PC setup is used. If the absolute value of the PC is only monitored, one is likely to miss the effect. Negative PCs are observed in bulk semiconductors such as Si [25], but also in QWs, and at interfaces [26].

Photocurrent bleaching/quenching: The terms PC *bleaching* [27] and *quenching* are frequently used synonymously. Like negative PC, this effect results in a PC reduction and is caused by carrier redistributions. Bleaching is mostly achieved by an *additional light source*. Sometimes the term PC bleaching is also used to point to a saturation of PCs at elevated excitation densities (of the probe beam) [28].

Bleaching is mostly induced by *extra illumination* with a monochromatic (laser) source. If a look-in based PC setup is used, the extra source is operated cw. Thus, the cw source that is causing the bleaching does not provide any AC PC contribution.

Figure 6.7 shows an example for a PC bleaching experiment [29] carried out at a QW structure that involves a fairly large, but finite, number (N) of defects, named D (N); see scheme. All spectra are measured in AC mode by a look-in based setup. The energetically lowest 1hh-1e transition at 1.53 eV is marked and divides the PC spectrum in two parts, namely the one at higher energies formed mainly by QW transitions and the one below 1.53 eV formed by 1hh-D transitions. The latter transitions populate the deep level D and leave free holes within the valence band (empty 1hh states) that generate the defect-related PC bands below 1.53 eV. If one illuminates the sample with a cw photon flux of 1.32 eV photons, the QW transitions remain (almost) unaffected, while the defect band becomes *bleached*. The latter effect is explained by absorption of the 1.32 eV photons by 1hh-D transitions, see the arrow in the scheme. If an increasing cw photon flux fills more and more D levels, there are no unoccupied defect sites available as final states for 1hh-D

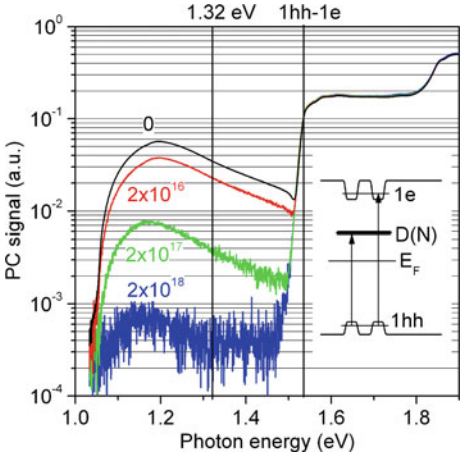

Fig. 6.7 Results of a PC bleaching experiment with additional irradiation of the sample. PC spectra are shown from a defective device for different incident photon fluxes of the additional continuous wave irradiation at a photon energy of 1.32 eV. The inset gives a scheme of the QW bandstructure including a defect band D(N) [29]

transitions, which created the defect-related AC PC. The quantification of this process allows the estimation of the absorption cross-section of the defects.

Pseudo-photoeffects: Illumination of semiconductors with light can cause modifications of their electric properties in ways that have not been addressed up to now: If the excitation light heats the sample, this might cause a PC signal because many parameters affecting PC depend on temperature. Such *bolometric PC*s are mostly considered an experimental artifact. Since bolometric effects are typically 'slow', variations of the excitation density and/or chopper frequency f are experimental approaches, which can help to identify them.

6.3 Experimental

6.3.1 Photocurrent Setups

Figure 6.8 show schemes of two typical PC setups, taken from experimental works. Both use a lamp as light source and a monochromator to define the photon energy interval which is used to probe the PC. In both cases, the light beam is directed to the sample and the photocurrent is pre-amplified. But there are important distinctions as well. Based on the setup, we will distinguish exemplarily between three approaches to PC measurements, namely modulated PC, constant PC for photon flux, and the constant photocurrent approach.

The first one is that Fig. 6.8a represents a setup that serves primarily for *modulated PC* measurements. *Modulated PC* here means that the originally continuous photon flux from the lamp is chopped and converted into a modulated one. Before the light hits the sample, a beamsplitter out-couples a part of the light in order to analyze its temporal behavior by using a fast photodiode. This is done because analysis of the *PC phase* φ is important for this type of AC PC measurements. Here, φ quantifies the phase difference between excitation light and PC signal; see inset left [30]. This delay is caused by 'slow' PC processes. 'Slow' are those that inverse time-constants are on the same order as the chopper frequency f or even longer.

This setup potentially allows us to measure PC spectra including modulus and absolute phase for each photon energy. Even if the knowledge about the absolute phase is not desired in a particular measurement, all types of measurements employing look-in amplification provide a relative phase value anyway.

As already mentioned before, PC spectra are often plotted for *constant photon flux*. There are two main experimental options to accomplish this goal:

- One takes the PC spectrum as it is originally measured and divides it by the 'instrument function' that is separately measured with a detector of known spectral sensitivity. This approach is convenient, but incorrect if there is any non-linear PC response.

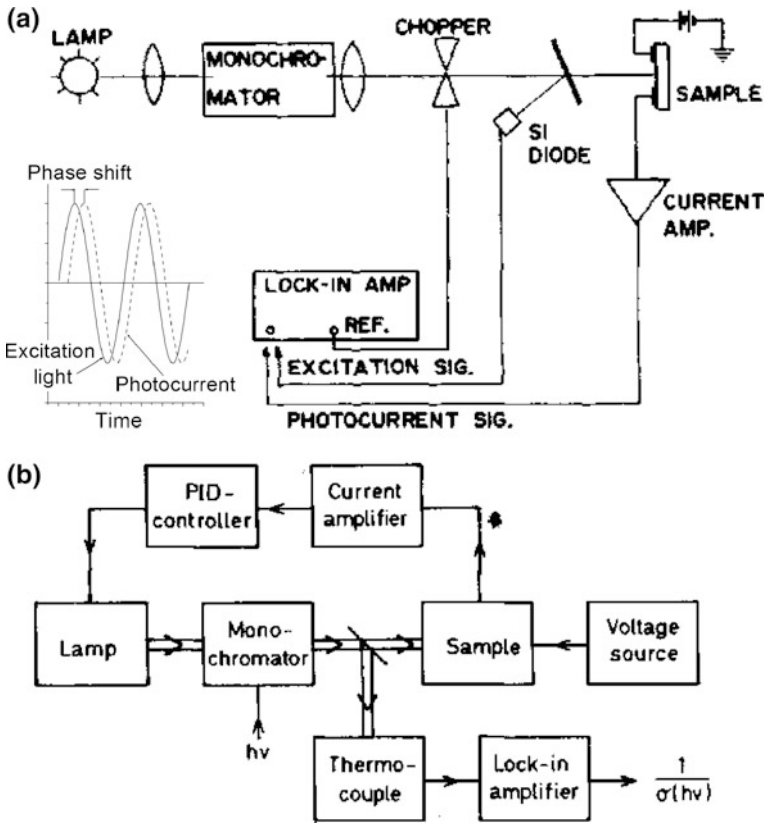

Fig. 6.8 Schematic diagrams of two different PC setups. **a** Schematic of a PC setup that serves for the accurate determination of the *phase shift* between modulated excitation light and PC signal; see inset [30]. This approach delivers information about carrier lifetimes provided that the inverse chopper frequency is of the same order as the time constants which describe the carrier kinetics. **b** Schematic of a PC setup that serves for the measurement of PC spectra taken for constant PC. This approach allows for the determination of absorption cross sections of deep level defects [20]

- The more complex approach is to establish a constant photon flux by inserting an attenuator, e.g. a circular variable neutral density filter, between lamp and sample. In this case, an additional detector is required to measure the actual photon flux. The signal is then used to control an attenuator via a feedback loop. This adjustment of the photon flux must be performed at each wavelength and will therefore substantially increase the measuring time. Moreover, all light fluxes must be attenuated to the lowest level within the considered wavelength interval.

Alternatively to the measurement under constant photon flux, it can also be interesting to measure spectra in a *constant photocurrent* regime. The setup depicted in Fig. 6.8b can perform such measurements. In this case, the photon flux is

measured by the lock-in amplifier and the PC signal is used to control the photon flux from the lamp via a feedback loop involving the lamps driver unit. Consequently, the resulting special kind of PC spectrum actually represents the photon flux (required for generating a certain PC) versus the photon energy. It is mainly used for the determination of absorption cross-sections of deep level defects [20].

Like other spectroscopic techniques addressed in this book, PC spectroscopy can be performed by using Fourier-spectrometers, as well. We call this approach FT PC [31, 32]. This type of measurement offers exactly the same advantages as addressed in Sects. 2.2.3 and 4.5.4. For a given measuring time FT PC offers a better signal-to-noise ratio. Such measurements require almost no modification of the spectrometer. The sample is placed into the sample compartment and the PC signal is fed into the preamplifier that is elsewise taking the detector signal.

However, there are also potential residual effects in the FT PC approach. In addition to the FT-related effects mentioned in Sects. 2.2.3 and 4.5.4, there are other effects, due to 'slow' PC contributions, which are mostly defect-related. This will be addressed later.

We will now briefly address the main elements that are part of PC setups according to the sequence of their involvement into the PC generation process:

Excitation sources: For PC applications, radiation sources with a wide and rather smooth spectrum (continuum sources) are needed. Therefore, black-body radiators are better suited than lamps that emit distinct single lines such as spectral lamps. Halogen lamps can be used for the VIS and the NIR, while SiC-*globars* sources meet the requirements in the MIR.

More costly, but featuring a substantially higher brightness, are *white light sources*, i.e. mode-locked fs-fiber lasers serving as pump and photonic fibers as light converter. They offer an almost flat spectrum (except for the pump laser wavelength; e.g. at 1064 nm) from the blue to about 2.4 μm. The same advantage with respect to brightness is offered by tunable solid-state lasers, such as Ti: Sapphire (750–1000 nm). But such lasers are even more costly than white light sources and offer rather limited continuous tuning ranges only. In addition, all types of tunable sources do not provide their own volition information on the actual emission wavelength. In case of laser sources, *wavemeters* can serve for this purpose. They are provided with a small fraction of the excitation light that is out-coupled via a beamsplitter. Such devices are commercially available and typically accomplish the wavelength measurement by using an internal interferometer.

Monochromator: Taken together with a lamp, the monochromator represents a classical 'tunable source' for PC excitation. The drawback of this combination is, of course, the limited photon flux which results in a rather low 'excitation power'. Therefore, the right choice of optics, monochromator, and its grating(s) is crucial. The compromise that is to be found is the one between the contradicting demands for high intensity of light (low focal length) and spectral resolution (long focal length). A larger grating promises high light throughput. *Order sorting filters* complementing the grating are of particular importance: this is because PC spectra typically cover wider spectral ranges than, e.g. PL spectra. In case of PL, it is unfortunate if the second order of another PL contribution (or even of the excitation

laser) fakes a PL signal. In case of PC, a halogen lamp, however, definitely emits at both 450 and 900 nm and therefore the 900 nm 'excitation beam' will contain 450 nm light for sure if it is not blocked by the right order sorting filter.

Notice that if a tunable laser and a wavemeter are used for excitation and wavelength reading, respectively, no monochromator is required.

Focusing optics: Clearly, the focusing optics define the diameter of the excitation spot on the sample surface and consequently the spatial resolution of the setup. But there is another important issue: since lamps serve as the PC excitation sources in most cases, there will often be a lack of light intensity. Therefore, the design of the focusing optics of a PC setup requires the same attention as the imaging optics of a PL setup; see Sect. 4.3.1.

Sample: Sample geometry and preparation, in particular of the contacts, are crucial for the success of any PC experiment. Therefore, we will address this separately in Sect. 6.3.2.

Amplifier: In Fig. 6.8, preamplifiers are attached to the sample. Together with R_{Ref}, the input resistance of this amplifier is a main parameter. The bandwidth requirements depend on the chosen chopper frequency.

Computer control: The computer control of the setup is something which is not directly related to the actual spectroscopic experiment. Basically, the same statements as given in Sect. 4.3.1 for PL setups are relevant. Again the 'degree of automatization' represents an important issue, which should be considered carefully.

A special feature of PC measurements is that they cover comparable wide spectral ranges with highly changing PC signal magnitudes. If the measurement is based on a lock-in amplifier, one should consider the option of implementing an automated switch of the effective measuring range of the look-in amplifier into the software. This will allow to trace PC signals across orders of magnitude in amplitude.

6.3.2 Sample Geometry

In contrast to other analytical techniques addressed in this book, sample geometry crucially influences the results obtained by PC measurements. This includes both sample and contact geometry. In Sect. 6.2.2, we outlined the relevance of the sample thickness d for the spectral range, in which successful PC analysis is useful. We mentioned that this corresponds to transmittance measurements. Thus, the impact of the parameter d is already discussed.

One sort of representative bulk crystal samples used for PC analysis are the so-called *Hall-bars*. Such samples are usually available from routine Hall-effect measurements at semiconductor wafers; see Fig. 6.9a. Stripes are cut from wafers that are typically 1–2 cm long and $\sim$1 mm wide. In this case, d corresponds to the wafer thickness, which is often on the order of 500 µm. Six contacts are usually attached. The contacts at the two end planes can also be used for the PC

measurement. Representative epitaxial samples are etched 'bridge-type' Hall-samples with 6–8 contacts and bringing to mind a beetle-shape; see Fig. 6.9b. Here the two end-plane contacts can be used for PC measurements, as well. In both cases, care must be taken either not to excite the contact regions or to cover them, e.g. by pieces of black paper. The locations where such covers should be placed are indicated by dotted squares; see Fig. 6.9a, b. The reason for this is that Schottky-contacts with space charge regions might be formed at metal-semiconductor interfaces. These regions might have modified photoelectrical properties compared to the bulk and interfere the results.

Sometimes contacts are also intentionally illuminated, e.g. in case of meander-like contact geometries, which are preferably used in photoresistors made of highly resistive materials.

If the sample is an epitaxial layer system such as a heterostructure, there are two principal geometries for the implementation of a PC measurement.

- First, excitation is made with the Poynting vector directed along the growth direction and measurement of *lateral* current transport takes within the plane of the epitaxial layer. This would be the case if the sample shown in Fig. 6.9b were be illuminated with light incidence perpendicular to the image plane. This might be considered the *standard approach* since the PC is measured across homogeneous material. The same excitation geometry is used to excite the bulk Hall-bar; see Fig. 6.9a.

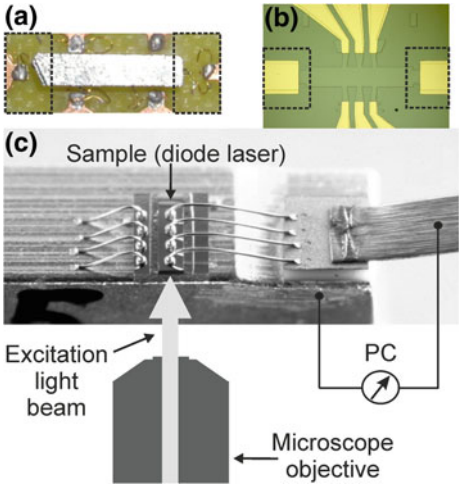

Fig. 6.9 Sample geometries suitable for PC measurements. **a** Hall bar made of bulk material (Klaus-Jürgen Friedland). **b** Hall beetle as used for analysis of epitaxial layers (W. Ted Masselink). The *dotted* areas mark positions close to contacts, which should not be illuminated or must be screened. **c** Diode laser which is illuminated at the front facet. This allows for in-plane excitation into the epitaxial structure of the device

- Second, excitation is implemented with the Poynting vector being in-plane and measurement of *vertical* current transport takes place across the heterojunction; see Fig. 6.9c. As an example, a diode laser is investigated in this particular geometry. Instead of the diode laser, there could also be a piece from an epitaxial structure clamped there. This approach has been pioneered by Blood [33] and has been named *edge photovoltage*. Even before that, Henry et al. [34] used this geometry in order to obtain PC spectra straight from the front facet of regular diode lasers such as shown in Fig. 6.9c. The use of the in-plane selection rules [35] for absorption of polarized light made this method even more selective, in particular, if QW structures or devices are analyzed [36, 37].

It is obvious that in both geometries, i.e. in standard approach and edge or in-plane excitation geometry, the effective sample thickness d may differ by orders of magnitude even if the same epitaxial structure is analyzed. This offers a variety of further analytical options.

As for the other analytical techniques addressed in the preceding chapters, the question regarding the *size of the probed sample* region is crucial. Obviously, the *lateral extension* is given by the excitation spot size, i.e. the way we focus the excitation light onto the sample.

For *vertical extension*, i.e. the one along the Poynting vector of the incident light (z-direction), we can use what we have derived for PL in Sect. 4.2.1 and what we have called 'information depth'. Notice that the 'information depth' is dependent on the absorption coefficient. Therefore we want to stress again the statement made in Sect. 6.2.3: If the absorption varies within a PC spectrum (and this is the standard situation), the 'information depth' also varies. Whether full saturation is reached or not depends on the spectral range which is probed and the sample thickness.

6.3.3 Direct and Time-Dependent PCs

If one measures *any optical spectrum* in a DC-measurement by tuning the wavelength, it is important to see how much time must be spend at each wavelength, e.g. at each particular monochromator position. This time will eventually determine the total measuring time and practically consists of three parts: First, the time until the new wavelength value is reached, second, the time that is needed for the signal to recover at the new spectral position to an (almost) constant value, and third, the actual measuring time (integration time). While the first is determined by (mechanical) features of the monochromator that is used, it is fair to choose the second to 2–3 times of the *time-constant of the actual PC recovery* τ_{PC}. The third can be chosen freely by the experimentalist; it eventually determines the signal-to-noise-ratio of the spectrum. The proper choice of these three contributions helps to optimize the experiment.

Steady-state PC spectroscopy: There are many reports claiming to have performed *steady-state* spectroscopy, while referring to experiments with chopped light and look-in detection. Although the term *steady-state* seems to indicate a type of DC spectroscopy, such measurements represent AC spectroscopy. Therefore, an additional time-constant comes into play, namely the inverse chopper frequency $1/f$. The term *steady-state*, however, is still (almost) correct as long as $1/f$ is long compared to interband-related τ_{PC}, i.e. for the rather low frequencies obtained by mechanical choppers.

AC PC measurements: Increasing the chopper frequency, i.e. lowering $1/f$ towards the same order as τ_{PC}, offers a way for the experimental determination of τ_{PC}: A sinusoidal excitation source with a modulation frequency $\omega = 2\pi f$, will result in a frequency dependent PC according to

$$I_{PC}(t) = M(\omega) \cdot \sin[\omega t + \varphi(\omega)]. \tag{6.20}$$

Here, $M(\omega)$ describes the damping of the PC with increasing frequency. The actual value of τ_{PC} can be determined either from $\varphi(\omega)$ or $M(\omega)$ by

$$\tau_{PC} = \frac{\tan(\varphi)}{2\pi f} \text{ or } \tau_{PC} = \frac{1}{2\pi f}\sqrt{\frac{1}{M(\omega)^2} - 1}, \text{ respectively.} \tag{6.21}$$

For pure interband PC, one expects $\tau_{PC} = \tau$, in which τ is the non-equilibrium carrier lifetime. In the early days of semiconductor physics, the analysis of $\varphi(\omega)$ been called phase method [38] and was considered a suitable method for τ-measurements, e.g. in Si. The same holds for analysis of $M(\omega)$ [39, 40].

In practical experiments $M(\omega)$ and $\varphi(\omega)$ can easily be obtained if a lock-in amplifier is used. However, it is also worthwhile, to analyze $\varphi(\omega)$ by visualizing excitation light and the PC-response on an oscilloscope screen. You might be surprised!

The link between τ_{PC} and τ: In practice, τ_{PC} typically exceeds τ, sometimes slightly, sometimes by many orders of magnitude. Thus, τ_{PC} is an effective time-constant. Mechanisms that cause the prolongations are

- *Extrinsic processes*: this has been addressed in Sect. 6.2.4. Of course, these 'slow' contributions are ignored in such lock-in-based PC experiments, where 'high' chopper frequencies are used. At best, only the spectral feature related to large time-constants (e.g. a 'defect band' at energies below E_g) is missed in the PC spectrum. But carriers that are confined in defects may be transferred to conducting states in bands, e.g. by thermionic emission and in this way impact on the PC spectrum.
- For *inhomogeneous semiconductors*, in particular if they contain *pn*-junctions, additional contributions must be considered in a way as it was done when time-constants of photodiodes are considered. This includes the

  - *diffusion time* of carriers towards the junction and
  - *transit time*, i.e. the transport time through the space charge region of a junction.

  Both contributions together are called *charge collecting time*.

- RC-time-constants are known to influence the speed of any electronic circuitry. In a PC measurement, the investigated sample becomes part of an electronic circuit as well; see Figs. 6.1 and 6.3. Thus, the capacitance C of a *pn*-junction within a PC sample (which is determined among others by the thickness of the 'space charge region') can become the part that governs PC kinetics, e.g. together with a high input resistance of the instrument.

The root mean square of the charge collecting time and the *RC*-time-constant is called *response time of a diode structure*. This term is predominantly used in order to specify the transient behavior of photodiodes. Considering PC spectroscopy, it gives a good estimate for τ_{PC}.

Except for these mechanisms that can explain the finding that τ_{PC} might be larger thanτ, there are also mechanisms causing the opposite. This is, e.g., surface recombination. A mechanism that might act towards both directions is band bending.

Therefore, τ_{PC} *as it is obtained in AC PC experiments cannot automatically be identified with*τ. *This is true in particular if vertical current transport through pn-junctions is probed. In this case*, *the response time of the diode structure is observed*, *which oftentimes exceeds* τ *by orders.*

Even if the condition $\tau_{PC} \ll 1/f$ is fully satisfied, a 'steady-state measurement' that uses lock-in amplification must not provide the same result as a genuine DC experiment. If, e.g., vertical transport through a structure, which includes a thin insulating layer, is probed, a genuine DC experiment will not provide any PC. In an experiment with lock-in detection, however, the insulating layer acts like a capacitor and PCs are detected.

The same holds for PC spectroscopy, if Fourier-transform spectrometers are employed. FT-based measurements are actually considered as DC measurements. But actually this is not true: For any mirror speed (of the moving mirror in the Michelson interferometer), PC contributions with a longer time constant than the inverse modulation frequency are cut. Even if this is not the case, the modulation given by the mirror motion creates an AC-like experimental situation, like it is known for lock-in detection. Comparing the results of measurements with different mirror speeds or using the step-can-option can be helpful in order to identify residual effects.

Modulated photocurrent technique: The *modulated PC technique* has been pioneered by Longeaud and published in a series of papers [41–46]. This method addresses the 'slow' defect-related processes, in particular re-emission processes. As proposed earlier by Oheda [30], $\varphi(\omega)$ is analyzed after sinusoidal excitation in a wide range of modulation frequencies. Temperature, doping, and excitation light intensity serve as additional parameters. The results are consistently explained by

modeling, presuming contributions from localized (defect-related) states within the gap. Eventually, the density of these states within the gap of bulk materials is determined. The method has been named *modulated PC* and has been applied to different homogeneous bulk semiconductors, among them doped GaAs [45], amorphous Si:H [41], and wide-gap 6H-SiC [47].

6.3.4 Transient Photocurrent Spectroscopy

Another type of time-resolved PC spectroscopy is performed if the PC-decay after a short impulsive optical excitation (typically $\hbar\omega > E_g$) is monitored. We call this approach *transient PC spectroscopy* or PC decay measurements. As in transient PL spectroscopy, a cardinal goal of this approach is to understand recombination kinetics, e.g. by measuring τ. Ideally, the observed PC decay will be mono-exponentially and the time constant that describes the transient will be the same τ_{PC} as it would be determined in an AC PC experiment from (6.20) and (6.21). Again the exclusive presence of interband PC should lead to $\tau_{PC} = \tau$.

Such PC decay measurements have been accomplished in the middle of the last century already [48]. Although the direct observation of a current transient is more straightforward than the analysis of $\varphi(\omega)$ as it was described in the preceding Sect. 6.3.3, the main error sources remain the same as they are listed there. In a *pn*-structure, e.g. one might come into a situation, where the observed τ_{PC}-value is not at all linked to τ.

Metzger et al. [5] compared the impact of charge separation, representing one important effect taking place in *pn*-structures, on transient PL and PC. At low excitation levels, the results have been found to be dominated by charge separation. As a result, PL decay is very fast, PC decay is very slow and the two approaches produce very different results. When the excitation level is increased, measurements become dominated by recombination, and the decay times associated with the two techniques converge.

If intrinsic τ-values in optoelectronic materials like III–V-structures should be determined, there is a preference for PL decay compared to PC decay spectroscopy. In indirect materials, however, electrical measurements are important for τ-analysis. Sometimes, τ_{PC} itself is of interest.

Photo-Induced Transient Spectroscopy: A special type of transient PC spectroscopy is the *Photo-Induced Transient Spectroscopy* (*PITS*), which has been applied, e.g. to the analysis of deep levels in GaAs by Hurtes et al. [49]. In contrast to the techniques addressed before, this transient approach considers ‘slow’ carrier kinetics. Fast processes linked to trapping, charge separation, or intrinsic recombination are not taken into account.

The excitation pulses (typically $\hbar\omega > E_g$) are long compared to τ with typical lengths on the order of some 10 ms. After the excitation is turned off, the PC transient is recorded on a millisecond scale, where the re-emission towards the bands of carriers from defect states slows down the influence of recombination. This slow decrease is analyzed by using two or more time-windows (multi-window approach) such as those known from DLTS. Thus, deep level spectra are recorded by going through temperature cycles. Many experimental details are provided by Fang et al. for GaAs samples [50], while Longeaud et al. [47] demonstrate an application to wide-gap 6H-SiC.

6.4 Selected Applications of Photocurrent Spectroscopy for Analytical Purposes

6.4.1 Intrinsic Interband PC

Interband PC can be employed to analyze the electronic bandstructure of semiconductor materials or structures. What type of information becomes accessible depends very much on the sample thickness d; see Sect. 6.2.2 and Fig. 6.3a. This has been stressed already when discussing these modeled spectra.

- For 'thick' samples ($\alpha(\hbar\omega) \cdot d > 1$), PC spectra exclusively provide information about extrinsic effects, such as the Urbach tail absorption region energetically below E_g, (parameter E_u) and about the surface recombination s.
- For 'thin' samples ($\alpha(\hbar\omega) \cdot d < 1$), intrinsic information becomes accessible, as well.

As long as $\alpha(\hbar\omega) \cdot d < 1$, the PC spectrum images the shape of the absorption spectrum $\alpha(\hbar\omega)$. For its analysis, the same strategies as those for the analysis of transmittance spectra can be applied; see Chap. 2.

Notice that the transmission spectra from thin samples in the spectral region around E_g are often affected by interference pattern. PC spectra are typically not (or less) affected because PC monitors the light that is absorbed, while a transmittance measurement monitors the transmitted light. This is a principal advantage of the PC technique. When we take into account the fact that the square-root-shaped absorption edge emerges out of the Urbach-region at $\alpha(\hbar\omega)$-values of several 10^3 cm^{-1}, information on intrinsic sample properties are obviously only accessible for samples thicknesses on the order of 10^{-4} cm = 1 μm or thinner, e.g. at epitaxial layers.

Tober et al. [51] analyzed PC data from InGaAs diodes with a method they called *differential PC spectroscopy*. They differentiated PC spectra with respect to the photon energy or measured the first derivative directly in a *modulation-spectroscopy* approach. In the latter case, they modulated the bias that was applied to the diodes. The derivative spectra were fit with a derivative functional form as it is normally used in conjunction with other differential techniques such as

piezoreflectance, photoreflectance, and electroreflectance. Transition energies were extracted and were found to agree well with those obtained from piezoreflectance spectra. The accuracy, within which E_g can determined, depends crucially on the chosen functional form as well as on the effective value of the absorption length d.

Tabatabaei et al. [52] used a similar approach called *differential photo-voltage spectroscopy*, which is used to characterize epitaxial multilayered and QW structures. A series of 8 quantum-confined transitions have been detected and have been assigned to what a model calculation has provided for the AlGaAs/GaAs-structure.

- At this point, we should note that the determination of the spectral position of quantum-confined transitions in a QW from PC spectra is rather straightforward as long as one follows the following simplified formula: The PC spectrum $I_{PC}(\hbar\omega)$ mirrors approximately $\alpha(\hbar\omega)$ of the QW. If $\alpha(\hbar\omega)$ has 'stairway shape', as expected for a QW, the first derivative $d\alpha(\hbar\omega)/d\hbar\omega$ will show its peaks at the onset of the steps, i.e. at the energies of the quantum-confined transitions. Moreover, the spectral position of the peaks in the $dI_{PC}(\hbar\omega)/d\hbar\omega$-curve are independent of any symmetric broadening effects. Even if the absolute spectral positions of the quantum-confined transitions are not exactly identified, small spectral shifts of them can be recognized well. In the end, the same is also true when PL spectra are considered.
- The condition $\alpha(\hbar\omega) \cdot d < 1$ must be fulfilled if *full* information on $\alpha(\hbar\omega)$ is desired. If only the spectral positions of optical transitions in QWs or QDs are needed, this condition must not be fully satisfied as long as one is able to identify the signature of the transitions. In the following, we will show examples that prove this.

An example is shown in Fig. 6.10. Here, the spectral positions of optical the transitions are plotted along a 10 mm wide 808 nm emitting high-power diode laser array, which is made of one monolithic semiconductor chip [53]. Two types of transitions are identified, namely from the QW and the waveguide, into which the QW is embedded. The mechanism that causes the non-uniformity is mechanical stress, which is introduced along the 10 mm wide device during the soldering onto the heat sink (packaging). Although QW and waveguide are necessarily under the

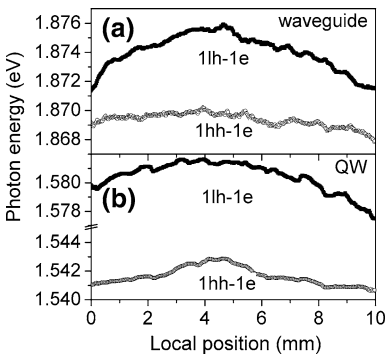

Fig. 6.10 Spectral positions of optical transitions that take place within the waveguide (**a**) and QW (**b**) of a laser structure along the local position of the 10 mm wide laser array [53]. The excitation is provided in-plane and the geometry corresponds to what is shown in Fig. 6.9c

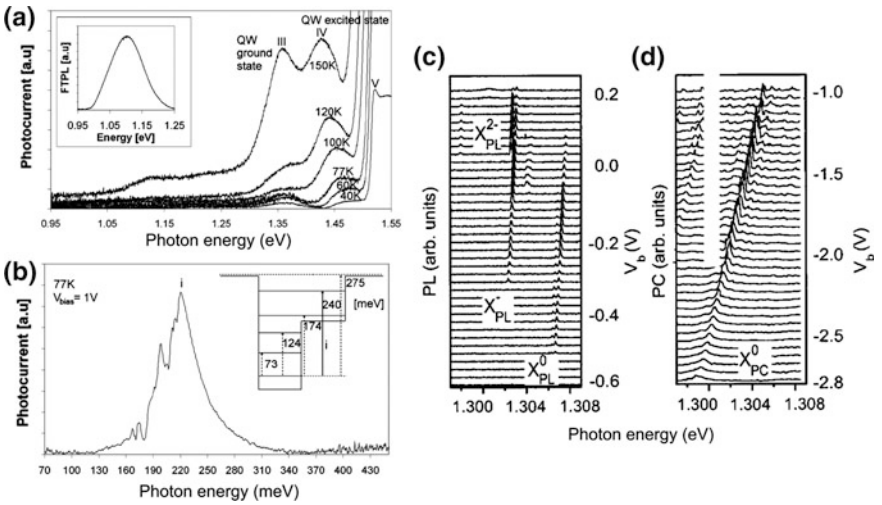

Fig. 6.11 **a** Temperature dependent *interband* PC spectra of a QD structure at an applied voltage of 1 V [54]. The peaks denoted as III and IV correspond to the QW ground state and excited state transitions, respectively. Peak V is the GaAs PC. The inset shows the FT PL spectrum of this structure. **b** *Intersubband* PC spectrum from the same structure, measured at 77 K and an applied bias of 1 V. The possible transitions from the QD ground state, the expected transition energies being derived from the interband measurements, are illustrated in the inset. The transition from the QD ground state to the QD excited state (marked I) is the dominating peak. **c**, **d** PL and PC spectra from a single-QD photodiode as a function of the bias voltage (V_b). PC only probes the neutral QDs, whereas in PL, the neutral X and charged excitonic states X^- and X^{-2} states are occupied according to the V_b [55]

same amount of stress, the magnitudes of the observed shifts differ substantially. This, however, can be conclusively explained by band-structure calculations for the QW and the waveguide materials. Thus, PC spectroscopy serves as an analytical tool for the analysis of packaging-induced stresses here.

Figure 6.11a, b show another example for PC analysis [54]. Here, the lateral PC of a structure is investigated, where QDs are embedded into a QW. The authors investigated both interband (a) and intersubband (b) PC. In Fig. 6.11c, PC spectra of a single self-assembled QD are shown, which were taken in vertical geometry [55]. The parameter is the bias voltage. The observed PC feature is assigned to excitonic transitions; see denotation in Sect. 4.4.3. The pronounced shift caused by the electric field is assigned to the quantum-confined Stark effect.

6.4.2 *Defect-Related (Extrinsic) Photoconductivity*

An important application of extrinsic PC is represented by extrinsic infrared detectors, which employ defect-related optical transitions. Liquid helium cooled

Ge:Au-detectors are important far infrared photoconductors. They are commercially available and used, e.g. in FT-spectrometers.

The determination of photoionization cross-sections of defects by using the constant PC technique [20] is one step towards the assignment of defect-related spectroscopic features to physical defects. As stressed in Sect. 6.2.5, this was a hot topic of basic research in semiconductor physics before people started dealing with QWs in the 1980s.

Defect-related PCs in QW structures have not been systematically investigated by far. Nevertheless, there are some studies. Aoki et al. [56] found defect related PC lines when investigating QW structures and assigned them to electron-acceptor absorption in the buffer layer. Ropers et al. [57] used FT PC in order to detect defect-related PC contributions within diode lasers. By fitting these contributions according to (6.18), the ionization energies of the defect levels were determined. For pristine devices, these defect levels have been found to be something like a finger-print of a given laser structure. Moreover, the defect-related PC contributions increased after device aging.

Internal transitions in defects, e.g. the excitation of bound electrons from the ground state of a hydrogen-like donor to the first excited state with no photo-ionization of the donor, are not expected to generate free carriers and thus, no PCs are expected. Stillman et al. [58], however, performed far-infrared PC measurements and found distinct lines that were caused by internal transitions in shallow donors in GaAs; see Fig. 6.12. The authors assigned the peaks to the isolated (ls-2p) and (ls-3p) transitions within the donor. From the energy of these peaks and their split in a magnetic field, a donor ionization energy of 5.86 ± 0.02 meV has been obtained. Obviously, there must have been a secondary effect, which increased the conductivity of their samples, when the electrons reached the exited states.

6.4.3 *Laser Beam Induced Current (LBIC)*

The term *Laser Beam Induced Current*, sometimes also Light Beam Induced Current or Optical Beam Induced Current (OBIC), has been created in reference to the term EBIC, which represents the well-known electron-beam-based pendant.

An LBIC measurement is a spatially resolved PC measurement, i.e. a scan or map, where only one single excitation wavelength is used. This idea came up even before suitable excitation lasers were available. Oroshnik et al. [59] reported on homogeneity tests of doped Ge-crystals by *photovoltaic scanning* or *photoscanning* by using a source of white light. Later, laser sources have been introduced, which allowed to create diffraction-limited probe spots.

The physics behind LBIC generation is, of course, the same as for PC. Typically, LBIC is excited by photons with $\hbar\omega > E_g$, i.e. by generation of free carriers due to interband excitation, resulting predominantly in intrinsic PCs. For $\hbar\omega > E_g$, LBIC

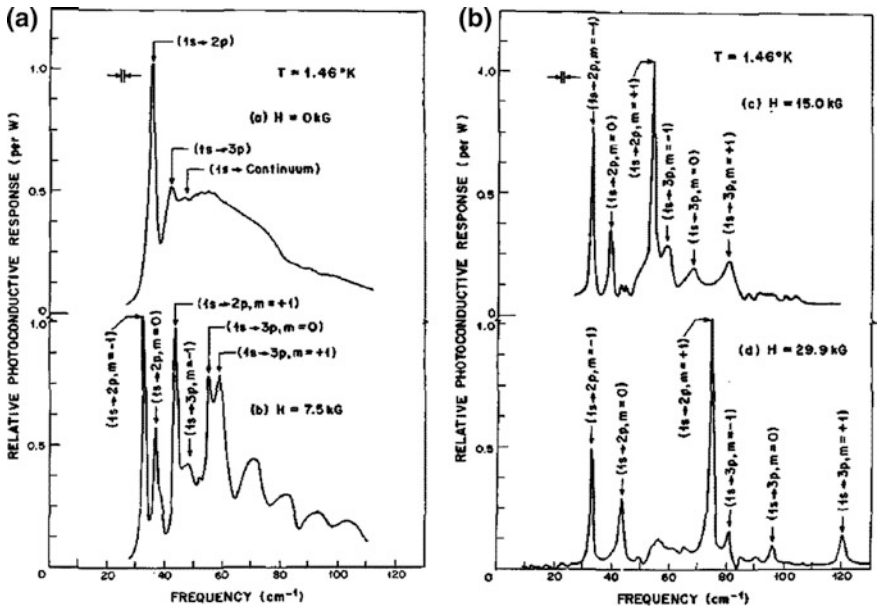

Fig. 6.12 Far-infrared PC due to internal transition of donors in high-purity GaAs for different external magnetic fields [58]

represents almost a one-to-one pendant to EBIC. In contrast to EBIC, LBIC is absolutely non-destructive.

Another advantage of LBIC compared to EBIC is its ability to implement *selective excitation*. This means that $\hbar\omega$ can be used in order to visualize effects, which have been studied before by monitoring PC spectra.

- For instance, an excitation wavelength $\hbar\omega < E_g$ could activate defect-related PC mechanisms, and reveal defect distributions in this way. This approach has been introduced by Lang et al. [60] and is called *scanning photocurrent microscopy*.
- For $\hbar\omega \gg E_g$, areas of enhanced surface recombination can become detectable.

The inset in Fig. 6.13 shows a scheme of an LBIC setup. The figure gives two linear LBIC scans taken along a 10 mm wide 980 nm emitting high-power diode laser array, which is made of one monolithic semiconductor chip that is subdivided into 25 parallel single emitters. Two excitation photon energies have been applied, one below and one above the absorption edge of the QW of the device. While both mirror the device architecture with the 25 emitters, the excitation energy of 1.17 eV reveals defect-related absorptions. Defect absorption beyond a uniform background (probably given by the epitaxy) is observed at the device edges and at emitters 2, 3, and 17 from the left. A technical peculiarity of this experiment is that it is a one-dimensional scan only. In order to meet the demand to hit the 1 μm thick active layer along a path of 10 mm perfectly, the excitation beam was shaped by a cylindrical lens to a 3 μm wide and 1 mm high 'light bar'. Thus the lateral spatial

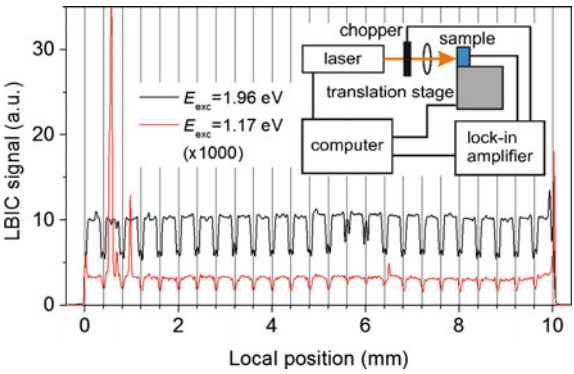

Fig. 6.13 LBIC data from a 1 cm wide diode laser array emitting at 808 nm (1.53 eV, representing the lowest QW-transition). The array consists of 25 emitters. Photons with 1.96 eV excites QW and waveguide and create an interband-like PC. Photon energies of 1.17 eV, however, can excite defects only. The resulting LBIC-scan is therefore indicative for defects and pinpoints degraded emitters. For the example shown, emitters 2, 3, and 17 (from the *left*) show differently pronounced defect signatures. The inset gives a scheme of an LBIC setup

resolution amounts to ~ 3 µm, while the vertical spatial resolution is given by the 1 µm thick active region, where the *pn*-junction represents the only photosensitive area at the device. The 1 mm vertical height of the light line ensures that the active region is hit by the laser beam even if the laser array is slightly tilted. Thus, this special LBIC setup represents a rather robust test stage for everyday device screening.

Figure 6.14 shows a two-dimensional LBIC map that has been taken from a quadratic silicon photodiode, which was placed slightly tilted on the scanning stage. The shape of the active area of the device is well reproduced including the reflection effects at the four edges. Inhomogeneities and dust particles (mainly bottom right) can be seen as well as an effect related to the scanning process itself that took a total measuring time of about 22 h (512×512 data points, look-in time constant 100 ms, dwell time at each position 300 ms). The look-in signal increased overnight because of reduced (unchopped) DC background lighting to the diode. Notice that the lab windows blinds were open all the time. Thus, the point of operation of the AC measurement shifted during the day into a non-linear region (saturation). The strength of this effect is explained by fact that the entire active area of the diode ($\sim 2 \times 2$ mm^2) has been effective in order to shift the operation point, while the LBIC signal has been generated by 20 µW of a 633 nm laser beam that was focused to ~ 3 µm in diameter. This example also illustrates the interplay between AC and DC signals in such look-in based experiments.

A high-performance LBIC setup is described by Rezek et al. [61] and is used to determine the opto-electronic properties of microcrystalline silicon films. In such samples, LBIC reveals built-in fields in the vicinity of grain boundaries, which serve for carrier separation and thus for the generation of a signal. The grain boundaries themselves appear dark because of enhanced recombination at these internal surfaces. Photocurrent generation and the effective transport properties in

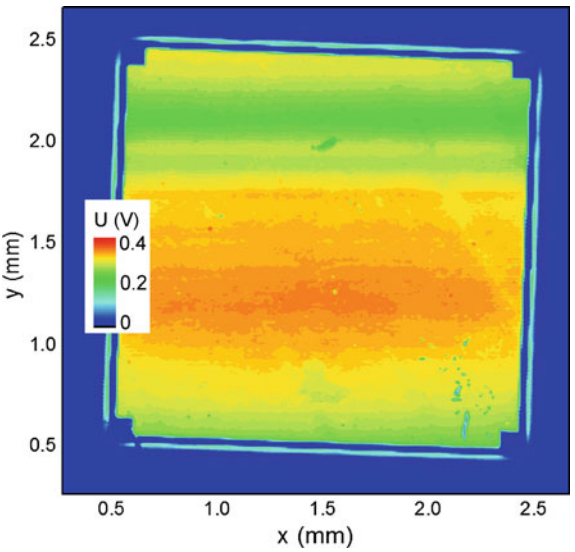

Fig. 6.14 LBIC map of the chip of a Si-photodiode

core-shell CdS/CdSe nanorod films have been analyzed by Kudera et al. [62] by using LBIC measurements. Ostendorf et al. [63] used LBIC maps that have been measured by using several excitation wavelengths in order to independently determine diffusion length and surface recombination across Si-samples.

To summarize, LBIC is an inexpensive, non-destructive, and versatile tool for semiconductor material and device analysis. It ideally complements PC spectroscopy because it spatially visualizes effects, which have been discovered only within PC spectra before. The excitation wavelength should be chosen according to what the PC analysis revealed as 'interesting'. The most common excitation photon energies are above E_g. In this case, a situation as known from EBIC is created. Frequently, microscopes are used for LBIC experiments. This allows us to achieve a spatial resolution which is set by the diffraction limit.

Near-field Optical Beam Induced Current (NOBIC)

Spatial resolutions beyond the diffraction limit can be achieved by replacing the laser beam as an excitation source with light that emerges from a nearfield-tip, such as shown in Fig. 4.26a.

It turned out that the application of NOBIC to the analysis of diode lasers was very fruitful because the thicknesses of epitaxial layers in the architecture of standard diode lasers ranges from 10 nm (e.g. QW) to several µm (e.g. cladding layers). In particular the range below 300 nm is hardly resolved by LBIC, while the resolution of NOBIC ($\sim$50 nm) matches this thickness range exactly. Moreover, cleaved facets of edge-emitting diode lasers are well accessible for fiber tips and suitable contacts are attached to the devices for power supply anyway. Measurements across the epilayers, in particular along the growth direction, allow a detailed *nanoscopic analysis* of

- spatial profiles of the confined waveguide modes of semiconductor lasers [64],
- potential gradients [65], and
- degradation effects [66] in different types of edge-emitting GaAs- and GaN-based devices.

References

1. J.W. Tomm, V. Strelchuk, A. Gerhardt, U. Zeimer, M. Zorn, H. Kissel, M. Weyers, J. Jiménez, J. Appl. Phys. **95**, 1122 (2004)
2. G. Duggan, G.B. Scott, J. Appl. Phys. **52**, 407 (1981)
3. H. Schneider, K.v. Klitzing, Phys. Rev. B **38**, 6160 (1988)
4. A.M. Fox, D.A.B. Miller, G. Livescu, J.E. Cunningham, W.Y. Jan, IEEE J. Quant. Electron. **27**, 2281 (1991)
5. W.K. Metzger, R.K. Ahrenkiel, J. Dashdorj, D.J. Friedman, Phys. Rev. B **71**, 035301 (2005)
6. J. Nelson, M. Paxman, K.W.J. Barnham, J.S. Roberts, C. Button, IEEE J. Quant. Electron. **29**, 1460 (1993)
7. H. Schneider, H.C. Liu, *Quantum Well Infrared Photodetectors: Physics and Applications*, vol. 126, 1st edn. (Springer, Berlin, 2006)
8. A. Coret, A. Haydar, Phys. Status Solidi (a) Appl. Res. **56**, 531 (1979)
9. A. Haydar, A. Coret, J. Phys. **C6**(7), C6 (1980)
10. J.W. Tomm, B. Ullrich, X.G. Qiu, Y. Segawa, A. Ohtomo, M. Kawasaki, H. Koinuma, J. Appl. Phys. **87**, 1844 (2000)
11. J. Kuhl, E.O. Gobel, T. Pfeiffer, A. Jonietz, Appl. Phys. A Mater. Sci. Process. **34**, 105 (1984)
12. D.V. Lang, R.A. Logan, M. Jaros, Phys. Rev. B **19**, 1015 (1979)
13. D.V. Lang, R.A. Logan, Phys. Rev. Lett. **39**, 635 (1977)
14. H.X. Jiang, G. Brown, J.Y. Lin, J. Appl. Phys. **69**, 6701 (1991)
15. H.X. Jiang, A. Dissanayake, J.Y. Lin, Phys. Rev. B **45**, 4520 (1992)
16. H.G. Grimmeiss, L.A. Ledebo, J. Appl. Phys. **46**, 2155 (1975)
17. G. Lucovsky, Solid State Commun. **3**, 299 (1965)
18. H.G. Grimmeiss, L.A. Ledebo, J. Phys. C Solid State Phys. **8**, 2615 (1975)
19. S. Braun, G.H.G., J. Appl. Phys. **45**, 2658 (1974)
20. B. Monemar, H.G. Grimmeiss, Prog. Cryst. Growth Charact. Mater. **5**, 47 (1982)
21. M. Takikawa, K. Kelting, G. Brunthaler, M. Takechi, J. Komeno, J. Appl. Phys. **65**, 3937 (1989)
22. D. Genzow, Phys. Status Solidi B Basic Res. **55**, 547 (1973)
23. T.S. Moss, J. Phys. Chem. Solids **22**, 117 (1961)
24. H. Nakata, A. Yokoyama, N. Tsubouchi, K. Fujii, Phys. B Condens. Matter **376**, 220 (2006)
25. C.M. Penchina, J.S. Moore, N. Holonyak, Phys. Rev. **143**, 634 (1966)
26. M.J. Chou, D.C. Tsui, G. Weimann, Appl. Phys. Lett. **47**, 609 (1985)
27. R.H. Bube, Phys. Rev. **99**, 1105 (1955)
28. E. Beham, A. Zrenner, F. Findeis, M. Bichler, G. Abstreiter, Phys. E-Low-Dimension. Syst. Nanostruct. **13**, 139 (2002)
29. J.W. Tomm, A. Bärwolff, T. Elsaesser, J. Luft, Appl. Phys. Lett. **77**, 747 (2000)
30. H. Oheda, J. Appl. Phys. **52**, 6693 (1981)
31. W.C. Mitchel, G.J. Brown, L.S. Rea, S.R. Smith, J. Appl. Phys. **71**, 246 (1992)
32. J.W. Tomm, A. Bärwolff, A. Jaeger, T. Elsaesser, J. Bollmann, W.T. Masselink, A. Gerhardt, J. Donecker, J. Appl. Phys. **84**, 1325 (1998)
33. P. Blood, J. Appl. Phys. **58**, 2288 (1985)
34. C.H. Henry, P.M. Petroff, R.A. Logan, F.R. Merritt, J. Appl. Phys. **50**, 3721 (1979)

35. J.S. Weiner, D.S. Chemla, D.A.B. Miller, H.A. Haus, A.C. Gossard, W. Wiegmann, C.A. Burrus, Appl. Phys. Lett. **47**, 664 (1985)
36. P.M. Smowton, P. Blood, P.C. Mogensen, D.P. Bour, Int. J. Optoelectron. **10**, 383 (1996)
37. J.W. Tomm, R. Müller, A. Bärwolff, T. Elsaesser, D. Lorenzen, F.X. Daiminger, A. Gerhardt, J. Donecker, Appl. Phys. Lett. **73**, 3908 (1998)
38. E. Harnik, A. Many, N.B. Grover, Rev. Sci. Instrum. **29**, 889 (1958)
39. N. Honma, C. Munakata, H. Itoh, T. Warabisako, Jpn. J. Appl. Phys. Part 1 Regul. Pap. Short Notes Rev. Pap. **25**, 743 (1986)
40. C. Munakata, N. Honma, H. Itoh, Jpn. J. Appl. Phys. Part 2 Lett. **22**, L103 (1983)
41. C. Longeaud, J.P. Kleider, Phys. Rev. B **45**, 11672 (1992)
42. C. Longeaud, J.A. Schmidt, J.P. Kleider, Phys. Rev. B **73**, 235316 (2006)
43. C. Longeaud, J.A. Schmidt, R.R. Koropecki, Phys. Rev. B **73**, 235317 (2006)
44. J.A. Schmidt, C. Longeaud, R.R. Koropecki, R. Arce, J.P. Kleider, J. Non-Cryst. Solids **354**, 2914 (2008)
45. C. Longeaud, J.P. Kleider, P. Kaminski, R. Kozlowski, M. Pawlowski, J. Cwirko, Semicond. Sci. Technol. **14**, 747 (1999)
46. J.A. Schmidt, C. Longeaud, J.P. Kleider, Thin Solid Films **493**, 319 (2005)
47. C. Longeaud, J.P. Kleider, P. Kaminski, R. Kozlowski, M. Miczuga, J. Phys.-Condens. Matter **21** (2009)
48. D.T. Stevenson, R.J. Keyes, J. Appl. Phys. **26**, 190 (1955)
49. C. Hurtes, M. Boulou, A. Mitonneau, D. Bois, Appl. Phys. Lett. **32**, 821 (1978)
50. Z.Q. Fang, L. Shan, T.E. Schlesinger, A.G. Milnes, Solid-State Electron. **32**, 405 (1989)
51. R.L. Tober, W.Q. Li, P.K. Bhattacharya, J. Appl. Phys. **71**, 3506 (1992)
52. S.A. Tabatabaei, A.A. Iliadis, C.E.C. Wood, J. Electron. Mater. **24**, 87 (1995)
53. J.W. Tomm, A. Gerhardt, R. Muller, M.L. Biermann, J.P. Holland, D. Lorenzen, E. Kaulfersch, Appl. Phys. Lett. **82**, 4193 (2003)
54. L. Hoglund, C. Asplund, Q. Wang, S. Almqvist, H. Malm, E. Petrini, J.Y. Andersson, P.O. Holtz, H. Pettersson, Appl. Phys. Lett. **88**, 213510 (2006)
55. F. Findeis, M. Baier, E. Beham, A. Zrenner, G. Abstreiter, Appl. Phys. Lett. **78**, 2958 (2001)
56. K. Aoki, M. Sakamoto, T. Tanigawa, Phys. E-Low-Dimension. Syst. Nanostructures **40**, 1642 (2008)
57. C. Ropers, T.Q. Tien, C. Lienau, J.W. Tomm, P. Brick, N. Linder, B. Mayer, M. Muller, S. Tautz, W. Schmid, Appl. Phys. Lett. **88**, 133513 (2006)
58. G.E. Stillman, C.M. Wolfe, J.O. Dimmock, Solid State Commun. **7**, 921 (1969)
59. J. Oroshnik, A. Many, J. Electrochem. Soc. **106**, 360 (1959)
60. D.V. Lang, C.H. Henry, Solid-State Electron. **21**, 1519 (1978)
61. B. Rezek, C.E. Nebel, M. Stutzmann, J. Non-Cryst. Solids **266**, 315 (2000)
62. S. Kudera, Y. Zhang, E. Di Fabrizio, L. Manna, R. Krahne, Phys. Rev. B **86**, 075307 1 (2012)
63. H.-C. Ostendorf, A.L. Endrös, Appl. Phys. Lett. **71**, 3275 (1997)
64. T. Guenther, V. Malyarchuk, J.W. Tomm, R. Muller, C. Lienau, J. Luft, Appl. Phys. Lett. **78**, 1463 (2001)
65. S. Friede, S. Kuehn, J.W. Tomm, V. Hoffmann, U. Zeimer, M. Weyers, M. Kneissl, T. Elsaesser, Semicond. Sci. Technol. **29**, 112001 (2014)
66. A. Richter, J.W. Tomm, C. Lienau, J. Luft, Appl. Phys. Lett. **69**, 3981 (1996)

Index

J. Jimenez and J.W. Tomm, *Spectroscopic Analysis of Optoelectronic Semiconductors*, Springer Series in Optical Sciences 202,
DOI 10.1007/978-3-319-42349-4